

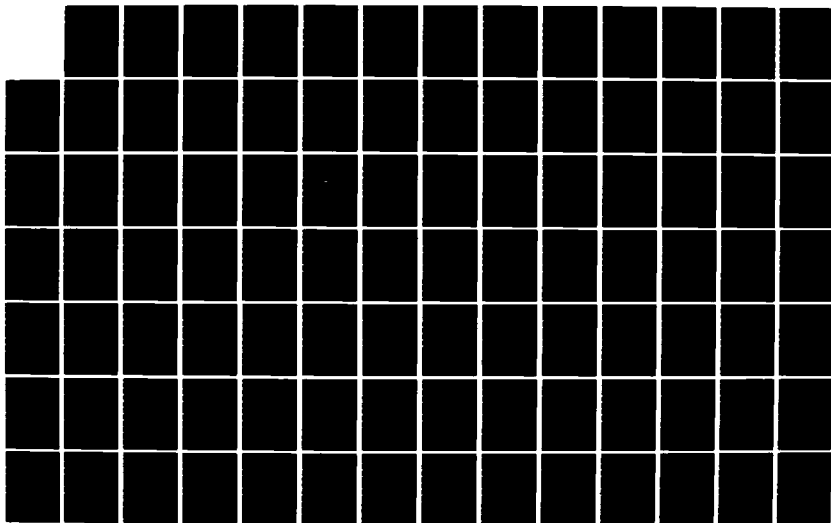
AD-A133 136

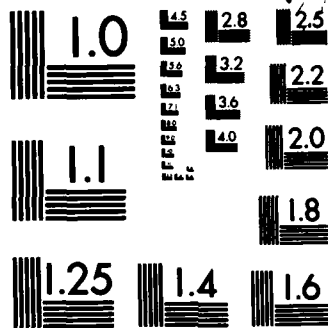
GROWTH PROCESSES OF SNOW(U) MASSACHUSETTS INST OF TECH  
CAMBRIDGE K K LO MAY 83 AFGL-TR-83-0105  
F19628-80-C-0021

1/2

UNCLASSIFIED

F/G 8/12 NL





MICROCOPY RESOLUTION TEST CHART  
NATIONAL BUREAU OF STANDARDS-1963-A

12

AD-A133 136

AFGL-TR-83-0105

GROWTH PROCESSES OF SNOW

Kwok-Wai Kenneth Lo

Massachusetts Institute of Technology  
77 Massachusetts Avenue  
Cambridge, Massachusetts 02139

Final Report

1 November 1979 - 28 February 1983

May 1983

Approved for public release; distribution unlimited

DTIC FILE COPY

AIR FORCE GEOPHYSICS LABORATORY  
AIR FORCE SYSTEMS COMMAND  
UNITED STATES AIR FORCE  
HANSCOM AFB, MASSACHUSETTS 01731

DTIC  
SERIALIZED  
OCT 05 1983  
S  
E

83 09 30 006

This report has been reviewed by the ESD Public Affairs Office (PA) and is releasable to the National Technical Information Service (NTIS).

This technical report has been reviewed and is approved for publication

*Morton Glass*

MORTON GLASS  
Contract Manager

*Arnold A. Barnes, Jr.*

ARNOLD A. BARNES, JR.  
Chief, Cloud Physics Branch

FOR THE COMMANDER

*Robert A. McClatchey*

ROBERT A. McCLATCHEY  
Director, Meteorology Division

Qualified requestors may obtain additional copies from the Defense Technical Information Center. All others should apply to the National Technical Information Service.

If your address has changed, or if you wish to be removed from the mailing list, or if the addressee is no longer employed by your organization, please notify AFGL/DAA/LYC Hanscom AFB, MA 01731. This will assist us in maintaining a current mailing list.

Do not return copies of this report unless contractual obligations or notices on a specific document requires that it be returned.

Unclassified

SECURITY CLASSIFICATION OF THIS PAGE (When Data Entered)

REPORT DOCUMENTATION PAGE		READ INSTRUCTIONS BEFORE COMPLETING FORM
1. REPORT NUMBER AFGL-TR-83-0105	2. GOVT ACCESSION NO. <b>AD. 4133 136</b>	3. RECIPIENT'S CATALOG NUMBER
4. TITLE (and Subtitle) GROWTH PROCESSES OF SNOW		5. TYPE OF REPORT & PERIOD COVERED Final Report 1 Nov. 1979 - 28 Feb. 1983
		6. PERFORMING ORG. REPORT NUMBER
7. AUTHOR(s) Kwok-Wai Kenneth Lo		8. CONTRACT OR GRANT NUMBER(s) F19628-80-C-0021
9. PERFORMING ORGANIZATION NAME AND ADDRESS Massachusetts Institute of Technology 77 Massachusetts Avenue Cambridge, Massachusetts 02139		10. PROGRAM ELEMENT, PROJECT, TASK AREA & WORK UNIT NUMBERS 61102F 2310G5AE
11. CONTROLLING OFFICE NAME AND ADDRESS Air Force Geophysics Laboratory Hanscom AFB, Massachusetts 01731 Monitor/Morton Glass/LYC		12. REPORT DATE May 1983
		13. NUMBER OF PAGES 192
14. MONITORING AGENCY NAME & ADDRESS (if different from Controlling Office)		15. SECURITY CLASS. (of this report)  Unclassified
15a. DECLASSIFICATION/DOWNGRADING SCHEDULE		
16. DISTRIBUTION STATEMENT (of this Report)  Approved for public release; distribution unlimited.		
17. DISTRIBUTION STATEMENT (of the abstract entered in Block 20, if different from Report)		
18. SUPPLEMENTARY NOTES Submitted as partial fulfillment of the requirements for the Degree of Doctor of Science		
19. KEY WORDS (Continue on reverse side if necessary and identify by block number) Snow Growth Meteorology Cloud Physics Precipitation Growth Winter Storm Microphysics Ice Crystals		
20. ABSTRACT (Continue on reverse side if necessary and identify by block number) The growth of snow in winter storms is studied via observational and theoretical techniques. A new flight procedure termed the Advecting Spiral Descent (ASD) was employed by AFGL's instrumented C-130 aircraft to observe the height evolution of snow size spectra. These observations reveal that snow growth goes through three distinct stages: a vapor deposition stage, an aggregation stage and a secondary ice particle production stage. Theoretical models are used to simulate the observations of snow growth. These indicate that the secondary ice crystal production is due to the collisional breakup of snowflakes.		

DD FORM 1 JAN 73 1473

EDITION OF 1 NOV 65 IS OBSOLETE

Unclassified

SECURITY CLASSIFICATION OF THIS PAGE (When Data Entered)

## ACKNOWLEDGMENT

The author expresses his appreciation to his parents for their constant support and sacrifice.

The author would like to thank his thesis supervisor, Dr. Richard E. Passarelli, Jr. for his guidance in this project and his many simulating questions which lead to fruitful ideas. He also thanks his thesis committee, Drs. Henry Houghton, Kerry Emanuel and Edward Lorenz for their fine efforts. Thanks are due Mr. Spiros Geotis for his help and for Mr. Alan Siggia for his assistance in computer work. Dr. Edgerton is appreciated for his suggestion in the photographic method. Thanks are also given to Liz Manzi for secretarial assistance and Isabell Kole for drafting the figures.

The author's stay in M. I. T. is partially supported by a grant from Air Force Geophysics Laboratory, Air Force Systems Command under contract No. F19628-80-C-0021. The support of Dr. Arnold A. Barnes, Jr. and Mr. Morton Glass of the Cloud Physics Group, AFGL is acknowledged.

For	
&I	<input checked="" type="checkbox"/>
DTIC TAB	<input type="checkbox"/>
Unannounced	<input type="checkbox"/>
Justification	
By _____	
Distribution/	
Availability Codes	
Dist _____ and/or	
Dist _____	Special
A	



## TABLE OF CONTENTS

Abstract.....	2
Acknowledgment.....	4
Table of Contents.....	5
List of Figures.....	7
List of Tables.....	13
1. Introduction.....	14
2. ASD data and analyses.....	21
2.1 ASD data.....	21
2.2 Two-parameter data analyses.....	35
2.3 Interpretation of two-parameter data analyses.....	40
2.4 Horizontal gradients in the microphysical structure.....	43
2.5 Three-parameter data analyses.....	47
2.6 Comparisons with other studies.....	62
2.7 Counter-examples.....	67
3. Theoretical analyses.....	78
3.1 Basic equations and assumptions.....	80
3.2 Two-parameter formulations.....	87
3.2.1 Exponential fragment size distribution.....	89
3.2.2 Constant fragment number distribution.....	104

3.3	Three-parameter formulations.....	109
3.3.1	Exponential fragment size distribution.....	110
3.3.2	Constant fragment number distribution.....	124
3.4	Effects of different initial conditions.....	130
3.5	Investigations of rime-splintering.....	136
3.6	Deposition-aggregation-rime splintering simulation.....	147
3.6.1	Two-parameter formulation .....	147
3.6.2	Three-parameter formulation .....	151
3.7	Effects of melting.....	161
4.	Conclusions.....	167
 Appendices		
A.1	The growth of snow in winter storms: An airborne observational study.....	173
A.2	Laboratory investigation of collisional breakup.....	183
	References.....	189

## LIST OF FIGURES

2.1:	Surface map, West Coast, 1200 GMT 25 February, 1980 .....	24
2.2:	Surface map, West Coast, 1200 GMT 26 February, 1980 .....	25
2.3:	Surface map, East Coast, 1200 GMT 8 March, 1980	26
2.4:	Aircraft soundings for the three flights .....	27
2.5:	Snow-size spectra for spiral 1 (25 February, 1980) averaged over the various loops. Numbers on the right indicate loop numbers.....	28
2.6	Snow-size spectra for spiral 2 (26 February, 1980) averaged over the various loops. Numbers on the right indicate loop numbers .....	29
2.7	Snow-size spectra for spiral 3 (8 March, 1980) averaged over the various loops. Numbers on the right indicate loop numbers .....	30
2.8	Icing rate measurement for 25 February, 1980. Abscissa is time (in sec.) elapsed after the beginning of flight.....	32
2.9	ASSP particle concentration (with smallest size category ignored) for 25 February, 1980.....	32
2.10:	Icing rate measurement for 26 February, 1980. (Layout similar to Fig. 2.8).....	34
2.11:	ASSP particle concentration (with smallest size category ignored) for 26 February, 1980.....	34
2.12:	Icing rate measurement for 8 March, 1980. (Layout similar to Fig. 2.8) .....	36
2.13:	ASSP particle concentration (with smallest size category ignored) for 8 March, 1980 .....	36
2.14:	$N_0 - \lambda$ trajectories for the three spirals. See text for details .....	38
2.15:	Average particle diameter as a function of magnetic heading for spirals 1 and 2. Diameters in mm.....	44

- 2.16:  $N_0-\lambda$  trajectories for the four cardinal quadrants for spiral 2. The  $N_0$  scale refers to the north-east quadrant. The other quadrants are shifted downward by one-half decade each to differentiate the data ..... 46
- 2.17:  $N_x$  as a function of height, 25 February, 1980, the stages of snow growth are marked by dashed lines ..... 50
- 2.18:  $N_x$  as a function of height, 26 February, 1980, similar to Fig. 2.17 ..... 51
- 2.19:  $N_x$  as a function of height, 8 March, 1980, similar to Fig. 2.17 ..... 52
- 2.20:  $\lambda_x$  as a function of height, 25 February, 1980, the stages of snow growth are marked by dashed lines ..... 54
- 2.21:  $\lambda_x$  as a function of height, 26 February, 1980, similar to Fig. 2.20 ..... 55
- 2.22:  $\lambda_x$  as a function of height, 8 March, 1980, similar to Fig. 2.20 ..... 56
- 2.23:  $\sigma$  as a function of height, 25 February, 1980, the stages of snow growth are marked by dashed lines ..... 57
- 2.24: Illustration of positive and negative  $\sigma$  ..... 59
- 2.25:  $\sigma$  as a function of height, 26 February, 1980, similar to Fig. 2.23 ..... 60
- 2.26:  $\sigma$  as a function of height, 8 March, 1980, similar to Fig. 2.23 ..... 61
- 2.27: Related observational studies. See text for details ..... 63
- 2.28:  $N_0-\lambda$  trajectory of spiral flown by Gordon et al. 1982, environmental temperature is written next to each loop ..... 66
- 2.29:  $N_0-\lambda$  trajectory of first spiral on 14 April, 1981 ..... 68
- 2.30:  $N_0-\lambda$  trajectory of second spiral on 14 April, 1981 ..... 68
- 2.31:  $N_0-\lambda$  trajectory of first spiral on 17 April, 1981 ..... 69

2.32:	$N_0$ - $\lambda$ trajectory of second spiral on 17 April, 1981 .....	69
2.33:	$N_0$ - $\lambda$ trajectories for the four cardinal quadrants for first spiral on 14 April, 1981.....	71
2.34:	Aircraft soundings for spirals on 17 April, 1981 .....	72
2.35:	1-D precip probe total particle concentration and second moment against height for first spiral on 17 April, 1981 .....	73
2.36:	1-D precip probe total particle concentration and second moment against height for second spiral on 17 April, 1981 .....	73
2.37:	1-D precip probe second moment against height for the three spirals in 1980 .....	75
2.38:	1-D precip probe total concentration against height for the three spirals in 1980 .....	75
2.39:	Possible size distributions beyond the range detectable by the 200-Y probe at three different times .....	76
2.40:	Snow size spectra of the last few loops for the first spiral on 17 April, 1981 .....	77
2.41:	Snow size spectra of the last few loops for the second spiral on 17 April, 1981 .....	77
3.1:	Coalescence probability $q$ as a function of the total diameter $D'+D''$ and the constant $c$ .....	88
3.2:	Number of fragments resulting from collision of a 2 mm particle and particles of various sizes for different $\Lambda$ 's .....	88
3.3:	Two-parameter model evaluations for spiral on 25 February, 1980, exponential breakup fragment size distribution. See text for details .....	93
3.4:	Two-parameter model evaluations for spiral on 26 February, 1980, exponential breakup fragment size distribution .....	94
3.5	Effects of different updraft velocities on two-parameter model performance, exponential breakup fragment size distribution .....	98

- 3.6: Two-parameter model evaluations for spiral on 8 March, 1980 with  $\beta=0.75$ , exponential breakup fragment size distribution ..... 99
- 3.7: Two-parameter model evaluations for spiral on 8 March, 1980 with  $\beta=2$ , exponential breakup fragment size distribution ..... 99
- 3.8: Two-parameter model evaluations for spiral on 25 February, 1980 using various values of physical parameters. exponential breakup fragment size distribution ..... 105
- 3.9: Two-parameter model evaluations for spiral on 25 February, 1980, constant breakup fragment number distribution ..... 107
- 3.10: Two-parameter model evaluations for spiral on 26 February, 1980, constant breakup fragment number distribution ..... 107
- 3.11: Two-parameter model evaluations for spiral on 8 March, 1980, with  $\beta=0.75$ , constant breakup fragment number distribution ..... 108
- 3.12: Two-parameter model evaluations for spiral on 8 March, 1980, with  $\beta=2$ , constant breakup fragment number distribution ..... 108
- 3.13:  $N_*$  from three-parameter model evaluations for spiral on 25 February, 1980, exponential breakup fragment size distribution, effects of various values of physical parameters illustrated ..... 114
- 3.14:  $\lambda_*$  for 25 February, 1980, similar to Fig. 3.13. 115
- 3.15:  $\sigma$  for 25 February, 1980, similar to Fig. 3.13. 116
- 3.16:  $N_*$  from three-parameter model evaluations for spiral on 8 March, 1980, exponential breakup fragment size distribution,  $\beta=0.75$  ..... 118
- 3.17:  $\lambda_*$  for 8 March, 1980, similar to Fig. 3.16 ..... 119
- 3.18:  $\sigma$  for 8 March, 1980, similar to Fig. 3.16 ..... 120
- 3.19:  $N_*$  from three-parameter model evaluations for spiral on 8 March, 1980, exponential breakup fragment size distribution,  $\beta=2$  ..... 121
- 3.20:  $\lambda_*$  for 8 March, 1980, similar to Fig. 3.19 ..... 122
- 3.21:  $\sigma$  for 8 March, 1980, similar to Fig. 3.19 ..... 123

3. 22:	$N_*$ from three-parameter model evaluations for spiral on 25 February, 1980, constant fragment number distribution .....	127
3. 23:	$\lambda_*$ for 25 February, 1980, similar to Fig. 3. 22 .....	128
3. 24:	$\sigma$ for 25 February, 1980, similar to Fig. 3. 22 .....	129
3. 25:	$N_*$ from three-parameter model evaluations for spiral on 8 March, 1980, constant fragment number distribution, $\beta=0.75$ .....	131
3. 26:	$\lambda_*$ for 8 March, 1980, similar to Fig. 3. 25 .....	132
3. 27:	$\sigma$ for 8 March, 1980, similar to Fig. 3. 25 .....	133
3. 28:	Effect of different initial concentrations, the smooth curves are from top to bottom 10 times, 5 times and actual total concentrations, $N_0-\lambda$ trajectories for 26 February, 1980 .....	135
3. 29:	ASSP number density of particles greater than 24 microns .....	138
3. 30:	Change of saturation vapor pressure with respect ice, $S_{v,i}$ , saturation vapor pressure with respect to water, $S_{w,i}$ and supercooled droplet radius with height, updraft 50 cm/s .....	145
3. 31:	Similar to Fig. 3. 30, updraft 20 cm/s .....	145
3. 32:	Two-parameter model of deposition, aggregation and rime-splintering, 25 February, 1980 .....	149
3. 33:	Two-parameter model of deposition, aggregation and rime-splintering, 26 February, 1980 .....	150
3. 34:	Two-parameter model of deposition, aggregation and rime-splintering, 8 March, 1980 .....	150
3. 35:	$N_*$ from three-parameter model of deposition, aggregation and rime-splintering, 25 February, 1980 .....	155
3. 36:	$\lambda_*$ from three-parameter model of deposition, aggregation and rime-splintering, 25 February, 1980 .....	156
3. 37:	$\sigma$ from three-parameter model of deposition, aggregation and rime-splintering, 25 February, 1980 .....	157

3.38:	$N_*$ from three-parameter model of deposition, aggregation and rime-splintering with weak breakup 8 March, 1980 .....	158
3.39:	Similar to Fig. 3.38 but with no rime-splintering .....	158
3.40:	$\lambda_*$ from three-parameter model of deposition, aggregation and rime-splintering with weak breakup 8 March, 1980 .....	159
3.41:	Similar to Fig. 3.40 but with no rime-splintering .....	159
3.42:	$\sigma$ from three-parameter model of deposition, aggregation and rime-splintering with weak breakup 8 March, 1980 .....	160
3.43:	Similar to Fig. 3.42 but with no rime-splintering .....	160
3.44:	Two-parameter fit to melting .....	164
3.45:	Three-parameter fit to melting .....	166
A.2.1:	Laboratory set-up investigating collisional breakup .....	184
A.2.2:	Sample 1 of crystal fragments .....	186
A.2.3:	Sample 2 of crystal fragments .....	187

## LIST OF TABLES

3.1:	Values of the physical parameters used in the two-parameter model (c. g. s. units).....	96
3.2:	Tabulation of $\lambda_0$ .....	96
3.3:	First turning point of $N_0$ .....	103
3.4:	Values of physical parameters used in the three-parameter model (c. g. s. units).....	103
3.5:	Splinter production rates by rime-splintering and particle depletion rates by aggregation.....	151
3.6:	Values of parameters used in aggregation-deposition-rime splintering simulations (c. g. s. units) .....	151
A.2.1:	Samples of fragment size distribution resulting from laboratory breakup experiments .....	188

## CHAPTER 1

## INTRODUCTION

A knowledge of snow growth is important not only in the understanding of wintertime precipitation itself, but also in other kinds of precipitation when the Wegener-Bergeron process is important. Besides the understanding of precipitation processes, the investigation of snow growth mechanisms is also essential to artificial cloud seeding and to small scale parameterization in large-scale general circulation models and in numerical weather prediction models.

The study of snow growth can be by different means, such as laboratory investigation, numerical modelling, in situ observations and mathematical analysis. Each of these approaches has its advantages and limitations. Laboratory investigations on snow growth have the advantage of being able to study it in a controlled environment. The temperature, humidity and other factors can be under strict control of the experimenter. However, the conditions inside a laboratory are rather ideal and can be quite different from

the actual atmospheric environment. In addition, because of the difficulty of performing laboratory experiments, the physical processes of snow growth can be studied only one at a time. Laboratory investigations on secondary ice crystal production by crystal-crystal collision has been performed by Vardiman (1978) who stresses the possibility of collisional breakup in explaining the presence of the high density of ice crystals in stratiform clouds with embedded convection. The drawback of this experiment is that ice crystals are caused to impact on hard surface which is quite different from the effect of crystal-crystal collision. Blanchard and Spencer (1970) perform experiments on the binary interactions of raindrops. They establish the importance of drop breakup in determining an exponential drop size distribution. Mossop and Hallet (1974), Hallet and Mossop (1974) and Mossop (1976) report laboratory experiments on secondary ice crystal production due to rime-splintering. They conclude that the rate of splinter production is a function of the concentration of supercooled liquid water droplets larger than 24 microns between  $-8^{\circ}\text{C}$  and  $-3^{\circ}\text{C}$ .

Numerical modelling has the advantage of being able to incorporate many physical processes of snow growth plus the interaction between microphysics and dynamics in a single study. The drawback of numerical modelling is that physical insights can easily be lost in a large model. Moreover, the

computation time required for a full model can be enormous. Young (1975) performs numerical model of raindrop evolution with the physical processes of condensation, coalescence and breakup. It is found that the effect of collisional breakup dominates over the effect of spontaneous breakup and produces an exponential raindrop size distribution. The results are insensitive to the collision efficiency and the steady-state spectrum is insensitive to the number of breakup fragment. Gillespie and List (1976) study the evolution of raindrop size distributions in steady state rainshafts using a numerical stochastic coalescence-breakup model. The results conclude that there is only one equilibrium distribution which depends on the rainfall rate for each Marshall-Palmer distribution. Leighton (1980) uses a numerical model to study the deposition and aggregation processes of snowflakes and concludes that the assumption of exponential snow size distribution is valid and he also confirms the analytical results of Passarelli (1978b).

In situ observations of snow growth became feasible since the development of laser imaging probes. This technique of studying snow growth has one advantage which no other techniques have in that what is observed is also what actually happens in the atmosphere. However, the data obtained, such as the snow size distribution (e.g. Lo and Passarelli, 1982a) and the two dimensional shapes of snow

crystals (e.g. Dyer and Glass, 1982), are the results of snow growth, while the physical processes of snow growth have to be inferred from these data. The changes of snow-size spectra with height have been performed by Passarelli (1978a, c) and by Houze et al. (1979). The findings show that snow size spectra change rather systematically with height. A way to interpret the change of snow-size spectra will be presented in chapter 2. Gordon et al (1982) uses a technique similar to Lo and Passarelli (1982a). They conclude that snow growth goes through four stages where different physical processes predominate, namely the vapor deposition stage, the aggregation stage, the secondary ice crystal production stage and the an aggregation stage.

Analytical studies of snow growth provides the best insight concerning the physical mechanism of snow growth. But, in order to simplify the mathematics so that analytical solutions can be obtained, many assumptions have to be made in the set up of the problem. Also, in order to keep the mathematical problem tractable, only a few of the physical processes can be treated at one time. Srivastava (1971) studies the effect of coalescence and breakup in raindrop growth and concludes that the binary interactions give rise to an equilibrium size distribution slope. Passarelli (1978b) calculated the evolution of snow-size distribution in a winter-time stratiform snow situation using an analytical

model with vapor deposition and aggregation. He concludes that the equilibrium snow size spectra owe their existence to the counteracting effects of deposition and aggregation growth.

Previously, the main thrust of the study of the microphysical processes of precipitation growth has been on raindrops. Few investigations have been made to study the snow growth processes more comprehensively. The study presented here is an attempt to give a comprehensive picture of the snow growth processes once the snow crystals have been initiated. The methodology used is basically a combination of all four techniques, with particular emphases on in situ aircraft observations and mathematical analyses.

Chapter 2 presents the in situ observational data and their analyses. The observations are made by using a single aircraft. This new flight plan is devised so as to permit one to observe the height evolution of snow-size spectra in a reference frame where the effects of horizontal gradients and temporal changes in the atmosphere are minimized (Lo and Passarelli, 1982a, see appendix 1). This flight plan, termed the advecting spiral descent (ASD), requires an aircraft to start aloft in a mesoscale precipitation area (e.g. a snow shaft, Marshall, 1953) and spiral downward in a constant bank angle, descending at approximately the mean fallspeed of

snow. The loops of the spiral drift with the wind. The analysis is performed by averaging spectra over a complete loop of the spiral, serving to average any horizontal inhomogeneities.

The snow-size spectra are first analysed using the conventional negative exponential size distribution. From the behavior of the size spectra, the physical processes of snow growth can be inferred. From these analyses, the horizontal gradients of microphysical structure are also studied. The data are then analysed using a negative exponential, power law snow-size distribution. This new technique of describing the size distribution provides certain new insights. Finally, these data are compared with other flight data.

Chapter 3 presents theoretical models of snow growth. The physical processes represented in the models include vapor deposition, aggregation, collisional breakup and rime-splintering. The basic equation makes use of the stochastic collection formulation. Snow size spectra are represented either in a negative exponential distribution or in a negative exponential, power law distribution (Lo and Passarelli, 1982b). From the basic equation, moment conservation equations are derived. The equations are simplified analytically as far as possible and the resulting

equations are then solved numerically. The results are compared with the observational data presented in chapter 2. The question of secondary production is further addressed.

In order to facilitate the formulation of the collisional breakup term, laboratory experiments on the collisional breakup fragment size distribution of snow particles are performed and are presented in appendix 2.

The conclusions for the entire study and suggestions for future work are provided in chapter 4.

## Chapter 2

### ASD DATA AND ANALYSES

#### 2.1 ASD Data

Advecting spiral descents were flown with an Air Force Geophysics Laboratory C-130 aircraft that is equipped with thermodynamic and cloud physics sensors (Barnes et al., 1982). The thermodynamic sensors are a dew point hygrometer and total air temperature probe. The cloud physics sensors include a Ewer probe for total water and ice, icing rate detector, Johnsons-Williams (J-W) cloud water probe, total water content indicator, formvar hydrometeor replicator and several Particle Measuring Systems (PMS) probes, including an axially scattering spectrometer probe (ASSP), a 1-D cloud probe, a 1-D precipitation probe, a 2-D cloud probe and a 2-D precipitation probe (Knollenberg, 1970).

In this study, basically only the data from the 1-D precipitation probe have been used in the quantitative analyses. This is a laser imaging probe that counts and sizes particles into 15 size categories ranging from 300 to 4500 microns. The data from the 1-D cloud probe (which

measures particles in the size range of 20 to 300 microns) are not used because there is a serious discrepancy in the number density at the size range where the cloud probe and the precipitation probe overlap. It is true that certain investigators have attempted to smooth the differences but the smoothing techniques tend to be rather artificial (Belksy et.al., 1981). The 2-D data are used qualitatively to determine the crystal type. No quantitative analyses of the 2-D data have been done. The data from the J-W water content probe, icing rate detector probe and ASSP are used to determine cloud liquid water content. However, there is a problem inherent with the ASSP in snow-storm situations. The ASSP operates on a light scattering principle and therefore can easily give false counts from the light scattered or reflected off the snow particles.

There is a difficulty in using the airborne temperature measurement in that the true air temperature computed is sometimes lower than the dew point temperature by approximately 1°C. In plotting the soundings, saturation is assumed whenever this happens.

Extensive analyses from three flights are presented with supplementary data from other flights. Two of the three flights were made off the coast of Washington (25 and 26 February 1980) and one off the coast of New Hampshire (8

March 1980). One ASD was performed on each day and these will be referred to as spirals 1, 2 and 3 respectively. All three spirals took place in winter cyclonic storms. Spiral 1 was flown just ahead of an occluded front (Fig. 2.1) and spiral 2 was flown approximately 100 km east of a low-pressure center (Fig. 2.2). Spiral 3 was flown in the warm sector of a cyclonic storm (Fig. 2.3). The soundings obtained from the aircraft data (Fig. 2.4) indicate that the atmosphere was slightly more stable than moist adiabatic and was saturated or near saturated in all cases. The height and temperature ranges for the three spirals are given in Table 2.1.

Snow size spectra averaged over a complete loop are shown in Figs. 2.5, 2.6 and 2.7 for spirals 1, 2 and 3 respectively. The spectra are labeled consecutively from the top to the bottom loops of the spiral. Because the spectra are almost negative exponential, the plots on a linear-log scale result in straight lines. Therefore, the concept of intercept and slope can be applied here. The spectra from the first spiral show an initial monotonic increase in the intercept while the slope remains relatively constant through loop 12, after which there is a rapid decrease in both the slope and intercept during loops 13 and 14. The remainder of the loops show essentially no change. The vertical separation between successive loops is 200 m.

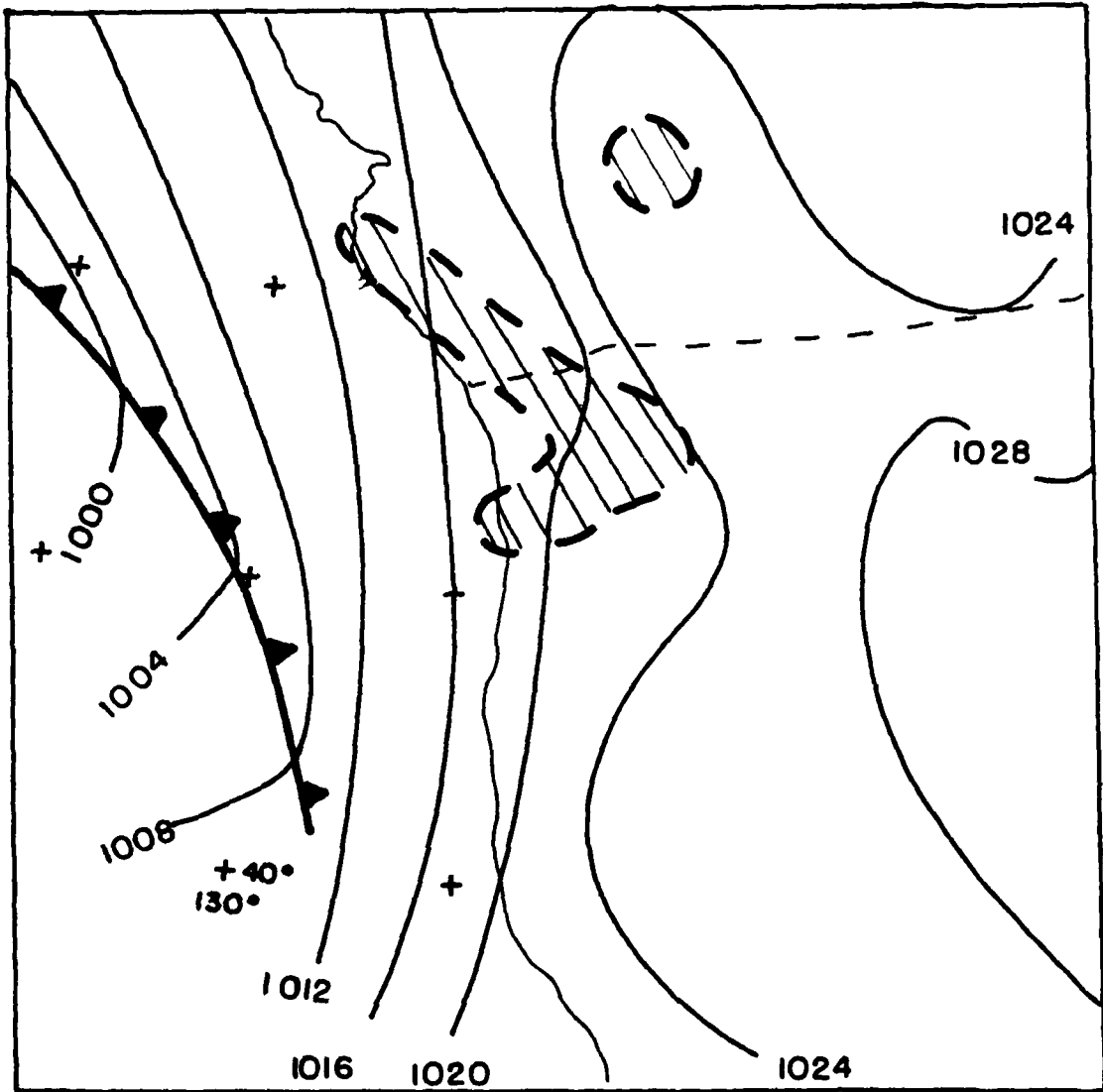


Fig.2.1: Surface map, West Coast, 1200 GMT 25 February, 1980

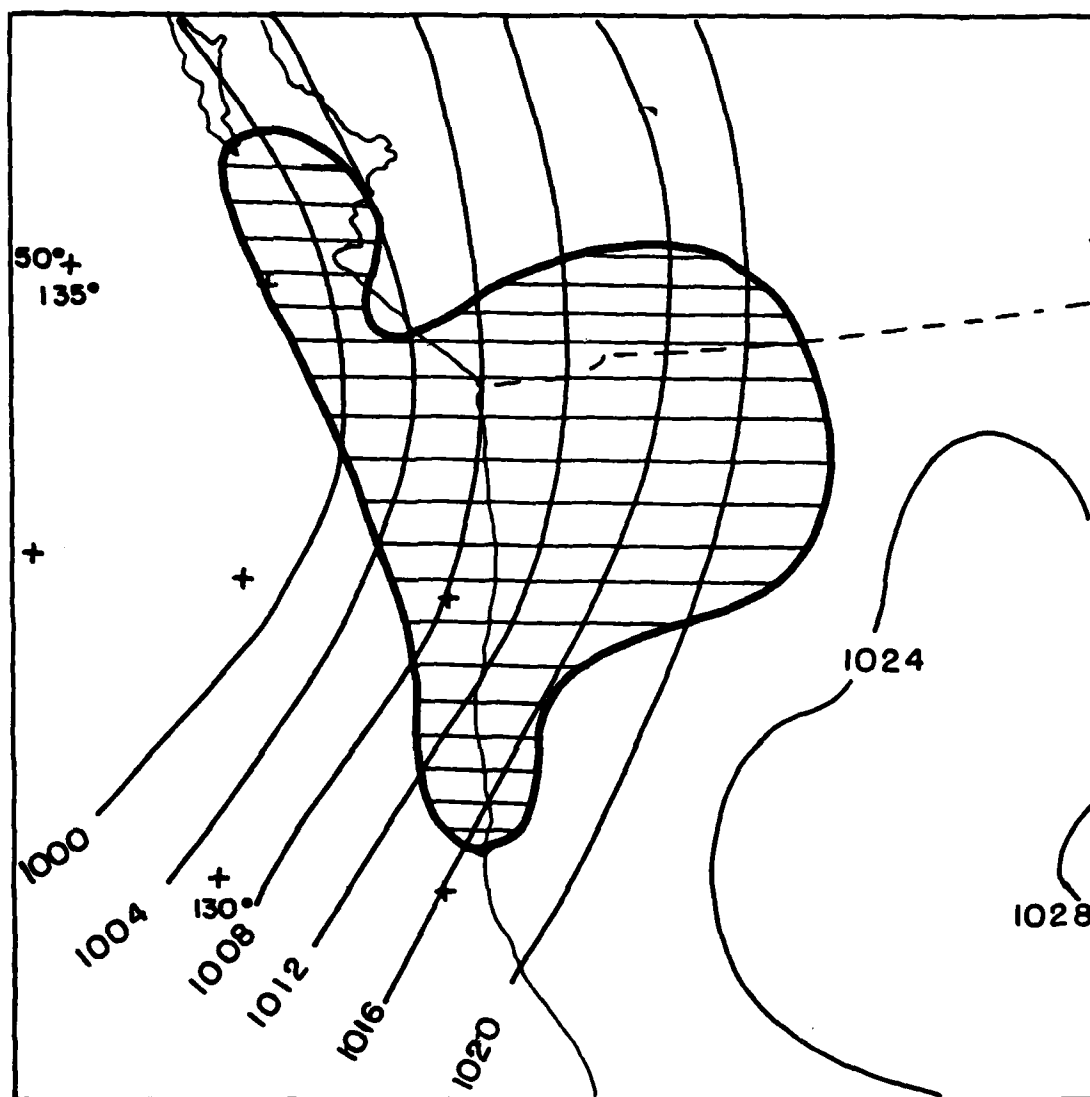


Fig.2.2: Surface map, West Coast, 1200 GMT 26 February, 1980

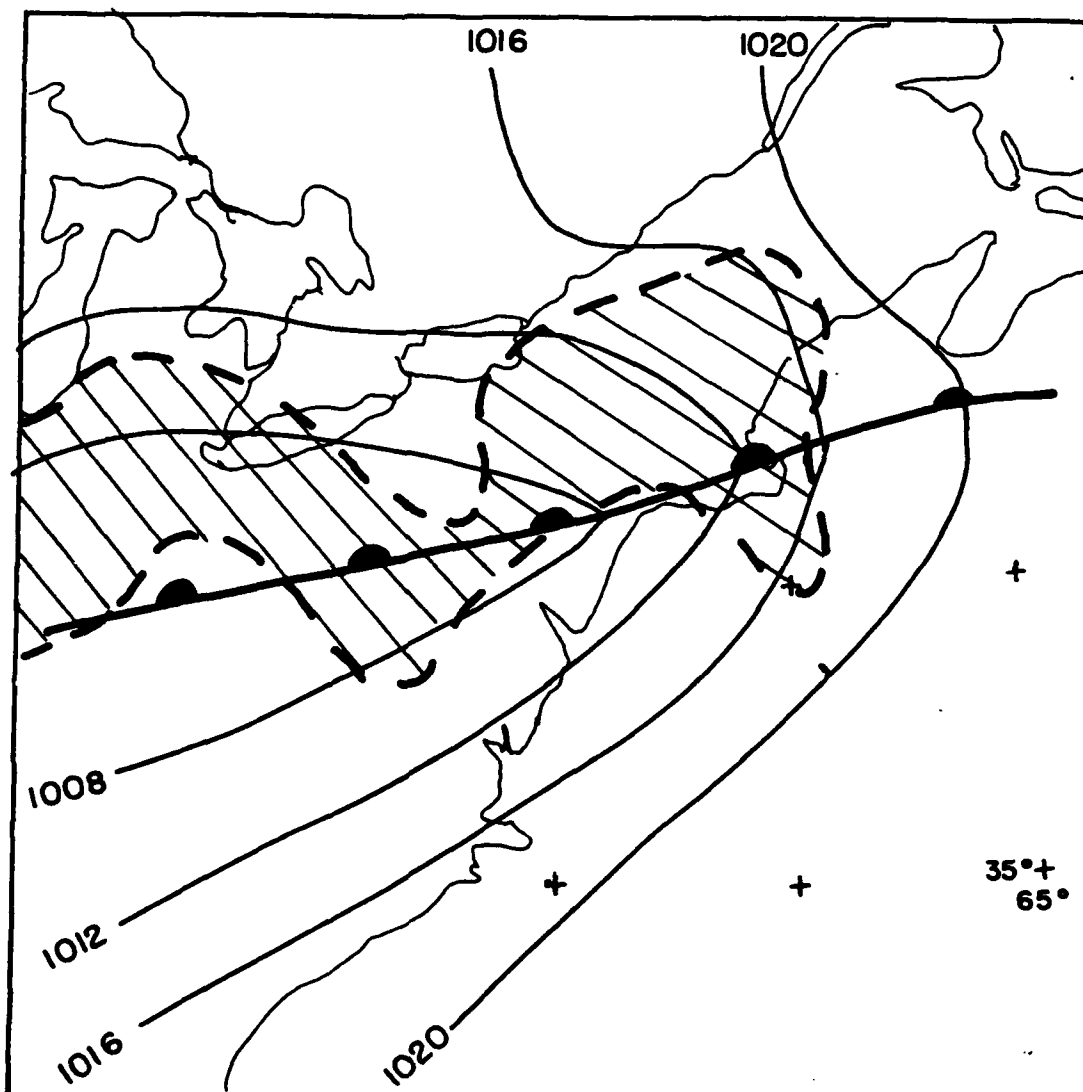


Fig.2.3: Surface map, East Coast, 1200 GMT 8 March, 1980

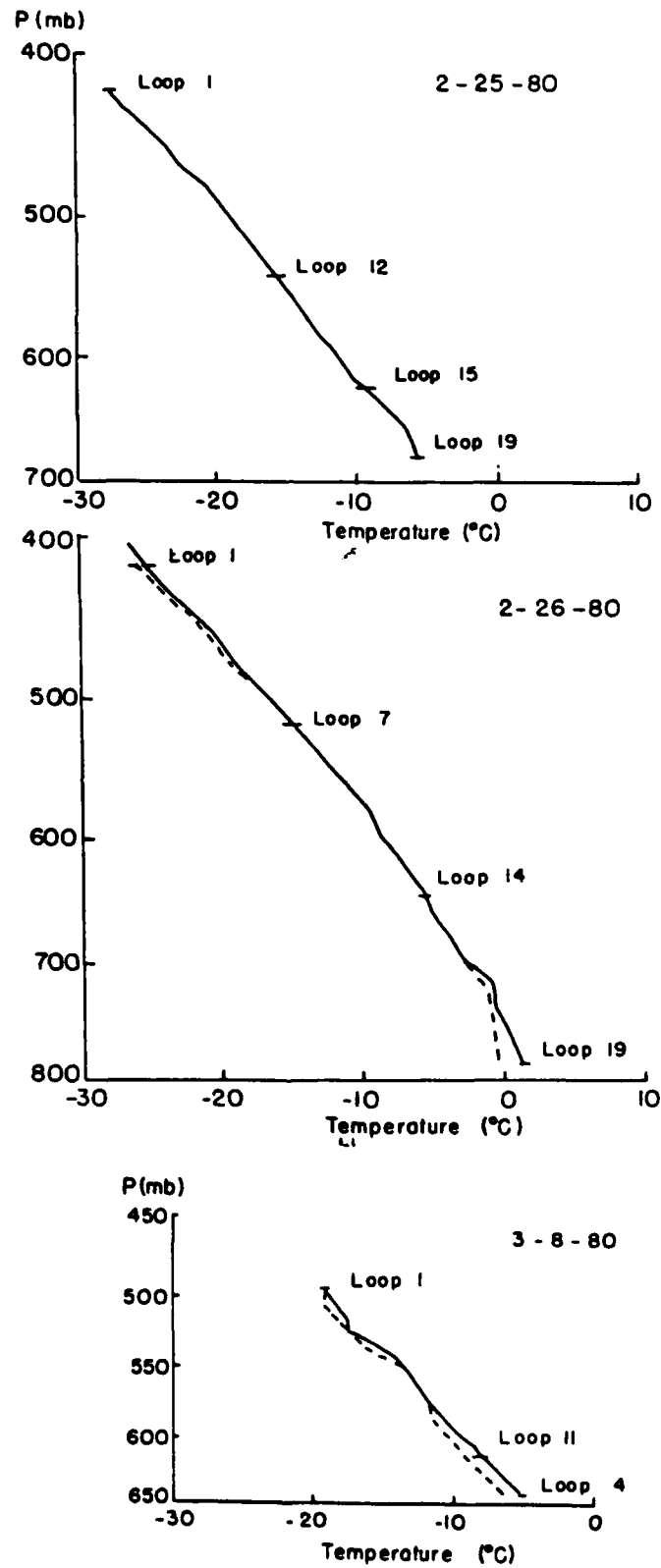


Fig.2.4: Aircraft soundings for the three flights

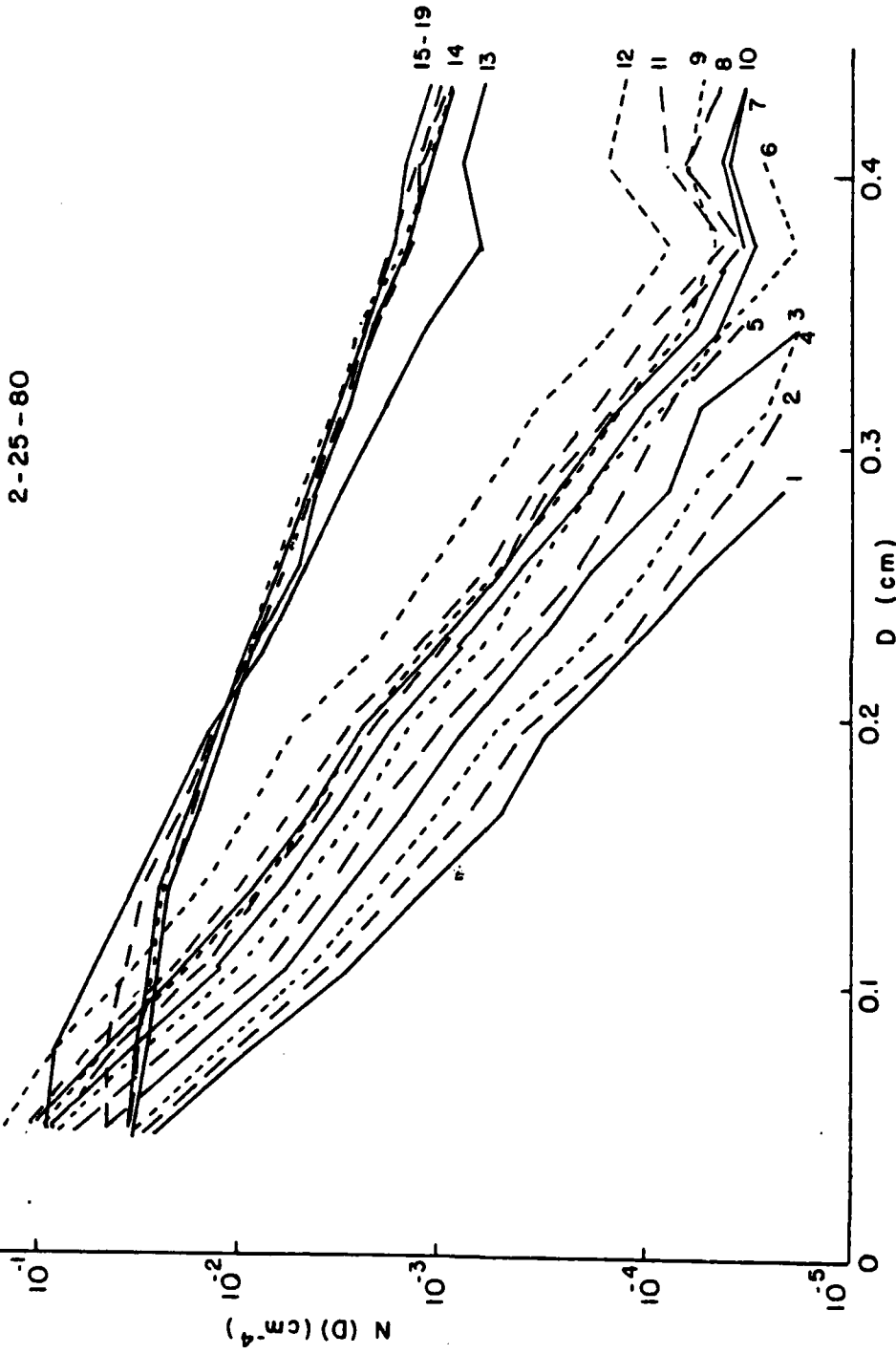


Fig.2.5: Snow-size spectra for spiral 1 (25 February, 1980) averaged over the various loops. Numbers on the right indicate loop numbers

2-26-80

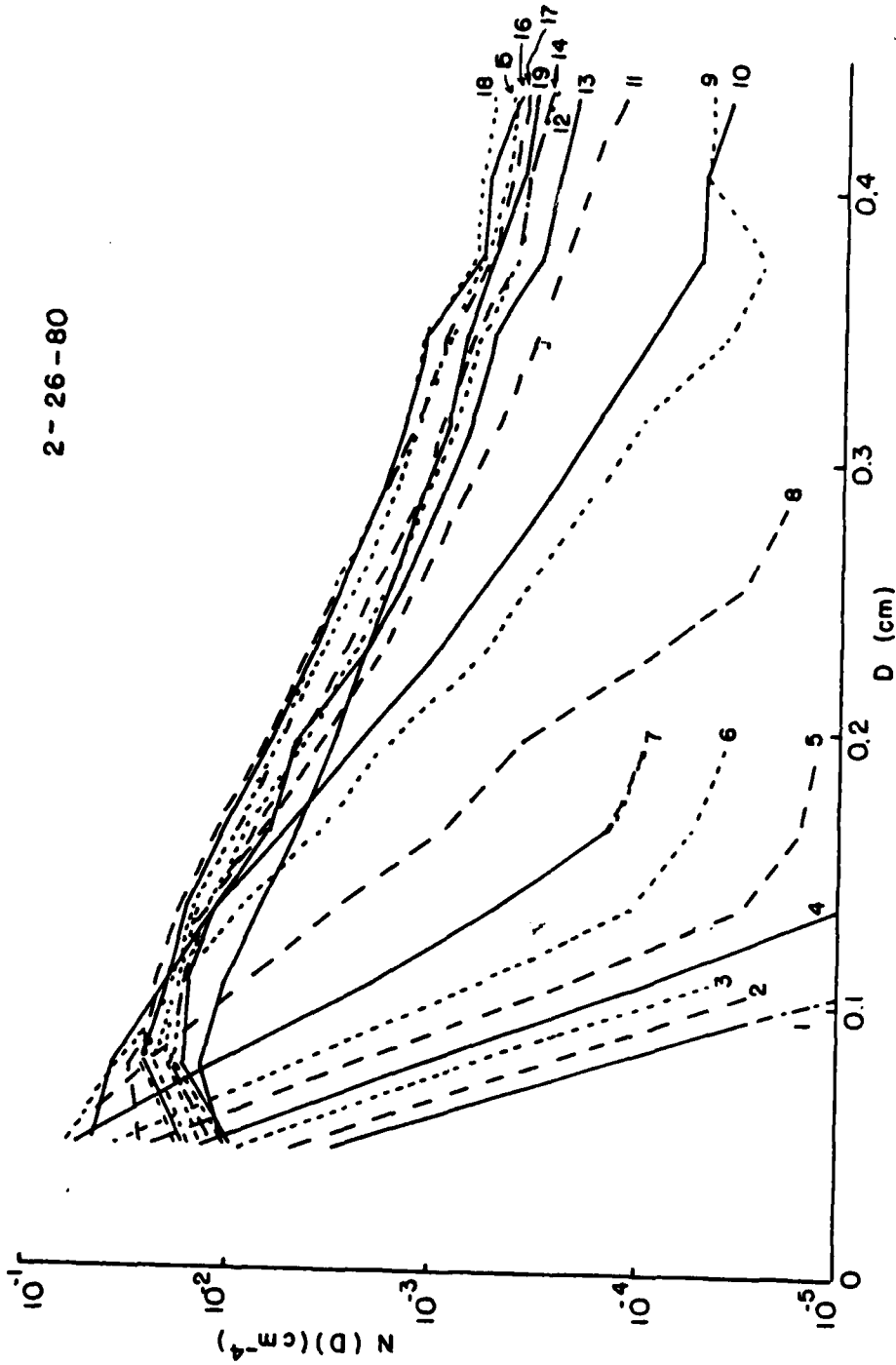


Fig.2.6: Snow-size spectra for spiral 2 (26 February, 1980) averaged over the various loops. Numbers on the right indicate loop numbers

3-8-80

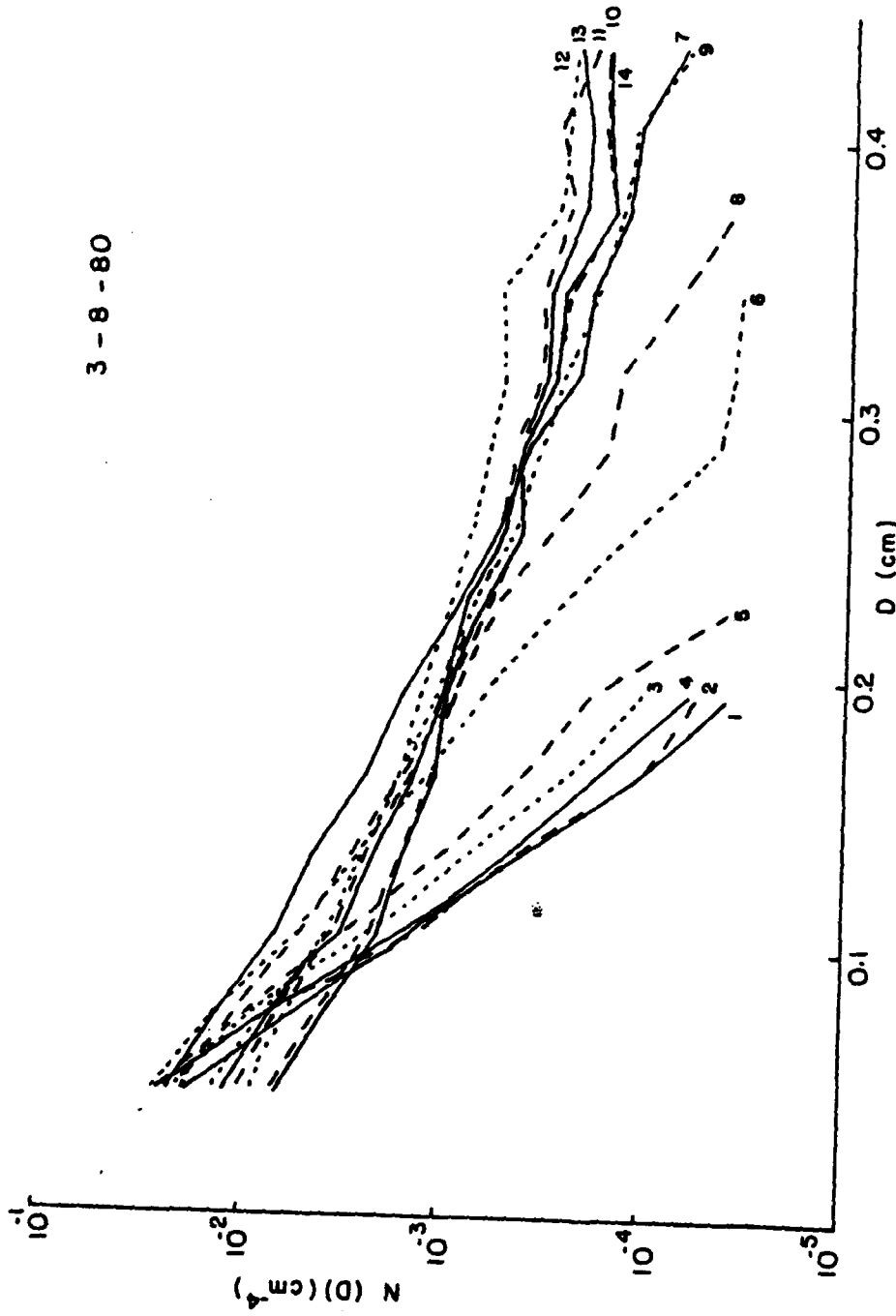


Fig.2.7: Snow-size spectra for spiral 3 (8 March, 1980) averaged over the various loops. Numbers on the right indicate loop numbers

The spectra from the second spiral show a similar behavior. The intercept shows an initial monotonic increase while the slope remains approximately constant from loops 1 through 7. Then both the intercept and the slope decrease from loops 7 through 14. The spectra of loops 15 to 19 are almost constant. The vertical separation between successive loops is also 200 m for this case.

The spectra from the third spiral indicate a somewhat different behavior. There was not a stage where the intercept increases while the slope remains constant. Both the intercept and the slope decrease from loop 1 to loop 10. Then the slope and the intercept remain more or less constant for loops 11 through 14. The vertical separation between successive loops is about 100 m for this case.

The data from the J-W cloud water probe are extremely noisy. So, the occurrence of supercooled liquid water is determined using the Rosemont icing rate detector data and the ASSP data. Fig. 2.8 shows the icing rate measurements for the spiral on 25 February 1980. The icing probe is a rod protruding outside the aircraft. In the 'dry' state, the rod has a certain natural vibration frequency. When there is supercooled liquid water in the atmosphere, icing would develop on the rod, thus changing the mass of the rod. Therefore, the vibration frequency of the rod changes. The

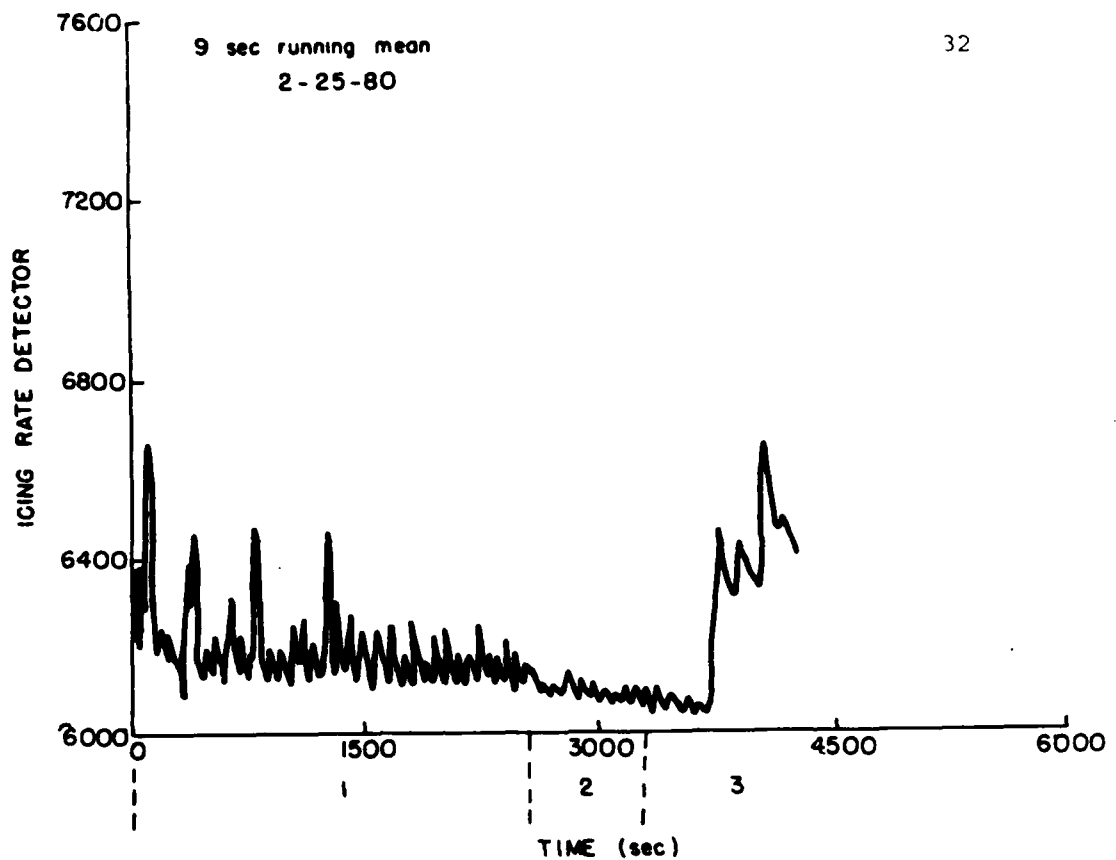


Fig.2.8: Icing rate measurement for 25 February, 1980. Abscissa is time (in sec.) elapsed after the beginning of flight.

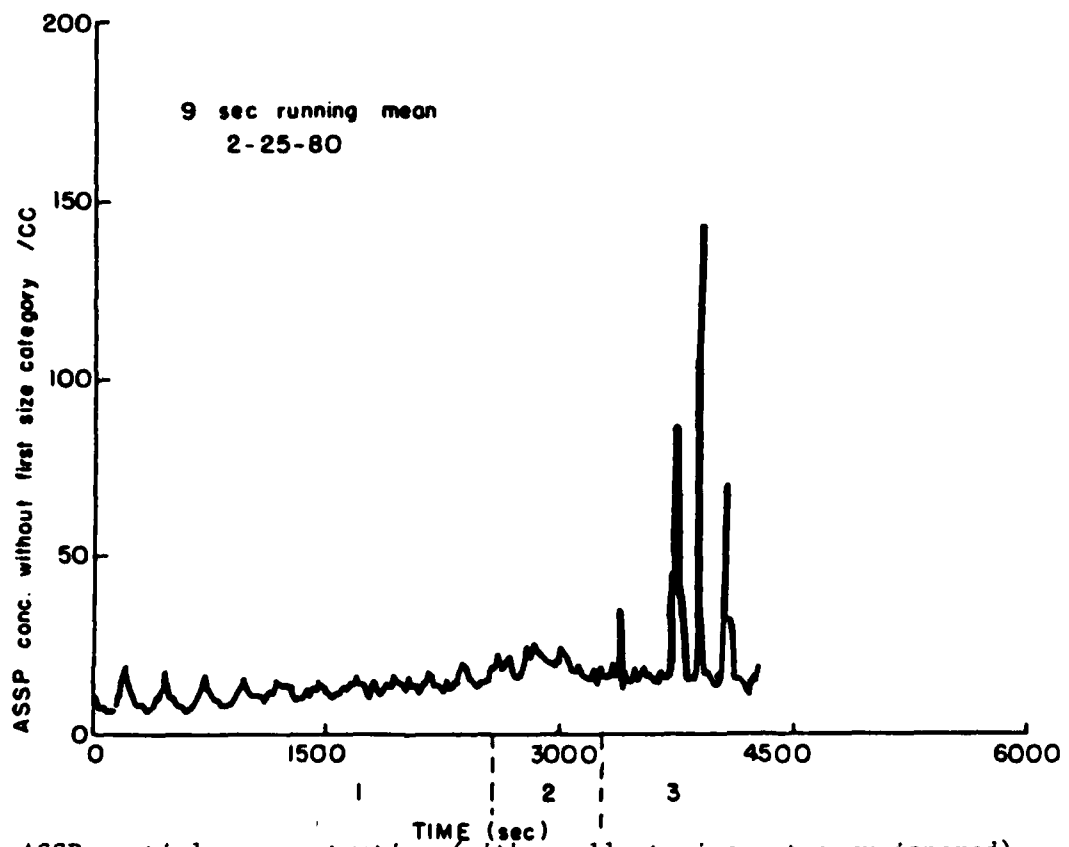


Fig.2.9: ASSP particle concentration (with smallest size category ignored) for 25 February, 1980

liquid water content is proportional to the change in frequency which is in turn proportional to the derivative of the trace shown in the figures. In order to smooth the data, a nine minute running mean technique is applied. The data are plotted against the time elapsed since the beginning of the spiral. The data indicate that supercooled liquid water is present at the end of the spiral (~3500 sec. after the start of the spiral). The time when the snow growth mechanism changes is also marked on the graph. The concentration of particles detected by the ASSP (with the smallest size category ignored and also smoothed by a nine minute running mean) (Fig. 2.9) indicates huge increases around 3500 sec. This again suggests the existence of supercooled liquid water and/or secondary production of ice particles.

The data of the icing rate detector for the spiral on 26 February 1980 are plotted in Fig. 2.10. They indicate that there is liquid water at 1500 sec., then at 3300 sec., then at 3900 sec. and at 4200 sec. Finally, at 4500 sec. the icing rate detector goes through a complete cycle. These show that patches of supercooled liquid water can be found throughout most of the flight and the liquid water content is even higher at the end. The ASSP concentration is plotted in Fig. 2.11. The data show that there is no change in concentration until 3300 sec. and 3900 sec. However, there

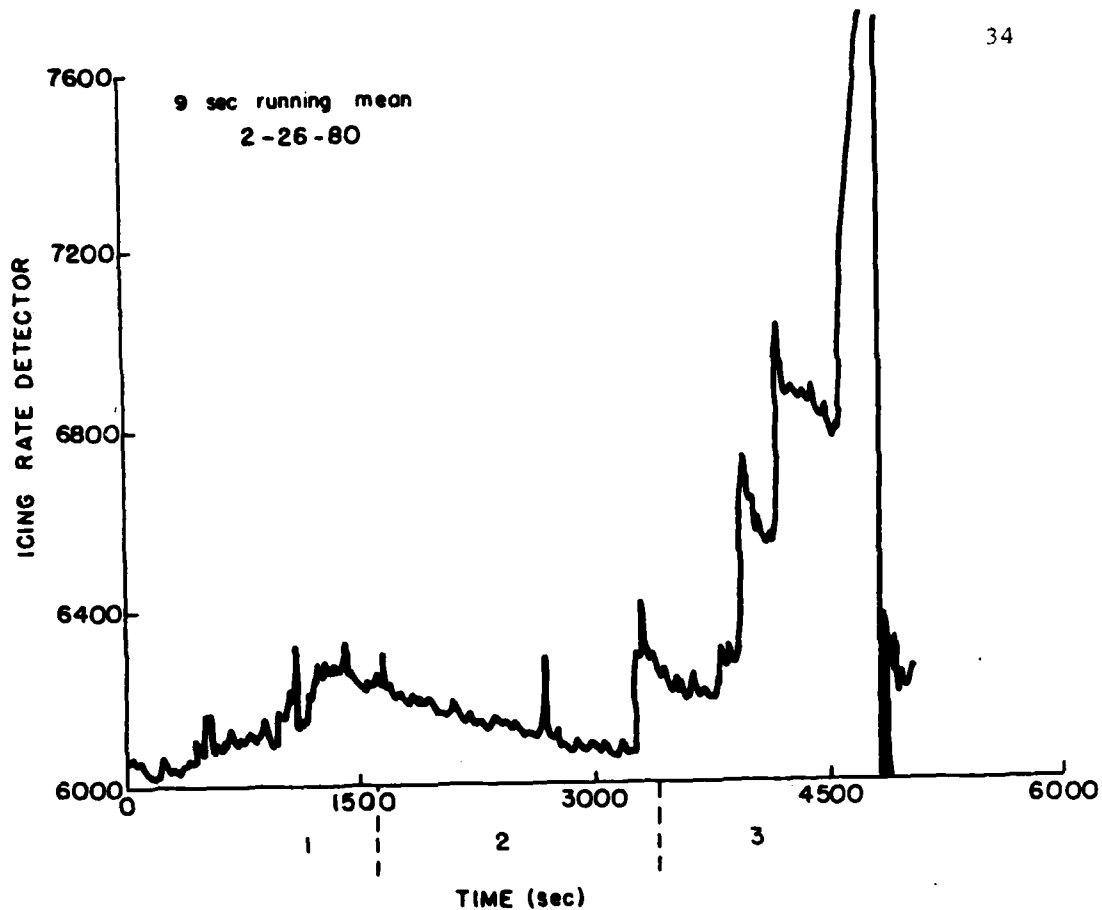


Fig.2.10: Icing rate measurement for 26 February, 1980 (Layout similar to Fig.2.8)

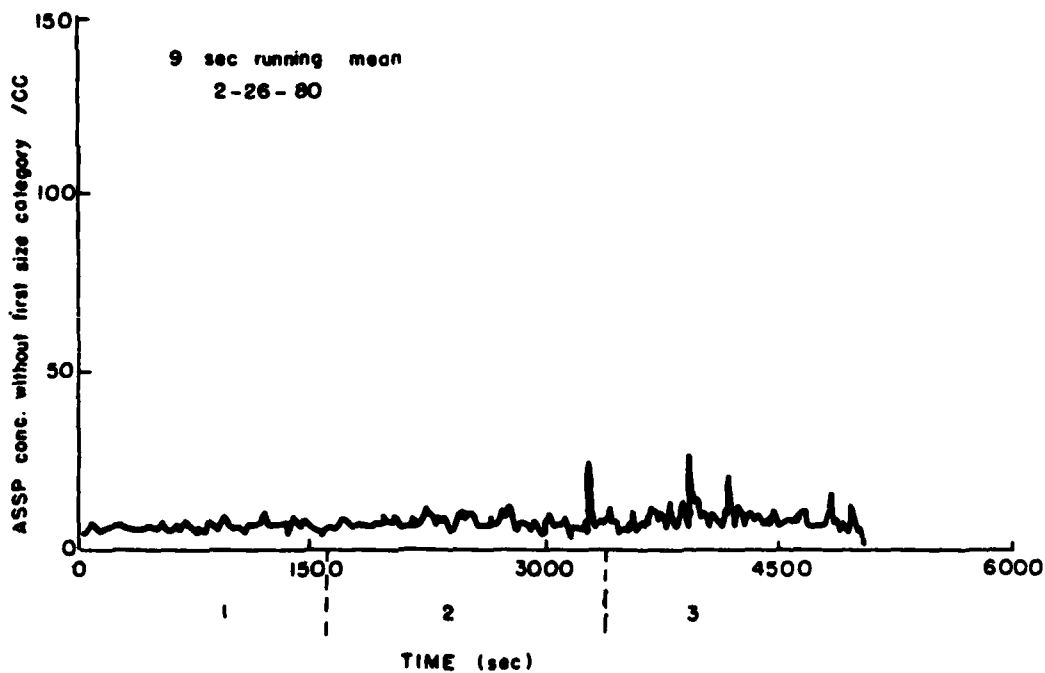


Fig.2.11: ASSP particle concentration (with smallest size category ignored) for 26 February, 1980

is no big increase in concentration at 4500 sec. when the icing rate detector goes through a complete cycle. The icing rate detector is located about 3 m from the ASSP, which could explain the apparent incoherence. The overall concentration for this spiral is lower than that of 25 February 1980.

The icing rate detector data and ASSP detected concentration for the spiral on 8 March 1980 are plotted in Figs. 2.12 and 2.13. From the graphs, no liquid water is evident for this spiral. In summary, supercooled liquid water is present but rare in some of the flights but its occurrence is not correlated with any particular stage of snow growth.

## 2.2 Two-parameter data analyses

Because of the quasi-exponential behavior it is possible to approximate the spectra by an exponential form such that (Gunn and Marshall, 1958)

$$N(D)dD = N_0 e^{-\lambda D} dD \quad (2.1)$$

where  $N(D)dD$  is the particle concentration in the diameter interval  $[D, D+dD]$ ,  $N_0$  is the intercept and  $\lambda$  the

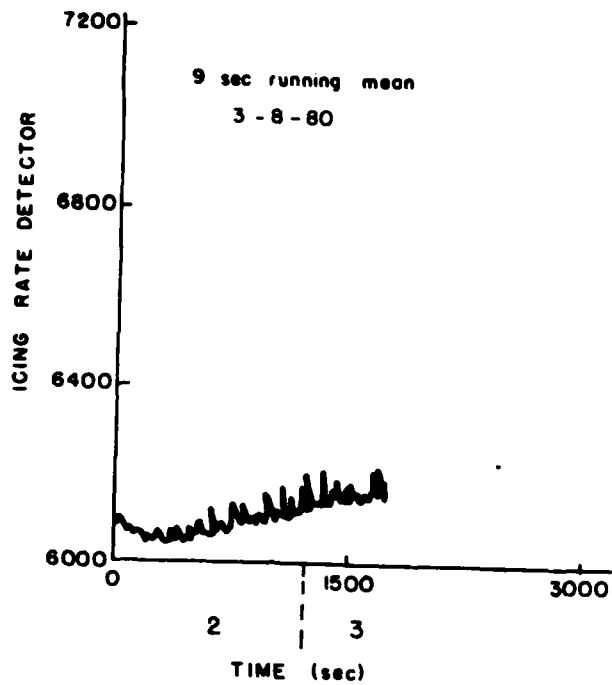


Fig.2.12: Icing rate measurement for 8 March, 1980 (layout similar to Fig.2.8)

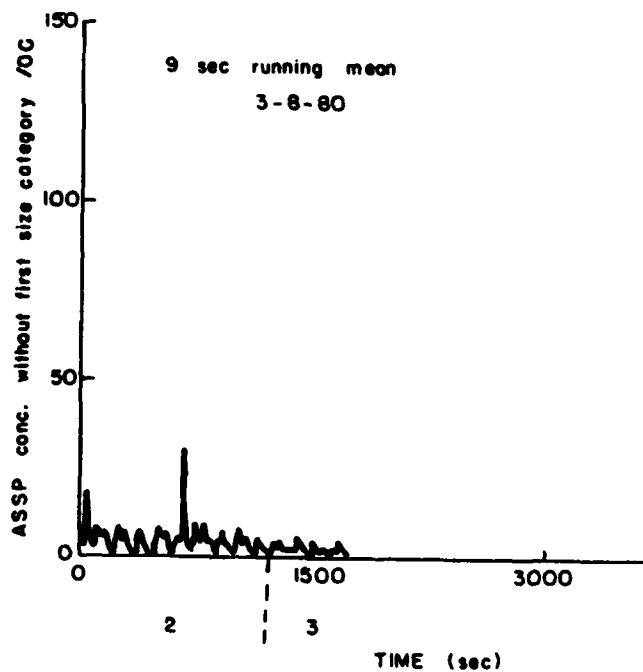


Fig.2.13: ASSP particle concentration (with smallest size category ignored) for 8 March, 1980

distribution slope. Here  $D$  is the actual 1-dimensional particle size measured by the laser imaging probe. Using a least-squares regression technique,  $N_0$  and  $\lambda$  for each spectrum can be found. In order to ensure adequate statistics, it is stipulated that for any size category to be included in the regression calculation the total number of particles counted in that size category must be greater than 10 for the complete loop. Fig. 2.14 shows the data from the three spirals in  $\log_{10} N_0 - \log_{10} \lambda$  space (hereafter  $N_0 - \lambda$  space). The loop numbers are indicated next to the data points which are connected sequentially by a line. Environmental temperatures are indicated for places where significant changes occur.

This type of spectral display is convenient because a straight line in  $N_0 - \lambda$  space corresponds to a constant moment of an exponential distribution, since the  $j$ th moment of a spectrum is

$$M_j = \int_0^{\infty} D^j N_0 e^{-\lambda D} dD = \frac{N_0 \Gamma(j+1)}{\lambda^{j+1}} \quad (2.2)$$

Hence in logarithmic  $N_0 - \lambda$  space, the moment  $M_j$  is constant along any straight line having slope  $(j+1)$ .

The behavior of the spectra in Figs. 2.5, 2.6 and 2.7 can be discussed in terms of the trajectory of the spectral

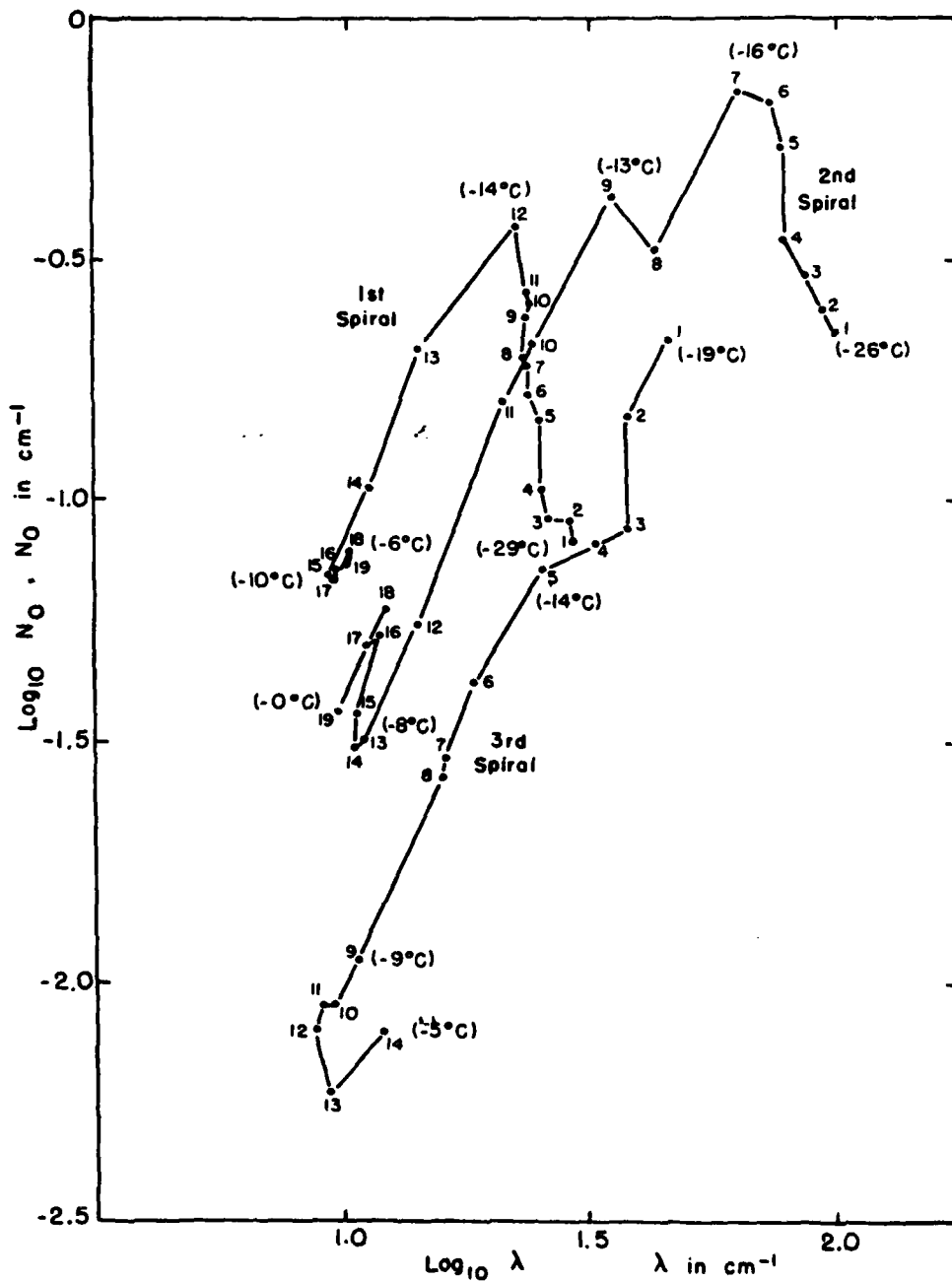


Fig.2.14:  $N_O$ - $\lambda$  trajectories for the three spirals. See text for details

evolution in  $N_0-\lambda$  space in Fig. 2. 14. For spiral 1, there is a gradual increase in  $N_0$  and a slight decrease in  $\lambda$  from loop 1 through loop 12 such that the slope of the  $N_0-\lambda$  trajectory is negative, implying that all spectral moments are increasing. At loop 12 the spectral evolution changes dramatically and both  $N_0$  and  $\lambda$  decrease until loop 15. After that  $N_0$  and  $\lambda$  assume approximately constant values. The second spiral shows a similar pattern of three stages of evolution. Stage 1 (loops 1 through 7) is characterized by an increase in  $N_0$  accompanied by relatively little change in  $\lambda$ . Stage 2 (loops 7 through 14) is characterized by a rapid decrease in both  $N_0$  and  $\lambda$ . Stage 3 is marked by an apparent cessation of spectral evolution. The third spiral does not show the presence of stage 1. Both  $N_0$  and  $\lambda$  decrease from loops 1 through 10. Then loops 10 through 14 indicate that the spectral evolution has come to a halt.

The  $N_0-\lambda$  trajectories for the second stage of growth (both intercept and slope decreasing) are roughly parallel for all three spirals, having slopes ranging from 1.80 to 1.95. This suggests that during this phase of spectral evolution, the sum of the diameters of snow particles is a conservative property of the distribution. These three cases also suggest that the distribution slope,  $\lambda$ , has a minimum value of approximately  $10 \text{ cm}^{-1}$ , which characterizes the third

stage of evolution.

### 2.3 Interpretation of two-parameter data analyses

The effect of deposition growth on the size distribution is characterized by how the rate of change of the particle diameter depends on the particle diameter, i.e.,

$$\frac{dD}{dt} \propto D^{\delta} \quad (2.3)$$

For  $\delta > 0$ , larger particles grow more quickly in diameter space and one would expect the distribution slope to decrease. For  $\delta < 0$ , depositional growth will cause the distribution to steepen. For snow, the particle mass varies approximately with the square of the particle diameter and the rate of change of mass is directly proportional to the particle diameter so that  $\delta \approx 0$ . Hence, to a first approximation, all sizes will grow at the same rate in diameter space and the distribution slope will remain constant. The intercept will increase since the smaller, more numerous particles will grow into larger sizes. In the absence of a source of small particles, a lower limit to the size distribution will develop.

The first stage of particle growth (observed for spirals

1 and 2) is consistent with deposition growth. This is not to say that other physical processes are not occurring but that deposition is dominating. Also in this stage, the increase in  $N_0$  and slight decrease in  $\lambda$  indicate an increase in the total concentration of particles. This is probably due to the growth of small particles into sizes detectable by the 200-Y probe. The source of these small particles could be either nucleation and/or secondary production.

The second stage of growth, where both  $N_0$  and  $\lambda$  decrease, is observed for all three spirals. This is characteristic of aggregation which depletes small particles and creates large ones. The ASD data for spirals 1 and 2 show a very sudden transition from the dominance of deposition to aggregation. During the deposition growth phase the particles are small and collisions are rare, eventually deposition produces a sufficient number of large particles for aggregation to commence. Once started, the large particles produced by aggregation accelerate the aggregation process and rapidly deplete the smaller particles. This accounts for the sudden transition and the very rapid evolution of the size distribution after the transition. For spirals 1 and 2 the transition occurs at  $-15^\circ\text{C}$  which is in the dendritic growth temperature range. This implies that the tendency for dendrites to form aggregates (e.g., Jiusto and Weickmann, 1973) may play a role

in the transition to aggregation growth. However the model calculations described by Passarelli (1978a,b,c) and the computations presented in the next section do not require a change in the particle geometry or collision efficiency to simulate the first two stages of growth.

The most puzzling behavior is the apparent sudden end to aggregation. The spectra cease evolution when the slope reaches approximately  $10 \text{ cm}^{-1}$ . This suggests that the depletion of small particles is balanced by a production mechanism. This mechanism can be either primary production or secondary production or both. The temperature range for this stage is  $0^\circ\text{C}$  to  $-10^\circ\text{C}$ , where ice nucleation is not predominant (Fletcher, 1962) and so the probability of primary production is low. Moreover large particles produced by aggregation are somehow depleted. This suggests that breakup is occurring. In view of the presence of liquid water, there is also the possibility of rime-splintering.

The fact that all three spirals evolve to the same slope suggests collisional breakup. This hypothesis is drawn from previous work on drop coalescence and breakup which demonstrates that coalescence and collisional breakup leads to equilibrium distributions which have the same slope, regardless of the precipitation rate (Gillespie and List, 1976 and Srivastava, 1978). The latter author concludes that

raindrop size distributions tend to have approximately a constant slope and an intercept proportional to rainfall content. This is in agreement with Blanchard and Spencer's (1970) observations on raindrop size distributions in which binary interaction processes would produce exponential distributions with a constant slope.

#### 2.4 Horizontal gradients in the microphysical structure

In order to examine the horizontal gradient in the size distribution, the mean diameter of all particles measured by the 200-Y spectra as a function of aircraft magnetic heading is plotted in Fig. 2.15 for the first and second spirals. Each loop is represented by a separate graph and the loops are stacked vertically in accordance with their height. The approximate diameter of each loop is 6 km. The loop in which the spectra transformed from first to second stage of growth (the peak in the  $N_0 - \lambda$  trajectory) is indicated by a star in each case. Before the transition, the mean diameter is essentially uniform within each loop and gradually increases with depth. (Not all upper-level loops are shown). However, after the transition, horizontal inhomogeneities develop very rapidly. The features are correlated from one loop to the next.

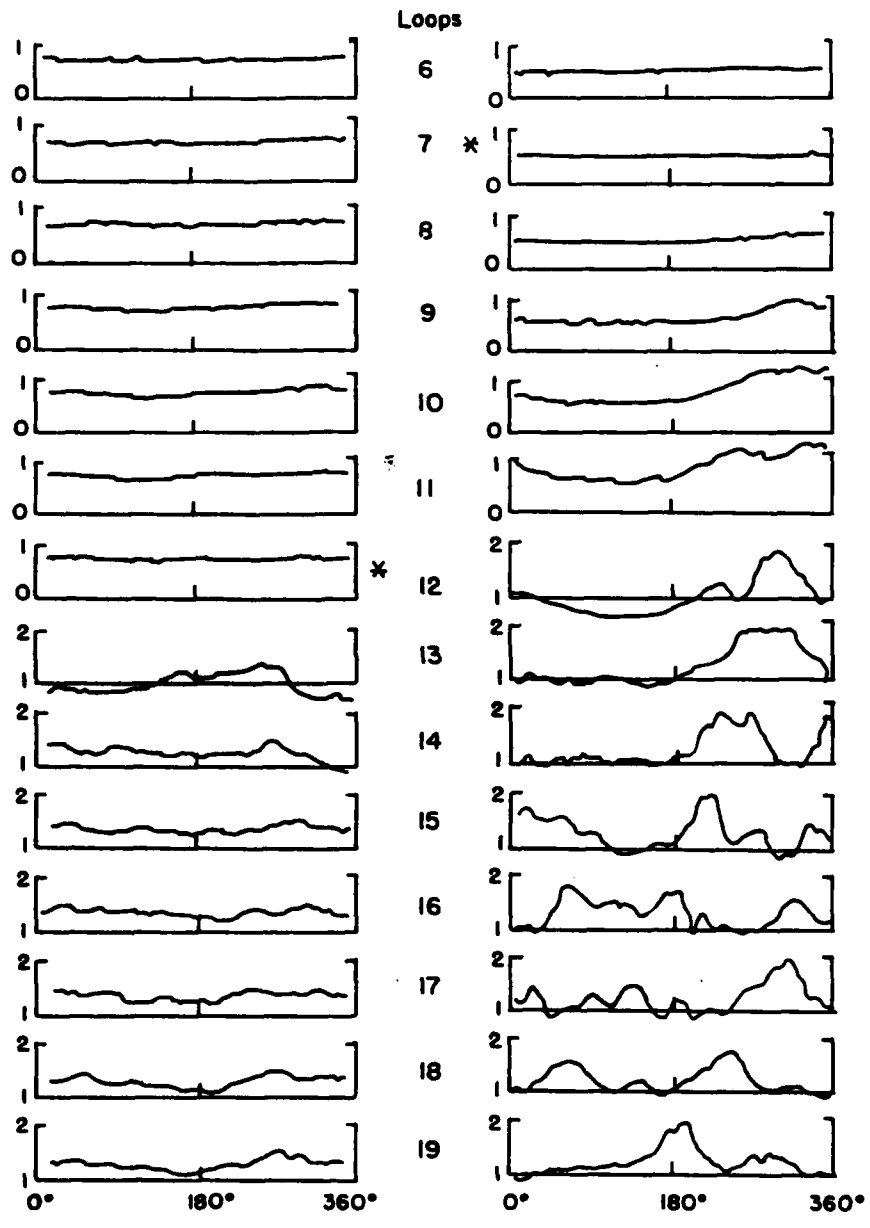


Fig.2.15: Average particle diameter as a function of magnetic heading for spirals 1 and 2. Diameters in mm.

One interesting feature in the second spiral is that at loop 9, the average particle diameter has its maximum around 320 magnetic heading. Then, this maximum shifts gradually towards the west and then the south. This perhaps indicates that the wind shear is turning cyclonically downward (or anticyclonically upward) and the snow particles are being carried around with it.

To examine the point-to-point behavior of the spectra, we arbitrarily divide each loop into four quadrants bounded by the cardinal directions. Ideally the spectral evolution can be studied by examining the height evolution of spectra averaged over a particular quadrant rather than over an entire loop. Fig. 2.16 shows an example of the  $N_p - \lambda$  evolution for the second spiral for the four quadrants. The  $N_p$  scale is different for each quadrant in order to separate the four quadrants. Note that the four  $N_p - \lambda$  trajectories all show the same general features. However, the west-north quadrant starts rapid stage 2 growth earlier than the other quadrants (e.g., examine loops 9 and 10 in Fig. 2.15).

Fig. 2.16 illustrates that even if we examine portions of a loop the spectral evolution is coherent. This is consistent with the previous discussions. Also, the rapid development of horizontal gradients of mean diameter are apparently related to the fact that spectra in different

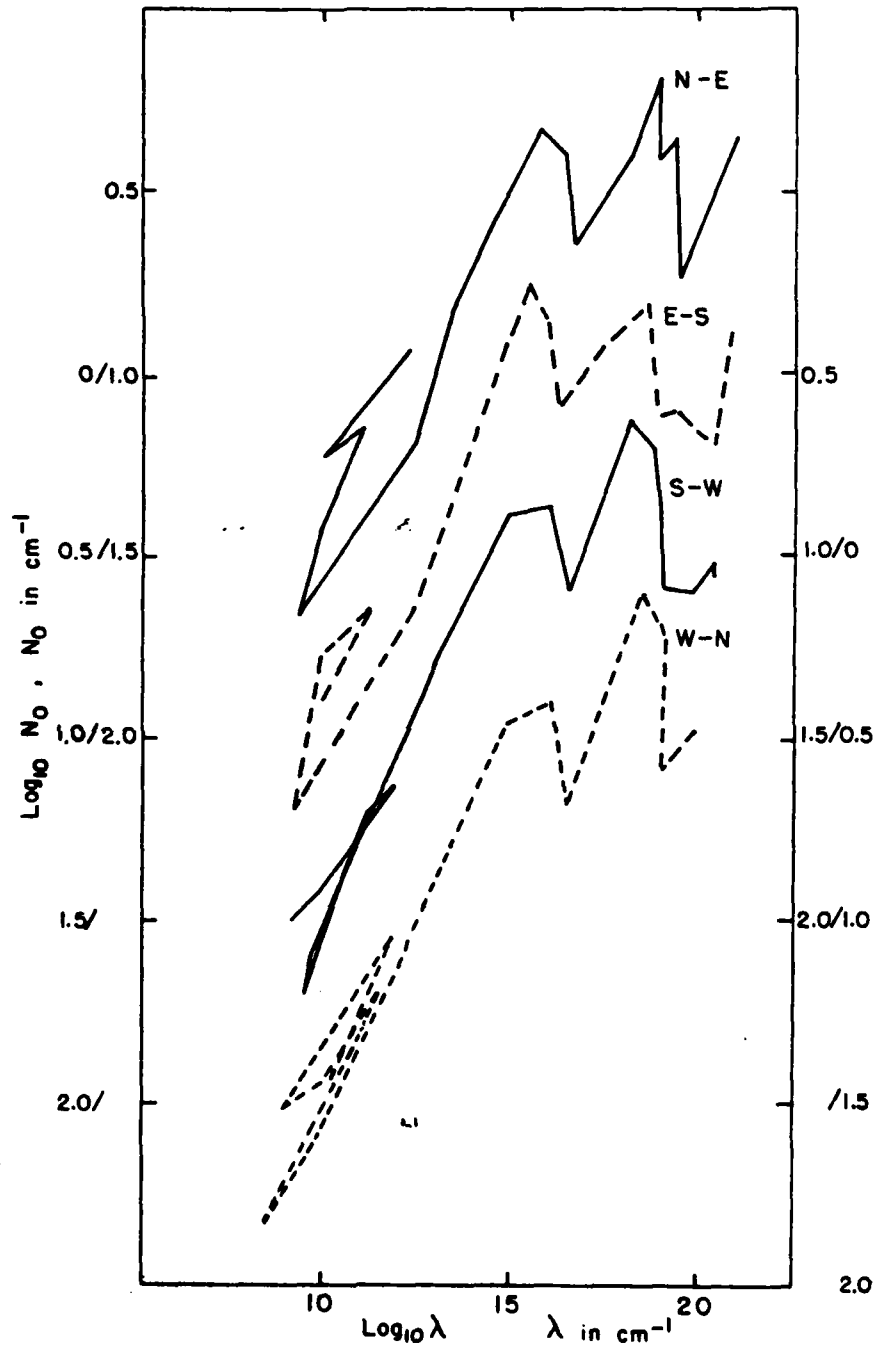


Fig.2.16:  $N_0$ - $\lambda$  trajectories for the four cardinal quadrants for spiral 2. The  $N_0$  scale refers to the northeast quadrant. The other quadrants are shifted downward by one-half decade each to differentiate the data

regions undergo the transition from deposition to aggregation at different heights.

## 2.5 Three-parameter analyses

Snow-size spectra have conventionally been represented by a two-parameter negative exponential distribution (2.1). This expression has the advantage of being mathematically simple. However, this expression is not a good description of the small end of the spectrum. A three-parameter negative exponential-power law distribution,

$$N(D)dD = N_*(h)e^{-\lambda_* D} D^r dD, \quad (2.4)$$

where  $N(D)dD$  is the number density of particles with diameters in the range  $D$  and  $D+dD$ , provides another degree of freedom. Hence, it can provide a better fit to the observed snow-size spectra, even at the small end. Such three-parameter distributions have been used by Takeuchi (1978) and Uplinger (1981) to describe raindrop size spectra. Any theoretical analysis using a three-parameter size distribution will also have one more dimension to manipulate.

Discretizing (2.4) into

$$\log_{10} N_i = \log_{10} N_x - \lambda_x D_i \log_{10} e + \sigma \log_{10} D_i + \text{error.} \quad (2.5)$$

$$\text{Let } x_i = D_i$$

$$y_i = \log_{10} N_i$$

$$a = \log_{10} N_x$$

$$b = \lambda_x \log_{10} e$$

$$c = \sigma$$

$$s = \text{number of size categories}$$

Using least-squares fit regressions, a, b and c can be found from the spectra to be

$$a = \frac{\sum_{i=1}^s y_i}{s} + \frac{b \sum_{i=1}^s x_i}{s} - \frac{c \sum_{i=1}^s \log_{10} x_i}{s} \quad (2.6)$$

$$b = F_1 + cF_2 \quad (2.7)$$

$$c = \frac{F_1 \left( \frac{\sum_{i=1}^s x_i \log_{10} x_i}{s} - \frac{\sum_{i=1}^s x_i}{s} \frac{\sum_{i=1}^s \log_{10} x_i}{s} \right) + \left( \frac{\sum_{i=1}^s y_i \sum_{i=1}^s \log_{10} x_i}{s} - \frac{\sum_{i=1}^s y_i}{s} \frac{\sum_{i=1}^s \log_{10} x_i}{s} \right)}{F_2 \left( \frac{\sum_{i=1}^s x_i \sum_{i=1}^s \log_{10} x_i}{s} - \frac{\sum_{i=1}^s x_i}{s} \frac{\sum_{i=1}^s \log_{10} x_i}{s} \right) + \left( \frac{\sum_{i=1}^s (\log_{10} x_i)^2}{s} - \left( \frac{\sum_{i=1}^s \log_{10} x_i}{s} \right)^2 \right)} \quad (2.8)$$

$$\text{where } F_1 = \frac{\sum_{i=1}^s x_i y_i - \frac{\sum_{i=1}^s x_i}{s} \frac{\sum_{i=1}^s y_i}{s}}{\frac{(\sum_{i=1}^s x_i)^2}{s} - \sum_{i=1}^s (x_i)^2}$$

$$F_2 = \frac{\frac{\sum_{i=1}^S X_i \sum_{i=1}^S \log_{10} X_i}{S} - \sum_{i=1}^S X_i \log_{10} X_i}{\frac{(\sum_{i=1}^S X_i)^2}{S} - \sum_{i=1}^S (X_i)^2}$$

The results for  $N_x$  from spiral 1 is shown in Fig. 2.17.  $N_x$ , the 'intercept' goes through three distinct stages as snow grows. First,  $N_x$  increases slowly. Then  $N_x$  takes a rapid rise and a rapid fall. Finally  $N_x$  remains relatively constant. These three stages correspond to the deposition, aggregation and collisional breakup stages in the two-parameter analyses. Fig. 2.18 shows the change of  $N_x$  with height for the second spiral. The data appear to be extremely noisy especially at the beginning of the spiral. This is probably due to the lower particle number density in that portion of the spiral. Also note that the scale in this figure is different from that for spiral 1. Still, the general behavior of  $N_x$  is similar to that of the first spiral.  $N_x$  first increases, then it decreases and finally takes on a somewhat constant value.

Fig. 2.19 shows the evolution of  $N_x$  with height for the third spiral. The result for this spiral is rather different from those of the previous two spirals. As recalled from the two-parameter analyses (Fig. 2.14), this is the spiral in

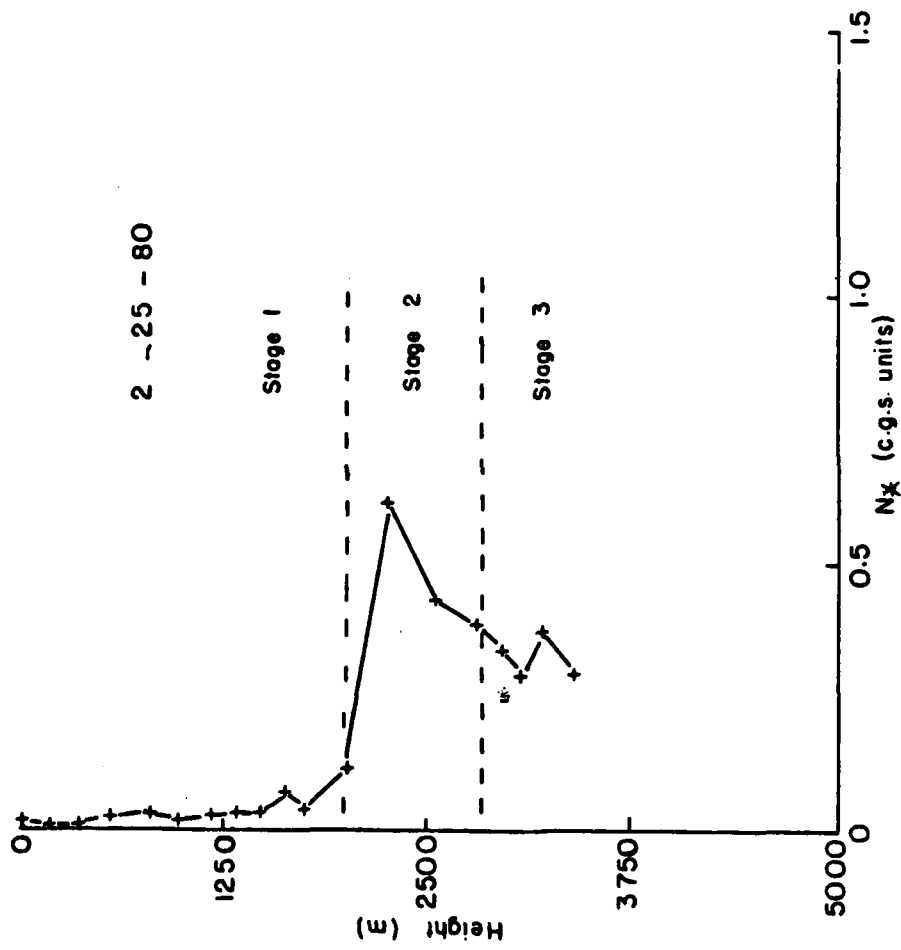


Fig.2.17:  $N_*$  as a function of height, 25 February, 1980. The stages of snow growth are marked by dashed lines.

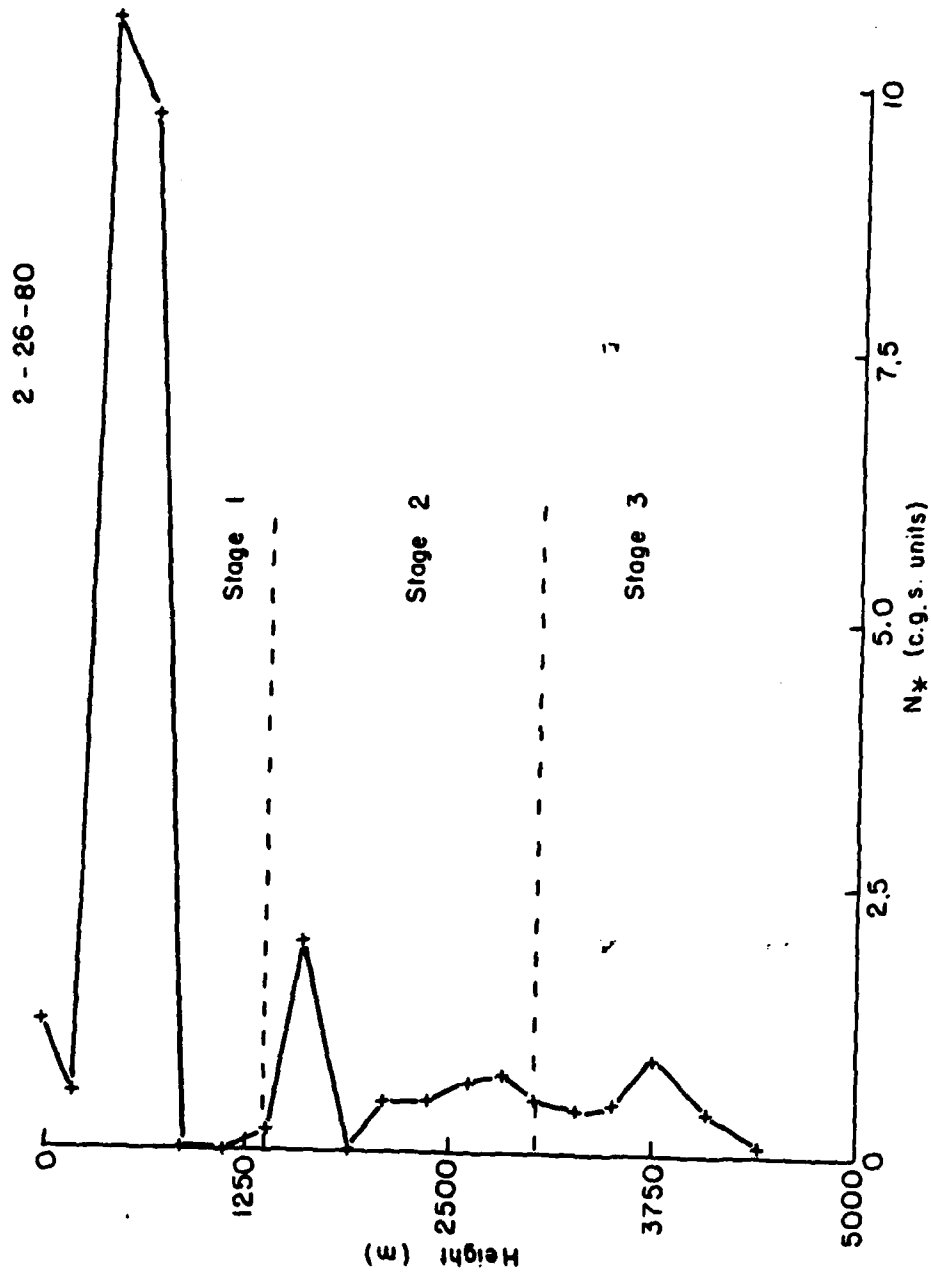


Fig.2.18:  $N_*$  as a function of height, 26 February, 1980, similar to Fig.2.17.

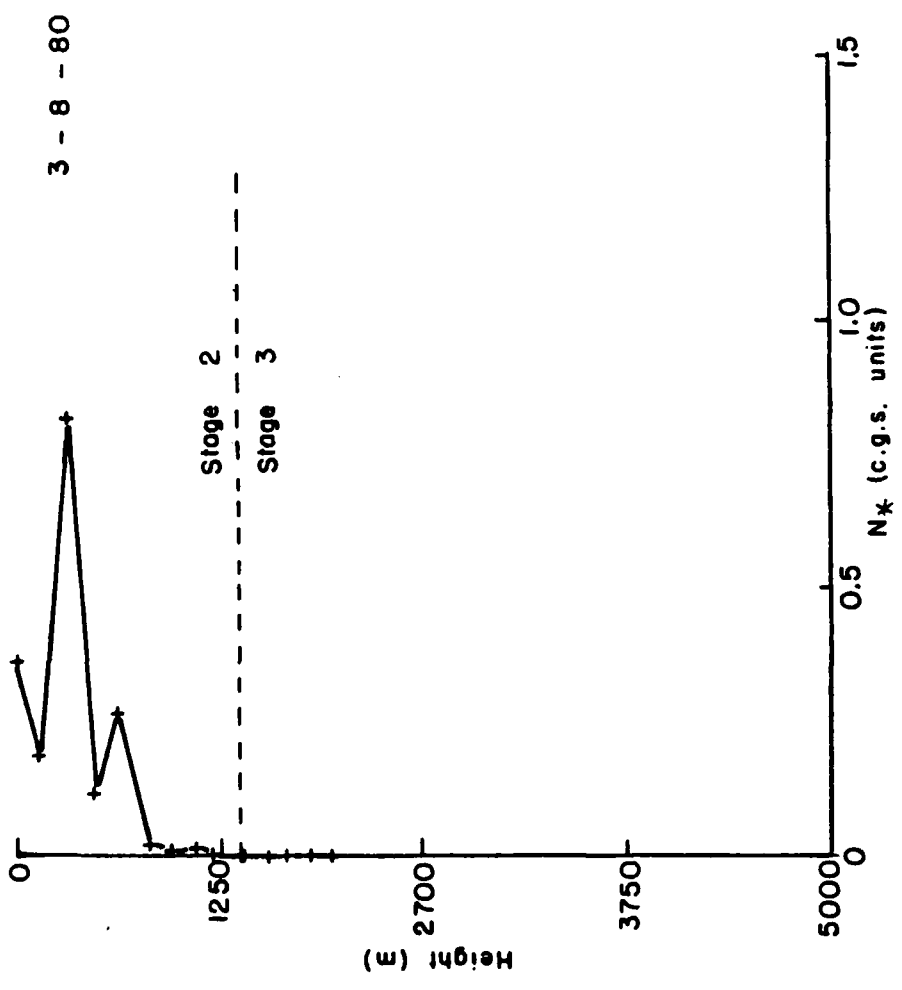


Fig.2.19:  $N_*$  as a function of height, 8 March, 1980, similar to Fig.2.17

which there is no stage 1 (where  $N_0$  increases and  $\lambda$  stays more or less constant). Except for the third and fifth loops,  $N_x$  is generally decreasing. Comparing this with the two-parameter model, loops 1 through 10 correspond to stage 2 and loops 10 through 14 correspond to stage 3. That means in stage 2, where aggregation is the dominant effect, small particles are being depleted and  $N_x$  is decreasing. In stage 3, where aggregation and collisional breakup come to an equilibrium,  $N_x$  is approximately constant.

Figs. 2.20, 2.21 and 2.22 show the change of  $\lambda_x$ , the exponent, with height for spirals 1, 2 and 3 respectively.  $\lambda_x$  decreases monotonically as the snow crystals fall. This is similar to the behavior of  $\lambda$  in the two-parameter analyses. In the last few loops of each of the spirals,  $\lambda_x$  would become more or less constant. However, unlike the two-parameter analyses, the terminal values of  $\lambda_x$  are different for each of the spirals. This is probably due to the fact that  $\lambda_x$  is sensitive to the value of  $\sigma$ . As will be seen later,  $\sigma$  is quite different for each of the spirals.

Fig. 2.23 gives the change of  $\sigma$  with height for spiral 1. The observed values indicate that in the early part of the flight,  $\sigma$  is negative and has an approximately constant value. Suddenly,  $\sigma$  changes to become positive and then it takes on a more or less constant value. The place where

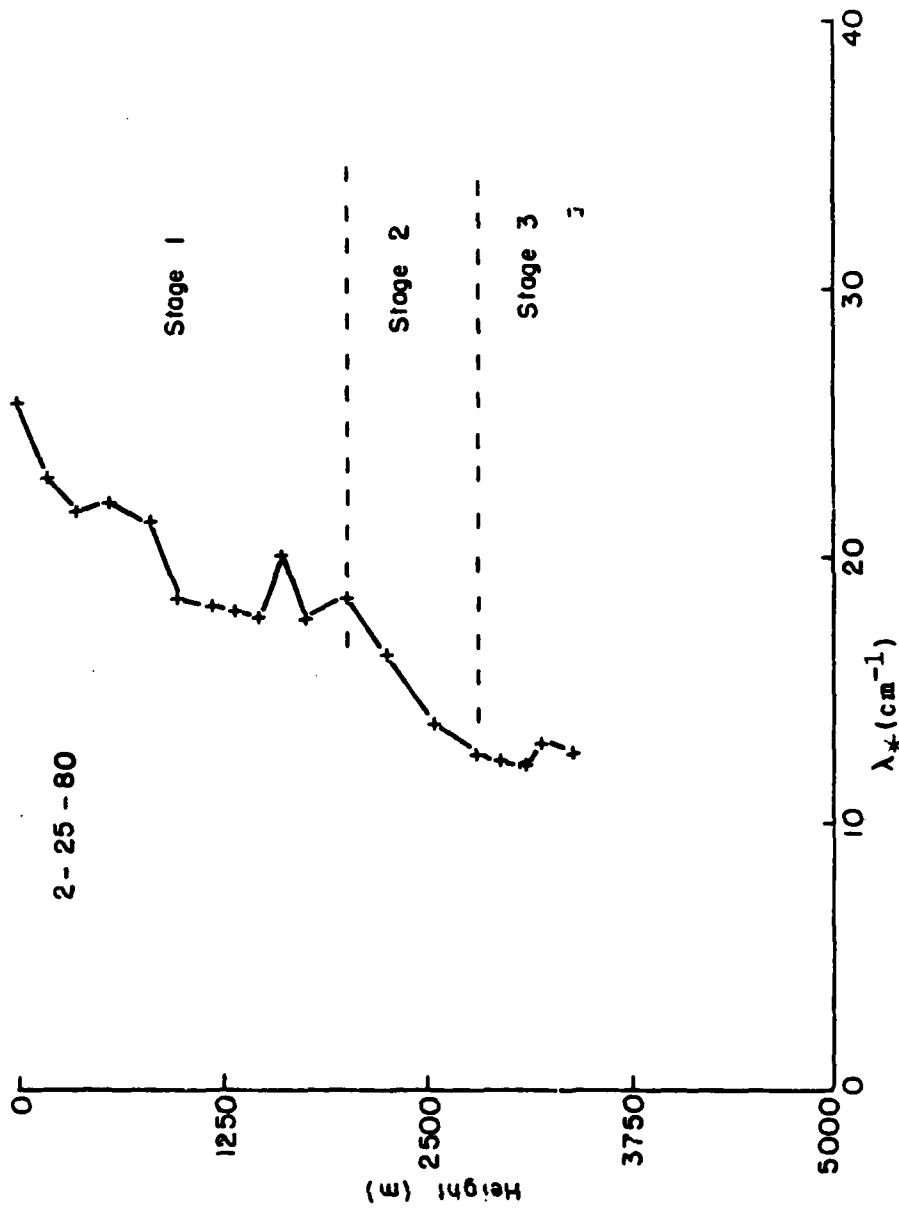


Fig.2.20:  $\lambda_*$  as a function of height, 25 February, 1980. The stages of snow growth are marked by dashed lines.

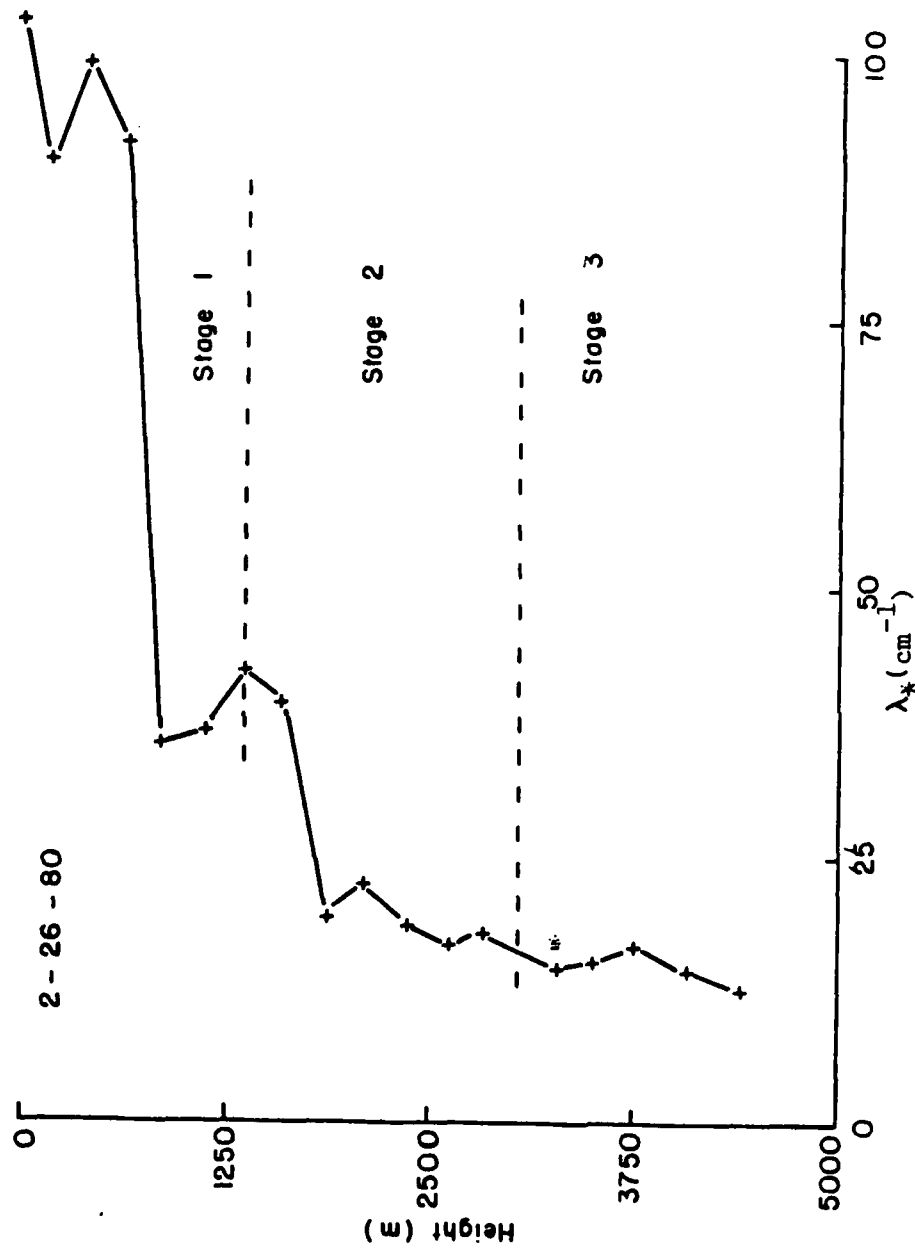


Fig.2.21:  $\lambda_*$  as a function of height, 26 February, 1980, similar to Fig.2.20

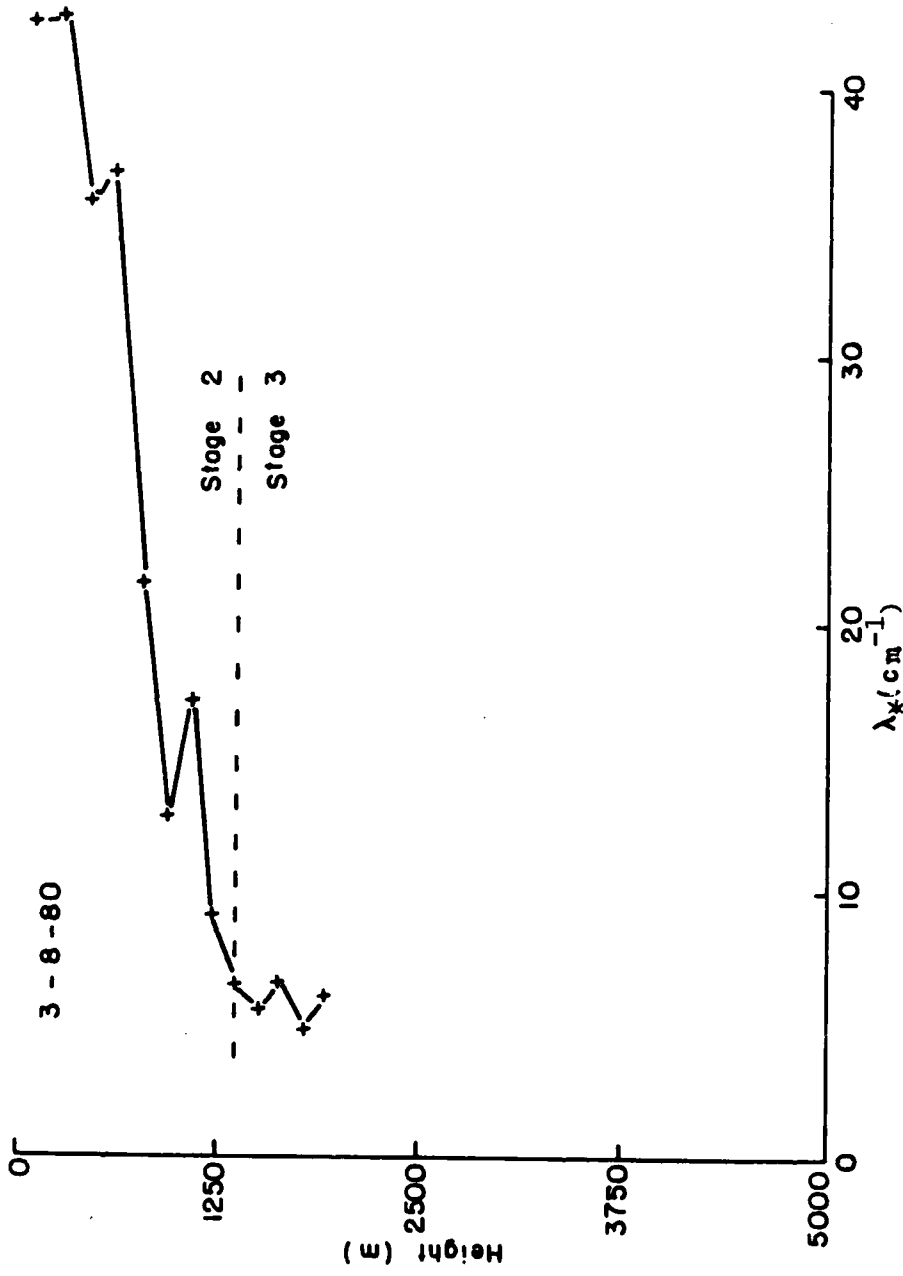


Fig.2.22:  $\lambda_*$  as a function of height, 8March, 1980, similar to Fig.2.20

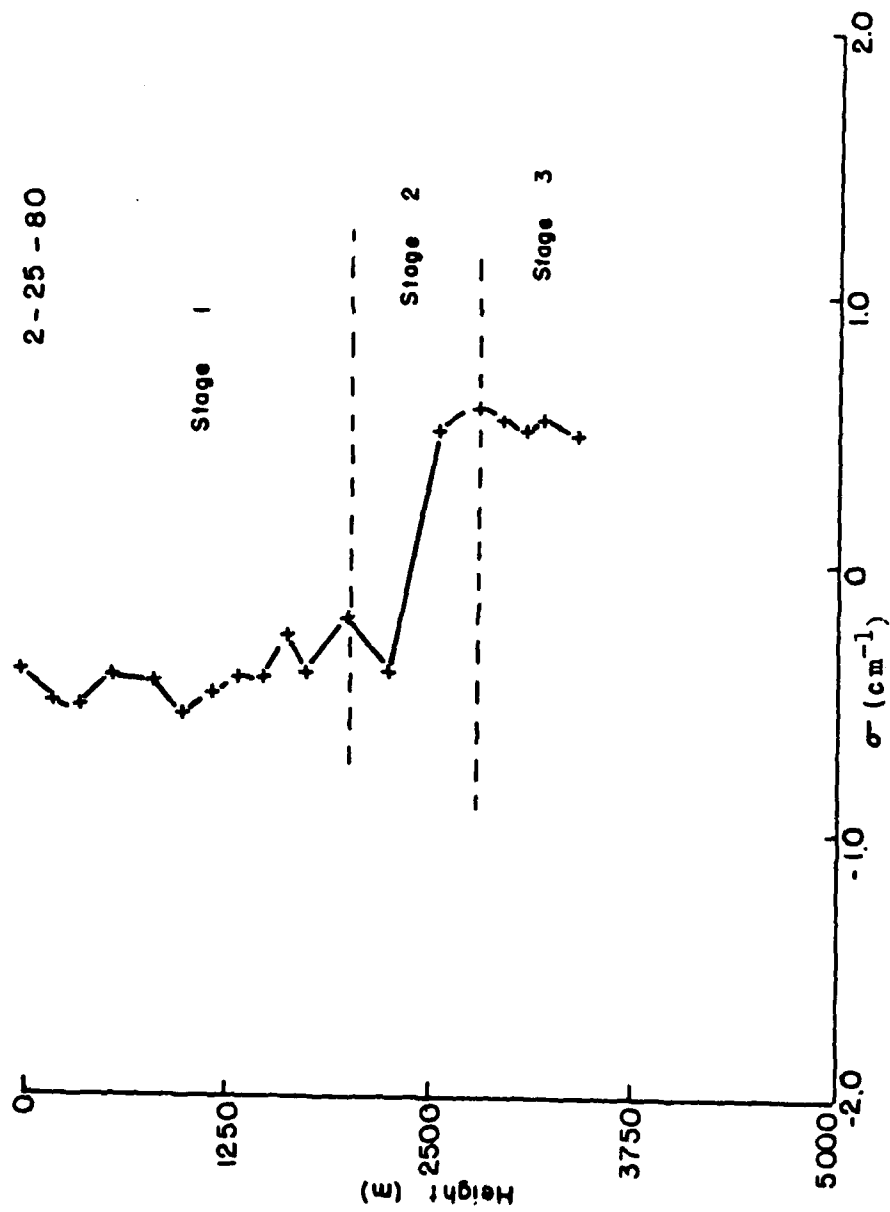


Fig.2.23:  $\sigma$  as a function of height, 25 February, 1980. The stages of snow growth are marked by dashed lines.

$\sigma$  makes the sudden change from negative to positive corresponds to the middle of the aggregation stage. A negative  $\sigma$  means that there are many more small particles than large particles and a positive  $\sigma$  means that the number of small particles is limited and there is a size at which the particle density peaks (Fig. 2.24). The sudden change from negative to positive implies that at the aggregation stage, small particles are depleted very rapidly.

Fig. 2.25 shows the change of  $\sigma$  with height for spiral 2. Just as the case of  $N_x$  for the same spiral, the values of  $\sigma$  are very noisy. If we ignore the first four loops,  $\sigma$  is initially negative. Then it increases to become positive and then stays approximately constant. This is similar to that of spiral 1.

Fig. 2.26 shows  $\sigma$  versus height for spiral 3. Here the evolution of  $\sigma$  is vastly different from the previous two cases. Instead of having an initially negative value,  $\sigma$  is initially positive and then it decreases into the negative from loop 1 through loop 10 (corresponding to stage 2 in the two-parameter analysis).  $\sigma$  remains negative from loops 10 through 14 (corresponding to the third stage in the two-parameter analyses). Physically, this means that the number density of small particles increases faster than that of the larger particles. This could imply either the

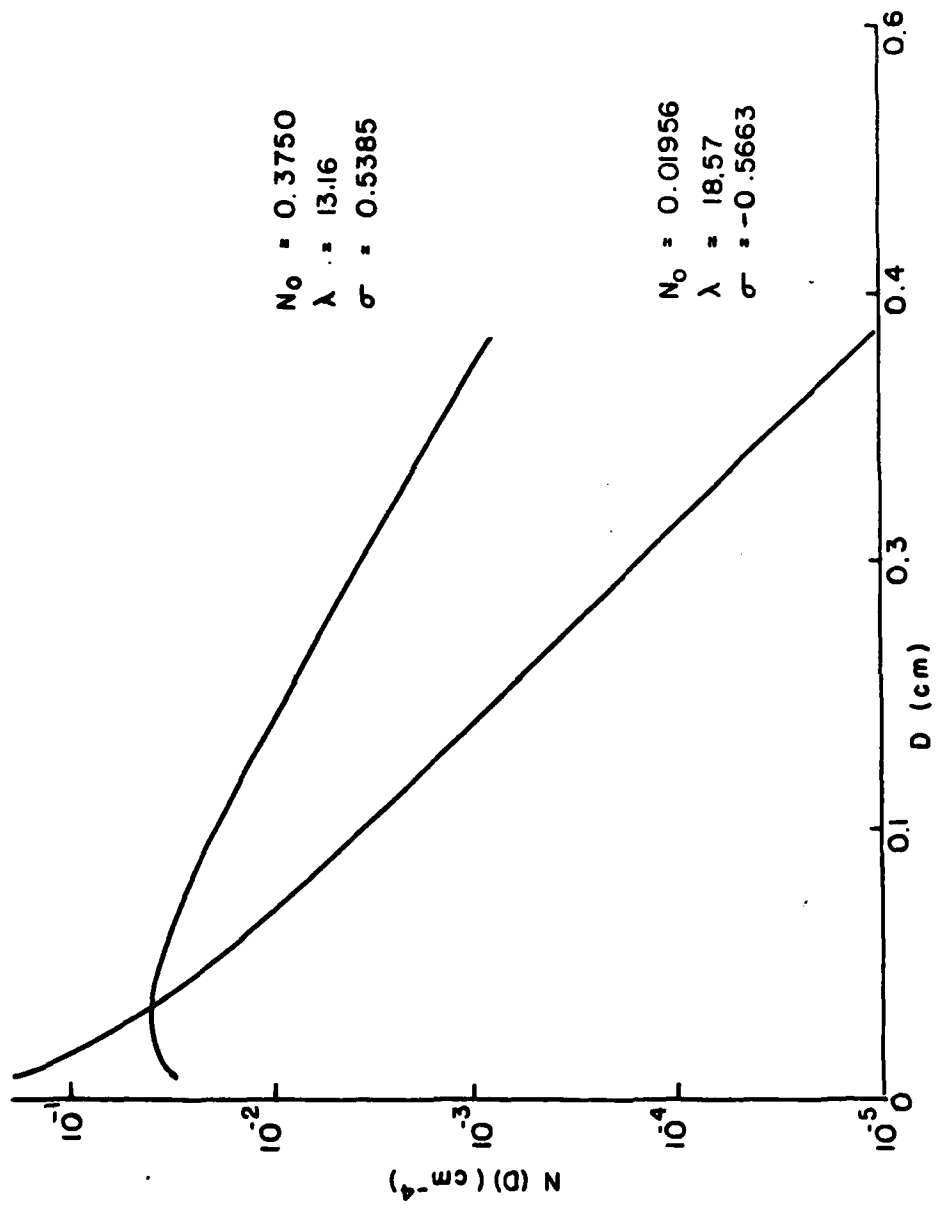


Fig.2.24: Illustration of positive and negative  $\sigma$

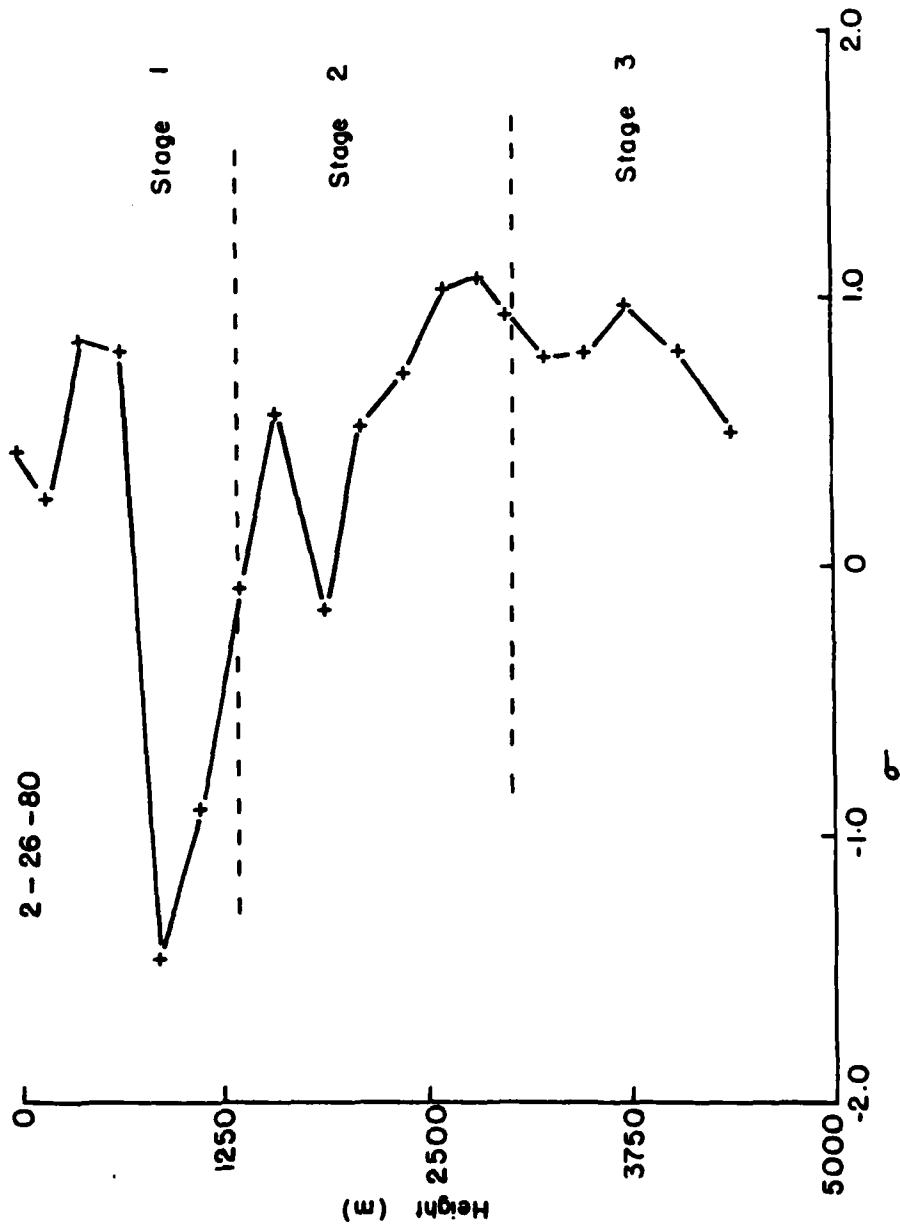


Fig.2.25:  $\sigma$  as a function of height, 26 February, 1980, similar to Fig.2.23  
 $\sigma$  is dimensionless.

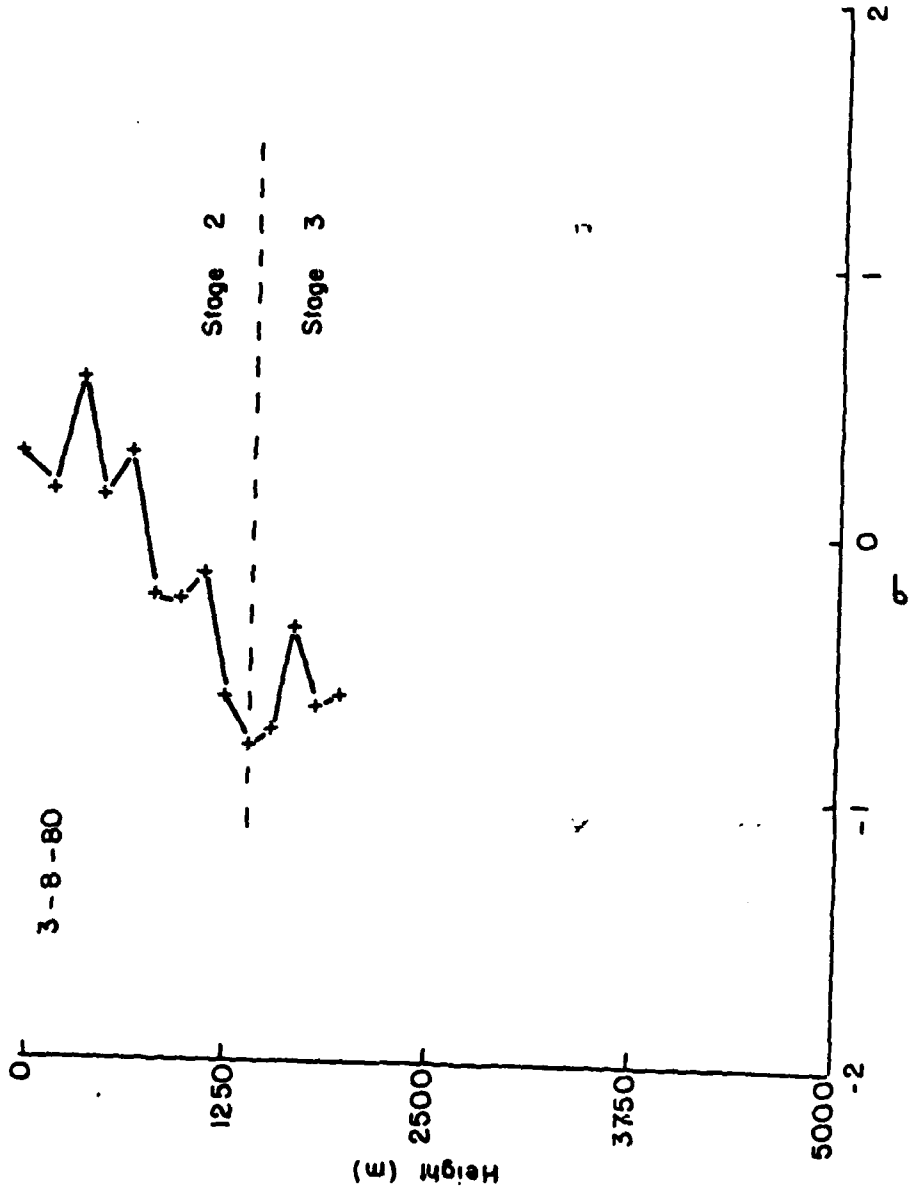
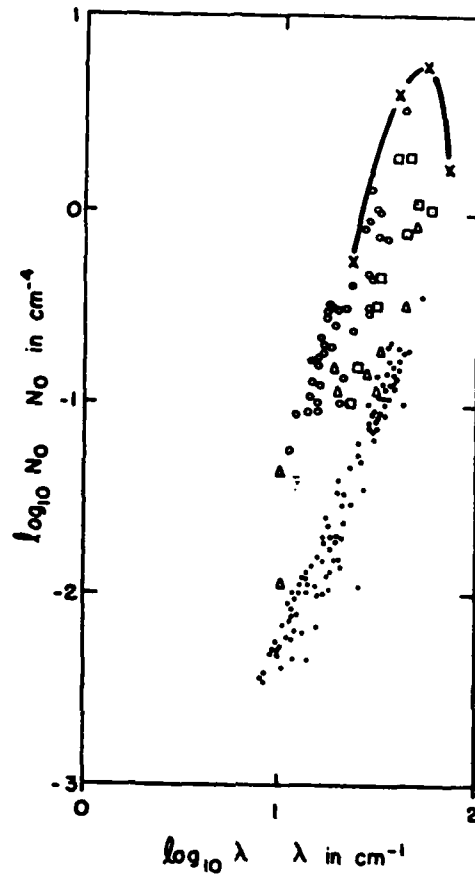


Fig.2.26:  $\sigma$  as a function of height, 8 March, 1980, similar to Fig.2.23

probability of collisional breakup is high or the number of fragments generated during collisional breakup is extremely high or both. This question will be investigated in the section on theoretical analyses.

## 2.6 Comparisons with other studies

Some recent observational studies of snow-size spectra have shown a spectral behavior similar to the ASD results, although the scatter is typically much greater. This is possibly due to the fact that the data are not taken in a manner as coherent as the ASD. Passarelli (1978a,c) employed similar instrumentation but a different vertical sampling scheme. The aircraft was placed in either a constant ascent or descent while flying a constant heading. Particle size distributions were averaged over 15 s intervals. The spectra from flights on 6 and 10 March, 1975 are shown in  $N_0 - \lambda$  space in Fig. 2.27. While spectra obtained via the ASD technique show a very systematic behavior with height, the spectra obtained on these two days do not. The spectra apparently lie on a line corresponding to the second stage, but the position is random. The spectra for each day are very well differentiated in  $N_0 - \lambda$  space which probably reflects the very different environmental conditions on the two days.



- o 6 Mar 1975 (Passarelli 1978a)
- 10 Mar 1975 ( " " )
- x-x 26 Nov 1975 ( " 1978c)
- Δ 22 Jan 1975 (Houze et al, 1980)
- 8 Dec 1976 ( " et al 1980)

Fig.2.27: Related observational studies. See text for details.

Passarelli (1978c) also averaged particle size spectra over 10 km horizontal passes at various altitudes. The data for a flight on 26 November 1975 are also shown in Fig. 2.27. The passes are spaced at 600 m and timed at 10 min apart, which is approximately the time required for snow to fall from one level to the next. The results show a first and second stage. Vertical incidence radar measurements on this day indicated fairly steady precipitation while the aircraft was sampling.

Houze et al., (1979, 1980) employed a similar technique by flying level passes although no attempt was made to follow snow from level to level. The spectra for flights on 22 January 1976 and 8 December 1976 are also shown in Fig. 2.27. The data are more scattered, perhaps because transient environmental conditions are manifested over the long sampling paths. However, the observed spectra are still within the values from the other cases. Although the height for each spectrum is not indicated, Houze et al. (1979) show that  $N_0$  and  $\lambda$  decrease with increasing temperature. Based on the general trend that temperature increases with decreasing altitude, it can be inferred that  $N_0$  and  $\lambda$  decrease with decreasing altitude, which is in agreement with the second stage concept.

Gordon et al. (1982) flew an elongated figure-eight

pattern while the plane was descending at 1 or 2 m/s, approximately the fallspeed of snow. The figure-eight was oriented normal to the orientation of a rain band. Their analyses technique is similar to that used for the ASD. The data are derived from a PMS 2D-P precipitation probe, but it is not clear how the 2-dimensional data are reduced to 1 dimension. Their results for 15 February 1982 are plotted in Fig. 2.28. From the results in  $N_0 - \lambda$  space, their findings are similar to those from the spirals. However, they conclude that there are four stages of snow growth. The first stage, at temperature below  $-22^\circ\text{C}$ , snow growth is dominated by nucleation and deposition, which basically agrees with the findings from the ASD data. The second stage, between  $-11^\circ\text{C}$  and  $-22^\circ\text{C}$  is where aggregation is dominant, which again agrees with the ASD data. The third stage, from  $-4^\circ\text{C}$  to  $-10^\circ\text{C}$ , is where secondary ice crystal production, and aggregation are dominant. In contrast to this study, these authors conclude that secondary ice crystal production is due to a rime-splintering mechanism. They base their reasoning for rime-splintering on the concentration of particles (assumed to be water drops) larger than 24 microns as counted by the Forward Scattering Spectrometer Probe (FSSP). As has been presented earlier, the particle counts from the FSSP during snow conditions are rather unreliable. Gordon et al. did not use other instruments, such as the J-W probe or icing rate detector to double check the presence of liquid water.

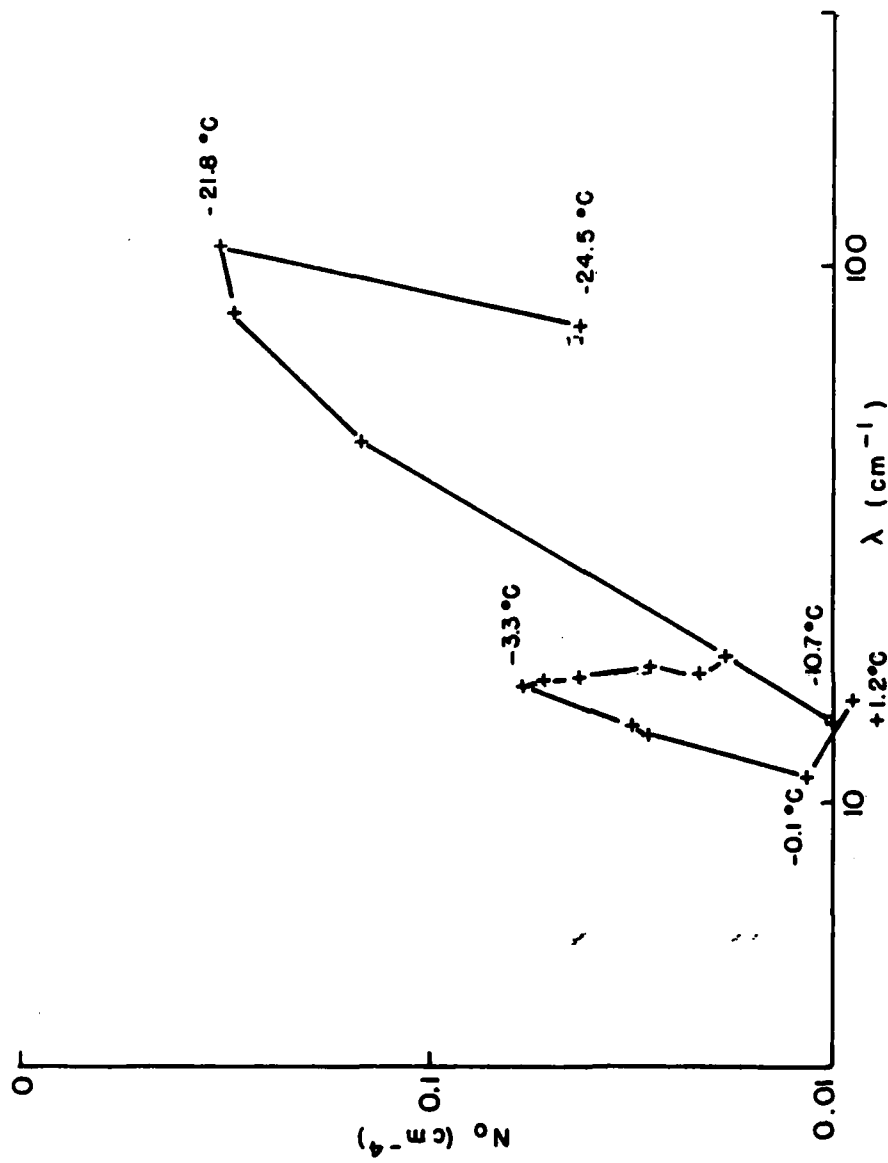


Fig. 2.28:  $N_o - \lambda$  trajectory of spiral flown by Gordon et.al., 1982, environmental temperature is written next to each loop.

So, the occurrence of rime-splintering is not well substantiated. The fourth stage, from  $-4^{\circ}\text{C}$  to  $0^{\circ}\text{C}$ , is where only aggregation is observed. Except for spiral 2, the ASD data did not reach such a high temperature and both  $N_0$  and  $\lambda$  decrease between the last two loops (18 and 19, between temperature  $-2^{\circ}\text{C}$  and  $0^{\circ}\text{C}$ ).

It is revealing that all observed values indicate that the slope,  $\lambda$ , always terminates at around  $10\text{ cm}^{-1}$ . This is in accord with the ASD results which suggest collisional breakup. No matter what the height and environmental conditions are, the observed  $N_0$  values are within three orders of magnitude and the  $\lambda$  values are within one order of magnitude.

## 2.8 Counter-examples

The results from four spirals flown in 1981 (on an AFGL C-130 aircraft) are shown in Figs. 2.29, 2.30, 2.31 and 2.32, two each on April 14, 1981 and on April 17, 1981. The results for the two spirals on April 14 do not indicate the three-stage snow growth processes. The flights took place in pre-frontal showery conditions and the temperature for these spirals is rather high. The changes of  $N_0$ - $\lambda$  for the four cardinal quadrants of the two spirals indicate that there is no horizontal

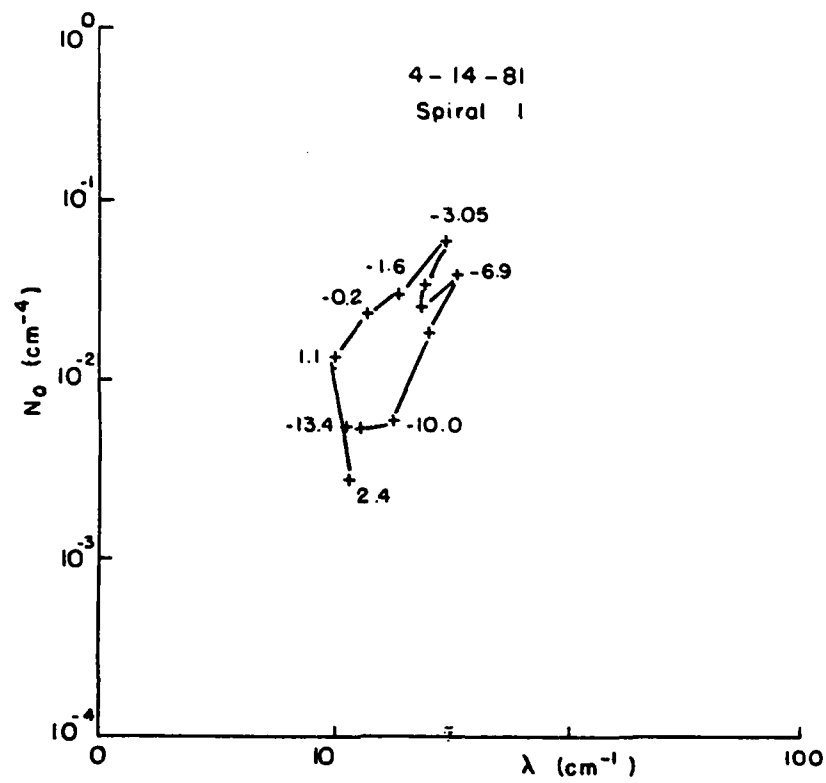


Fig.2.29:  $N_0$ - $\lambda$  trajectory of first spiral on 14 April, 1981

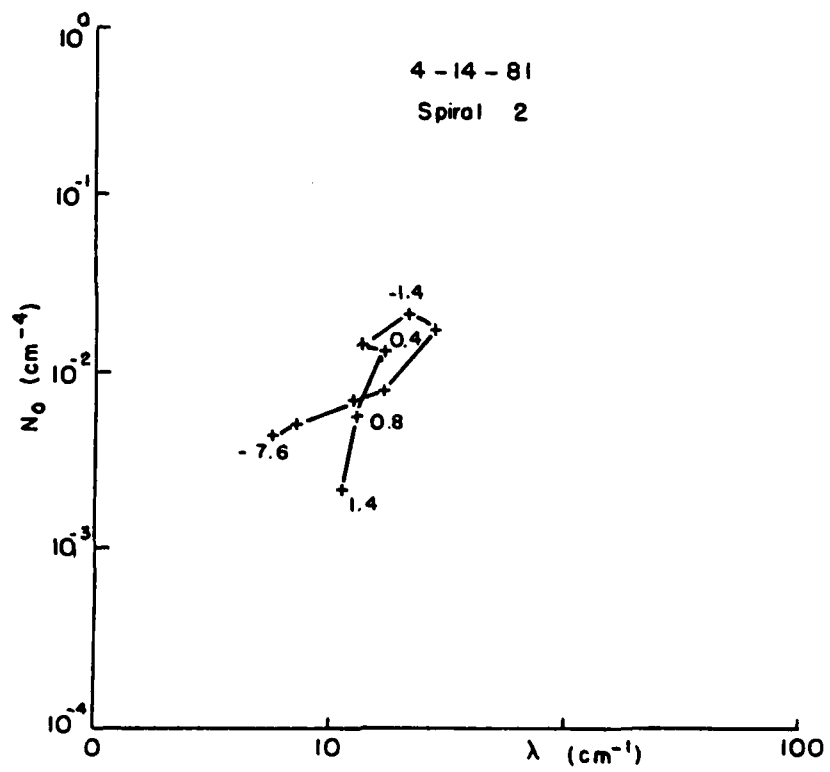


Fig.2.30:  $N_0$ - $\lambda$  trajectory of second spiral on 14 April, 1981

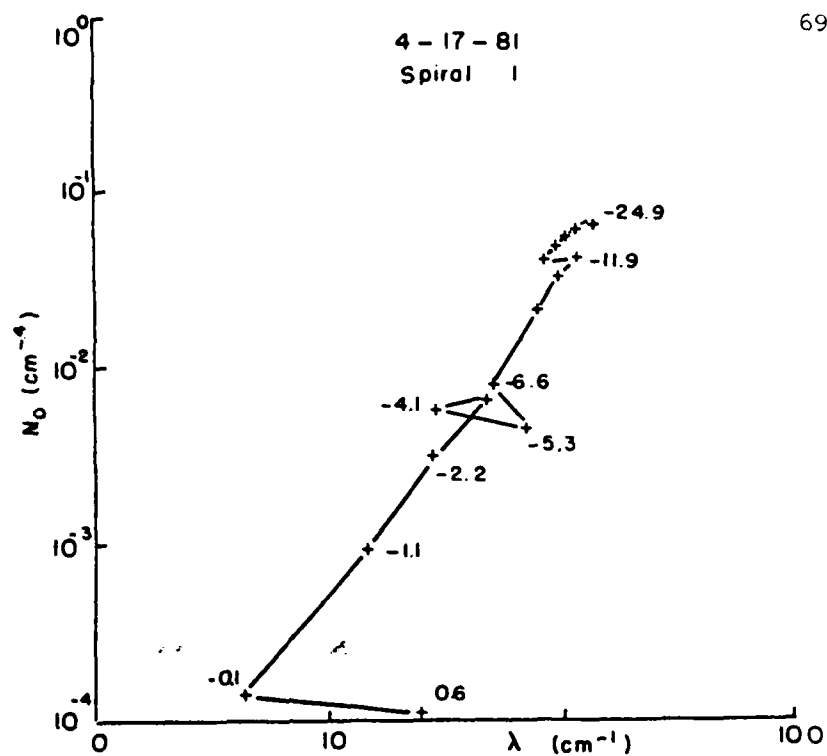


Fig.2.31:  $N_0$ - $\lambda$  trajectory of first spiral on 17 April, 1981

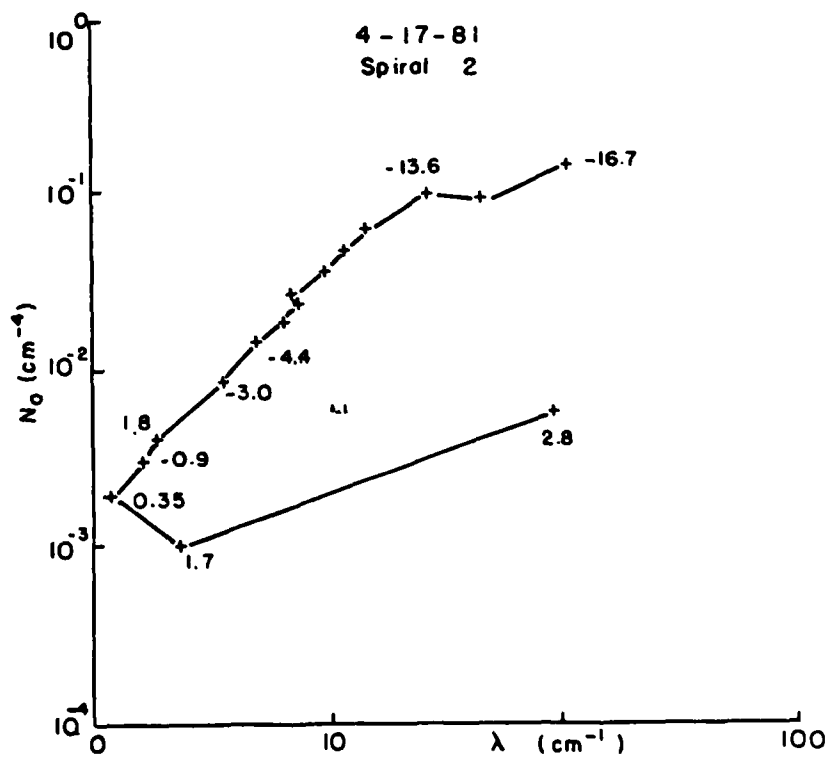


Fig.2.32:  $N_0$ - $\lambda$  trajectory of second spiral on 17 April, 1981

homogeneity. Fig. 2.33 is the example from the first spiral on this day. The changes of  $N_0 - \lambda$  are disorganized and incoherent for the four quadrants. In conclusion, it can be said that the ASD will work only when the precipitation is widespread and horizontally homogeneous. It will not work in showery conditions.

The changes for  $N_0$  and  $\lambda$  from the spirals on April 17, 1981 (Figs. 2.31 and 2.32) have one peculiar behavior which is not found in any other spirals, namely that the slope,  $\lambda$ , kept on decreasing even beyond the 10 cm<sup>1</sup> until melting. The synoptic conditions where the flights took place are a weak system between a surface ridge and a surface trough with warm air advection from the gulf. From the temperature and dew point taken on the plane, the environmental conditions are clearly subsaturated (Fig. 2.34). The changes of total particle concentration from the 1-D precipitation probe with height for the two spirals are shown in Figs. 2.35 and 2.36. Except for the first few loops of the spirals, the concentration is decreasing (compare the change of concentration with height for the 1980 spirals in Fig. 2.37). Also plotted on the figure is the second moment. The changes of the sum of the second moment are comparable to those of the total concentration. Since the mass of a snowflake is approximately proportional to the square of the diameter, the sum of the second moment is proportional to the total mass.

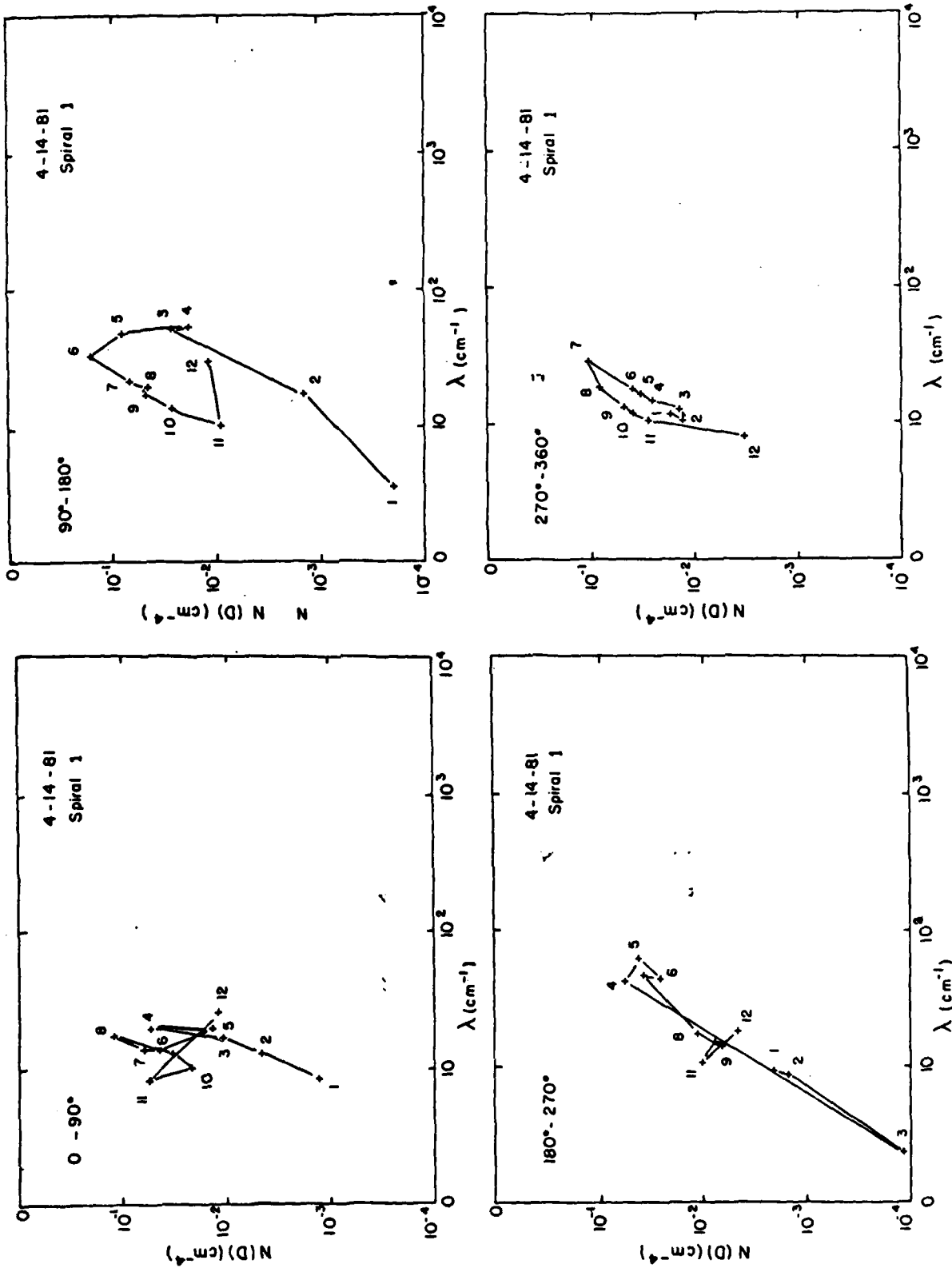


Fig.2.33:  $N_0$ - $\lambda$  trajectories for the four cardinal quadrants of first spiral on 14 April, 1981

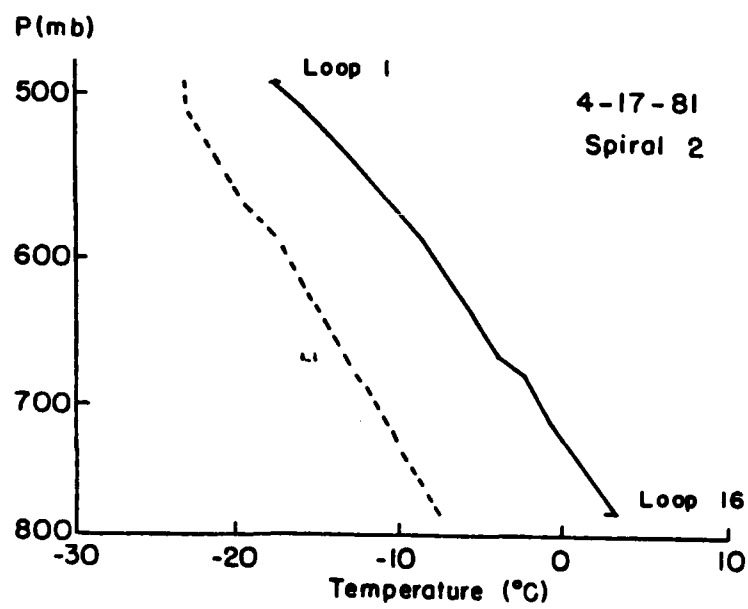
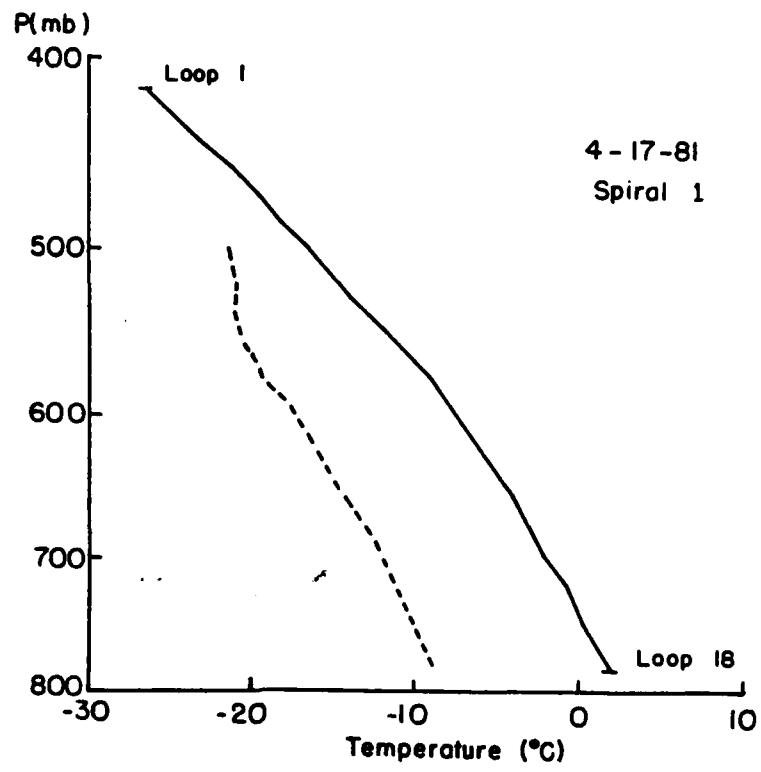


Fig.2.34: Aircraft soundings for spirals on 17 April, 1981

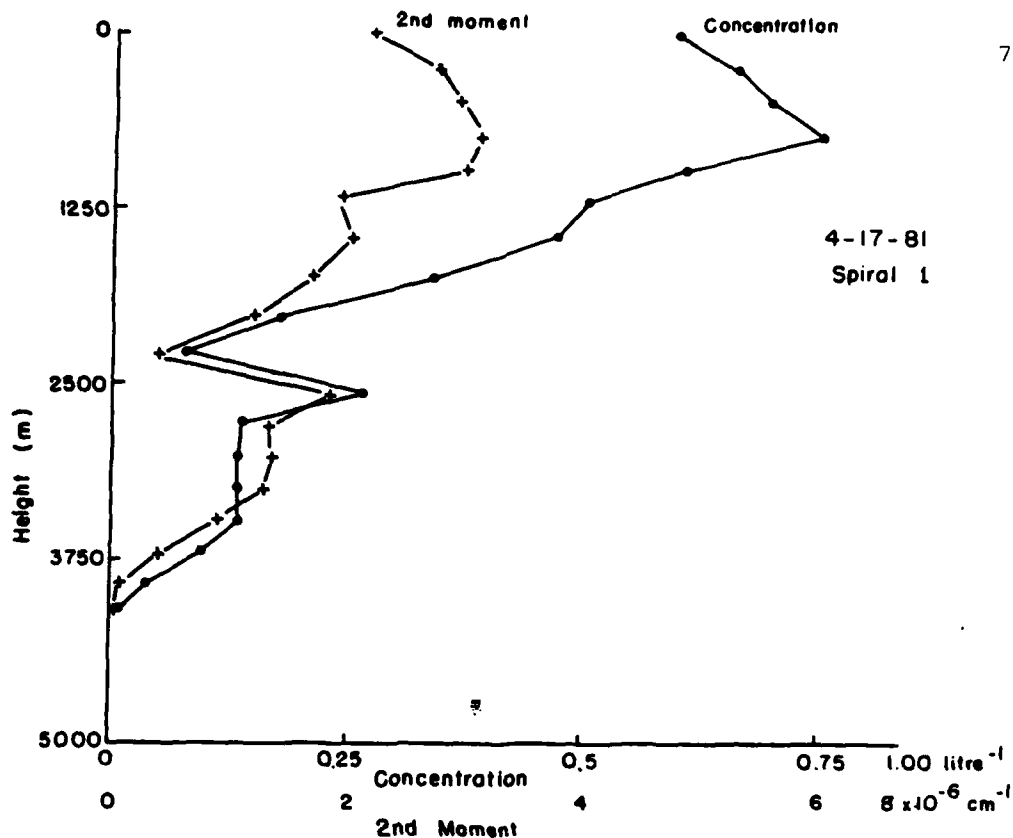


Fig.2.35: 1-D precip probe total particle concentration and second moment against height for first spiral on 17 April, 1981

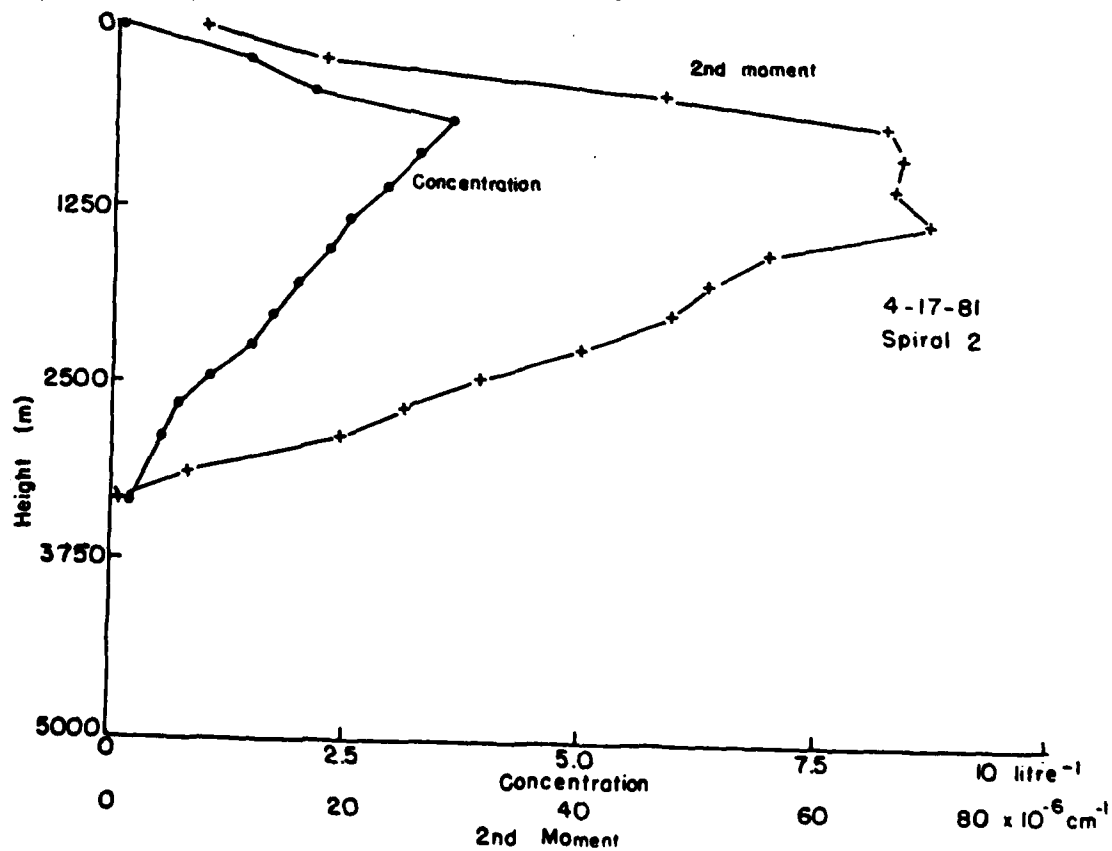


Fig.2.36: 1-D precip probe total particle concentration and second moment against height for second spiral on 17 April, 1981

So, a decrease in both the total concentration and the total mass implies that particles are evaporating due to subsaturation (compare Figs. 2.37 and 2.38 for the 1980 ASDs). In contrast to the 1980 2-D data, the 2-D images for these two cases indicate an absence of needles in the third stage. This also suggests that the atmosphere is subsaturated.

A possible explanation is that the number of large particles is being maintained by aggregation, while collisional breakup generates minute particles that are not detectable by the 1-D precip probe (Fig. 2.39). Under conditions of deposition, these small particles will grow into detectable sizes, but, under conditions of subsaturation, these small particles not only cannot grow into detectable sizes, but rather they are evaporated. The 200-Y probe can only detect particles in a limited range. As depicted in Fig. 2.39, it could be that the size distribution detected by the probe decreases in both the 'intercept' and the 'slope' and so the slope will decrease below the  $10 \text{ cm}^{-1}$  limit observed in the other spirals. Figs. 2.40 and 2.41 show the evolution of the last few spectra in the two spirals. The behaviour of the two spirals which are flown on the same day and in similar environmental conditions are consistent. If this hypothesis is true, then it can also be postulated that the collisional breakup fragments are composed mainly of small particles.

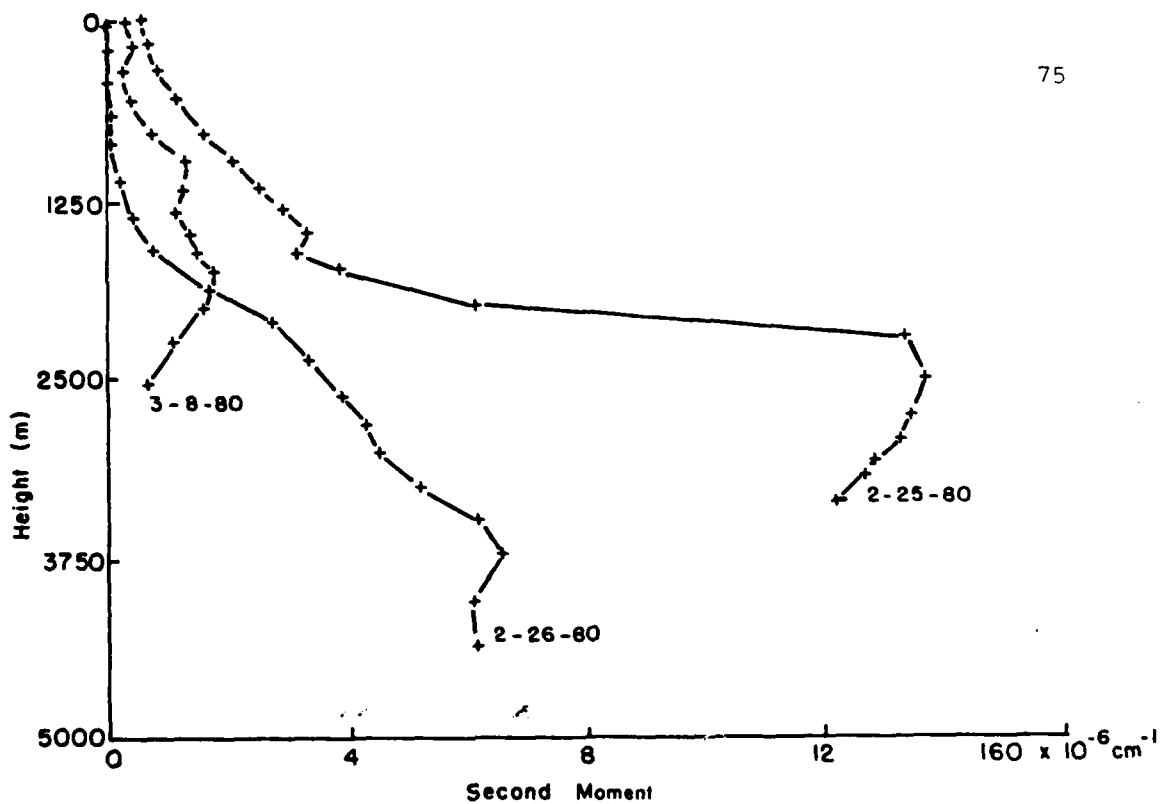


Fig.2.37: 1-D precip probe second moment against height for the three spirals in 1980

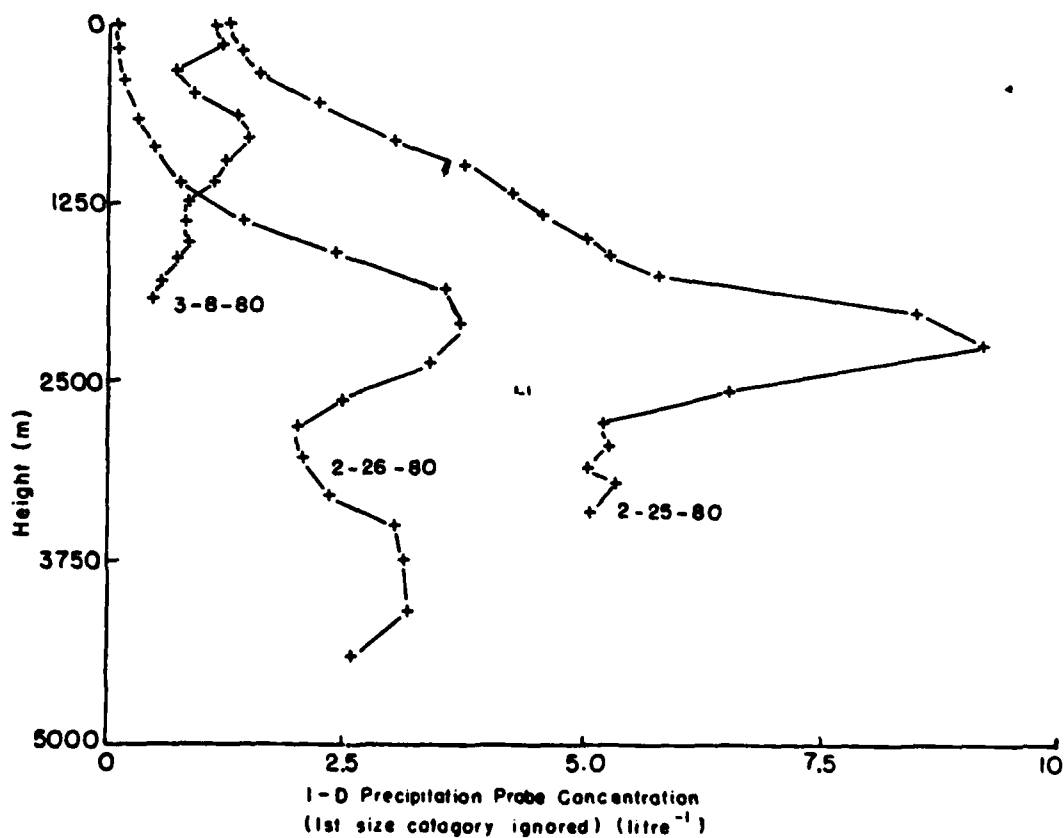


Fig.2.38: 1-D precip probe total concentration against height for the three spirals in 1980

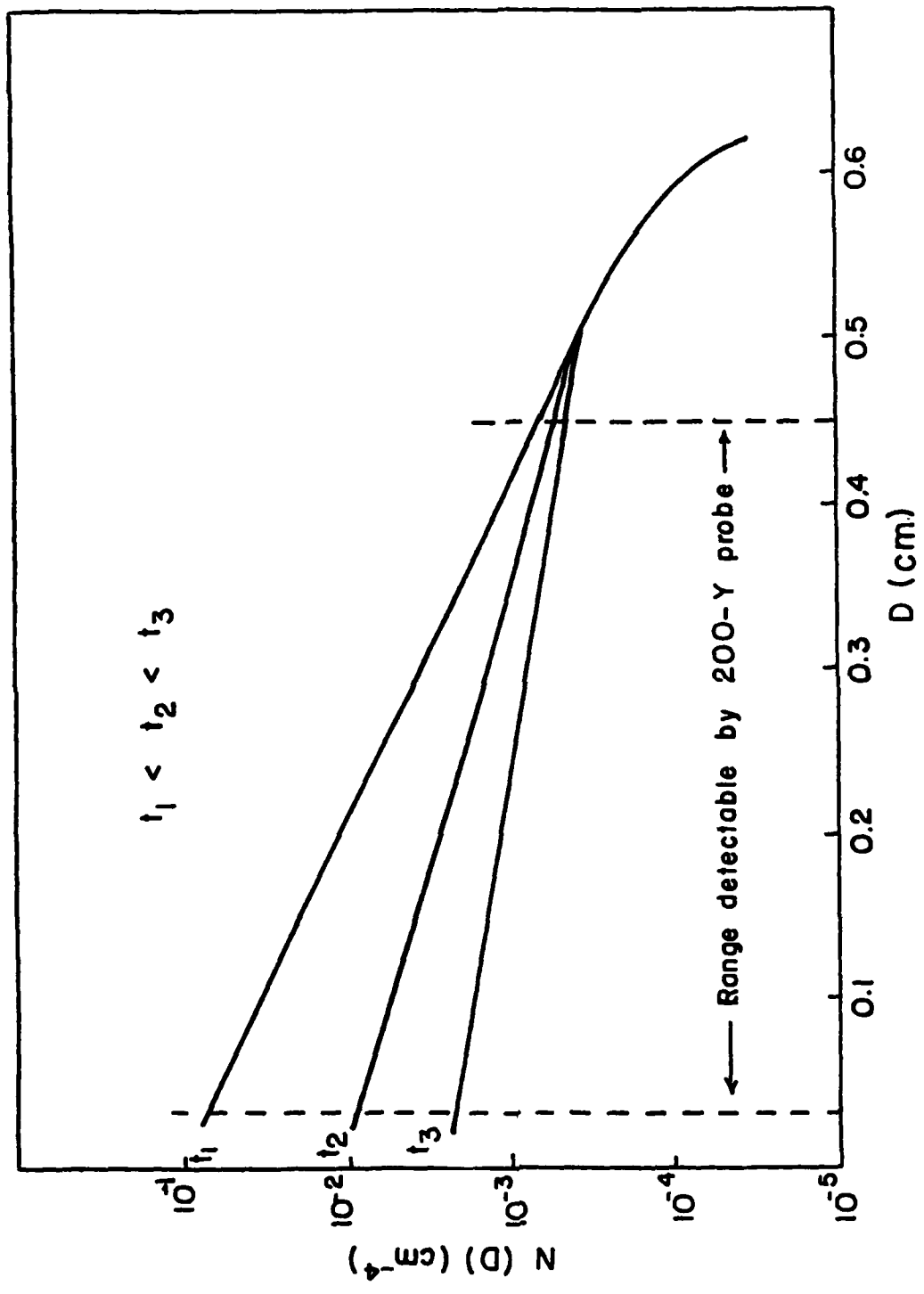


Fig. 2.39: Possible size distributions beyond the range detectable by the 200-Y probe at three different times

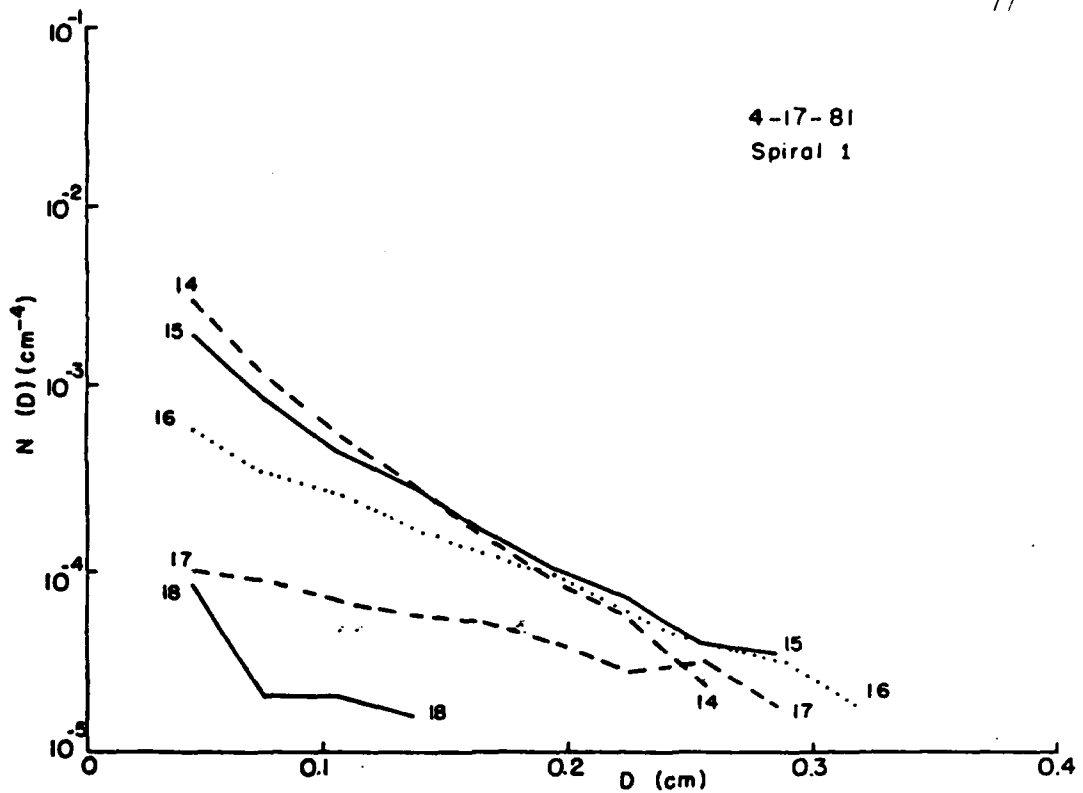


Fig.2.40: Snow size spectra of the last few loops for the first spiral on 17 April, 1981

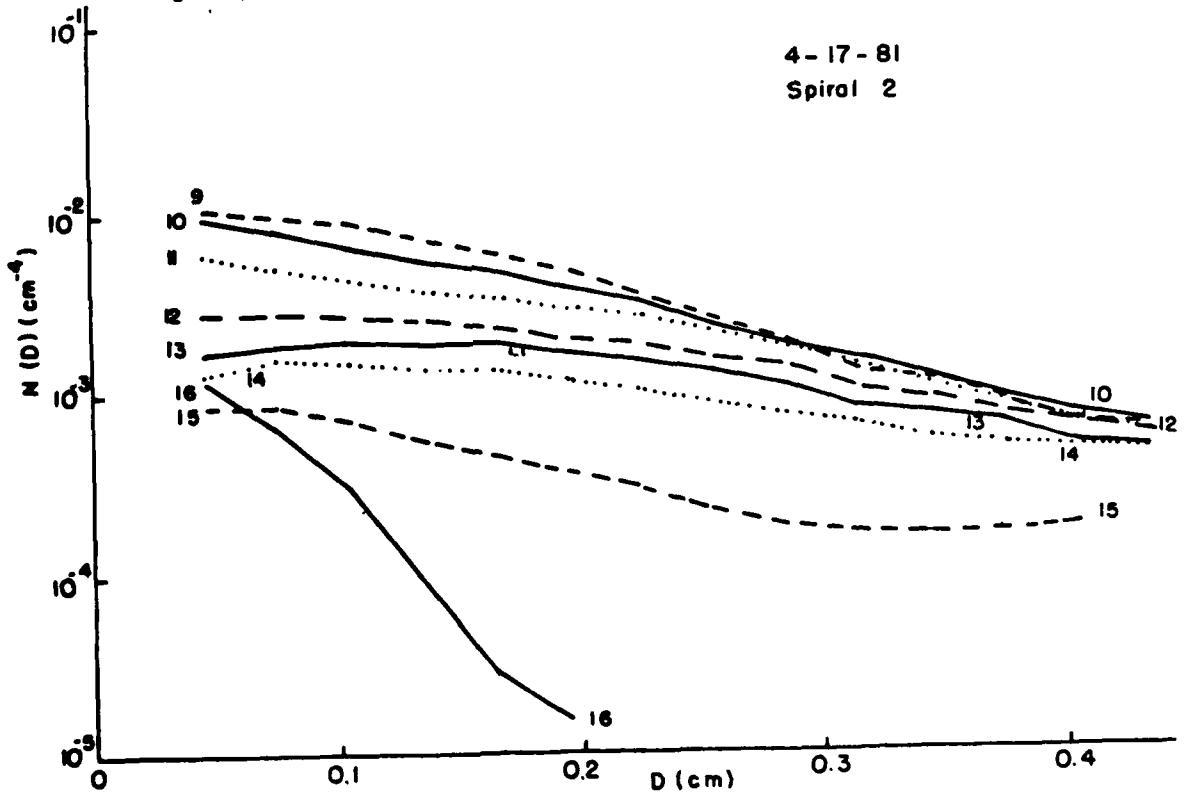


Fig.2.41: Snow size spectra of the last few loops for the second spiral on 17 April, 1981

## CHAPTER 3

## THEORETICAL ANALYSES

The ASD data presented in the last chapter reveal that snow growth goes through different distinct stages and the intuitive explanation suggests that the stages are deposition, aggregation and collisional breakup. If this conjecture can be supported by a rigorous theoretical treatment, then the intuition is confirmed to be valid. In order to accomplish this, various theoretical models have been developed and tested. In this chapter, such models incorporating the physical processes of vapor deposition, sedimentation due to differential particle fallspeed, aggregation, collisional breakup and rime-splintering are presented.

The first type of model has a two-parameter particle size distribution (2.1). The physical processes represented are deposition, aggregation and collisional breakup. Two forms of collisional breakup are used. The first one assumes that the fragments generated from collisions are distributed in a negative-exponential distribution. The second one assumes that the number of fragments generated from each

collision event is a constant, regardless of the size of the colliding particles. Computations are performed using the values of  $N_0$  and  $\lambda$  from the first loop of the 1980 spirals as initial conditions. The results from the models compare well with the observations and so the intuitive explanations of the observations are well supported by theory.

The second type of model has a three-parameter particle size distribution (2.4). Again, two forms of collisional breakup are used. In this type of model, the results from using a negative-exponential distribution of fragment sizes give satisfactory results compared to the observations. But, the results from using the other fragment size distribution do not. From the results of both the two-parameter models and the three-parameter models, it is found that collisional breakup is an important snow-growth mechanism, especially when the temperature is close to melting. Another result is that when two snow particles collide, they are more likely to aggregate than to break up. However, when they do break up, they generate numerous small particles.

The effect of different initial particle concentration on the evolution of size spectra is studied with two-parameter models. Increasing the concentration without increasing the mass causes the change from deposition stage to aggregation stage to start earlier than before, but the

change from aggregation to collisional breakup stages is delayed.

The problem of rime-splintering is studied next. Theoretical models with the processes of deposition, aggregation and rime-splintering are developed. The results are compared with the observational results from the spirals. They show that rime-splintering is not likely to be a predominant mechanism in this kind of precipitation.

To end the chapter, the effects of melting on the change from snow-size spectra to rain drop spectra are discussed.

### 3.1 Basic equations and assumptions

If  $f(x, h, t)dx$  is the concentration of particles with mass between  $x$  and  $x+dx$  at height  $h$  and time  $t$ , then the change in the number density due to nucleation, vapor deposition, sedimentation due to differential particle fallspeed, aggregation, collisional breakup and rime-splintering can be formulated using the stochastic collisional model as (Scott, 1968; Drake, 1972; Passarelli, 1978b and Srivastava, 1978):

$$\begin{aligned}
& \frac{\partial}{\partial t} f(x, h, t) \\
&= - \frac{\partial}{\partial x} \{ [w - V(x)] f(x, h, t) \} + c(t, h) \zeta(x) - \frac{\partial}{\partial x} \{ \dot{x} f(x, h, t) \} \\
&+ \frac{1}{2} \int_0^x f(x-x', h, t) f(x', h, t) K(x-x', x') q(x-x', x') dx' \\
&- f(x, h, t) \int_0^{\infty} f(x', h, t) K(x, x') q(x, x') dx' \\
&+ \frac{1}{2} \iint_0^{\infty} S(x|x', x'') f(x', h, t) f(x'', h, t) K(x', x'') \\
&\quad [1 - q(x', x'')] dx' dx'' \\
&- f(x, h, t) \int_0^{\infty} f(x', h, t) K(x, x') [1 - q(x, x')] dx' \\
&+ \int_0^{\infty} \pi E \left( \frac{D}{2} + \frac{d}{2} \right) [V(x) - u] n' f(x, h, t) dx
\end{aligned} \tag{3.1}$$

where  $w$  = updraft velocity

$V(x)$  = terminal fallspeed of particle with mass  $x$

$u$  = terminal fallspeed of supercooled droplets

$\dot{x}$  = rate of change of mass due to vapor deposition

$\zeta(x)$  = Dirac delta function

$c(t, h)$  = nucleation function

$K(x', x'')$  = collisional kernel between particles of mass  $x'$  and  $x''$

$q(x', x'')$  = probability of aggregation when two particles of mass  $x'$  and  $x''$  collide

$S(x|x', x'')$  = number of fragments with mass between  $x$  and  $x+dx$  when particles with mass  $x'$  and  $x''$  collide and break up

$D$  = diameter of snow particle with mass  $x$

$d$  = diameter of supercooled liquid droplets

$n'$  = number of supercooled liquid droplets

$E$  = collisional efficiency between snow particles and supercooled liquid droplets

The first term on the right hand side is the sedimentation due to differential particle fallspeed. The second term is the increase in concentration due to nucleation. The Dirac delta function is used because nucleation can only increase the concentration but cannot affect the mass or the reflectivity factor. The third term is the change of particle spectrum due to vapor deposition on snow crystals. The fourth term is the production of particles due to crystal-crystal aggregation. The fifth term is the depletion due to aggregation. The sixth term is the production of particles due to collisional breakup. The seventh term is the depletion of particles due to collisional breakup. The eighth term is the increase in concentration due to rime-splintering. Again, this term can only affect the concentration but not the mass or the reflectivity factor.

The fragment size distribution is constrained by the following relationship:

$$S(x|x', x'') = 0 \quad \text{if } x > x' + x'' \quad (3.2)$$

Physically, this means that when two particles collide, no fragment can be larger than the sum of the mass of the original particles. Also,

$$x' + x'' = \int_0^{\infty} x S(x|x', x'') dx. \quad (3.3)$$

This means that the total mass of all fragments must equal the total mass of the parent particles.

From these basic equations, the moment conservation equations can be derived. Denoting the total particle concentration,  $n(h, t)$ , by

$$n(h, t) = \int_0^{\infty} f(x, h, t) dx \quad (3.4)$$

and the vertical flux of particle concentration,  $n_f(h, t)$ , by

$$n_f(h, t) = \int_0^{\infty} V(x) f(x, h, t) dx. \quad (3.5)$$

the zeroth moment conservation equation can then be written as

$$\begin{aligned} \frac{\partial n(h, t)}{\partial t} &= \frac{\partial n_f(h, t)}{\partial h} \\ &- \frac{1}{2} \int_0^{\infty} \int_0^{\infty} f(x', h, t) f(x'', h, t) K(x', x'') q(x', x'') dx' dx'' \\ &+ \frac{1}{2} \int_0^{\infty} \int_0^{\infty} \int_0^{\infty} S(x | x', x'') f(x', h, t) f(x'', h, t) K(x', x'') \\ &\quad [1 - q(x', x'')] dx dx' dx'' \\ &- \int_0^{\infty} \int_0^{\infty} f(x', h, t) f(x'', h, t) K(x', x'') [1 - q(x', x'')] dx' dx'' \end{aligned} \quad (3.6)$$

Denoting the total particle mass by  $\chi$  and the vertical mass flux by  $\chi_f$ ,

$$\chi = \int_0^{\infty} x f(x, h, t) dx \quad (3.7)$$

and

$$\chi_f = \int_0^{\infty} V(x) x f(x, h, t) dx \quad (3.8)$$

The first moment conservation equation can be written as

$$\frac{\partial Z}{\partial t} = \frac{\partial Z_f}{\partial h} + \int_0^{\infty} x f(x, h, t) dx \quad (3.9)$$

Denoting the second moment of the mass, which may be interpreted as the radar reflectivity factor, as  $Z(h, t)$  and the vertical flux of the second moment as  $Z_f(h, t)$ ,

$$Z = \int_0^{\infty} x^2 f(x, h, t) dx \quad (3.10)$$

$$Z_f = \int_0^{\infty} V(x) x^2 f(x, h, t) dx \quad (3.11)$$

the second moment conservation can be written as

$$\begin{aligned} \frac{\partial Z}{\partial t} = & \frac{\partial Z_f}{\partial h} + \int_0^{\infty} 2x f(x, h, t) dx \\ & + \int_0^{\infty} \int_0^{\infty} x' x'' f(x', h, t) f(x'', h, t) K(x', x'') q(x', x'') dx' dx'' \\ & + \frac{1}{2} \int_0^{\infty} \int_0^{\infty} \int_0^{\infty} \frac{x^2}{2} S(x; x', x'') f(x', h, t) f(x'', h, t) K(x', x'') \\ & [1 - q(x', x'')] dx dx' dx'' \\ & - \int_0^{\infty} \int_0^{\infty} x^2 f(x, h, t) f(x', h, t) K(x, x') [1 - q(x, x')] dx dx' \end{aligned} \quad (3.12)$$

Since snow is falling downward towards the ground, it is easier both analytically and conceptually to take a reference level of height and designate it as  $h=0$  (e.g., at the top of a snowshaft or at the beginning of an ASD). Then  $h$  increases downwards.

Since the observations are done in a widespread, slow updraft wintertime snowstorm, steady precipitation can be assumed. When this assumption is applied to the theory, all time derivatives and dependencies in the moment conservation

equations are eliminated. Moreover, the convergence of upward flux of moisture is balanced by the increase in the downward flux of precipitation,

$$\frac{\partial X_f}{\partial h} = \frac{\partial \omega p_{vs}}{\partial h} \quad (3.13)$$

where  $p_{vs}$  = saturation vapor density.

Integrating with respect to height gives, if the downward flux of precipitation is taken to be positive,

$$X_f - X_{f_0} = \omega p_{vs} - \omega p_{v_0} \quad (3.14)$$

where the subscript 0 indicates the initial condition. By the equation of state and the Clausius-Clapeyron equation, the saturation vapor density as a function of height is

$$p_{vs} = \frac{6.11}{RT_0} \exp\left[\frac{L}{R}\left(\frac{1}{273} - \frac{1}{T_0}\right)\right] \exp\left(-\frac{L\gamma h}{RT_0^2}\right) \quad (3.15)$$

where  $L$  = latent heat of sublimation

$R$  = gas constant for water

$\gamma$  = atmospheric lapse rate

$T_0$  = initial temperature

At  $h = 0$ ,

$$p_{vs} = \frac{6.11}{RT_0} \exp\left\{\frac{L}{R}\left(\frac{1}{273} - \frac{1}{T_0}\right)\right\}, \quad (3.16)$$

and denoting

$$A = \frac{LW}{RT_0} \quad (3.17)$$

yields,

$$X_f - X_{f_0} = w \rho_{vso} (e^{AL} - 1)$$

For  $X_f \gg X_{f_0}$ ,  $AL \gg 1$

$$X_f = w \rho_{vso} e^{AL} \quad (3.18)$$

So, for a known atmospheric lapse rate, the precipitation mass flux is determined by the updraft velocity.

Other assumptions that are made in order to simplify the computations include: The rate of growth of a particle due to vapor deposition,

$$\dot{x} = g(h)D \quad (3.19)$$

where  $g(h)$  is a function depending on height and temperature. The mass-diameter and mass-terminal fallspeed relationships are

$$x = \alpha D^\beta \quad (3.20)$$

$$v = aD^b \quad (3.21)$$

where  $\alpha$ ,  $\beta$ ,  $a$  and  $b$  are constants depending on the snowfall type. The collision kernel is formulated according to the geometric kernel,

$$K(x', x'') = \frac{\pi}{4} (D' + D'')^2 E |V(D') - V(D'')| \quad (3.22)$$

where  $E$  = collision efficiency.

From the elastic properties of ice (Hobbs, 1974), it can be assumed that the larger a snow crystal, the more easily it breaks upon collision. Mathematically, the coalescence probability can be represented by

$$q(x', x'') = e^{-c(D'+D'')} \quad (3.23)$$

where  $c$  is a constant. The exponential form is chosen to facilitate the mathematical analysis. A plot of the coalescence probability is shown in Fig. 3.1.

All the mathematical analyses that follow make use of the above assumptions.

### 3.2 Two-parameter formulations

The snow size spectrum,  $f(x, h)dx$ , can be represented by a Gunn and Marshall (1958) type negative exponential distribution,

$$f(x, h)dx = N_0(h)e^{-\lambda(h)D} dD \quad (3.24)$$

where  $N_0(h)$  and  $\lambda(h)$  are functions of height. In this formulation, there is one independent variable,  $h$ , and two dependent variables,  $N_0$  and  $\lambda$ . (Kessler, 1969; Srivastava, 1971, and Passarelli, 1978a, b)

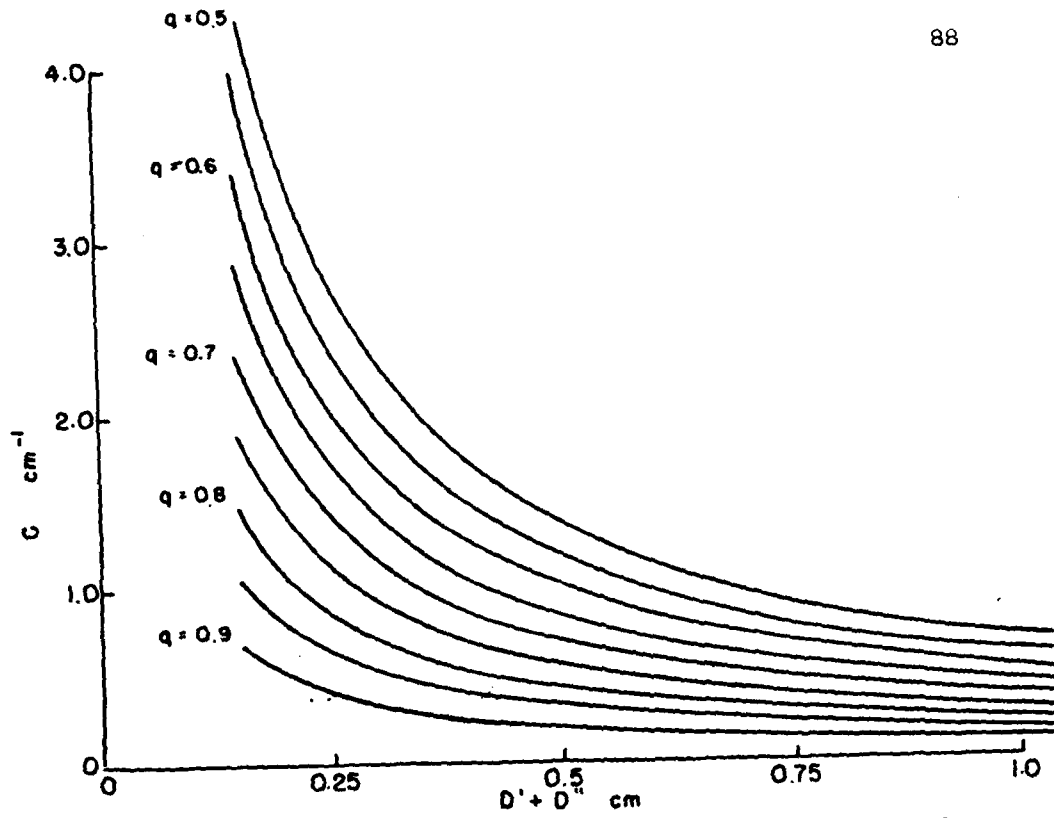


Fig.3.1: Coalescence probability,  $q$ , as a function of the total diameter  $D' + D''$  and the constant  $c$

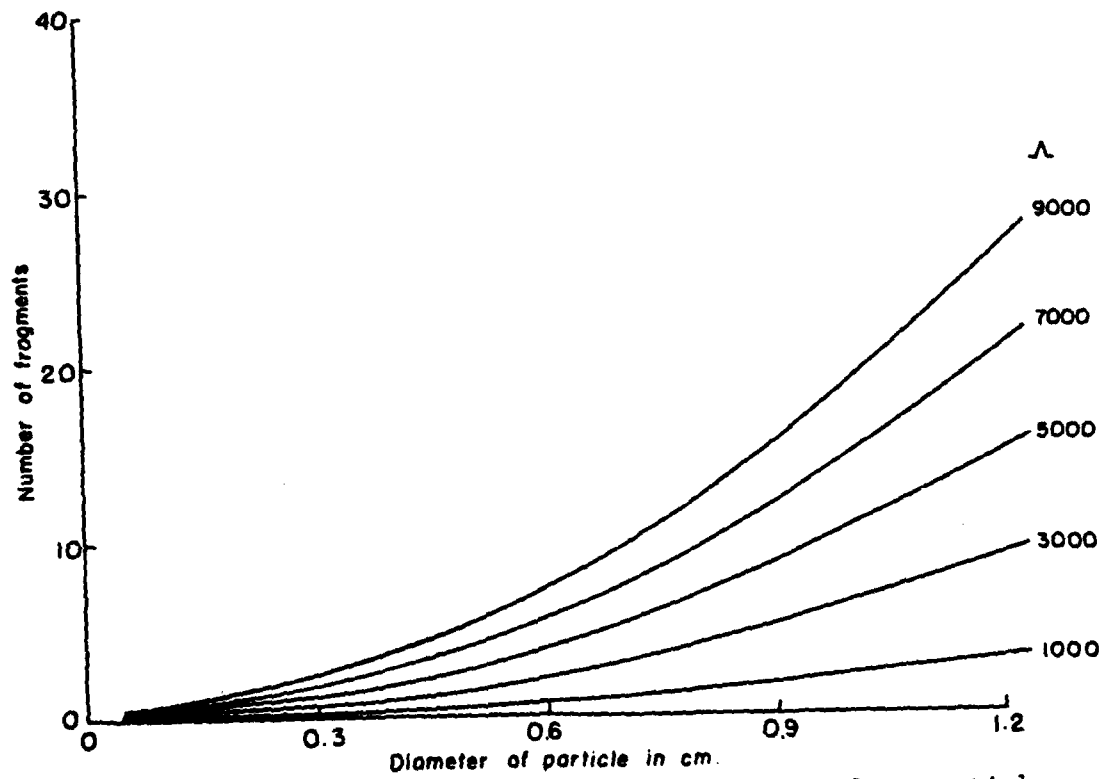


Fig.3.2: Number of fragments resulting from collision of a 2 mm particle and particles of various sizes for different  $\lambda$ 's

### 3.2.1 Exponential fragment size distribution

Previous studies (e.g., Vardiman, 1978) have shown that the larger the crystals, the more fragments are generated during collisions. The laboratory investigations which are to be described in appendix 2 indicate that the fragments are in an approximately negative exponential size distribution. These motivate the formulation of the fragment size distribution to be

$$S(x|x', x'') = (x' + x'') \Lambda^2 e^{-\Lambda x} \quad (3.25)$$

where  $\Lambda$  is a constant. The total number of fragments is

$$\int_0^{\infty} S(x|x', x'') dx = (x' + x'') \Lambda \quad (3.26)$$

which implies that the larger the particles, the more numerous are the fragments. Plots of the number of fragments resulting from the collision of a 2 mm particle and particles of various sizes for different  $\Lambda$ 's are shown in Fig. 3.2.

From this formulation, the first moment conservation equation can be written as:

$$\frac{\partial X_1}{\partial t} = -\frac{g N_2}{\lambda^2} \quad (3.27)$$

For the second moment conservation equation, the collisional integrals can be simplified by scaling, e.g., let  $(\lambda + c)D_1 = X$  and  $(\lambda + c)D_2 = Y$ , then

$$\alpha^2 N_2^2 \frac{\pi}{4} - E a \int_0^{\infty} \int_0^{\infty} D_1^b D_2^b (D_1 + D_2)^2 |D^b - D^b| e^{-(\lambda+c)(D_1+D_2)} dD_1 dD_2$$

$$= \frac{\alpha^2 N_0^2 \frac{\pi}{4} E a}{(\lambda+c)^{b+2\beta+4}} \int_0^\infty \int_0^\infty x^\beta y^\beta (x+y)^2 (x^b - y^b) e^{-(x+y)} dx dy.$$

Then the second moment conservation equation is

$$\begin{aligned} \frac{\partial Z_2}{\partial t} = & \frac{2\alpha g N_0 \Gamma(\beta+2)}{\lambda^{\beta+2}} + \frac{2\alpha^2 N_0^2 \frac{\pi}{4} E a I_1}{(\lambda+c)^{b+2\beta+4}} \\ & + \frac{4\alpha N_0^2 \frac{\pi}{4} E a I_2}{\lambda^{b+\beta+4}} - \frac{4\alpha N_0^2 \frac{\pi}{4} E a I_2}{\lambda(\lambda+c)^{b+\beta+4}} \\ & - \frac{2\alpha^2 N_0^2 \frac{\pi}{4} E a I_3}{\lambda^{b+2\beta+4}} + \frac{2\alpha^2 N_0^2 \frac{\pi}{4} E a I_3}{(\lambda+c)^{b+2\beta+4}} \end{aligned} \quad (3.28)$$

where

$$I_1 = \int_0^\infty \int_0^\infty x^\beta y^\beta (x+y)^2 (x^b - y^b) e^{-(x+y)} dy dx \quad (3.29)$$

$$I_2 = \frac{1}{2} \int_0^\infty \int_0^\infty x^\beta (x+y)^2 (x^b - y^b) e^{-(x+y)} dx dy \quad (3.30)$$

$$I_3 = \frac{1}{2} \int_0^\infty \int_0^\infty x^{2\beta} (x+y)^2 (x^b - y^b) e^{-(x+y)} dx dy \quad (3.31)$$

and where  $\Gamma$  is the gamma function. The integral can be expressed as hypergeometric functions, e.g.,

$$\begin{aligned} I_1 = & \frac{\Gamma(b+2+4)}{2^{b+2\beta+4}} \\ & \cdot \left\{ \frac{{}_2F_1(1, b+2\beta+4; \beta+2; \frac{1}{2})}{\beta+1} - \frac{{}_2F_1(1, b+2\beta+4; b+\beta+2; \frac{1}{2})}{b+\beta+1} \right. \\ & + 2 \frac{{}_2F_1(1, b+2\beta+4; \beta+3; \frac{1}{2})}{\beta+2} - 2 \frac{{}_2F_1(1, b+2\beta+4; b+\beta+3; \frac{1}{2})}{b+\beta+2} \\ & \left. + \frac{{}_2F_1(1, b+2\beta+4; \beta+4; \frac{1}{2})}{\beta+3} - \frac{{}_2F_1(1, b+2\beta+4; b+\beta+4; \frac{1}{2})}{b+\beta+3} \right\} \end{aligned} \quad (3.32)$$

Making use of the vertical flux of precipitation mass, the dependent variable  $N$  can be removed via

$$N_0 = \frac{\chi_f \lambda^{b+\beta+1}}{a \alpha \Gamma(b+\beta+1)} \quad (3.33)$$

The function for the rate of change of particle mass due to vapor deposition can be avoided by making use of the first moment,

$$g(h) = \frac{\left(\frac{\partial \chi_f}{\partial h}\right) a \alpha \Gamma(b+\beta+1)}{\chi_f \lambda^{b+\beta+1}} \quad (3.34)$$

Finally, the change of with height is given by an implicit equation

$$\begin{aligned} \frac{\partial \lambda}{\partial h} &= \frac{\left(\frac{\partial \chi_f}{\partial h}\right) \lambda}{\chi_f \beta} \left(1 - \frac{2 \Gamma(\beta+2) \Gamma(b+\beta+1)}{\Gamma(b+2\beta+1)}\right) \\ &- \frac{2 \frac{I}{4} E \chi_f \lambda^{2b+3\beta+3} I_1}{a \alpha \beta (\lambda+c)^{b+2\beta+4} \Gamma(b+\beta+1) \Gamma(b+2\beta+1)} \\ &- \frac{4 \left(\frac{\eta}{4}\right) E \chi_f \lambda^{b+2\beta-1} I_2}{\Lambda a \alpha^2 \beta \Gamma(b+\beta+1) \Gamma(b+2\beta+1)} \quad (3.35) \\ &+ \frac{4 \left(\frac{\pi}{4}\right) E \chi_f \lambda^{2b+3\beta+3} I_2}{\Lambda a \alpha^2 \beta (\lambda+c)^{b+2\beta+4} \Gamma(b+\beta+1) \Gamma(b+2\beta+1)} \\ &+ \frac{2 \frac{I}{4} E \chi_f \lambda^{b+\beta-1} I_3}{a \alpha \beta \Gamma(b+\beta+1) \Gamma(b+2\beta+1)} \end{aligned}$$

$$N_3 = \frac{2 \frac{\pi}{4} E \chi_f \lambda^{2b+3\beta+3} I_3}{a \alpha \beta (\lambda+c)^{b+\beta+4} \Gamma(b+\beta+1) \Gamma(b+2\beta+1)}$$

$\lambda$  is obtained by numerically solving (3.35) in height steps. Once  $\lambda$  is obtained,  $N_3$  can be found from (3.33).

In the computations, the values of  $N_3$  and  $\lambda$  from the first loop of an ASD are taken as the initial conditions. Because of the lack of published values on the collision efficiency,  $E$ , it is taken to be 1.0 for all cases. The magnitude of the constants  $a$ ,  $b$ ,  $\alpha$  and  $\beta$  are guided by the values of Locatelli and Hobbs, 1974. But the actual values of  $a$ ,  $b$ ,  $\alpha$ ,  $\beta$ ,  $c$  and  $\Lambda$  used in the computations are determined by trial and error so that the theoretically predicted values duplicate the values from observations. This approach for determining the constants may seem rather empirical but due to the lack of published values of these constants, this is the only way. In fact, one of the purposes of this study is to compare the theoretical values with the observational findings so as to deduce the relative magnitudes of the various constants.

The results from this formulation are plotted against the observations in  $N_3 - \lambda$  space. Figs. 3.3 and 3.4 show the results for 25 Feb., 1980 and 26 Feb., 1980. The values of

2-25-80

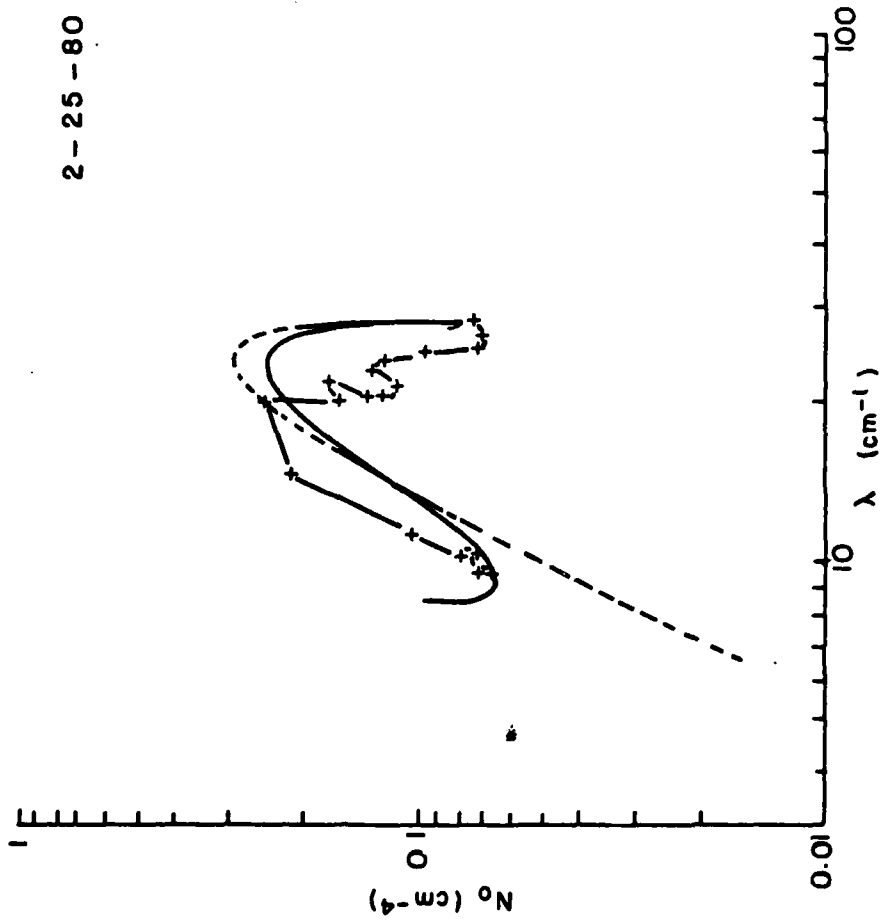


Fig.3.3: Two-parameter model evaluations for spiral on 25 February, 1980, exponential breakup fragment size distribution. See text for details.

2 - 26 - 80

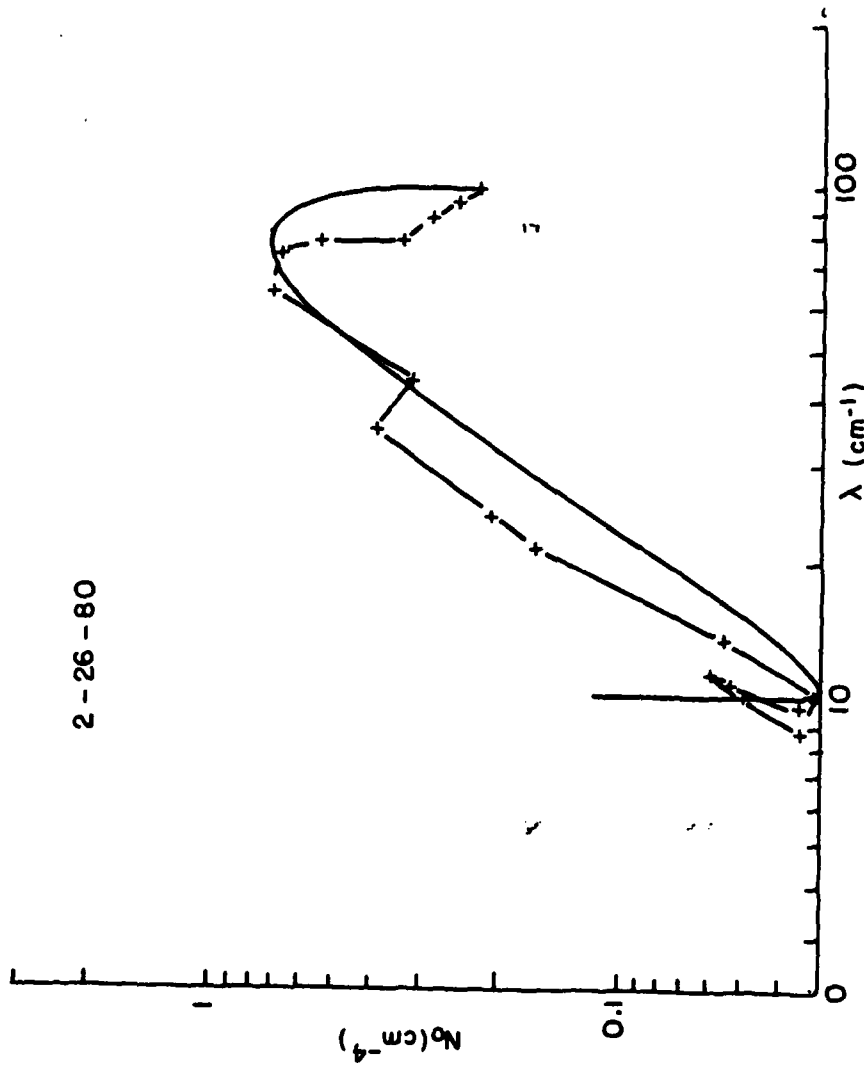


Fig.3.4: Two-parameter model evaluations for spiral on 26 February, 1980, exponential breakup fragment size distribution

the constants  $a$ ,  $b$ ,  $c$ ,  $\alpha$ ,  $\beta$ ,  $w$  and  $\Lambda$  are listed in Table 3.1. Since the actual updraft for the three cases, 25 and 26 February, 1980 and 8 March, 1980, is in the vicinity of 10 cm/s, so  $w$  has been set to 10 cm/s in all the calculations. The effect of different values of  $w$  on the computation is being shown later. The results from the theory also show that snow growth goes through three distinct stages. In the first stage, the intercept,  $N_0$ , increases rapidly while the slope,  $\lambda$ , remains constant. This duplicates the deposition stage in the observational data. The second stage of growth is where both  $N_0$  and  $\lambda$  decrease rapidly. This duplicates the aggregation stage from the observations.

The results from the theoretical model but with  $c$  set to 0 (i.e. no collisional breakup process) are also plotted in Fig. 3.3 as a dashed line. The results from this formulation have only two stages. The first stage is when  $N_0$  increases while  $\lambda$  remains almost constant. The second stage is when both  $N_0$  and  $\lambda$  decrease rapidly. In this formulation, there seems to be no end to the decrease of  $N_0$  and  $\lambda$ .

The results from the theoretical model with collisional breakup ( $c > 0$ ) have a third stage where  $N_0$  increases and  $\lambda$  remains constant. From previous studies (e.g., Srivastava, 1978) it is concluded that aggregation and collisional breakup processes can balance one another so as to produce an

Fig.	Date	a	b	$\alpha$	$\beta$	E	w	c	$\Lambda$	$N_g$
3	2-25-80	100	0.15	0.002	2.15	1	10	0.055	9000	
4	2-26-80	100	0.15	0.002	1.55	1	10	1.0	3500	
7	3-08-80	100	0.15	0.002	0.75	1	10	0.65	10000	
8	3-08-80	100	0.15	0.002	2.0	1	10	1.5		
9	2-25-80	100	0.15	0.002	1.95	1	10	0.07	1750	
10	2-26-80	100	0.15	0.002	1.25	1	10	0.25		15
11	3-08-80	100	0.15	0.002	0.75	1	10	0.65		20
12	3-08-80	100	0.15	0.002	2.0	1	10	1.5		0.1/0.5

Table 3.1: Values of the physical parameters used in the two-parameter model (c.g.s. units)

$\alpha$	$\beta$	b	c	$\Lambda$	$\lambda_o$	$\lambda$ in model
0.002	2.15	0.15	0.055	9000	9.99	8.30
0.002	1.5	0.15	1.0	3500	16.24	11.35
0.002	0.75	0.15	0.65	10000	9.99	7.43
0.002	2.0	0.15	1.5	1750	-0.75	8.11

Table 3.2: Tabulation of  $\lambda_o$

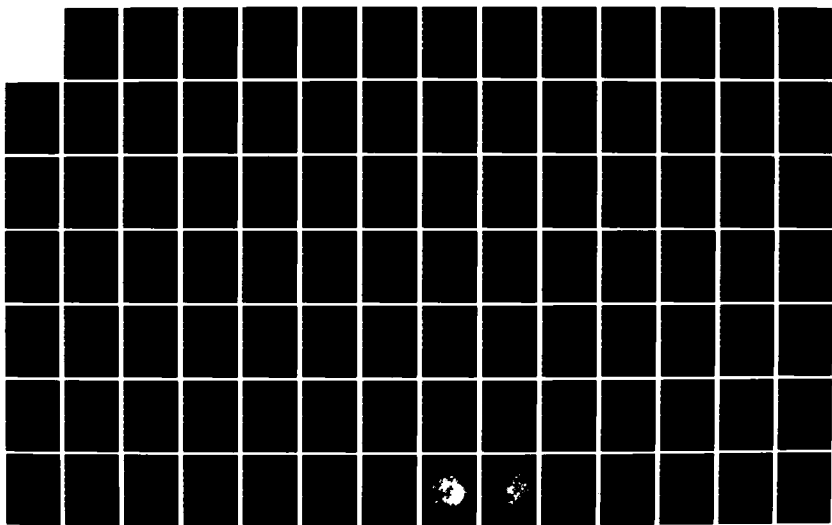
AD-A133 136

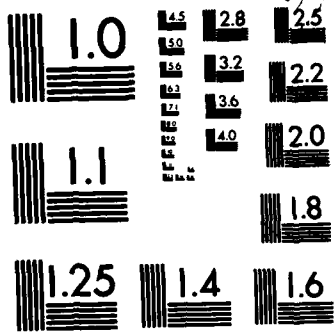
GROWTH PROCESSES OF SNOW(U) MASSACHUSETTS INST OF TECH  
CAMBRIDGE K K LO MAY 83 AFGL-TR-83-0105  
F19628-80-C-0021

2/2

UNCLASSIFIED

F/G 8/12 NL





MICROCOPY RESOLUTION TEST CHART  
NATIONAL BUREAU OF STANDARDS-1963-A

equilibrium slope. This is clearly the case here. The introduction of the collisional breakup process into the model halts the decrease in  $\lambda$  and leads to an equilibrium. The reason that  $N_0$  keeps on increasing is because vapor deposition is still going on and if  $\lambda$  is constant,  $N_0$  has to increase so as to accommodate the increase in mass.

Fig. 3.5 shows the effect of varying the updraft velocity while keeping all other parameters constant for the case of 26 Feb., 1980. The differences in updraft velocities affect only the position where the first stage changes to the second stage and does not affect the final  $\lambda$ . Since the updraft velocity affects the deposition rate, so a change of updraft velocity will naturally affect where the first stage changes to the second stage. The stronger the updraft, the greater  $N_0$  has to be in order to accommodate the additional mass. The fact that the updraft does not affect the final  $\lambda$  is consistent with former studies of Srivastava (1978) that the equilibrium  $\lambda$  resulting from aggregation and collisional breakup is independent of updraft velocity. The observations from section 2.8 show that for subsaturation cases, the final slope will be affected. This might be due to the microphysical processes, as are explained in that section.

The results from the case of 8 March, 1980 are also plotted in Figs. 3.6 and 3.7. This is the case where there is

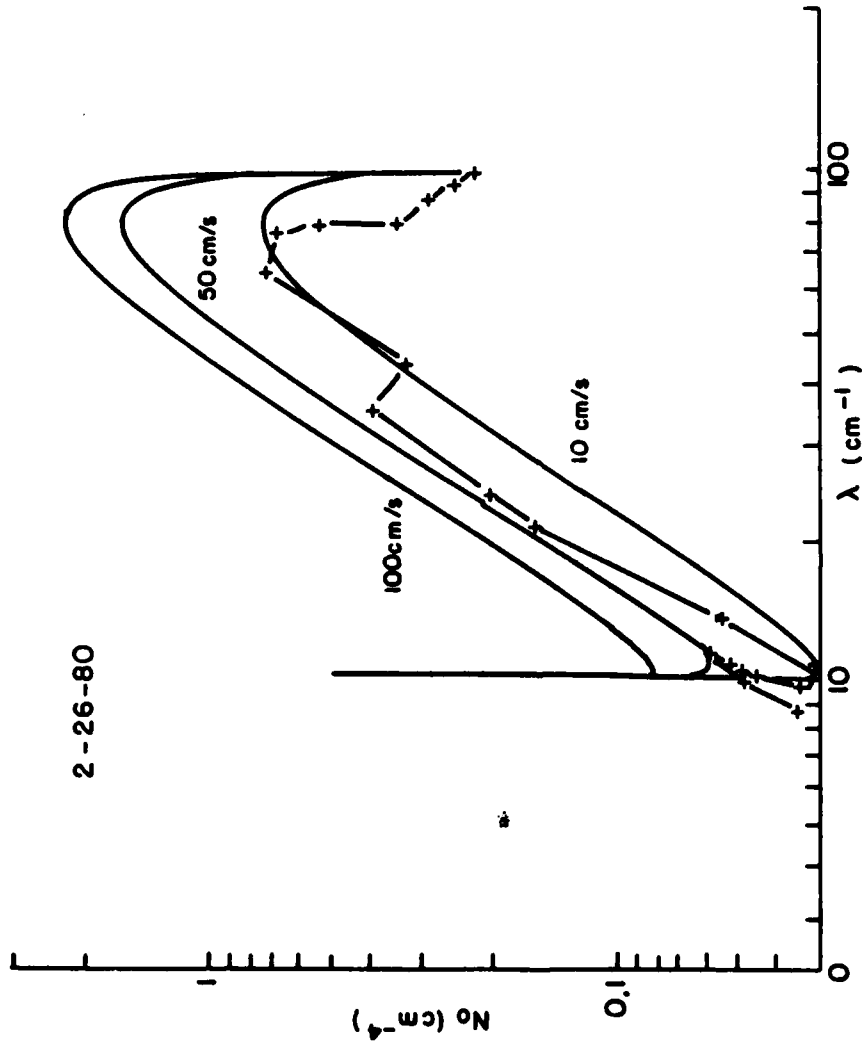


Fig.3.5: Effects of different updraft velocities on two-parameter model performance, exponential breakup fragment size distribution

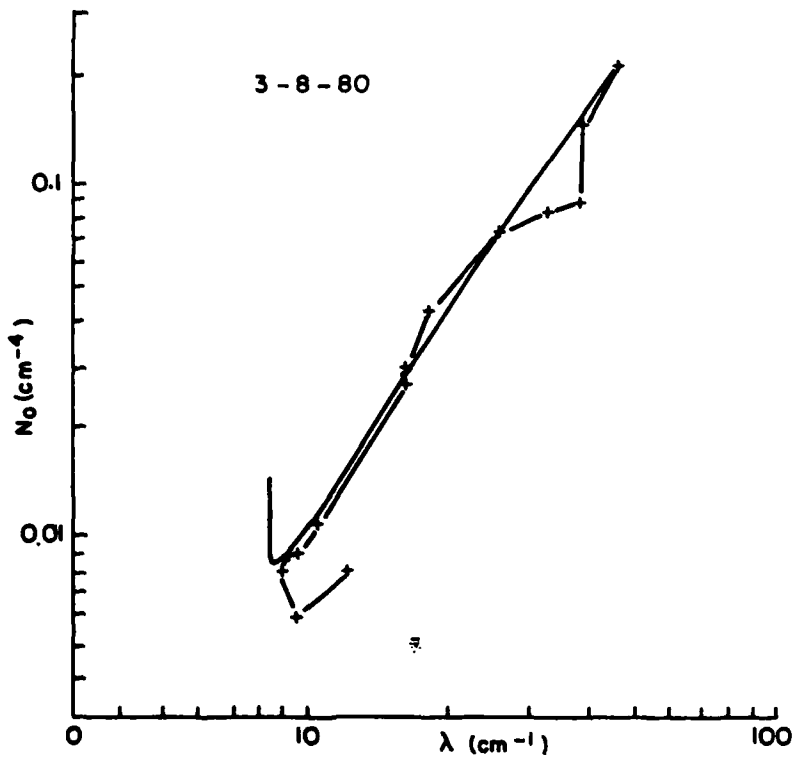


Fig.3.6: Two-parameter model evaluations for spiral on 8 March, 1980, with  $\beta=0.75$ , exponential breakup fragment size distribution

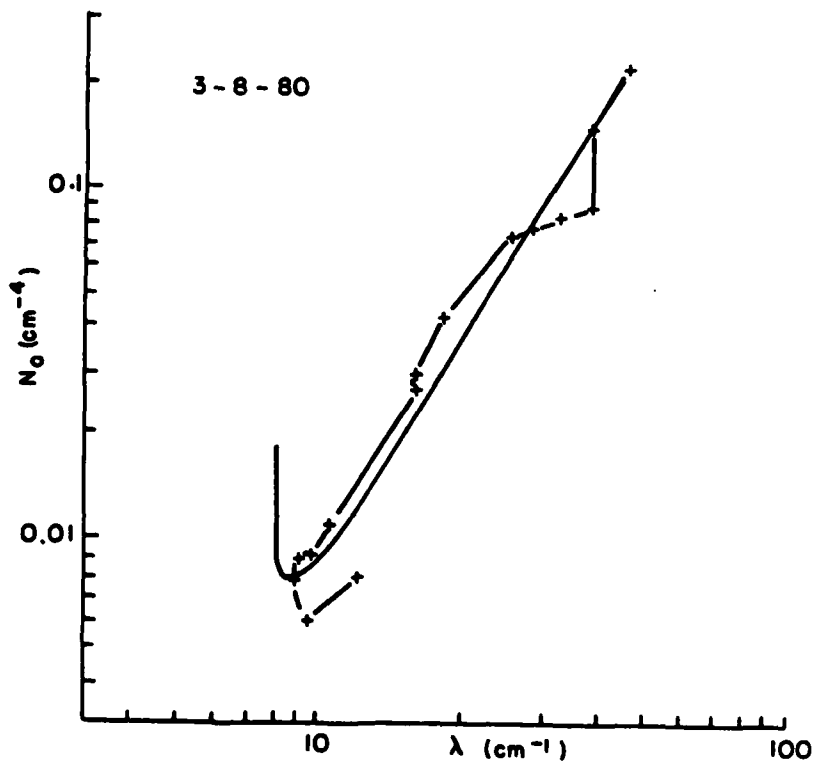


Fig.3.7: Two-parameter model evaluations for spiral on 8 March, 1980, with  $\beta=2$ , exponential breakup fragment size distribution

not an initial stage where  $N_0$  increases while  $\lambda$  remains constant. In the process of finding the set of parameters in which the theoretical model can best duplicate the observations, it is discovered that two sets of parameters can more or less duplicate good fits (Table 3.1). One of the sets requires  $\beta$ , the mass-diameter power to be 2 which is within published values. The other set requires  $\beta$  to be 0.75 which is too small. Moreover, this set requires  $\Lambda$ , the breakup exponent to be 10000, which implies the number of breakup fragments to be high. Results from the other breakup formulation and from the three-parameter formulations can be used to clarify the situation.

A simple analytical expression of the equilibrium slope can be obtained by assuming no vapor deposition. Then the first moment conservation equation becomes,

$$-\frac{\partial \chi_f}{\partial h} = 0$$

which implies

$$\chi_f = \frac{a \alpha N_0 \Gamma(b+\beta+1)}{\lambda^{b+\beta+1}} = \text{constant} \quad (3.36)$$

The second moment equation is

$$\begin{aligned} \frac{\partial Z}{\partial h} &= \frac{N_0^2 \alpha^2 \frac{\eta}{4} E a I_1}{(\lambda+c)^{b+2\beta+4}} \\ &+ \frac{N_0^2 2 \alpha \frac{\eta}{4} E a I_1}{\Lambda \lambda^{b+\beta+4}} - \frac{N_0^2 2 \alpha \frac{\eta}{4} E a I_2}{\Lambda (\lambda+c)^{b+\beta+4}} \end{aligned} \quad (3.37)$$

$$-\frac{N_0^2 \alpha^2 \frac{\pi}{4} E a I_3}{\lambda^{b+2\beta+4}} + \frac{N_0^2 \alpha^2 \frac{\pi}{4} E a I_3}{(\lambda + c)^{b+2\beta+4}}$$

From these two equations and setting  $\frac{\partial \lambda}{\partial h}$  to 0, the equilibrium slope,  $\lambda_0$ , is expressed by

$$\frac{2 I_2 \lambda_0^{\beta}}{\Lambda \alpha} - I_3 = \lambda_0^{b+2\beta+4} \left[ \frac{-I_1 + I_3}{(\lambda_0 + c)^{b+2\beta+4}} + \frac{2 I_2}{\Lambda \alpha (\lambda_0 + c)^{b+\beta+4}} \right] \quad (3.38)$$

This expression shows that the equilibrium slope is dependent on the density ( $\alpha$  and  $\beta$ ), the fallspeed ( $b$ ) and the breakup parameters ( $\Lambda$  and  $c$ ) and is independent of the mass flux, the updraft and the collisional efficiency.  $\lambda_0$  obtained by using the values of parameters used in the model agrees well with the final  $\lambda$  value obtained in the model (Table 3.2). The only exception is the 8 March, 1980 case with  $\beta=2$ , in which the  $\lambda_0$  obtained is even unrealistically negative. As will be seen in the later sections, computations using  $\beta=2$  for the 8 March, 1980 case fail to produce satisfactory results, which says something about the suitability of this set of parameters. (3.38) indicates that the equilibrium slope depends only on the density of snow, the coalescence probability and the breakup fragment distribution. The observations show that the equilibrium slopes are approximately the same for all flights. So, if the equilibrium slopes are approximately the same for the various

flights, this might suggest that the density of snow and its breakup properties are interrelated.

The values of  $N_0$  and  $\lambda$  where the first stage of snow growth changes to the second stage can be analytically obtained by neglecting collisional breakup. Then by setting  $\frac{\partial N_0}{\partial h}$  to be 0,

$$\left( \frac{N_0 a \alpha \Gamma(b+\beta+1)}{\chi_f} \right)^{\frac{b+\beta+2}{b+\beta+1}} = \left[ \frac{a \alpha \beta \Gamma(b+\beta+1) \Gamma(b+2\beta+1)}{(b+\beta+1) \Gamma \Gamma \Gamma} \left( \frac{\chi_f'}{\chi_f} \right) \right] \quad (3.39)$$

$$\cdot \left[ 1 + \frac{(b+\beta+1)}{\beta} \left( 1 - \frac{2 \Gamma(\beta+2) \Gamma(b+\beta+1)}{\Gamma(b+2\beta+1)} \right) \right]$$

The values of  $N_0$  and  $\lambda$  obtained from (3.39) for the different spirals are shown in Table 3.3. These values are close to the values obtained from the model. But this shows that the collisional breakup process does have a weak effect on the change from the first stage to the second stage.

$N_0$	1.23	0.4662	0.18309	0.075261
$\lambda$	5.38	38.9	28.5	21.2

Table 3.3: First turning point of  $N_0$ 

Fig.	Date	a	b	$\alpha$	$\beta$	E	w	c	$\Lambda$	$N_0$
13-15	2-25-80	100	0.15	0.002	2.1	1	10	0.1	5000	
16-18	3-08-80	100	0.15	0.002	0.75	1	10	0.5	10000	
19-21	3-08-80	100	0.15	0.002	2.0	1	10	3.0	8000	
22-24	2-25-80	100	0.15	0.002	1.7	1	10	0.2/0.1		25/7.5
25-27	3-08-80	100	0.15	0.002	0.75	1	10	0.5		5

Table 3.4: Values of physical parameters used in the three-parameter model (c.g.s units)

In order to illustrate the effect of changing the values of the various physical parameters on the results, the results from computations using different values of the parameters are plotted in Fig. 3.8. The case used is the spiral on 25 Feb., 1980. The values of  $c$  used ranges from 0.05 to 1.5, which means that  $q$ , the probability that two particles will aggregate when they collide, is above 80% for most particles. The values of  $\Lambda$  used range from 1750 to 10000.  $\Lambda > 5000$  implies that the number of breakup fragments can easily be more than 10. From the values of  $c$  and  $\Lambda$ , it appears that when two snow particles collide, they are more likely to aggregate than to break up, but when they do break up, they generate numerous fragments. The larger the parent particles, the more numerous the fragments.

### 3.2.2 Constant fragment number distribution

In this formulation, the fragment size distribution is assumed to be

$$S(x|x', x'') = N_s \zeta\left(x - \frac{X' + X''}{N_s}\right). \quad (3.40)$$

This means that when two snow crystals collide and break up, they generate  $N_s$  equal mass fragments. So, the number of fragments does not depend on the size of the parent

2-25-80

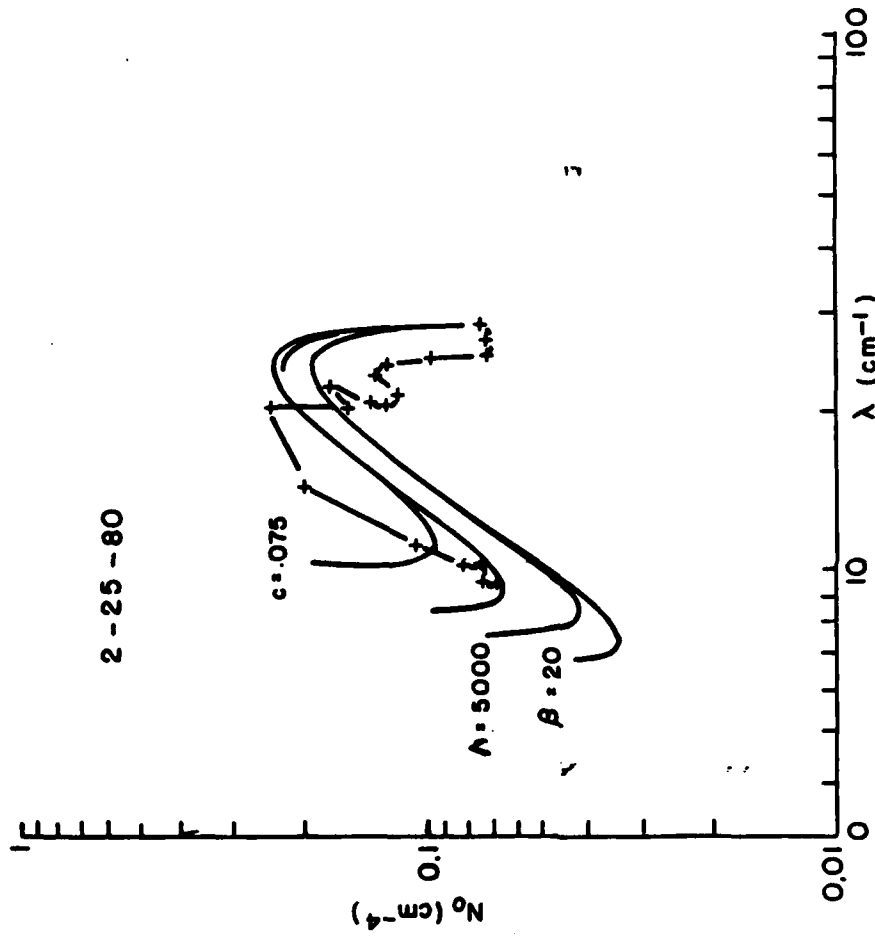


Fig.3.8: Two-parameter model evaluations for spiral on 25 February, 1980 using various values of physical parameters, exponential breakup fragment size distribution

particles, but the mass of fragment does.

Using a technique similar to that of the previous section, the change of  $\lambda$ , the spectrum slope, with height can be written as an implicit equation,

$$\frac{\partial \lambda}{\partial h} = \frac{\left(\frac{\partial \lambda}{\partial h}\right) \lambda}{\chi_f \beta} \left[ 1 - \frac{2 \Gamma(\beta+2) \Gamma(b+\beta+1)}{\Gamma(b+2\beta+1)} \right]$$

$$- \frac{2 \frac{\pi}{4} E \chi_f \lambda^{b+\beta-1} I_1}{N_s \alpha \beta \Gamma(b+\beta+1) \Gamma(b+2\beta+1)} \quad (3.41)$$

$$- \frac{\left(-1 + \frac{1}{N_s}\right) \cdot 2 \frac{\pi}{4} E \chi_f \lambda^{b+\beta-1} I_3}{\alpha \beta \Gamma(b+\beta+1) \Gamma(b+2\beta+1)}$$

$$+ \frac{\left(-1 + \frac{1}{N_s}\right) \cdot 2 \frac{\pi}{4} E \chi_f \lambda^{2b+3\beta+3} (I_1 + I_3)}{\alpha \beta (\lambda+c)^{b+2\beta+4} \Gamma(b+\beta+1) \Gamma(b+2\beta+1)}$$

where  $I_1$  and  $I_3$  are (3.29) and (3.31) in the previous section. Again, the implicit equation is solved numerically in height steps and  $N_0$ 's are obtained from (3.33). Results from this formulation for the three different cases are plotted against observations in Figs. 3.9-3.12 and the values of the physical parameters used are listed in Table 3.1. Except for the case of 8 March, 1980, the results from this formulation are very similar to the results from the exponential fragment size distribution formulation. From the quality of fit to the 25 Feb., 1980 and the 26 Feb., 1980 cases, it appears that there

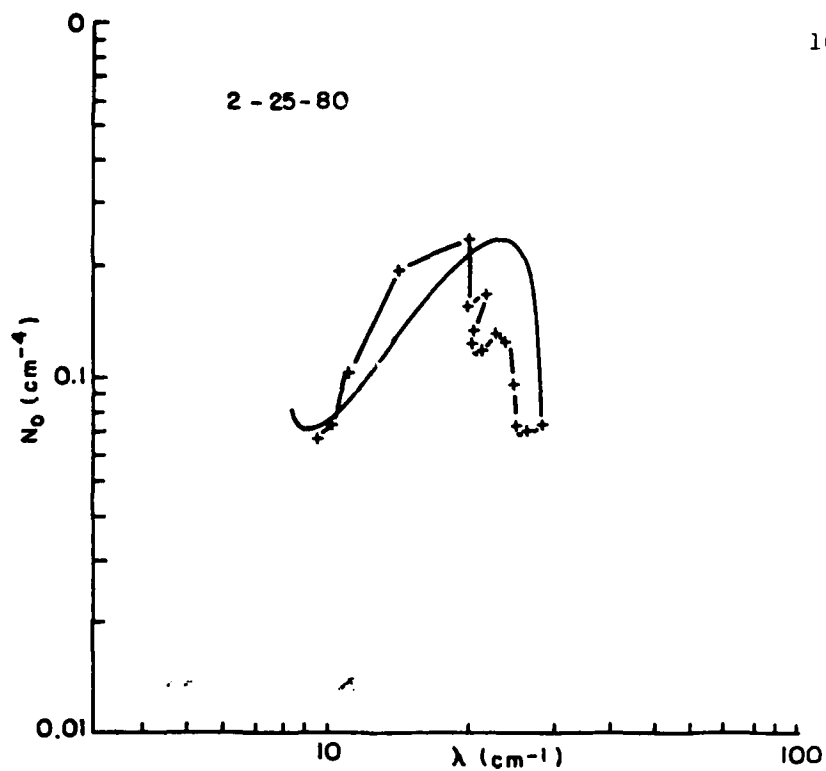


Fig.3.9: Two-parameter model evaluations for spiral on 25 February, 1980, constant breakup fragment number distribution

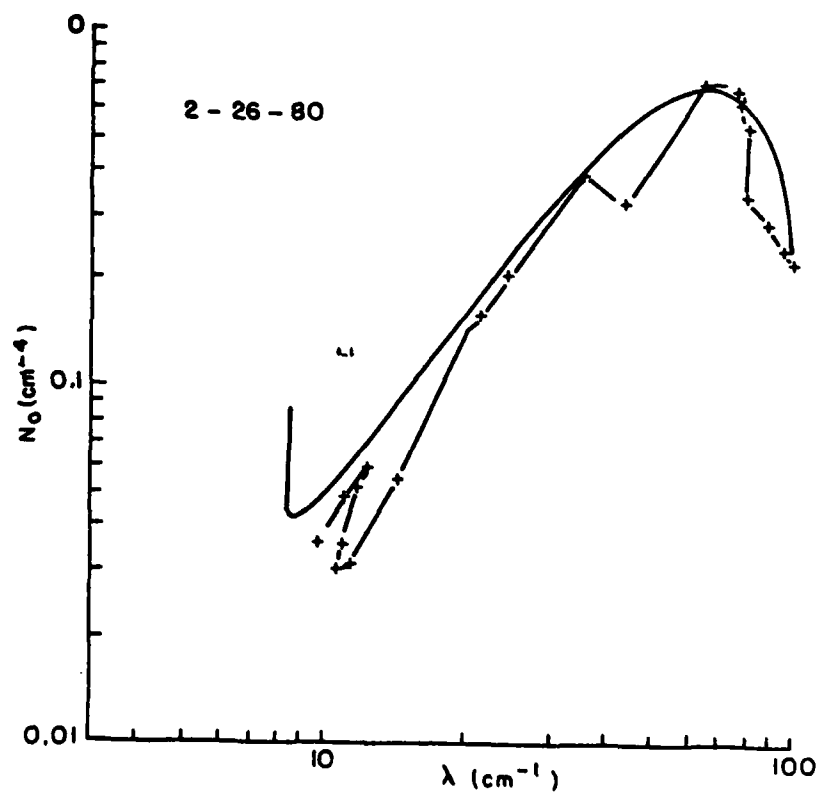


Fig.3.10: Two-parameter model evaluations for spiral on 26 February, 1980, constant breakup fragment number distribution

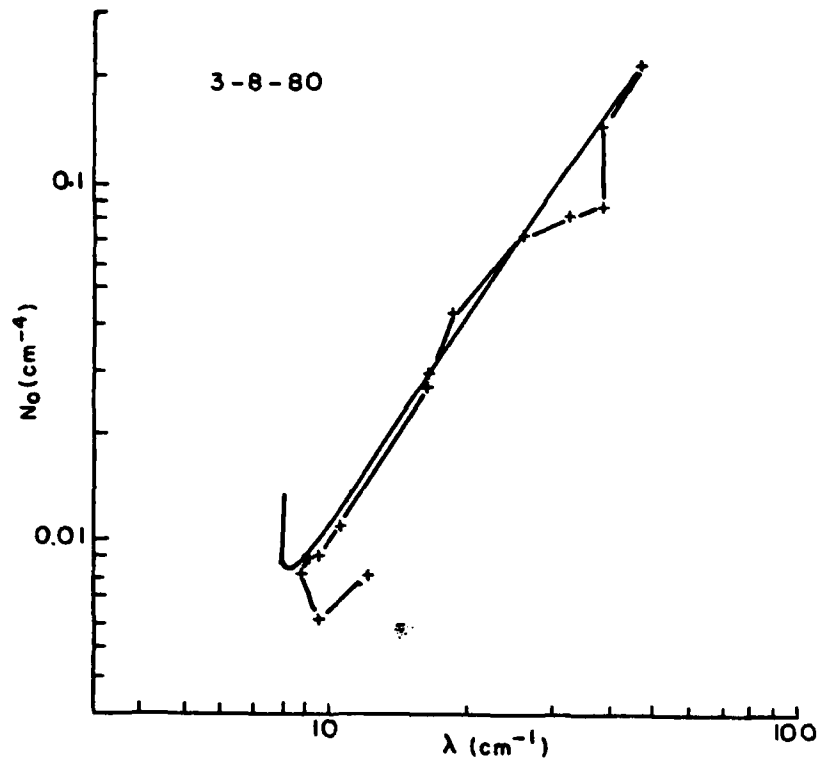


Fig.3.11: Two-parameter model evaluations for spiral on 8 March, 1980 with  $\beta=0.75$ , constant breakup fragment number distribution

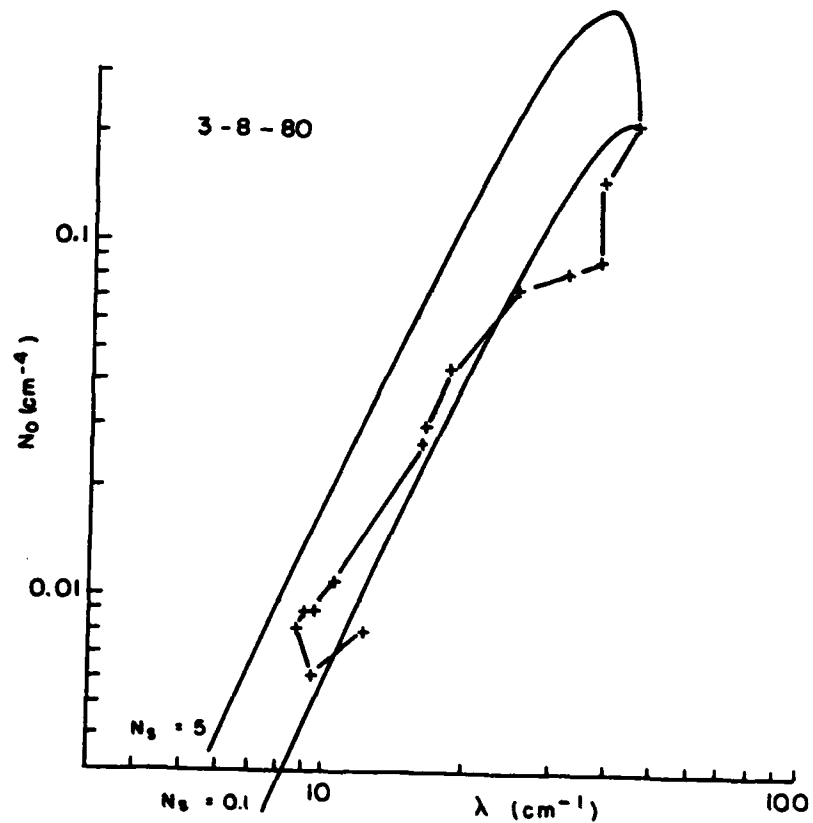


Fig.3.12: Two-parameter model evaluations for spiral on 8 March, 1980 with  $\beta=2$ , constant breakup fragment number distribution

is not much difference between the two formulations. However, for the 8 March case, the model from this formulation can fit the observations only by using the set of parameters which require  $\beta$ , the mass-diameter power to be 0.75. When  $\beta$  equals 2, the model results cannot duplicate the observations even after many trials (e.g., Fig. 3.12). Another point is the fragment number,  $N_f$ , required in the model with  $\beta=0.75$  is only 7.5 which is not high. A full interpretation of the implications from the values of the physical parameters will be discussed after the presentation of the three-parameter models.

### 3.3 Three-parameter formulations

In this formulation, snow-size spectrum is represented by

$$f(x, h)dx = N_x(h) e^{-\lambda_x(h)D} D^{\sigma(h)} dD \quad (3.42)$$

where  $N_x$ ,  $\lambda_x$  and  $\sigma$  are functions of height,  $h$ . In this formulation,  $h$  is the independent variable, while  $N_x$ ,  $\lambda_x$  and  $\sigma$  are three dependent variables.

### 3.3.1 Exponential fragment size distribution

The fragment size distribution  $S(x|x', x'')$  is formulated according to (3.25) as  $(x'+x'') \Lambda^2 e^{-\Lambda x}$ . From this formulation, the zeroth moment conservation equation can be written as

$$\frac{\partial n}{\partial h} = \frac{N_x^2 \frac{\pi}{4} E a I_4}{(\lambda_x + c)^{b+2\sigma+4}} - \frac{2N_x^2 \frac{\pi}{4} E a I_4}{\lambda_x^{b+2\sigma+4}} + \frac{\alpha \Lambda N_x^2 \frac{\pi}{4} E a I_5}{\lambda_x^{b+\beta+2\sigma+4}} - \frac{\Lambda \alpha N_x^2 \frac{\pi}{4} E a I_5}{(\lambda + c)^{b+\beta+2\sigma+4}} \quad (3.43)$$

where

$$I_4 = \int_0^\infty \int_0^\infty x^\sigma y^\sigma (x+y)^2 (x^b - y^b) e^{-(x+y)} dy dx, \quad (3.44)$$

$$I_5 = \int_0^\infty \int_0^\infty x^{\beta+\sigma} y^\sigma (x+y)^2 |x^b - y^b| e^{-(x+y)} dx dy \quad (3.45)$$

The first moment conservation equation is

$$\frac{\partial \chi_1}{\partial h} = - \frac{g(h) N_x \Gamma(\sigma+2)}{\lambda_x^{\sigma+2}} \quad (3.46)$$

The second moment conservation equation is

$$\begin{aligned} \frac{\partial Z}{\partial h} = & \frac{2 \alpha g N_x^2 \Gamma(\beta + \sigma + 2)}{\lambda_x^{\beta + \sigma + 2}} + \frac{2 \alpha^2 N_x^2 \frac{\pi}{4} E a I_6}{(\lambda_x + c)^{b+2\beta+2\sigma+4}} \\ & + \frac{2 \alpha N_x^2 \frac{\pi}{4} E a I_5}{\Lambda \lambda_x^{b+\beta+2\sigma+4}} - \frac{2 \alpha N_x^2 \frac{\pi}{4} E a I_5}{\Lambda (\lambda_x + c)^{b+\beta+2\sigma+4}} \\ & - \frac{2 \alpha^2 N_x^2 \frac{\pi}{4} E a I_7}{\lambda_x^{b+2\beta+2\sigma+4}} + \frac{2 \alpha^2 N_x^2 \frac{\pi}{4} E a I_7}{(\lambda_x + c)^{b+2\beta+2\sigma+4}} \end{aligned} \quad (3.47)$$

where

$$I_6 = \int_0^{\infty} \int_0^x x^{\beta+\sigma} y^{\beta+\sigma} (x+y)^2 (x^b - y^b) e^{-(x+y)} dy dx \quad (3.48)$$

$$I_7 = \int_0^{\infty} \int_0^{\infty} x^{2\beta+\sigma} y^{\sigma} (x+y)^2 (x^b - y^b) e^{-(x+y)} dx dy \quad (3.49)$$

Similar to that of the two-parameter formulation,  $N_x$  can be removed by using the precipitation mass flux,

$$N_x = \frac{\chi_f \lambda_x^{b+\beta+\sigma+1}}{a \alpha \Gamma(b+\beta+\sigma+1)} \quad (3.50)$$

and by making use of the first moment, the rate of change of particle mass due to vapor deposition can be avoided,

$$g(h) = \frac{(\frac{\partial \chi_f}{\partial h}) a \alpha \Gamma(b+\beta+\sigma+1)}{\chi_f \lambda_x^{b+\beta-1} \Gamma(\sigma+2)} \quad (3.51)$$

After these manipulations, two implicit equations in  $\lambda_x$  and  $\sigma$  are derived as functions of height.

$$\begin{aligned} \frac{\partial \lambda_x}{\partial h} = & - \frac{\lambda_x (\frac{\partial \chi_f}{\partial h})}{\beta \chi_f} - \frac{\lambda_x}{\beta \Gamma(b+\sigma+1)} \left[ \int_0^{\infty} x^{b+\sigma} \ln x e^{-x} dx \right] \frac{\partial \sigma}{\partial h} \\ & + \frac{\lambda_x}{\beta \Gamma(b+\beta+\sigma+1)} \left[ \int_0^{\infty} x^{b+\beta+\sigma} \ln x e^{-x} dx \right] \frac{\partial \sigma}{\partial h} \\ & + \frac{\frac{7}{4} E \chi_f \lambda_x^{2b+\beta+2\sigma+3} I_4}{a \alpha \beta (\lambda_x + c)^{b+2\sigma+4} \Gamma(b+\sigma+1) \Gamma(b+\beta+\sigma+1)} \\ & - \frac{2 \frac{7}{4} E \chi_f \lambda_x^{b+\beta-1} I_4}{a \alpha \beta \Gamma(b+\sigma+1) \Gamma(b+\beta+\sigma+1)} \\ & + \frac{\frac{7}{4} E \chi_f \lambda_x^{b-1} I_5}{a \beta \Gamma(b+\sigma+1) \Gamma(b+\beta+\sigma+1)} \\ & - \frac{\frac{7}{4} E \chi_f \lambda_x^{2b+\beta+2\sigma+3} I_5}{a \beta (\lambda_x + c)^{b+\beta+2\sigma+4} \Gamma(b+\sigma+1) \Gamma(b+\beta+\sigma+1)} \end{aligned} \quad (3.52)$$

and

$$\begin{aligned}
& \frac{\partial \sigma}{\partial h} \cdot \frac{\lambda}{\beta} \left( \frac{2}{\Gamma(b+\beta+\sigma+1)} \int_0^{\infty} x^{b+\beta+\sigma} \ln x e^{-x} dx \right. \\
& \quad - \frac{1}{\Gamma(b+\sigma+1)} \int_0^{\infty} x^{b+\sigma} \ln x e^{-x} dx \\
& \quad \left. - \frac{1}{\Gamma(b+2\beta+\sigma+1)} \int_0^{\infty} x^{b+2\beta+\sigma} \ln x e^{-x} dx \right) \\
& = \frac{2 \left( \frac{\partial \lambda}{\partial h} \right) \lambda}{\lambda \beta} - \frac{2 g \lambda^{\beta} \Gamma(\beta+\sigma+2)}{2 \alpha \beta \Gamma(b+2\beta+\sigma+1)} \\
& \quad - \frac{\frac{1}{2} E \chi_f \lambda_x^{2b+\beta+2\sigma+3} I_4}{2 \alpha \beta (\lambda_x+c)^{b+2\sigma+4} \Gamma(b+\sigma+1) \Gamma(b+\beta+\sigma+1)} \tag{3.53} \\
& \quad + \frac{2 \frac{1}{2} E \chi_f \lambda_x^{b+\beta-1} I_4}{2 \alpha \beta \Gamma(b+\sigma+1) \Gamma(b+\beta+\sigma+1)} \\
& \quad - \frac{\frac{1}{2} E \chi_f \lambda_x^{b-1} I_4}{\alpha \beta \Gamma(b+\sigma+1) \Gamma(b+\beta+\sigma+1)} \\
& \quad + \frac{\frac{1}{2} E \chi_f \lambda_x^{2b+\beta+2\sigma+3} I_5}{\alpha \beta (\lambda_x+c)^{b+\beta+2\sigma+4} \Gamma(b+\sigma+1) \Gamma(b+\beta+\sigma+1)} \\
& \quad - \frac{2 \frac{1}{2} E \chi_f \lambda_x^{b+2\beta-1} I_5}{\alpha \alpha^2 \beta \Gamma(b+\beta+\sigma+1) \Gamma(b+2\beta+\sigma+1)} \\
& \quad + \frac{2 \frac{1}{2} E \chi_f \lambda_x^{2b+3\beta+2\sigma+3} I_5}{\alpha \alpha^2 \beta (\lambda_x+c)^{b+\beta+2\sigma+4} \Gamma(b+\beta+\sigma+1) \Gamma(b+2\beta+\sigma+1)} \\
& \quad - \frac{2 \frac{1}{2} E \chi_f \lambda_x^{b+3\beta+2\sigma+3} I_6}{2 \alpha \beta (\lambda_x+c)^{b+2\beta+2\sigma+4} \Gamma(b+\beta+\sigma+1) \Gamma(b+2\beta+\sigma+1)} \\
& \quad + \frac{2 \frac{1}{2} E \chi_f \lambda_x^{b+\beta-1} I_7}{\alpha \beta \Gamma(b+\beta+\sigma+1) \Gamma(b+2\beta+\sigma+1)} \\
& \quad - \frac{2 \frac{1}{2} E \chi_f \lambda_x^{2b+3\beta+2\sigma+3} I_7}{\alpha \alpha \beta (\lambda_x+c)^{b+2\beta+2\sigma+4} \Gamma(b+\beta+\sigma+1) \Gamma(b+2\beta+\sigma+1)}
\end{aligned}$$

The integrals  $\int_0^{\infty} x^{b+\sigma} \ln x e^{-x} dx$ ,  $\int_0^{\infty} x^{b+\beta+\sigma} \ln x e^{-x} dx$  and  $\int_0^{\infty} x^{b+2\beta+\sigma} \ln x e^{-x} dx$  are computed using a Gauss-Laguerre quadrature. By using a second-order Runge-Kutta algorithm,  $\lambda_x$  and  $\sigma$  are computed in height steps from this set of two equations. The  $N_x$ ,  $\lambda_x$  and  $\sigma$  at the beginning of the ASD data are taken to be the initial conditions for computation. The choices of  $a$ ,  $b$ ,  $c$ ,  $\alpha$ ,  $\beta$ ,  $\omega$  and  $\Lambda$  are guided by the results from the two-parameter formulations.

Figs. 3.13, 3.14 and 3.15 compare the model results of  $N_x$ ,  $\lambda_x$  and  $\sigma$  against the observations from 25 Feb., 1980. In order to show the effects of changing the values of the physical parameters, results from the various computations are also plotted on the same diagrams. For  $N_x$ , the model can duplicate the three stages in the observations. First, there is a slow increase, then a rapid rise and a rapid fall and finally  $N_x$  takes on a more or less constant value. Just like the  $\lambda_x$  from the observation, the  $\lambda_x$  from the computation decreases monotonically with height, and then becomes approximately constant. For  $\sigma$ , the model result is negative for a short while. Then it changes rapidly to become positive and then becomes constant. Comparing this with the observational results, the change from positive to negative occurs too early for the theory. The positive values attained by the model are much too high. In fact it appears that the model result overshoots the equilibrium value before

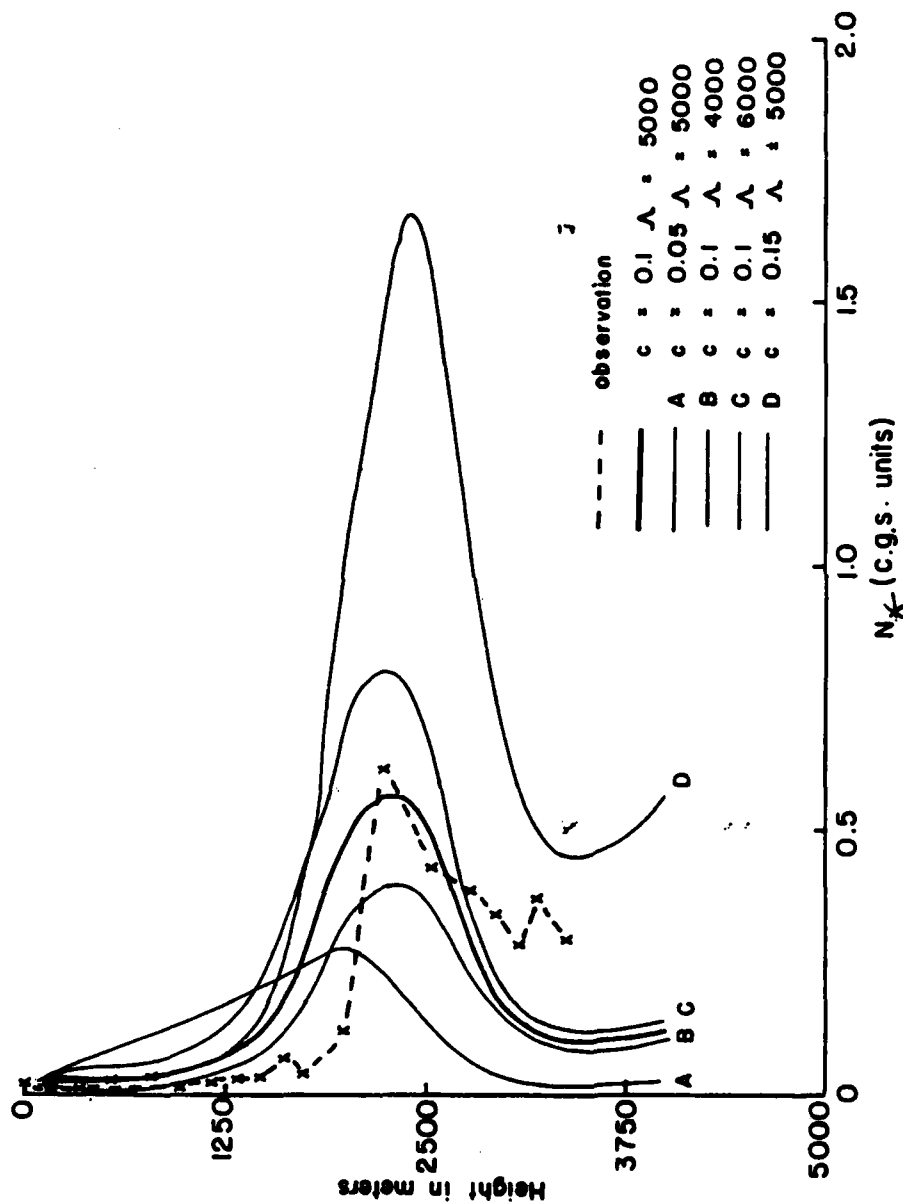


Fig.3.13:  $N_*$  from the three-parameter model evaluations for spiral on 25 February, 1980, exponential breakup fragment size distribution, effects of various values of physical parameters illustrated

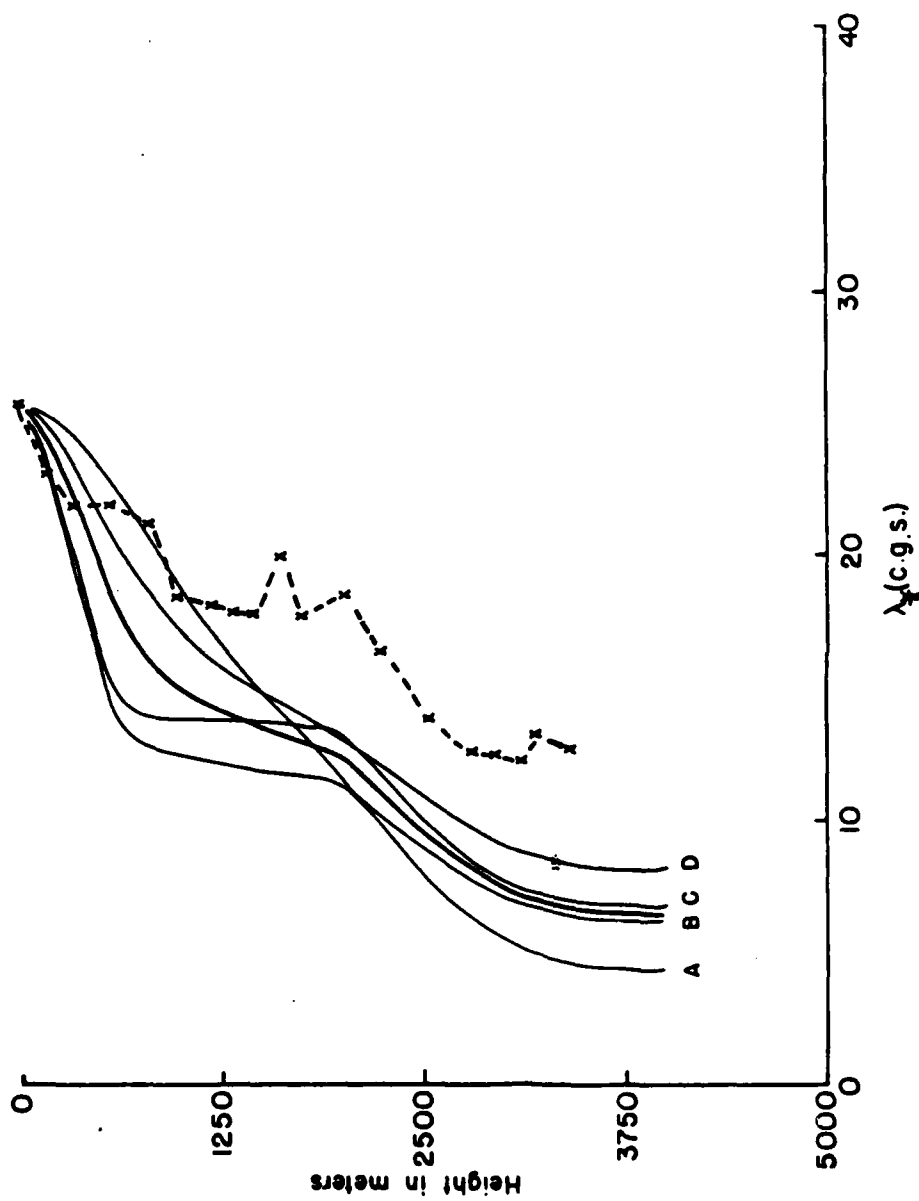


Fig.3.14:  $\lambda_w$  for 25 February, 1980, similar to Fig.3.13

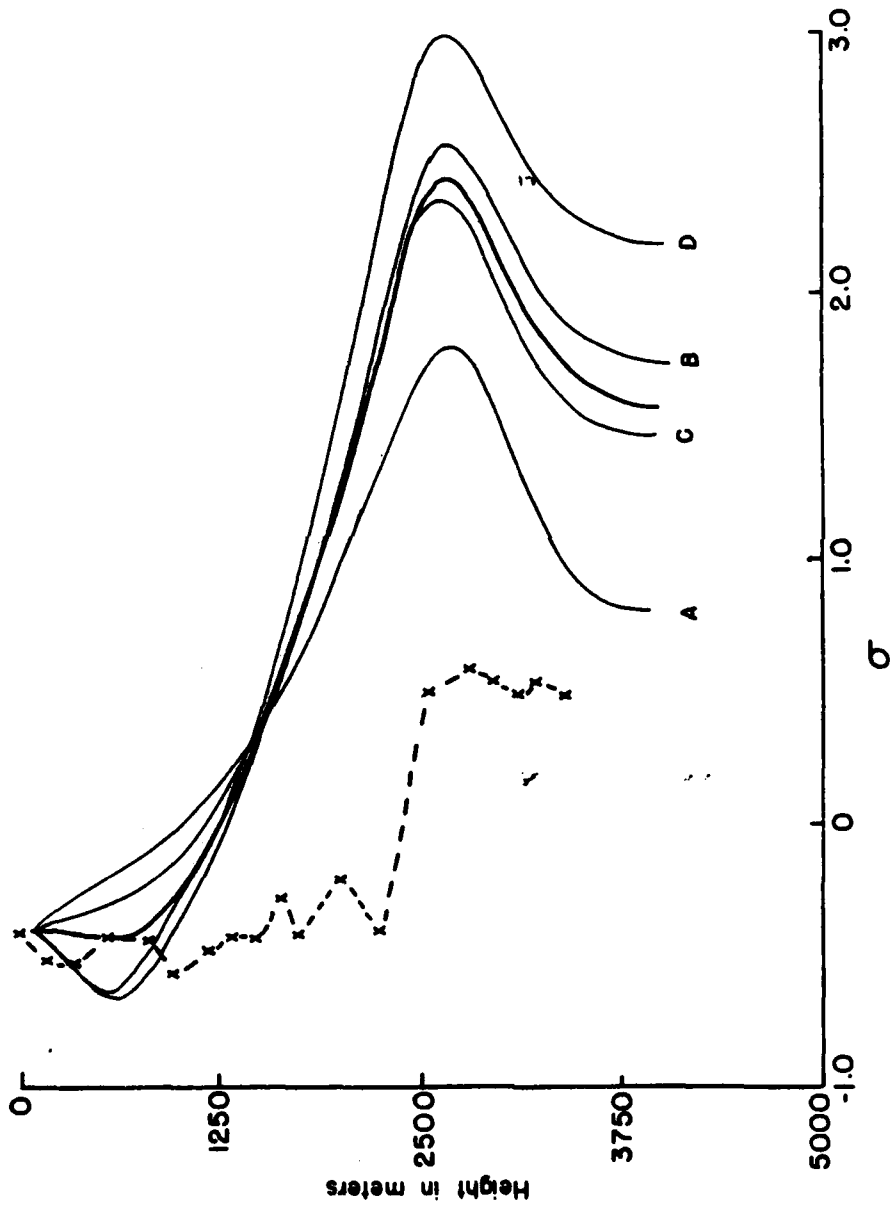


Fig.3.15:  $\sigma$  for 25 February, 1980, similar to Fig.3.13

it decreases back to the final value. In summary, the theoretical results can duplicate the different stages of snow growth. However, the quantitative agreement between the observations and the theory is not as good as in the two-parameter formulations. There are three reasons for this. First, a three-parameter analysis of data is more sensitive to noise in the data than a two-parameter data analysis. Secondly, it is always easier to fit two variables than to fit three variables. Finally, the accuracy of the smallest few size channels of the 200- $\mu$  are questionable. Ideally, if the data from the cloud probe could supplement this gap, the comparisons between the data and theory would be better.

Figs. 3.16-3.21 show the results from this formulation against the observations on 8 March, 1980. Guided by the results from the two-parameter model, two sets of parameter values are attempted and they are listed in Table 3.4. The  $N_x$  and  $\lambda_x$  from the set of parameters are similar. Both  $N_x$  and  $\lambda_x$  decrease rapidly and then become constant. These basically agree with the observational results. In the observations for  $N_x$ , except for the third and fifth loops, it decreases monotonically. The theory does not have the 'bumps' as such. It is not clear that the increases in  $N_x$  at these two loops are real or simply noise. The final value attained by  $\lambda_x$  in the theory is higher than that in the observations. The

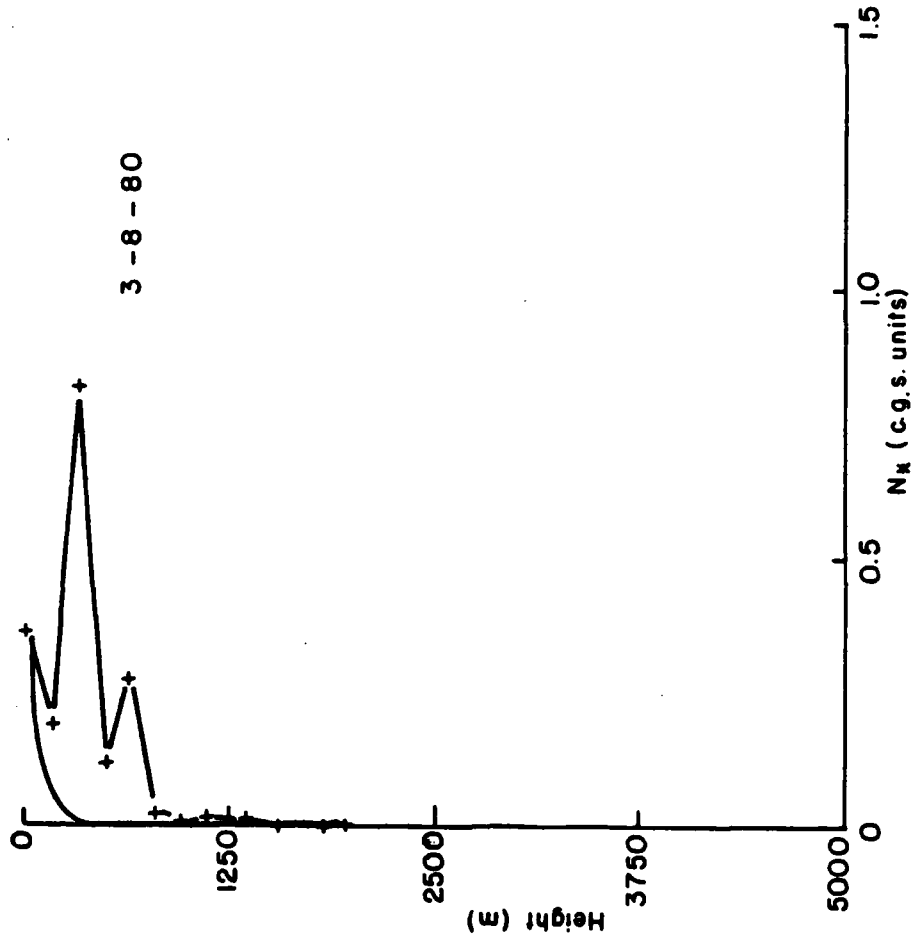


Fig. 3.16:  $N_*$  from three-parameter model evaluations for spiral on 8 March, 1980, exponential breakup fragment size distribution,  $\beta=0.75$

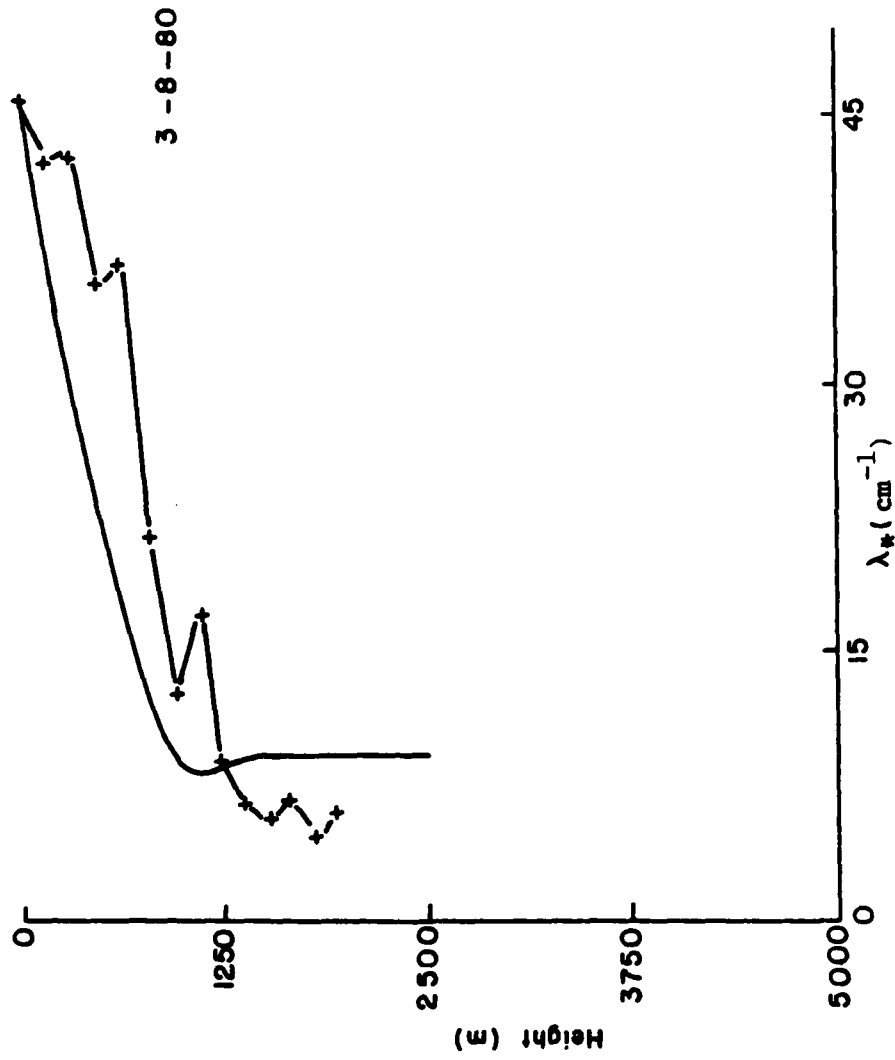


Fig.3.17:  $\lambda_*$  for 8 March, 1980, similar to Fig.3.16

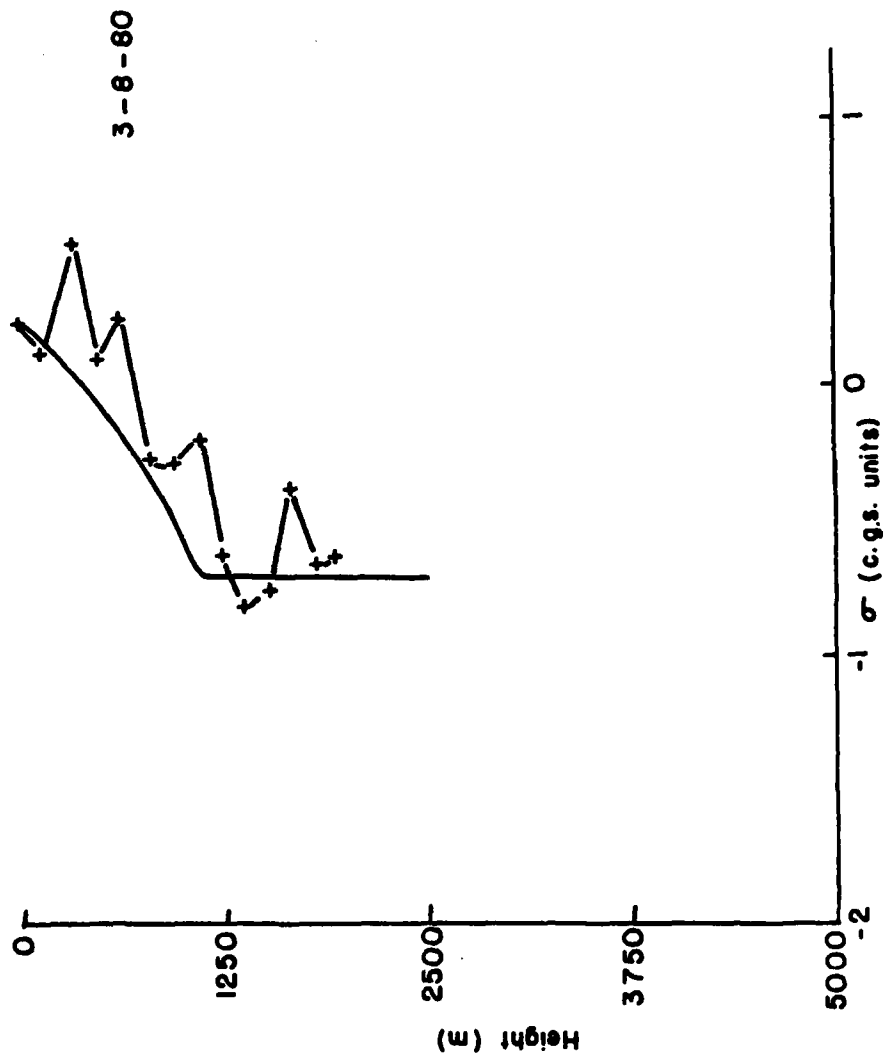


Fig.3.18:  $\sigma$  for 8 March, 1980, similar to Fig.3.16

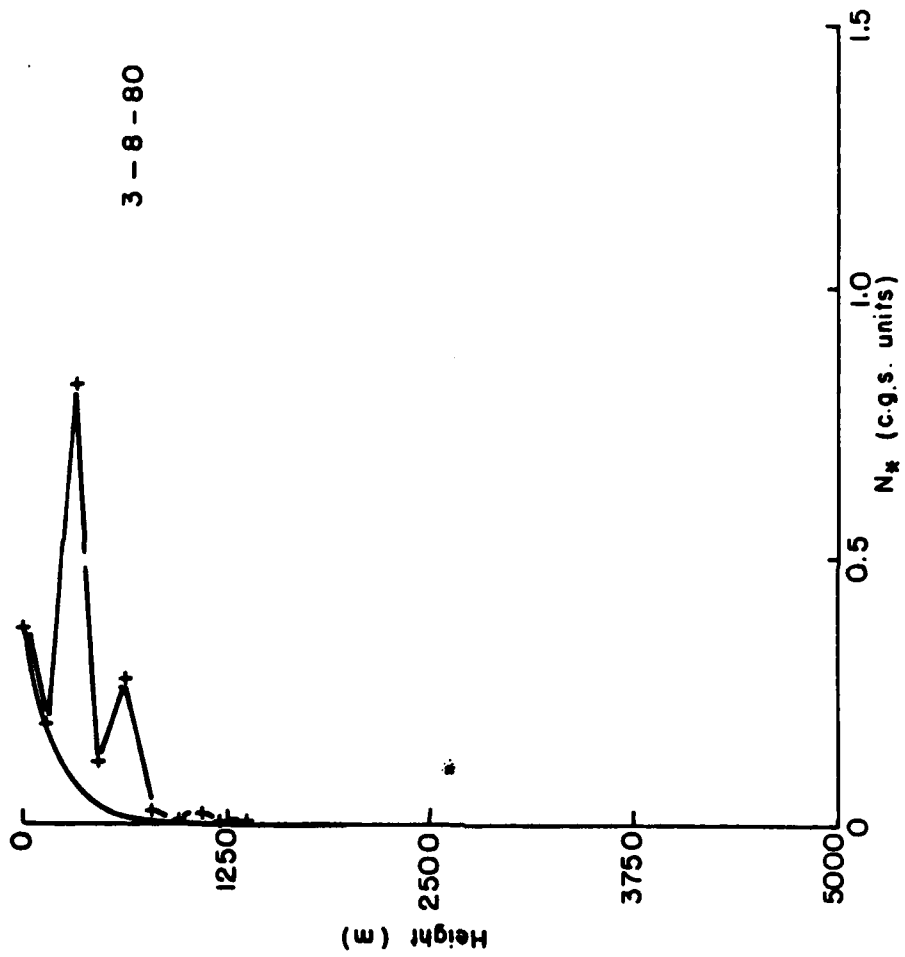


Fig.3.19:  $N_*$  from three-parameter model evaluations for spiral on 8 March, 1980, exponential breakup fragment size distribution,  $\beta=2$

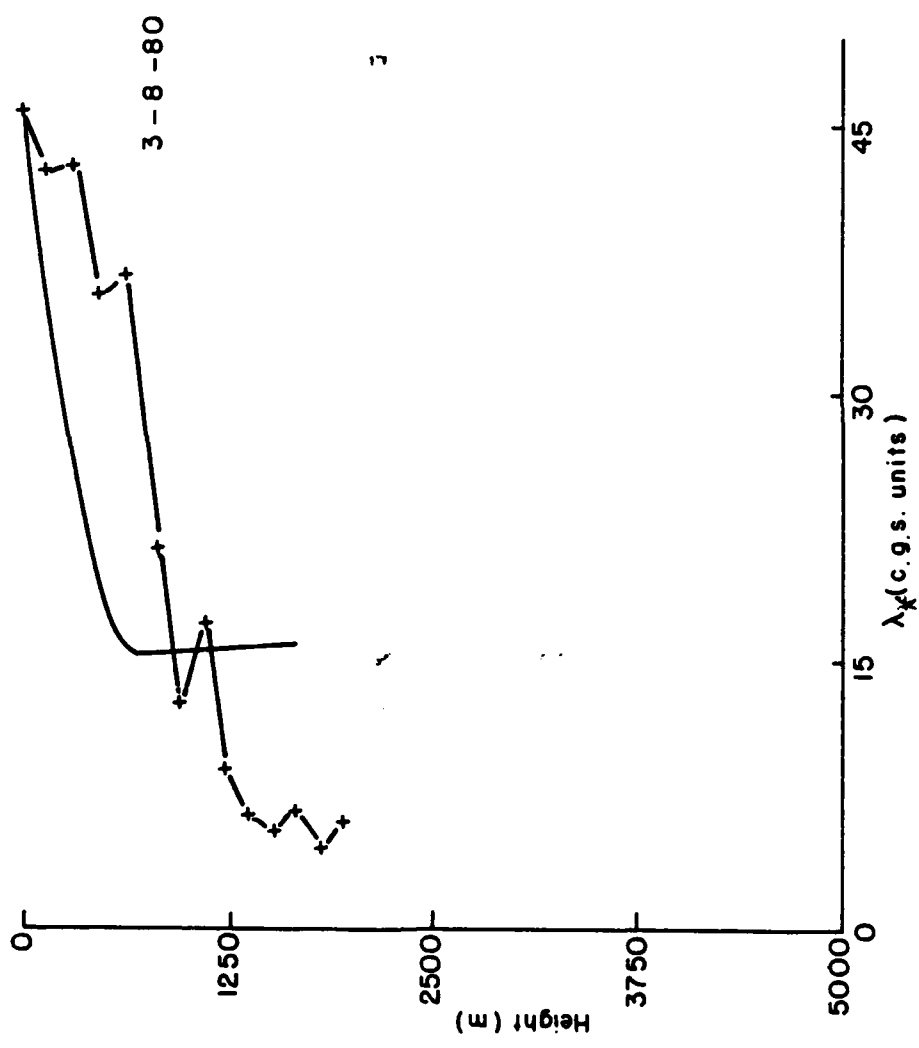


Fig.3.20:  $\lambda_*$  for 8 March, 1980, similar to Fig.3.19

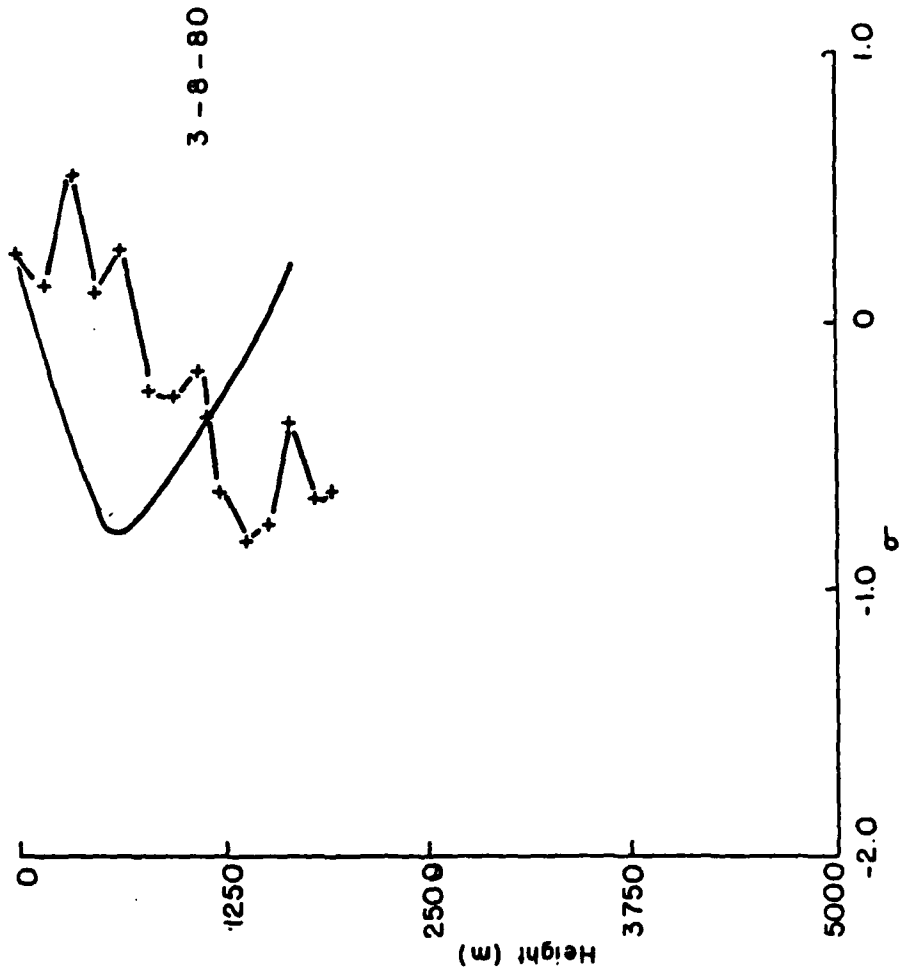


Fig.3.21:  $\sigma$  for 8 March, 1980, similar to Fig.3.19

major difference between the two sets of parameters lie in the results for  $\sigma$ . The results from the set that requires  $\beta=0.75$  decreases with height and then becomes constant while the results from the set that requires  $\beta=2.0$  decrease more rapidly and then increase again to become positive. It appears that the set of parameters that  $\beta=0.75$  duplicates the observations better. However, for  $\beta$ , the mass-diameter power, to be 0.75 is a bit too low. This implies the density of snow is small. The 2-D images do not indicate anything particularly different between this case and the cases on 25 Feb., 1980 and 26 Feb., 1980. The values of the breakup parameters imply that the number of fragments is high, which is expected because  $\sigma$  changes from positive to negative meaning small particles are generated faster than large particles.

### 3.3.2 Constant fragment number distribution

In this formulation, the fragment size distribution is assumed to be

$$S(x|x', x'') = N_s \delta(x - \frac{x' + x''}{N_s}) \quad (3.54)$$

Using a technique similar to that of the previous section, a set of two implicit equations are obtained,

$$\begin{aligned}
\frac{\partial \lambda_x}{\partial h} = & - \frac{\left(\frac{\partial \lambda_x}{\partial h}\right) \lambda_x}{\lambda_x \beta} - \frac{\lambda_x}{\beta \Gamma(b+\sigma+1)} \left[ \int_0^{\infty} x^{b+\sigma} \ln x e^{-x} dx \right] \frac{\partial \sigma}{\partial h} \\
& + \frac{\lambda_x}{\beta \Gamma(b+\beta+\sigma+1)} \left[ \int_0^{\infty} x^{b+\beta+\sigma} \ln x e^{-x} dx \right] \frac{\partial \sigma}{\partial h} \\
& + \frac{\left(\frac{N_2}{2}-1\right) \frac{\pi}{4} E \chi_f \lambda_x^{b+\beta-1} I_4}{\alpha \alpha \beta \Gamma(b+\sigma+1) \Gamma(b+\beta+\sigma+1)} \\
& - \frac{\left(\frac{N_2}{2}-\frac{1}{2}\right) \frac{\pi}{4} E \chi_f \lambda_x^{2b+\beta+2\sigma+3} I_4}{\alpha \alpha \beta (\lambda_x+c)^{b+2\sigma+4} \Gamma(b+\sigma+1) \Gamma(b+\beta+\sigma+1)}
\end{aligned} \tag{3.55}$$

and

$$\begin{aligned}
\frac{\partial \sigma}{\partial h} \cdot \frac{\lambda_x}{\beta} = & \frac{2 \int_0^{\infty} x^{b+\beta+\sigma} \ln x e^{-x} dx}{\Gamma(b+\beta+\sigma+1)} \\
& - \frac{\int_0^{\infty} x^{b+\sigma} \ln x e^{-x} dx}{\Gamma(b+\sigma+1)} \\
& - \frac{\int_0^{\infty} x^{b+2\beta+\sigma} \ln x e^{-x} dx}{\Gamma(b+2\beta+\sigma+1)} \\
= & \frac{2 \left(\frac{\partial \lambda_x}{\partial h}\right) \lambda_x}{\lambda_x \beta} \\
& - \frac{2 \alpha \lambda_x^{b+\beta} \Gamma(\beta+\sigma+2)}{\alpha \alpha \beta \Gamma(b+2\beta+\sigma+1)} \\
& + \frac{\left(\frac{N_2}{2}-1\right) \frac{\pi}{4} E \chi_f \lambda_x^{b+\beta-1} I_4}{\alpha \alpha \beta \Gamma(b+\sigma+1) \Gamma(b+\beta+\sigma+1)} \\
& - \frac{\left(\frac{N_2}{2}-\frac{1}{2}\right) \frac{\pi}{4} E \chi_f \lambda_x^{2b+\beta+2\sigma+3} I_4}{\alpha \alpha \beta (\lambda_x+c)^{b+2\sigma+4} \Gamma(b+\sigma+1) \Gamma(b+\beta+\sigma+1)} \\
& - \frac{2 \frac{\pi}{4} E \chi_f \lambda_x^{b+\beta-1} I_6}{N_2 \alpha \alpha \beta \Gamma(b+\beta+\sigma+1) \Gamma(b+2\beta+\sigma+1)} \\
& - \frac{\left(\frac{1}{N_2}-1\right) 2 \frac{\pi}{4} E \chi_f \lambda_x^{b+\beta-1} I_7}{\alpha \alpha \beta \Gamma(b+\beta+\sigma+1) \Gamma(b+2\beta+\sigma+1)}
\end{aligned} \tag{3.56}$$

$$+ \frac{\left(\frac{1}{N_s} - 1\right) 2 \frac{\pi}{4} E X_f \lambda_*^{2b+3\beta+2\sigma+3} (I_6 + I_7)}{a \alpha \beta (\lambda_* + c)^{b+2\beta+2\sigma+4} \Gamma(b+\beta+\sigma+1) \Gamma(b+2\beta+\sigma+1)}$$

where  $I_4$ ,  $I_6$  and  $I_7$  are from (3.44), (3.48) and (3.49) in the previous section.

The results from these formulations using the 25 Feb., 1980 case as initial conditions are shown Figs. 3.22, 3.23 and 3.24. Even after numerous attempts at adjusting the parameter values,  $N_x$ ,  $\lambda_x$  and  $\sigma$  obtained from this formulation cannot be made to fit the observations. As a last resort, one set of parameters is used from the beginning until the maximum of  $N_x$  and then a second set of parameters is used from then onwards until the end of the computations. Even after all these efforts,  $N_x$ ,  $\lambda_x$  and  $\sigma$  still cannot fit the observational results desirably. This probably implies that the exponential fragment size distribution is a better breakup formulation than the constant fragment number distribution. Physically, it is more reasonable to assume that when particles collide, they do not generate a constant number of fragments, but rather the larger the parent particles, the more numerous the fragments. Based on the laboratory experiments described in appendix 2, it is also more reasonable to assume that the particle sizes are in a

2-25-80

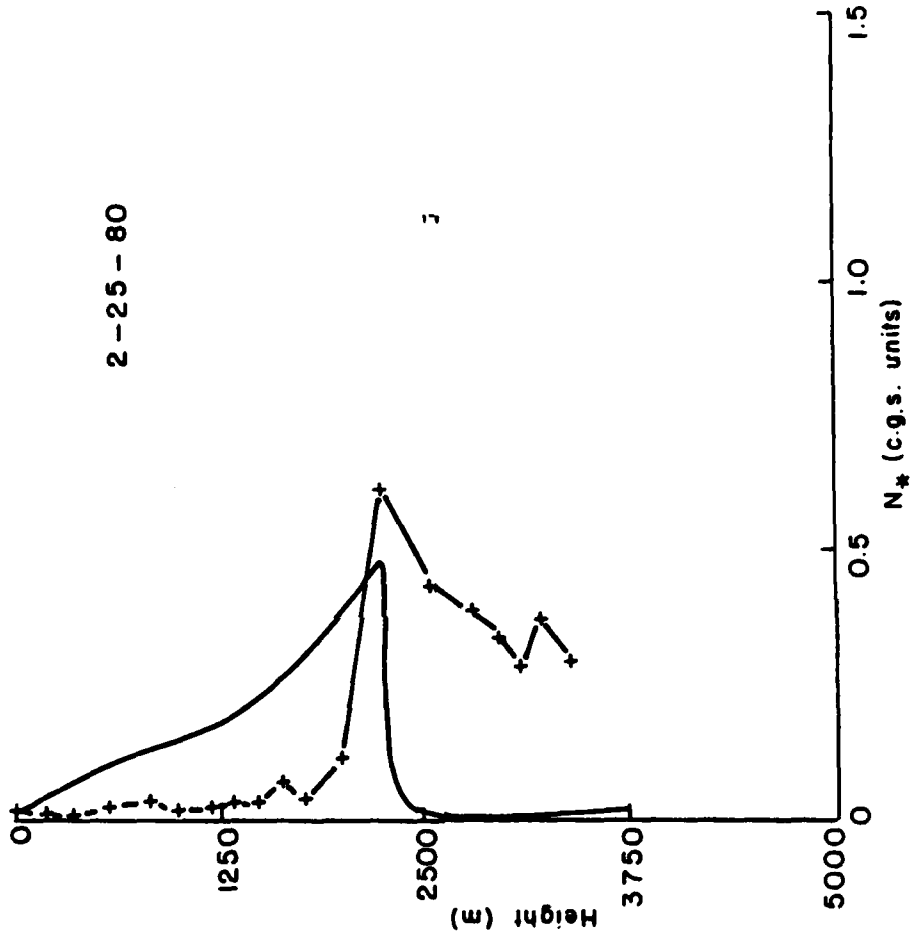


Fig.3.22:  $N_*$  from three-parameter model evaluations for spiral on 25 February, 1980, constant fragment number distribution

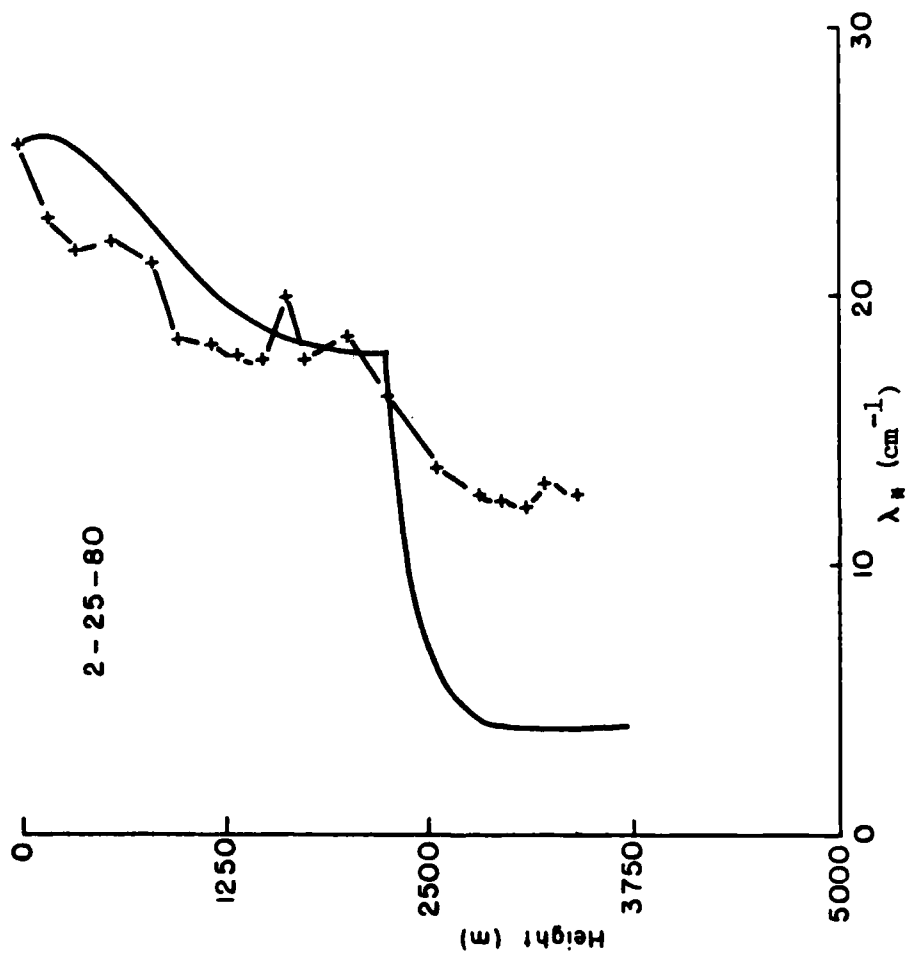


Fig.3.23:  $\lambda_*$  for 25 February, 1980, similar to Fig.3.22

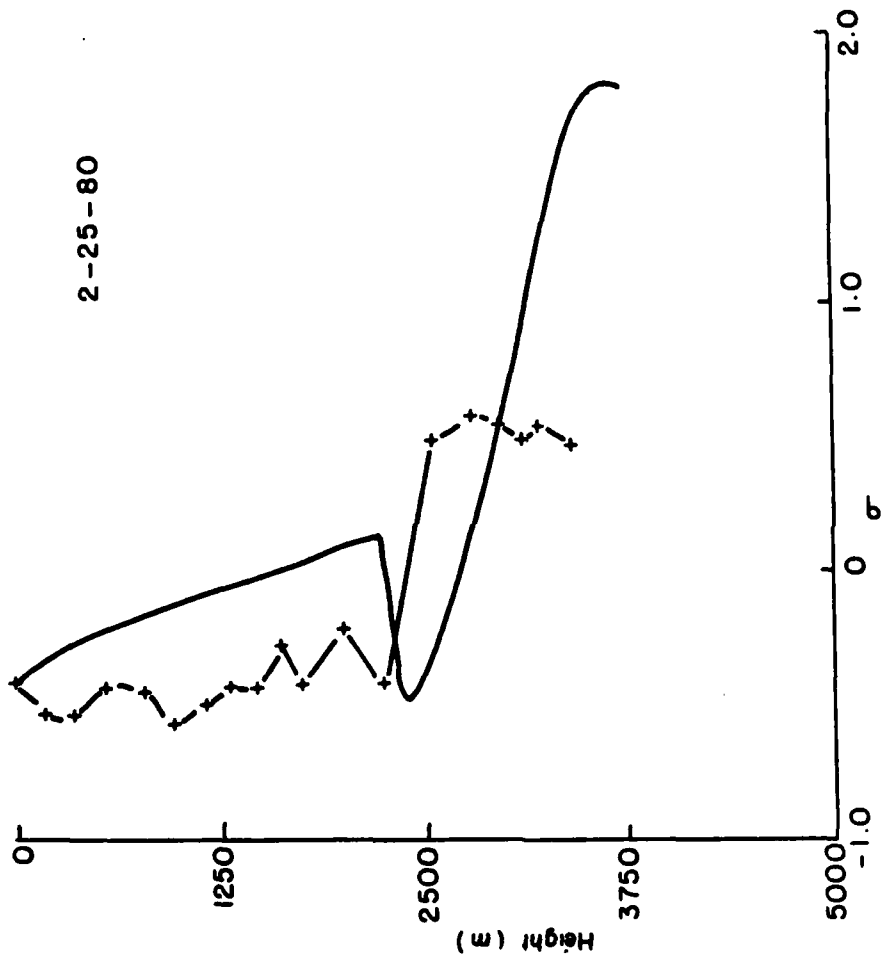


Fig.3.24:  $\sigma$  for 25 February, 1980, similar to Fig.3.22

negative exponential distribution than to assume that they have uniform sizes.

Figs. 3.25, 3.26 and 3.27 show the results from this formulation against the observations from 8 March, 1980. Only the set of parameters having  $\beta = 0.75$  is being used. (The values of the physical parameters used are listed in Table 3.4.) Both  $N_x$  and  $\lambda_x$  duplicate the observations competently. However, although  $\sigma$  decreases initially from positive to negative, it fails to maintain a constant value. Instead, it gradually increases to become positive again. This behavior is similar to the result from the exponential fragment size distribution with  $\beta$  equaling 2. Considering the results from both spirals, it appears that a negative exponential size spectrum is the better model for the breakup fragments.

#### 3.4 Effect of different initial concentrations

In order to study the effect of seeding (either natural or artificial), an attempt is made to modify the initial values of parameters so that the total concentration increases but not the total mass. For the two-parameter formulation, assuming the mass-diameter relationship to be

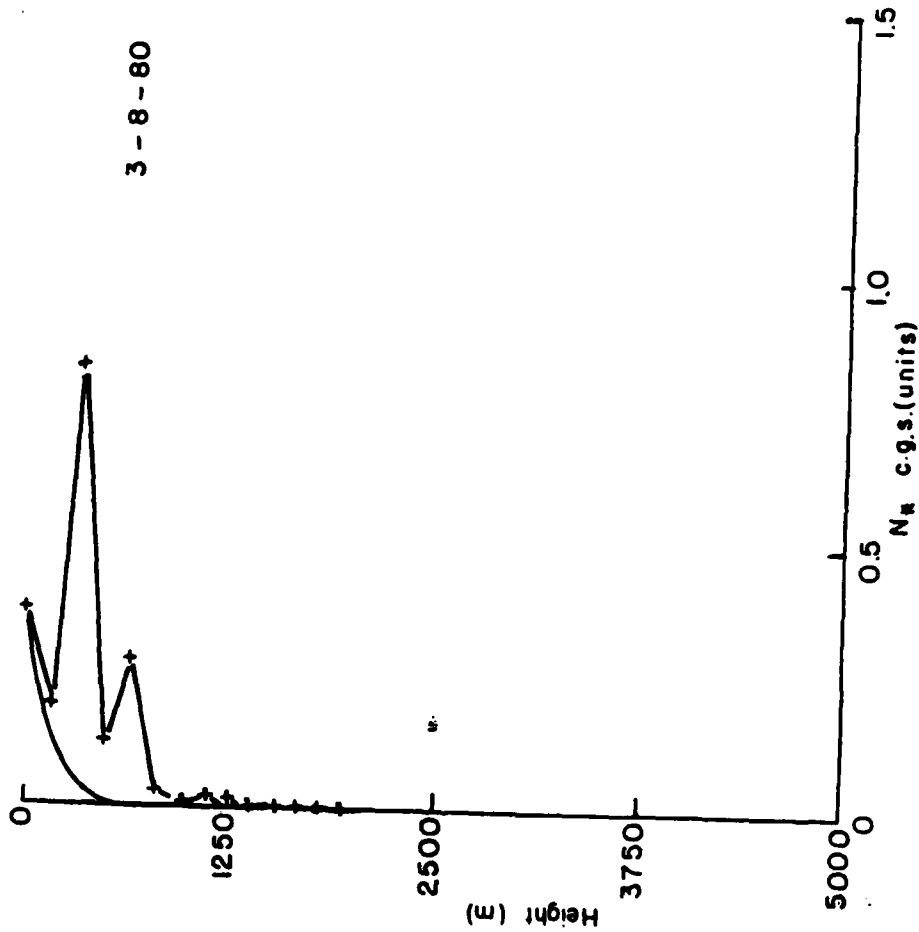


Fig.3.25:  $N_*$  from three-parameter model evaluations for spiral on 8 March, 1980, constant fragment number distribution,  $\beta=0.75$

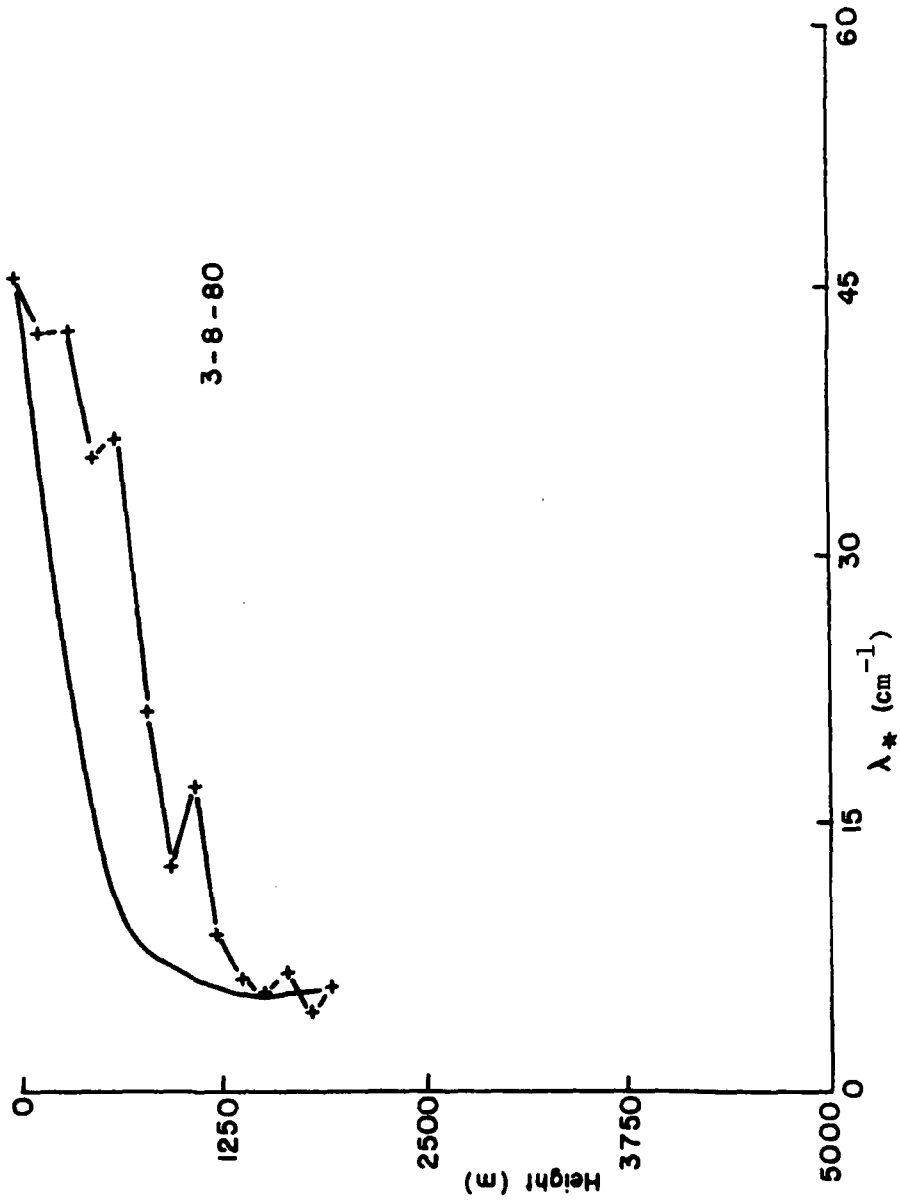


Fig.3.26:  $\lambda_*$  for 8 March, 1980, similar to Fig.3.25

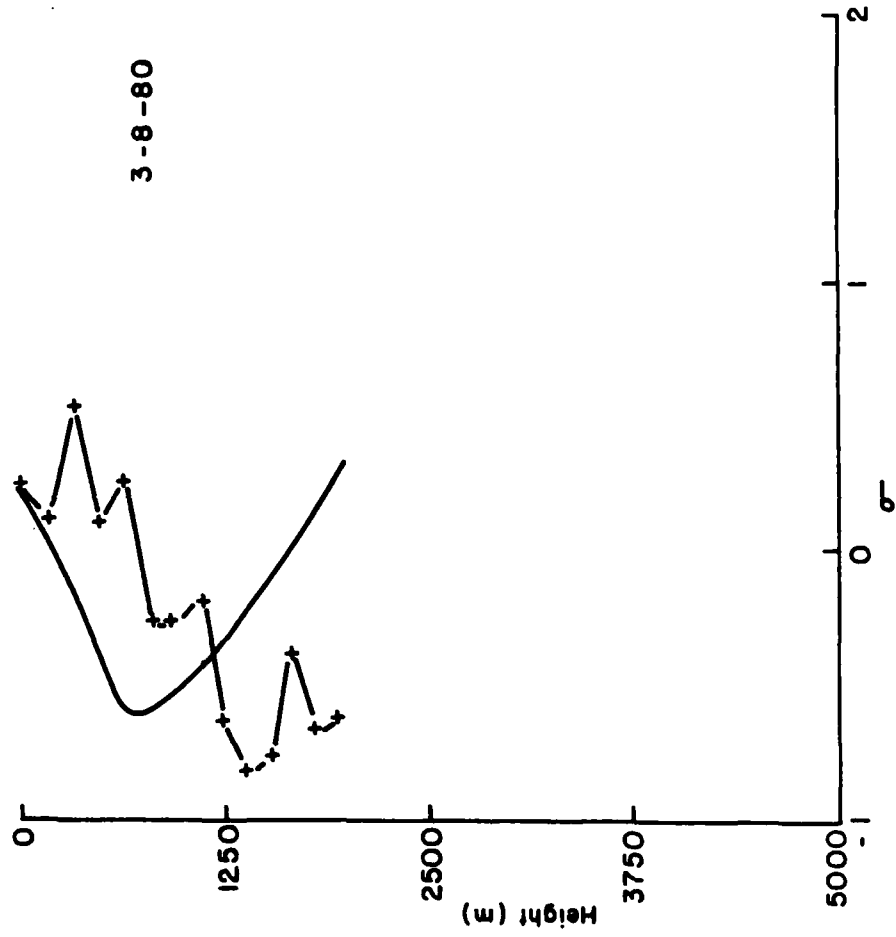


Fig.3.27:  $\sigma$  for 8 March, 1980, similar to Fig.3.25

$x = \alpha D^\beta$ , the total mass is

$$\int_0^\infty \alpha D^\beta N_0 e^{-\lambda D} dD = \frac{\alpha N_0 \Gamma(\beta+1)}{\lambda^{\beta+1}} \quad (3.57)$$

Constant total mass means

$$N_0 = \text{constant} \cdot \lambda^{\beta+1} \quad (3.58)$$

So, the change of concentration without the change of mass is

$$\frac{N_{0,2}}{\lambda_2} = \frac{N_{0,1}}{\lambda_1} \quad (3.59)$$

$$\text{where } N_{0,2} = N_{0,1} \left(\frac{\lambda_2}{\lambda_1}\right)^{\beta+1} \quad (3.60)$$

Using the case of 26 Feb., 1980 as an example, the initial total concentration is increased 5 and 10 times, without changing the total mass. The computations are done using the same set of parameters as is done before in section 3.2.2 and the results are plotted in Fig. 3.28. The results indicate that the change in the initial total concentration affects the change from the deposition stage to the aggregation stage but does not affect the final equilibrium. Increasing the initial concentration 5 times causes the aggregation stage to start approximately 50 meters earlier than before but delays the collisional stage by approximately 500 meters. Increasing the initial concentration by 10 times causes the aggregation stage to start approximately 100 meters earlier and delays the collisional stage by 600 meters.

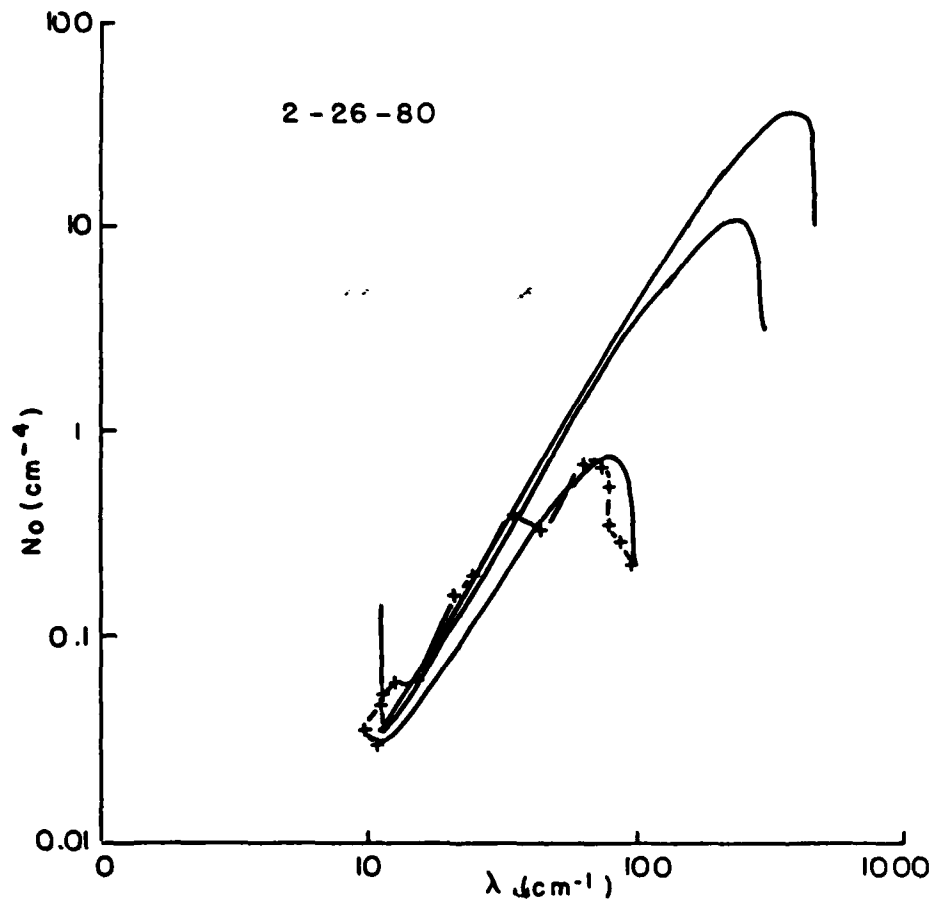


Fig.3.28: Effect of different initial concentrations, the smooth curves are from top to bottom 10 times, 5 times and actual total concentrations,  $N_0$ - $\lambda$  trajectories for 26 February, 1980

Physically, the increase in concentration without increasing the mass means that the number of collision increases. Quantitatively, the number of collisions is represented by

$$\frac{N_0^2 \pi E a}{\lambda^{b+4}} \int_0^\infty \int_0^\infty (x+y)^2 |x^b - y^b| e^{-(x+y)} dx dy$$

Since  $N_0$ 's and  $\lambda$ 's are related by (3.60), higher values of  $N_0$  and lower values of  $\lambda$  means higher number of collisions, resulting in an increase in aggregation events. Therefore, the aggregation stage starts earlier. On the other hand, increasing the concentration without increasing the mass means that the average size of particles are smaller. So, it would take longer for them to grow to such a size that collisional breakup becomes efficient. Since neither aggregation nor collisional breakup affects the total mass, so the final equilibrium position between these two processes depends only on the slope,  $\lambda$ , and not on the initial concentrations.

### 3.5 Investigations of rime-splintering

Mossop (1976) concludes from laboratory experiments that secondary ice particle production due to rime-splintering depends on the number density of supercooled drop greater

than 24 microns. Approximately, one ice splinter is thrown off for the accretion of every 250 drops greater than 24 microns. The temperature range for occurrence is between  $-3^{\circ}\text{C}$  and  $-8^{\circ}\text{C}$  with the production rate being greatest at  $-5^{\circ}\text{C}$ . Fig. 3.29 shows the number density of particles greater than 24 microns as measured by the Axially Scattering Spectrometer Probe. Based on Fig. 3.29 the splinter production rates of the three spirals can be estimated by assuming that these are supercooled water drops.

In unit time, the number of accreted drops by a single snow particle is

$$\pi E \left( \frac{D}{2} + \frac{d}{2} \right)^2 [V(D) - V(d)] n' \quad (3.61)$$

where  $D$  = diameter of ice particle

$d$  = diameter of supercooled droplet

$V(D)$ ,  $V(d)$  = terminal fallspeed of snow particle and drop respectively

$n'$  = number density of supercooled droplets

$E$  = collisional efficiency

Representing the number density of snow particles with diameters between  $D$  and  $D+dD$  as  $N(D)dD$ , then the total number of accretion events per unit time per unit volume is

$$\int_0^{\infty} \pi E \left( \frac{D}{2} + \frac{d}{2} \right)^2 [V(D) - V(d)] n' N(D) dD \quad (3.62)$$

Assuming  $N(D)dD = N_0 e^{-\lambda D} dD$ ,  $V = aD^b$ , and  $V(d) \ll V(D)$ , then the

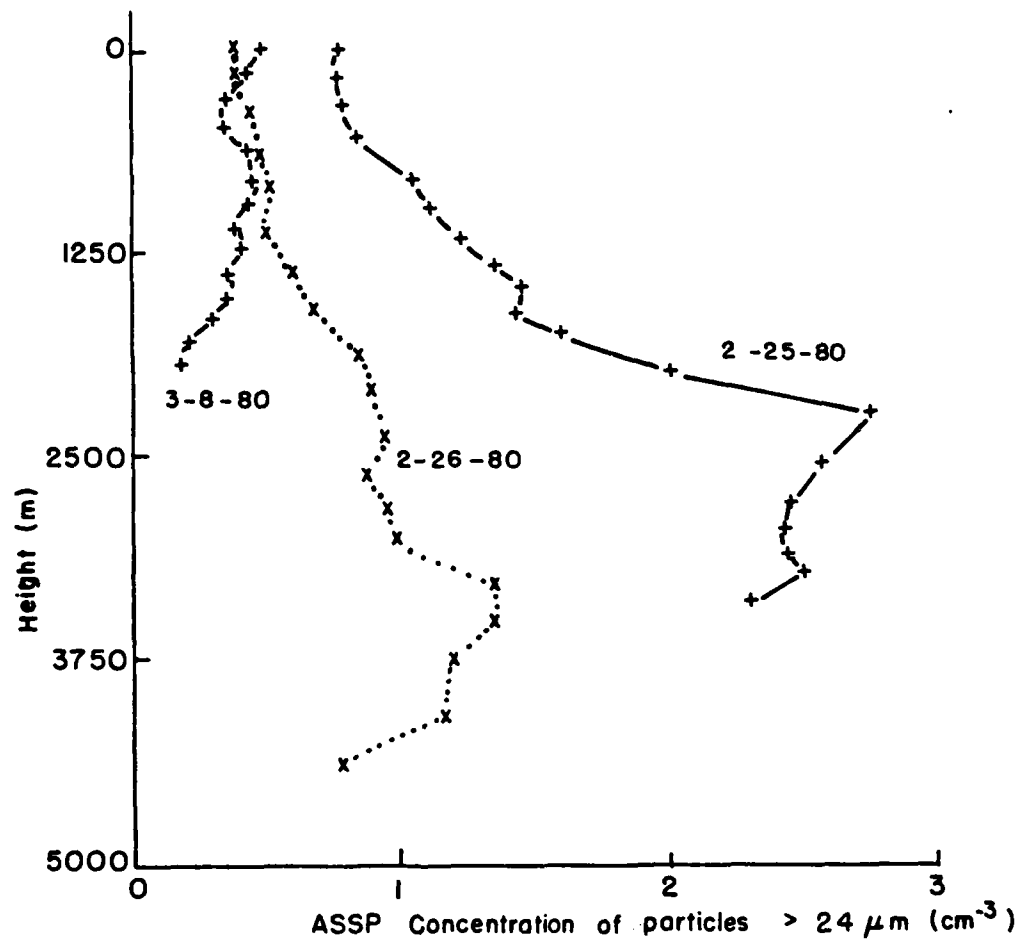


Fig.3.29: ASSP number density of particles greater than 24 microns

integral becomes

$$\frac{a\pi N_0 n'}{4} \left[ \frac{\Gamma(b+3)}{\lambda^{b+3}} + \frac{2d \Gamma(b+2)}{\lambda^{b+2}} + \frac{d^2 \Gamma(b+1)}{\lambda^{b+1}} \right] \quad (3.63)$$

Using typical values of  $a$  and  $b$  (Locatelli and Hobbs, 1974) and the observed values of  $n'$  from Fig. 3.29, the accretion rates for each spiral can be estimated. Based on Mossop's conclusion that one splinter is produced for every 250 accretions, the splinter production rate can also be estimated. The accretion rates and the production rates for the three spirals are listed in Table 3.5.

The particle depletion rate due to aggregation can be estimated using the stochastic model with a geometric kernel,

$$\iint_0^{\infty} N_0(D_1) N_0(D_2) \frac{\pi}{4} E a |D_1^b - D_2^b| (D_1 + D_2)^2 dD_1 dD_2 \quad (3.64)$$

The estimated depletion rates for the three spirals are also listed in Table 3.5.

From Table 3.5 it appears that the splinter production rate is compatible with the particle depletion rate. If the particles detected by the ASSP are really supercooled droplets, then the Mossop-Hallet splintering mechanism could account for the secondary particle production. As mentioned before, the ASSP probe operates on a light scattering principle and can easily give false counts from the light

scattered or reflected of the snow particles. Comparing Figs. 2.9, 2.11 and 2.13 with Fig. 2.38, the ASSP concentration and the 1-D precipitation probe concentration increase and decrease at around the same height. This suggests that it is possible that the ASSP counts are not liquid droplets but false counts from light scattered off the snow particles.

In order to answer the question whether the ASSP detected particles are supercooled water droplets, the possible sources of these supercooled droplets need be investigated. There are two possible sources: (1) The water droplets being initiated below the freezing level and then being carried upward with the updraft and (2) the droplets being initiated in situ by supersaturation.

In order to investigate the possible sources, a simple model is set up. Consider a closed parcel of saturated air initially at the freezing level with a monodisperse distribution of liquid water content,  $\chi$ , and the initial radius of droplets being  $r$  with a nucleus of NaCl of mass  $10^{-15}$  gm. In this parcel of air, the initial snow particle distribution is of the form  $N_0(h)e^{-\lambda(h)D}dD$ . The upward velocity of the parcel is taken to be the difference between the updraft velocity and the droplets terminal fallspeed. The air parcel is then lifted adiabatically. It is further assumed that there is no entrainment or mixing with the

environmental air. The output is the radius of the supercooled water droplets, vapor saturation ratio with respect to ice and vapor saturation ratio with respect to water. According to Beard and Pruppacher (1971), the ventilation factor for droplets of radius 20 micron is 1.04 and so the ventilation effect has been neglected in the calculations.

The change in saturation vapor ratio with respect to ice is computed by a modified form of Twomey, 1959.

$$\begin{aligned}
 dS = & \frac{\epsilon L g}{R_a T^2} \left( \frac{1}{C_p} - \frac{T}{L \epsilon} \right) dH \\
 & - \left[ \frac{\epsilon L_w}{R_a T^2} \left( \frac{L_w}{C_p} + \frac{P R_a T^2}{L_w \epsilon^2 e_w} \right) \frac{dw}{p_a} \right] \frac{e_w}{e_i} \\
 & - \frac{\epsilon L_i}{R_a T^2} \left( \frac{L_i}{C_p} + \frac{P R_a T^2}{L_i \epsilon^2 e_i} \right) \frac{dI}{p_a}
 \end{aligned} \tag{3.65}$$

- where S = supersaturation with respect to ice
- $e_i$  = saturation vapor pressure over plain ice
- $e_w$  = saturation vapor pressure over plain water
- T = temperature of air parcel
- $L_i$  = latent heat of sublimation
- $L_w$  = latent heat of evaporation
- $\epsilon$  =  $\frac{\text{molecular weight of water}}{\text{molecular weight of air}}$
- $p_a$  = density of air
- $R_a$  = gas constant of air
- C = specific heat of dry air at constant pressure

- $dH$  = change of height of air parcel  
 $dW$  = change of liquid water content  
 $dI$  = change of ice content  
 $g$  = gravitational acceleration of the earth  
 $p$  = atmospheric pressure

The first term on the right hand side is the production of water vapor due to lifting and cooling of the air parcel. The second term is the depletion (or production) of water vapor due to the condensation (or evaporation) of water droplets. The third term is the depletion of water vapor due to deposition from vapor to snow particles.

The growth of liquid droplets is computed by (Mason, 1971)

$$\frac{r dr}{dt} = \frac{S \left( \frac{e_i}{e_w} \right) - \frac{3.3 \times 10^{-5}}{T} + \frac{4.3 \gamma m_s}{M_s T}}{\frac{L \rho_L}{K T} \left( \frac{L}{R_a T} - 1 \right) + \frac{\rho_L R_a T}{D e_{s,w}}} \quad (3.66)$$

where  $r(h)$  = radius of water droplets as a function of height

- $\rho_L$  = density of water  
 $k$  = diffusivity of heat  
 $D$  = diffusivity of water vapor  
 $\gamma$  = number of ions per salt molecule  
 $m_s$  = mass of salt  
 $M_s$  = molecular weight of salt

$dr$  becomes negative when  $S$  is negative which means there is

evaporation. The change of liquid water content is given by

$$\frac{4}{3} \pi r^3 (h_2) - \frac{4}{3} \pi r^3 (h_1)$$

Assuming the snow particles are circular disks, and the mass of snow is related to its diameter by  $x = \alpha D^\beta$ , then the growth of snow particles is given by (Mason, 1971)

$$\frac{dD}{dt} = \frac{2S}{\frac{\alpha L_i}{kT} \left( \frac{L_i}{R_a T} - 1 \right) + \frac{\alpha R_a T}{D e_s}} \quad (3.67)$$

Assuming a negative exponential distribution of snow particles, the change in ice content is given by

$$dI = \frac{2(N_{s,2} - N_{s,1})\alpha}{\lambda^3} \quad (3.68)$$

where  $N_{s,1}$  is the initial intercept of snow-size distribution and  $N_{s,2}$  is found from

$$\log_{10} N_{s,2} = \log_{10} N_{s,1} + \frac{(N_{s,1} - N^* + dD)\lambda}{\lambda} \quad (3.69)$$

with  $N^*$  an arbitrary value. The temperature of the air parcel is computed by

$$dT = \left( -\frac{g dH}{c_p} + \frac{L_w dw}{c_p} + \frac{L_i dI}{c_p} \right) \quad (3.70)$$

The terminal fallspeed of the droplets is assumed to be (Rogers, 1979):

$$u = 8000 * r \quad (3.71)$$

where  $u$  = droplet terminal fallspeed in cm/sec

$r$  = droplet radius in cm

The upward velocity of the parcel is taken to be the difference between the updraft velocity and the terminal droplet fallspeed.

This set of equations is solved in height steps and the results are plotted in Figs. 3.30 and 3.31 with the initial conditions also listed in the figure captions. The liquid water content used is  $1 \text{ gm/m}^3$  and is extremely high for this type of cloud. A monodisperse cloud with droplets of radius 20 microns is also unrealistic. In real life, the cloud droplet distribution is approximately negative exponential, which means that there are more small drops and less large drops. Thus, this simple calculation simply indicates what happens in an extreme situation.

Also plotted on the graphs are the 'water saturation' lines which depict the amount of vapor supersaturation with respect to ice if the vapor pressure is kept at saturation with respect to water. The results show that the vapor pressure becomes subsaturated with respect to water starting a few decades of meters above the freezing level. This means that supercooled liquid water could not be initiated in situ. For small updraft, such as 20 cm/s, liquid water droplets cannot be maintained for a long distance and will be evaporated soon. For larger updraft, such as 50 cm/s, liquid water droplets will be maintained up to 1000 meters above

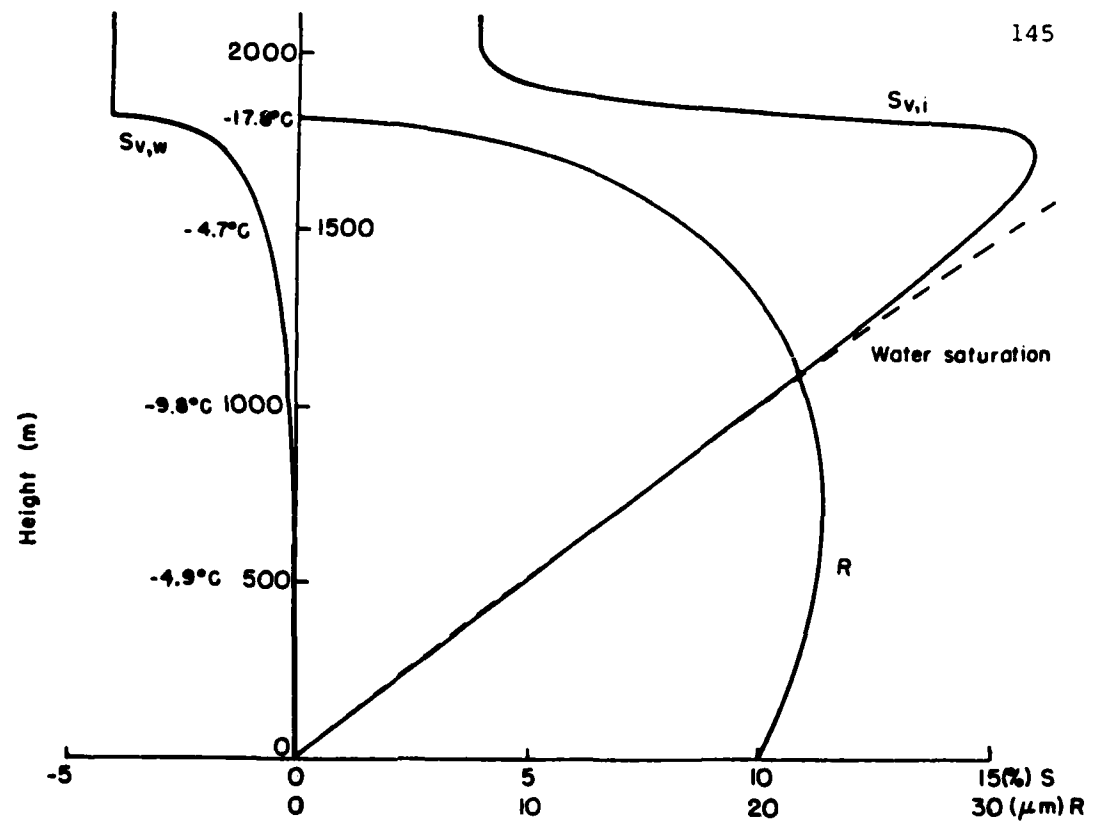


Fig.3.30: Change of saturation vapor pressure with respect to ice,  $S_{v,i}$ , saturation vapor pressure with respect to water,  $S_{v,w}$ , and supercooled droplet radius with height, updraft 50 cm/s

Snow particle distribution =  $0.1e^{-10D}$   
 Liquid water content = 1 gm/m<sup>3</sup>  
 Initial droplet radius = 20 microns

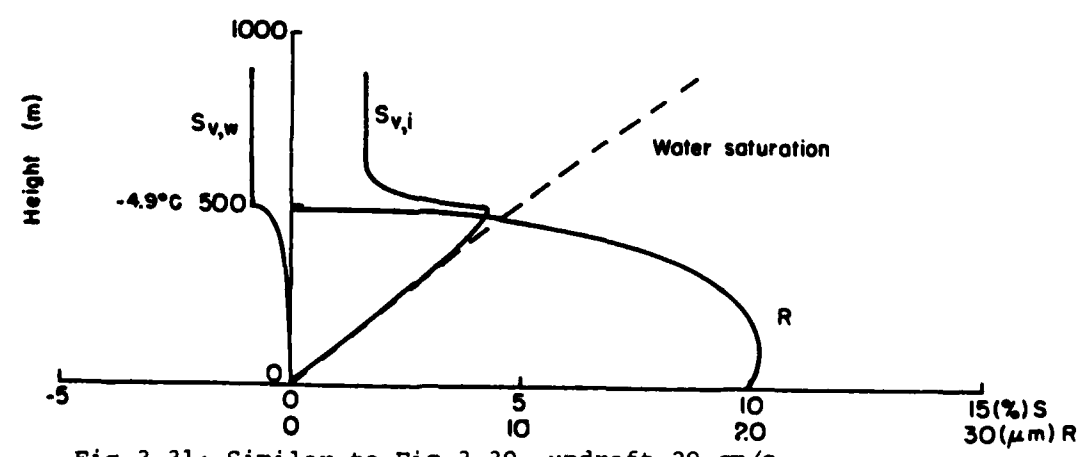


Fig.3.31: Similar to Fig.3.30, updraft 20 cm/s

freezing level. Then the question is whether the droplet can remain being supercooled without freezing at such temperature. This model of evaporation and condensation/deposition permits no moisture and temperature mixing between the parcel and the environment which is a reasonable assumption for widespread stratiform cloud. The results from this simple model is in general agreement with complicated models such as Mason and Chien, 1962 and Lee and Pruppacher, 1977.

In any case, the observed occurrence of the scant liquid water (Figs. 2.8 - 2.11) does not seem to correlate with the onset of the collisional stage. Figs. 2.12 and 2.13 clearly indicate that there is no supercooled liquid water for the case on 8 March, 1980. However there is still the third stage of snow growth.

Recent studies of ice particle breakup (Hobbs and Farber, 1972; Vardiman, 1978) emphasize that the coexistence of dense, rapidly falling graupel along with fragile aggregates and crystals may be necessary for collisional breakup. However, the observations here suggest that the presence of graupel is not required for breakup. The temperature where the spectra cease evolution is about  $-8^{\circ}\text{C}$  which is in the temperature range of scrolls (Nakaya, 1954) and hollow prisms (Mason, 1971). It could be that these

types of crystals are more fragile. Martner (1982) also reported the occurrence of secondary ice crystal production in the absence of supercooled liquid water.

### 3.6 Deposition-aggregation-rime splintering simulation

In order to study the possibility of the rime-splintering mechanism in this form of precipitation, an attempt is made to simulate snow growth with the physical processes of deposition, aggregation and rime-splintering.

#### 3.6.1 Two-parameter formulation

The theoretical representation of deposition and aggregation are as described above. According to the Hallet-Mossop theory, the rate of rime-splintering depends on the environmental liquid water content, which is not available in the theoretical model. Hence rime-splintering is represented by increasing the total particle concentration at each height step without changing the total mass. The computational procedure is that first the changes of  $N_0$  and  $\lambda$  are computed with a model having only deposition and

aggregation. Where  $N_0$  and  $\lambda$  arrives at their observational 'equilibrium' positions, the total particle concentration is made to increase by a fixed amount, i. e.,

$$\frac{N_2}{\lambda_2} - \frac{N_1}{\lambda_1} = K \quad (3.72)$$

In order to keep the mass constant, the change in  $N_0$  and  $\lambda$  is given by:

$$N_2 = \left(\frac{\lambda_2}{\lambda_1}\right)^{\beta+1} N_1 \quad (3.73)$$

$$\lambda_2 = \left[ \left(\frac{K}{N_1} + \frac{1}{\lambda_1}\right) \lambda_1^{\beta+1} \right]^{1/\beta} \quad (3.74)$$

In the computations, the values of  $K$  used are based on the splintering production rates listed in Table 3.5 multiplied by the time elapsed in one height step. The results for these computations for the three ASD are plotted in Figs. 3.32, 3.33 and 3.34. The value of physical parameters are listed in Table 3.6. It shows the increase in total concentration for certain initial  $N_0$  and  $\lambda$  and change of concentration. The results from the model indicate that riming can stop the decrease of  $\lambda$  for a certain while with  $N_0$  increasing. Then both  $N_0$  and  $\lambda$  decrease unceasingly. This formulation fails to predict the equilibrium  $\lambda$  that is observed. This is a further indication that the third stage of snow growth in the observational data cannot be caused by rime-splintering.

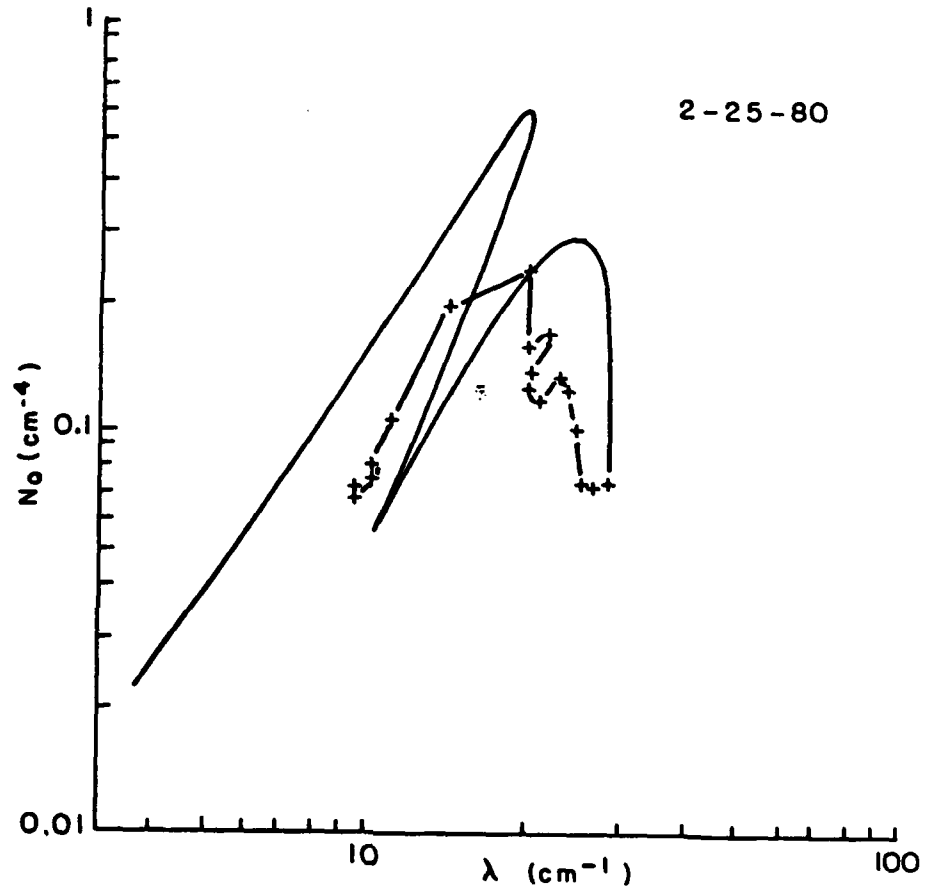


Fig.3.32: Two-parameter model of deposition, aggregation and rime-splintering, 25 February, 1980

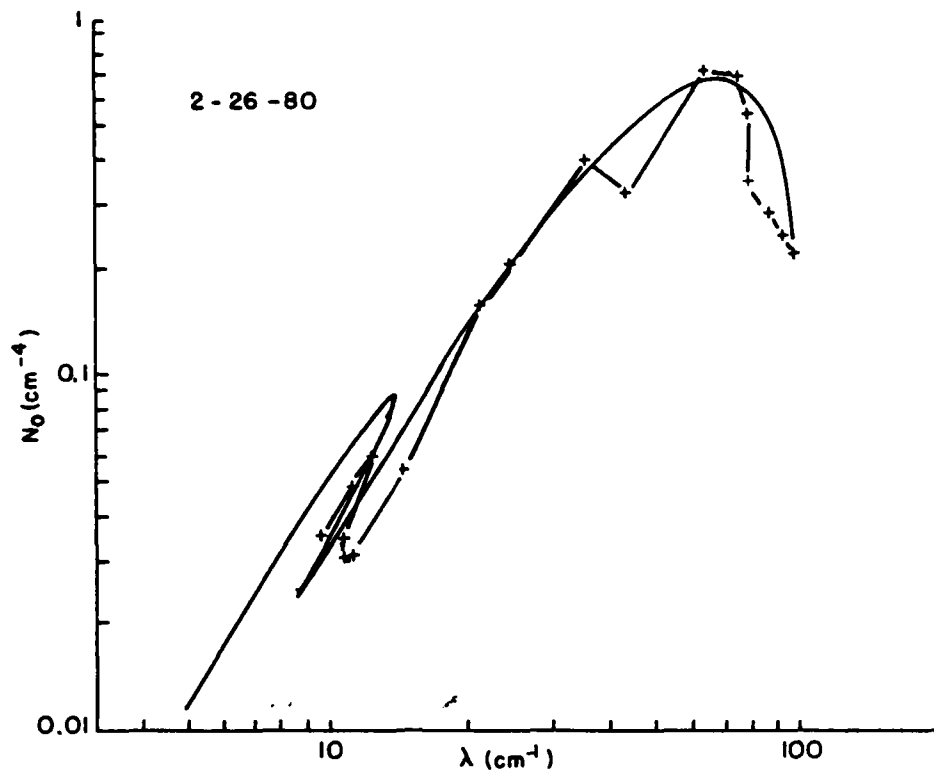


Fig.3.33: Two-parameter model of deposition, aggregation and rime-splintering, 26 February, 1980

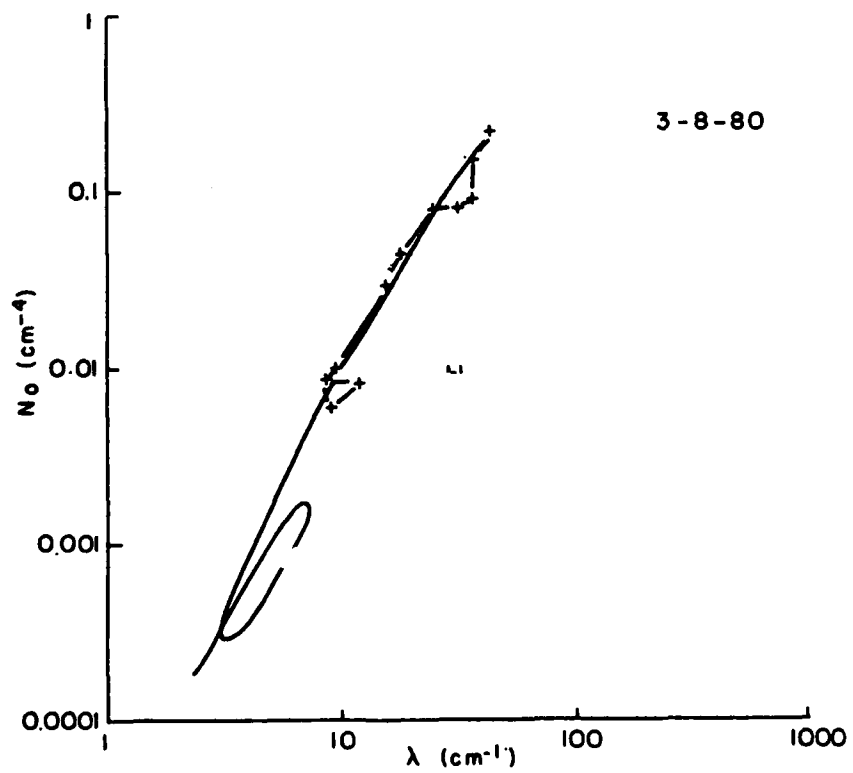


Fig.3.34: Two-parameter model of deposition, aggregation and rime-splintering, 8 March, 1980

	$N_0$	$\lambda$	$n'$	a	b	E	d	splinter prod. rate	depletion rate
Spiral 1	0.1	10	2	100	0.15	1	$2.4 \times 10^{-3}$	$1.05 \times 10^{-4} / \text{cm}^3 / \text{sec}$	$6.94 \times 10^{-5} / \text{cm}^3 / \text{sec}$
Spiral 2	0.04	10	1	100	0.15	1	$2.4 \times 10^{-3}$	$2.10 \times 10^{-5} / \text{cm}^3 / \text{sec}$	$1.11 \times 10^{-5} / \text{cm} / \text{sec}$
Spiral 3	0.006	10	0.2	100	0.15	1	$2.4 \times 10^{-3}$	$6.30 \times 10^{-7} / \text{cm}^3 / \text{sec}$	$2.50 \times 10^{-7} / \text{cm} / \text{sec}$

Table 3.5: Splinter production rates by rime-splintering and particle depletion rates by aggregation

Fig.	Date	a	b	$\alpha$	$\beta$	E	w	Change in Conc
29	2-25-80	100	0.15	0.002	2.05	1	10	$2.5 \times 10^{-3}$
30	2-26-80	100	0.15	0.002	1.25	1	10	$5.0 \times 10^{-4}$
31	3-08-80	100	0.15	0.002	0.75	1	10	$1.5 \times 10^{-5}$

Table 3.6: Values of parameters used in aggregation-deposition-rime splintering simulations (c.g.s. units)

### 3.6.2 Three-parameter formulation

In a three-parameter formulation, three moment conservation equations are derived. This means that the changes of the total particle concentration, the total mass and the total radar reflectivity factor are being completely controlled by the model. This makes the three-parameter formulation ideal to study the effect of rime-splintering, which affects only the total particle concentration without affecting the total mass and the total radar reflectivity factor. A three-parameter formulation with the physical processes of vapor deposition, aggregation and rime-splintering results in the following equations.

The change of particle concentration flux is given by

$$\frac{\partial N_f}{\partial t} = - \frac{N_x^2 \pi E a}{2 \lambda_*^{b+\sigma+4}} \int_0^\infty \int_0^\infty x^\sigma y^\sigma (x+y)^2 |x^b - y^b| e^{-(x+y)} dx dy + \frac{E_i \pi a \kappa' N_x P(b+\sigma+3)}{\lambda_*^{b+\sigma+3}} \quad (3.75)$$

where the first term on the right hand side is the depletion of particles due to aggregation and the second term is from (3.61) and is the production of particles due to rime-splintering. The other two moment conservation equations are similar to those presented earlier except that collisional breakup is being ignored. The derivation results in two implicit equations in  $\lambda_*$  and  $\sigma$ ,

$$\begin{aligned}
\frac{\partial \lambda_2}{\partial h} = & - \frac{\left(\frac{\partial \lambda_1}{\partial h}\right) \lambda_2}{\lambda_1 \beta} - \frac{\lambda_2}{\beta \Gamma(b+\sigma+1)} \left[ \int_0^\infty x^{b+\sigma} \ln x e^{-x} dx \right] \frac{\partial \sigma}{\partial h} \\
& + \frac{\lambda_2}{\beta \Gamma(b+\beta+\sigma+1)} \left[ \int_0^\infty x^{b+\beta+\sigma} \ln x e^{-x} dx \right] \frac{\partial \sigma}{\partial h} \\
& - \frac{\frac{\pi}{2} E \chi_1 \lambda_2^{b+\beta-1} I_1}{2 a \alpha \beta \Gamma(b+\sigma+1) \Gamma(b+\beta+\sigma+1)} \\
& + \frac{E_1 \pi \eta' \Gamma(b+\sigma+3)}{\lambda^2 \beta \Gamma(b+\sigma+1)} \tag{3.76}
\end{aligned}$$

and

$$\begin{aligned}
\frac{\partial \sigma}{\partial h} = & \frac{\int_0^\infty x^{b+2\beta+\sigma} \ln x e^{-x} dx}{\Gamma(b+2\beta+\sigma+1)} \\
& + \frac{\int_0^\infty x^{b+\sigma} \ln x e^{-x} dx}{\Gamma(b+\sigma+1)} \\
& - \frac{2 \int_0^\infty x^{b+\beta+\sigma} \ln x e^{-x} dx}{\Gamma(b+\beta+\sigma+1)} \\
= & \frac{2 \left(\frac{\partial \lambda_1}{\partial h}\right)}{\lambda_1} \left[ 1 + \frac{\Gamma(b+\beta+\sigma+1) \Gamma(\beta+\sigma+2)}{\Gamma(b+2\beta+\sigma+1) \Gamma(\sigma+2)} \right] \\
& - \frac{\frac{\pi}{2} E \chi_1 \lambda_2^{b+\beta-2} I_1}{2 a \alpha \Gamma(b+\sigma+1) \Gamma(b+\beta+\sigma+1)} \tag{3.77} \\
& + \frac{\frac{\pi}{2} E \chi_1 \lambda_2^{b+\beta-2} I_3}{a \alpha \Gamma(b+2\beta+\sigma+1) \Gamma(b+\beta+\sigma+1)} \\
& + \frac{E_1 \pi \eta' \Gamma(b+\sigma+3)}{\lambda^2 \Gamma(b+\sigma+1)}
\end{aligned}$$

where  $I_1$  and  $I_3$  are from (3.29) and (3.31).

In the computations, the values of  $n'$ , the concentration of droplets, is taken from the ASSP concentration of particles greater than 24 microns. The values of the other parameters are identical to those listed in Table 3.4. The results using the parameter values of the 25 Feb., 1980 case are plotted in Figs. 3.35-3.37. The computed evolution of  $N_d$ ,  $\lambda_d$  and  $\sigma$  do not match the observations desirably, especially for  $\sigma$ . The predicted  $\sigma$  is first negative, then positive and then negative again, while the observational value of  $\sigma$  is first negative and then positive.

In the computations of this deposition, aggregation and rime-splintering model using the condition of the 8 March, 1980 case, it is found that  $\lambda_d$  will become close to zero. When it does that, the computations become numerically unstable. In order to circumvent this problem the calculations are performed using a deposition, aggregation, collisional breakup and rime-splintering. The model is computed twice. The first time uses the observed value of  $n'$ , the number density of droplets greater than 24 microns and a small value of the breakup parameter,  $c = 0.005$  (Figs. 3.38, 3.40 and 3.42). The reason for using a small value of  $c$  is that on the one hand, the effect of breakup will not overshadow the effect of rime-splintering, while on

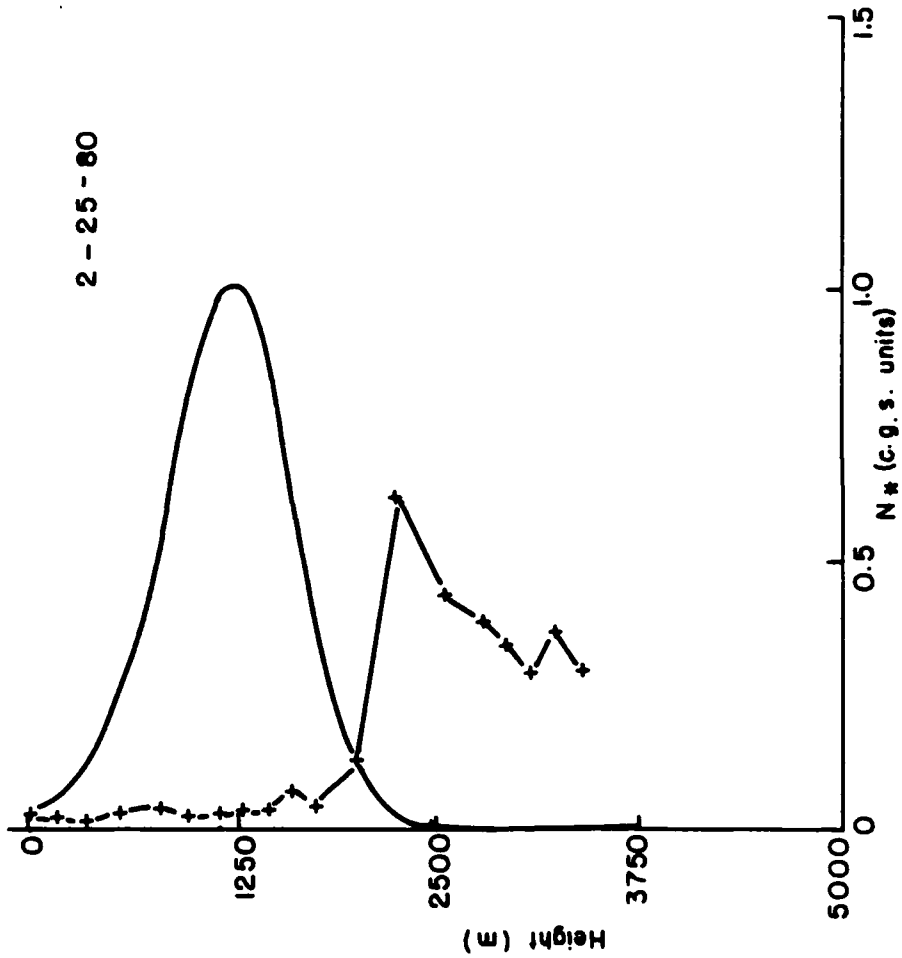


Fig. 3.35:  $N_*$  from three-parameter model of deposition, aggregation and rime-splintering, 25 February, 1980

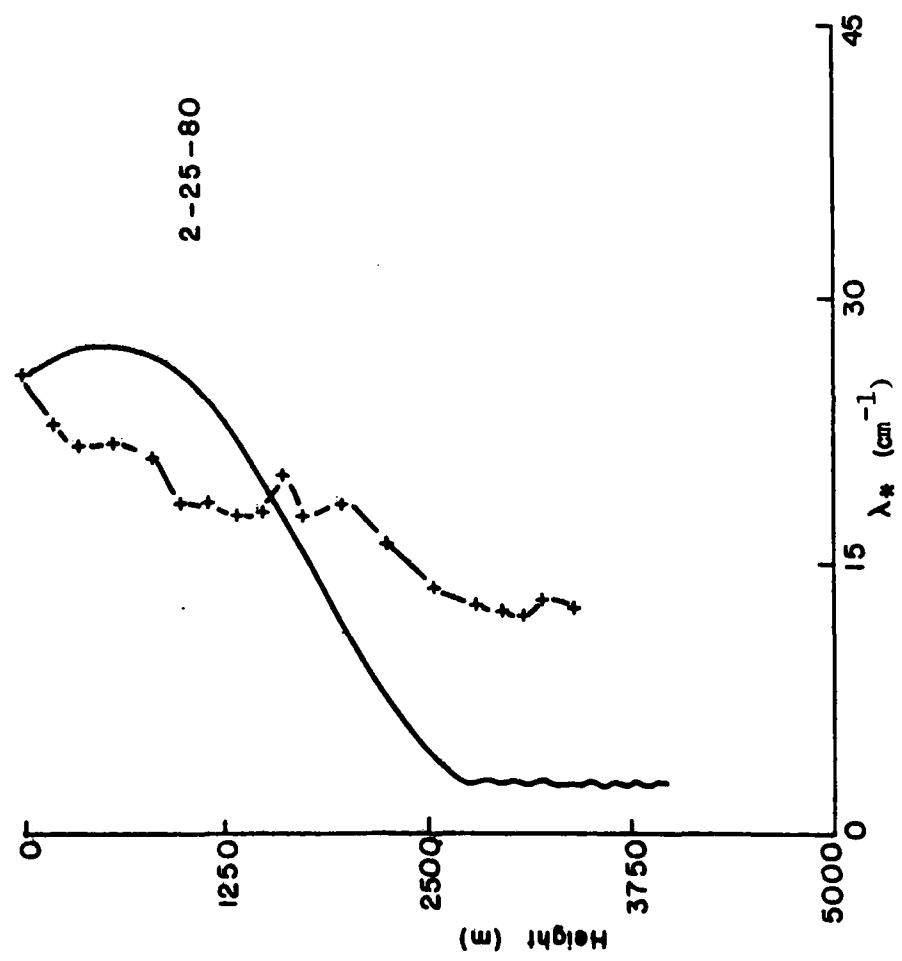


Fig. 3.36:  $\lambda_*$  from three-parameter model of deposition, aggregation and rime-splintering, 25 February, 1980

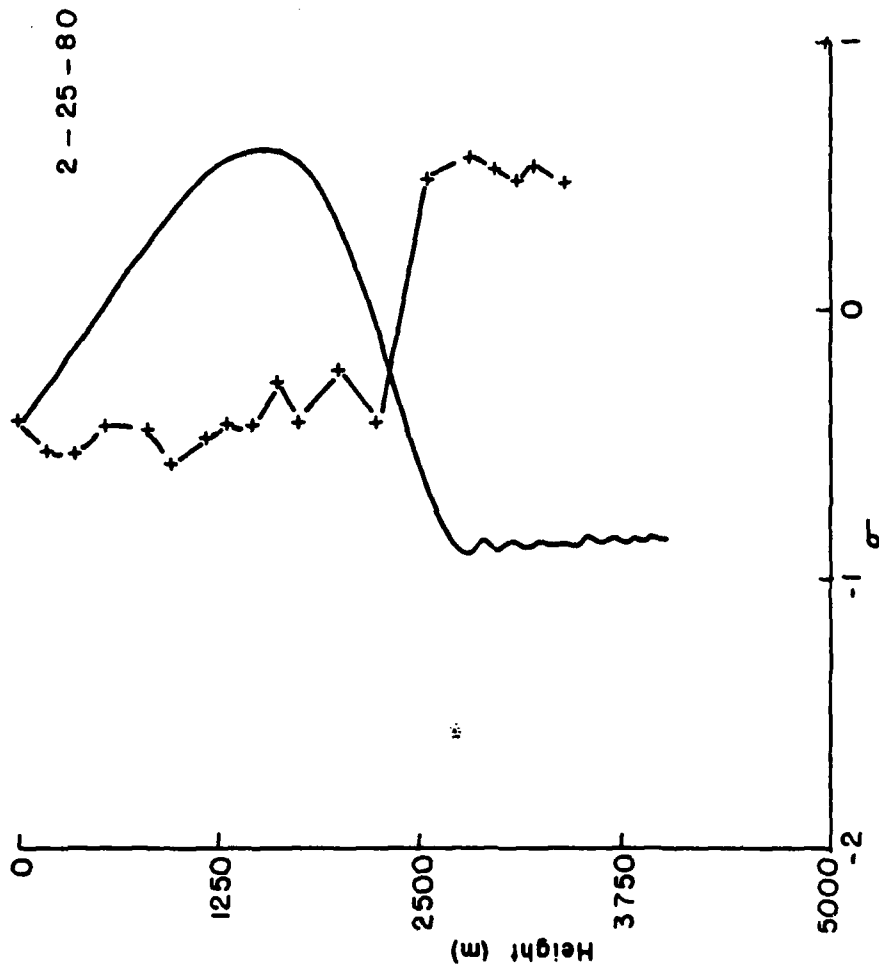


Fig.3.37:  $\sigma$  from three-parameter model of deposition, aggregation and rime-splintering, 25 February, 1980

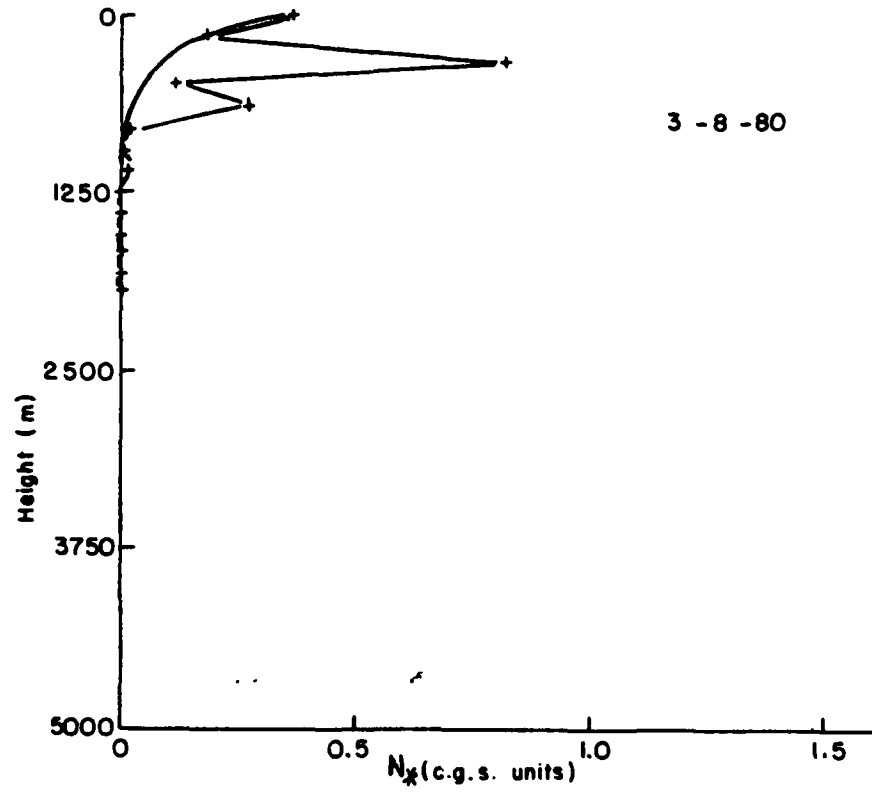


Fig.3.38:  $N_*$  from three-parameter model of deposition, aggregation and rime-splintering with weak breakup, 8 March, 1980

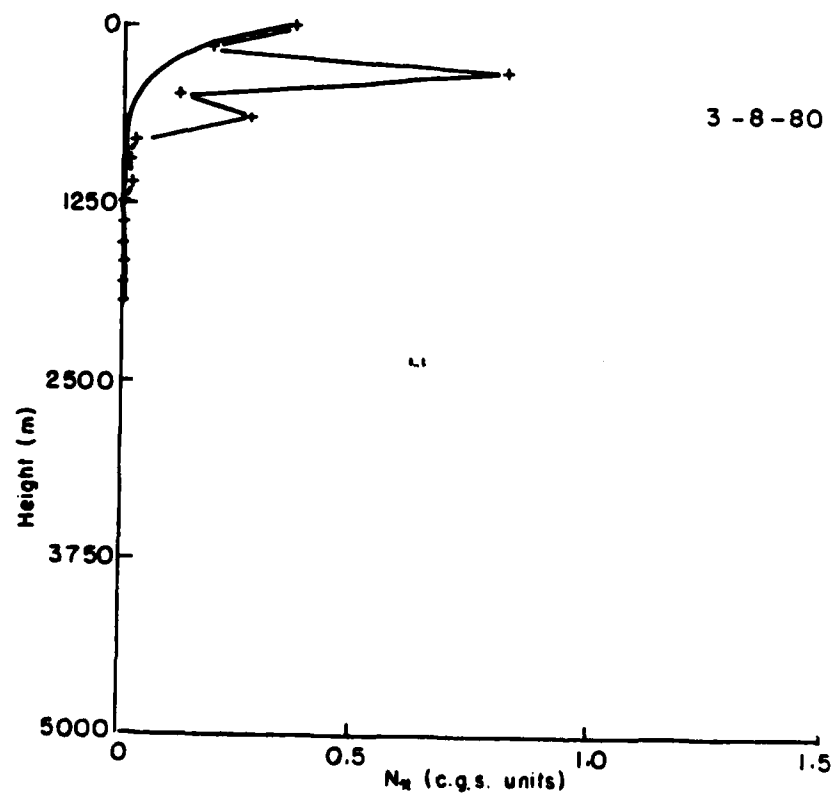


Fig.3.39: Similar to Fig.3.38 but with no rime-splintering

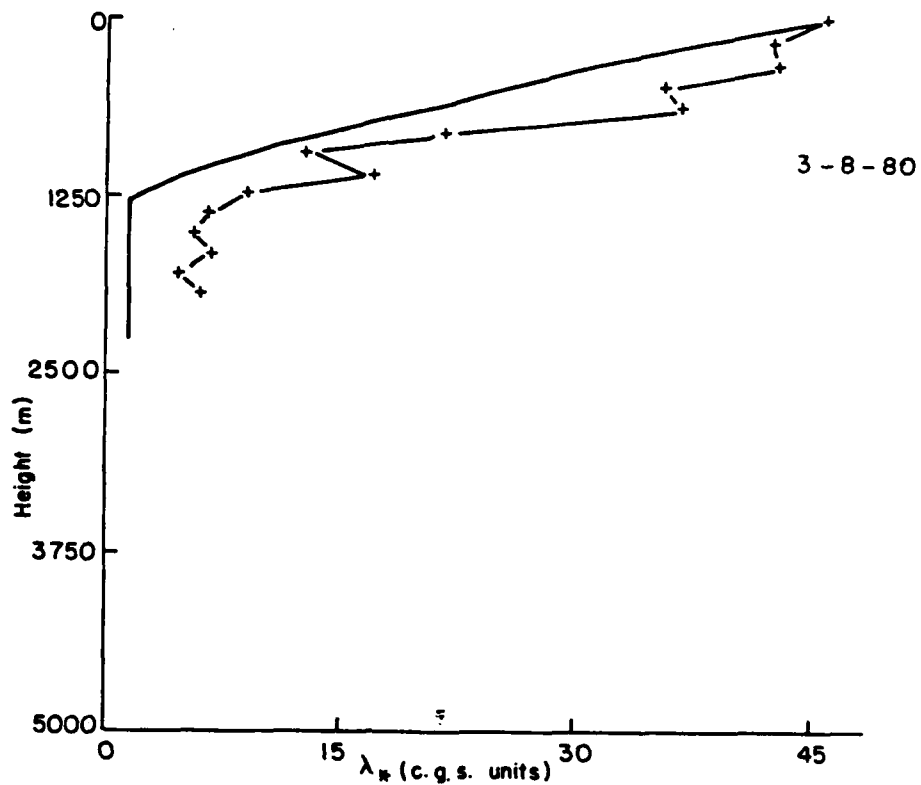


Fig.3.40:  $\lambda_*$  from three-parameter model of deposition, aggregation and rime-splintering with weak breakup, 8 March, 1980

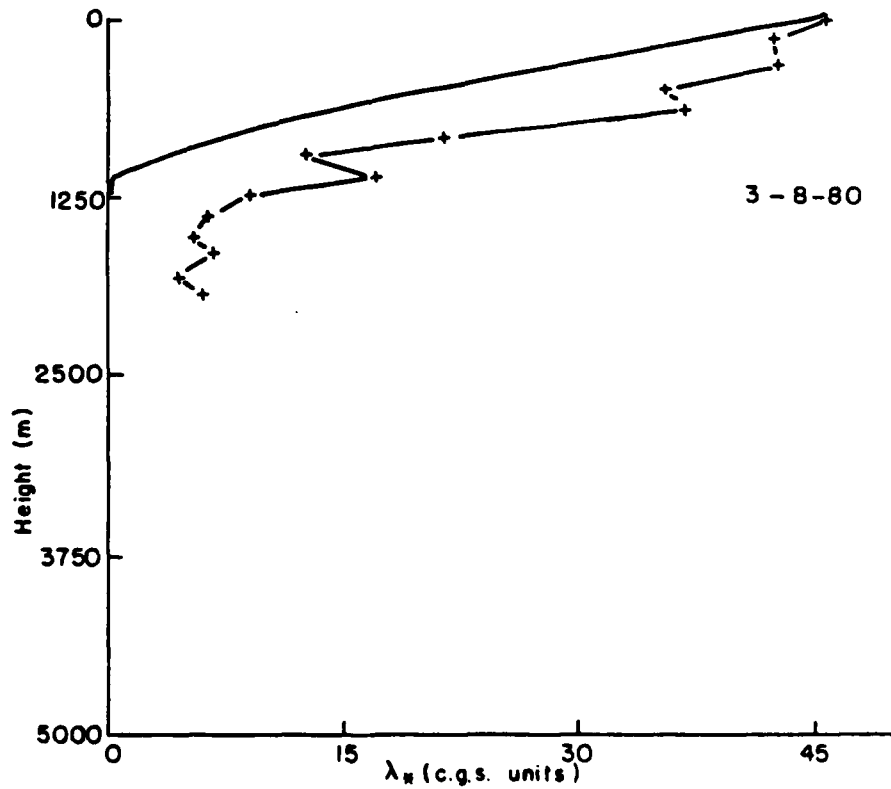


Fig.3.41: Similar to Fig.3.40 but with no rime-splintering

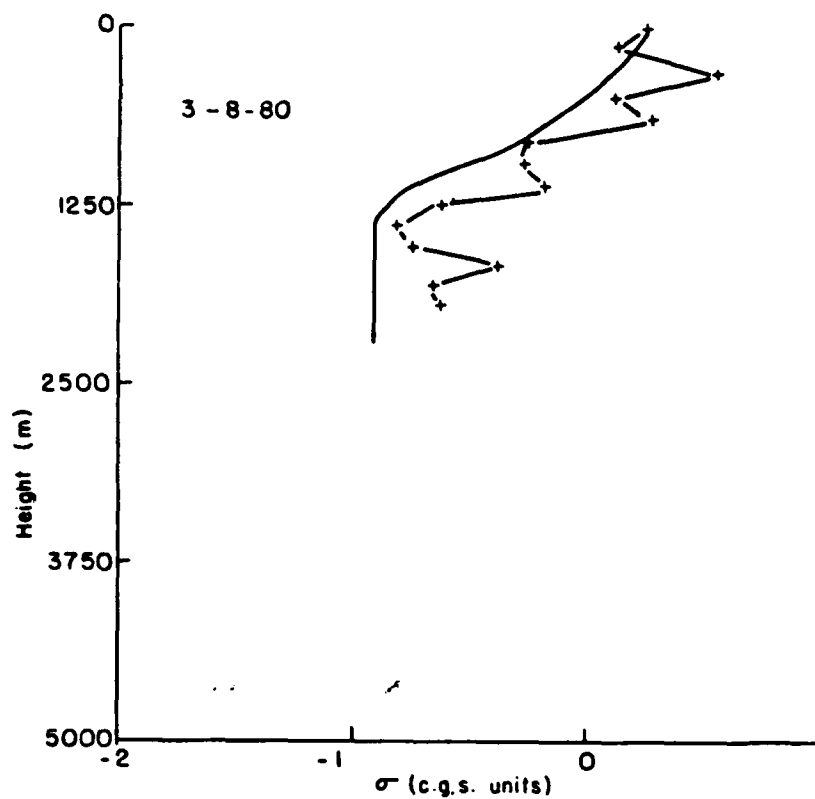


Fig.3.42:  $\sigma$  from three-parameter model of deposition, aggregation and rime-splintering with weak breakup, 8 March, 1980

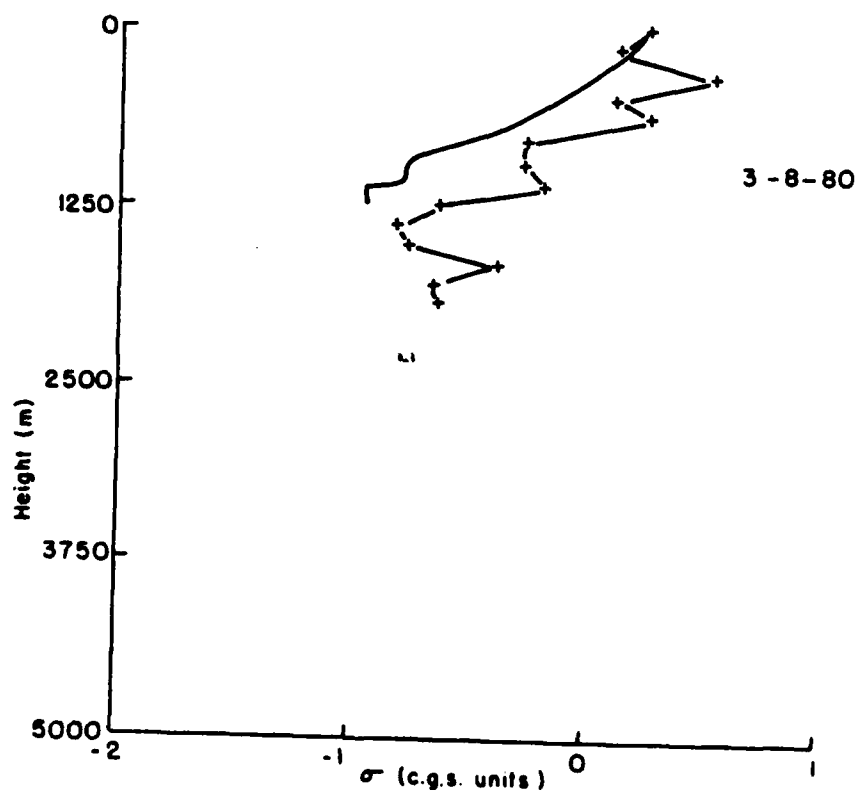


Fig.3.43: Similar to Fig.3.42 but with no rime-splintering

the other hand, the effect of breakup will prevent  $\lambda_z$  from becoming too small, thus causing numerical instability. The second computation is done with  $n' = 0$  and  $c = 0.005$  (Figs. 3.39, 3.41 and 3.43). The results from the two computations are then compared with each other and with the observations. By doing this comparison, the effect of rime-splintering can be seen. The results from the two computations show that rime-splintering has a slight effect on the evolution of  $\lambda_z$  and  $\sigma$  but the effect is not adequate to explain the evolution depicted in the observations.

### 3.7 Effects of melting

The evolution of snow-size spectra to rain-size spectra due to melting can be studied by assuming that all moment fluxes are conserved during melting. This is equivalent to saying that the terms on the right hand side of (3.1) are identically zero. For a two-parameter formulation, the conservation of mass flux is represented by,

$$\int_0^{\infty} a_s D^{b_s} \alpha D^{\beta} N_s e^{-\lambda_s D} dD = \int_0^{\infty} a_r D^{b_r} \frac{\pi}{6} \rho D^3 N_r e^{-\lambda_r D} dD \quad (3.78)$$

where the subscript s refers to snow and the subscript r refers to rain and  $a$ ,  $b$ ,  $\alpha$  and  $\beta$  are the same notations as in (3.20) and (3.21). The conservation of radar reflectivity flux is represented by,

$$\int_0^{\infty} a_s D^{b_s} \left( \frac{\alpha D^{\beta}}{\frac{1}{2} \rho} \right) N_s e^{-\lambda_s D} dD = \int_0^{\infty} a_r D^{b_r} D^6 N_r e^{-\lambda_r D} dD \quad (3.79)$$

Then,  $N_r$  and  $\lambda_r$  are

$$N_r = \frac{N_s a_s \alpha \lambda_r^{b_r+4} \Gamma(b_s+\beta+1)}{a_r \frac{1}{2} \rho \lambda_s^{b_s+\beta+1} \Gamma(b_r+4)} \quad (3.80)$$

$$\lambda_r = \left[ \lambda_s^{\beta} \frac{\frac{1}{2} \rho \Gamma(b_s+\beta+1)}{\alpha \Gamma(b_s+2\beta+1)} (b_r+6)(b_r+5)(b_r+4) \right]^{1/3} \quad (3.81)$$

Among the data from the spirals, there is only one case in which observations were made where snow had been completely melted. The data in this case, which is the second spiral on 17 April, 1981, is used to test the effect of melting on the spectrum. Using (Locatelli and Hobbs, 1974; Rogers, 1979 and in c.g.s. units)  $a_s = 100$ ,  $b_s = 0.15$ ,  $a_r = 1421$ ,  $b_r = 0.5$ ,  $\alpha = 0.002$ ,  $\beta = 2$ , the theoretically derived values for the melted spectrum can be computed. Fig. 3.44 shows the two-parameter fit to the observed spectra before and after melting. The spectrum predicted from theory is also plotted for comparison. The slope of the observed melted spectrum is shallower than the slope from theory while the intercepts are almost the same. The observed mass flux is about twice that of the computed mass flux. By varying the values of the parameters, it is found that the mass flux is rather sensitive to  $a_s$ , the fallspeed coefficient. If  $a_s = 250$  is used, the computed mass flux is more comparable to the observed value. This might suggest that the terminal fallspeed of the type of snow

immediately above the freezing level is larger. The computed spectrum from using  $a_s = 250$  is also plotted on Fig. 3.44. Comparing this spectrum with the observed one, it can be deduced that during melting, aggregation is more efficient than breakup. Thus small drops are depleted and large drops formed.

For a three-parameter formulation, the conservations of concentration flux, mass flux and radar reflectivity flux are given by,

$$\int_0^{\infty} a_s D^{b_s} N_s e^{-\lambda_s D} D^{\sigma_s} dD = \int_0^{\infty} a_r D^{b_r} N_r e^{-\lambda_r D} D^{\sigma_r} dD \quad (3.82)$$

$$\begin{aligned} \int_0^{\infty} a_s D^{b_s} \alpha D^{\beta} N_s e^{-\lambda_s D} D^{\sigma_s} dD \\ = \int_0^{\infty} a_r D^{b_r} \frac{\pi}{6} \rho D^3 N_r e^{-\lambda_r D} D^{\sigma_r} dD \end{aligned} \quad (3.83)$$

$$\begin{aligned} \int_0^{\infty} a_s D^{b_s} \left( \frac{\pi D^{\beta}}{6 \rho} \right)^2 N_s e^{-\lambda_s D} D^{\sigma_s} dD \\ = \int_0^{\infty} a_r D^{b_r} D^6 N_r e^{-\lambda_r D} D^{\sigma_r} dD \end{aligned} \quad (3.84)$$

Then  $N_r$ ,  $\lambda_r$  and  $\sigma_r$  are obtained by,

$$N_r = \frac{N_s a_s \lambda_r^{b_r + \sigma_r + 1} \Gamma(b_s + \sigma_s + 1)}{a_r \lambda_s^{b_s + \sigma_s + 1} \Gamma(b_r + \sigma_r + 1)} \quad (3.85)$$

$$\lambda_r = \left[ \lambda_s^{\beta} \frac{\pi}{6 \alpha} \rho \frac{\Gamma(b_r + \sigma_r + 4) \Gamma(b_s + \sigma_s + 1)}{\Gamma(b_r + \sigma_r + 1) \Gamma(b_s + \beta + \sigma_s + 1)} \right]^{1/3} \quad (3.86)$$

$$\frac{\Gamma(b_s + 2\beta + \sigma_s + 1)}{\Gamma^2(b_s + \beta + \sigma_s + 1)} = \frac{(b_r + \sigma_r + 6)(b_r + \sigma_r + 5)(b_r + \sigma_r + 4)}{(b_r + \sigma_r + 3)(b_r + \sigma_r + 2)(b_r + \sigma_r + 1)} \quad (3.87)$$

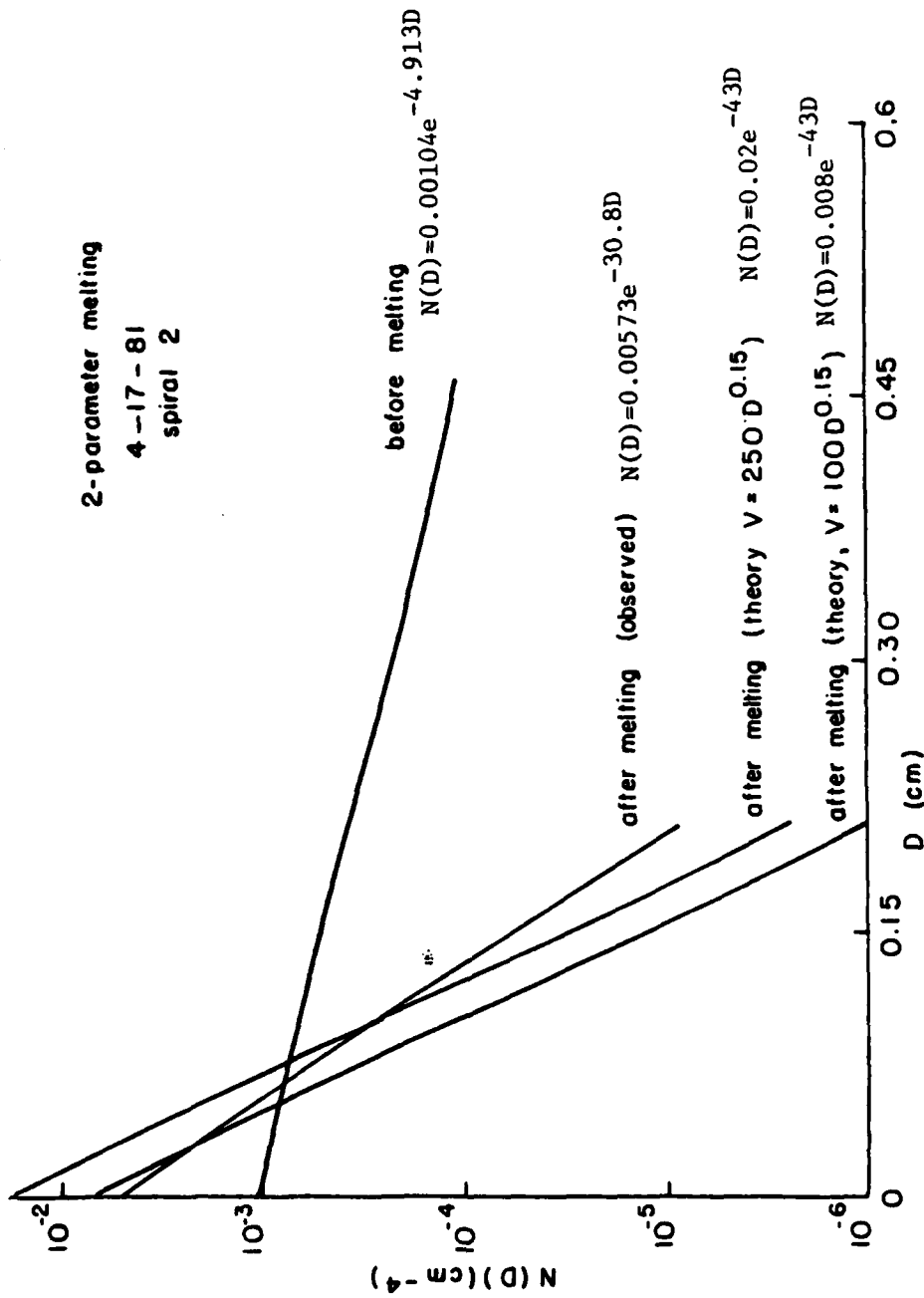


Fig.3.44: Two-parameter fit to melting

Fig. 3.45 shows the three-parameter spectra before and after melting. The results are similar to those obtained from the two-parameter formulations. Again the physical implications from these results are similar to those obtained from the two-parameter analyses. It is interesting to see that during melting, the resulting raindrop size spectrum is always subexponential.

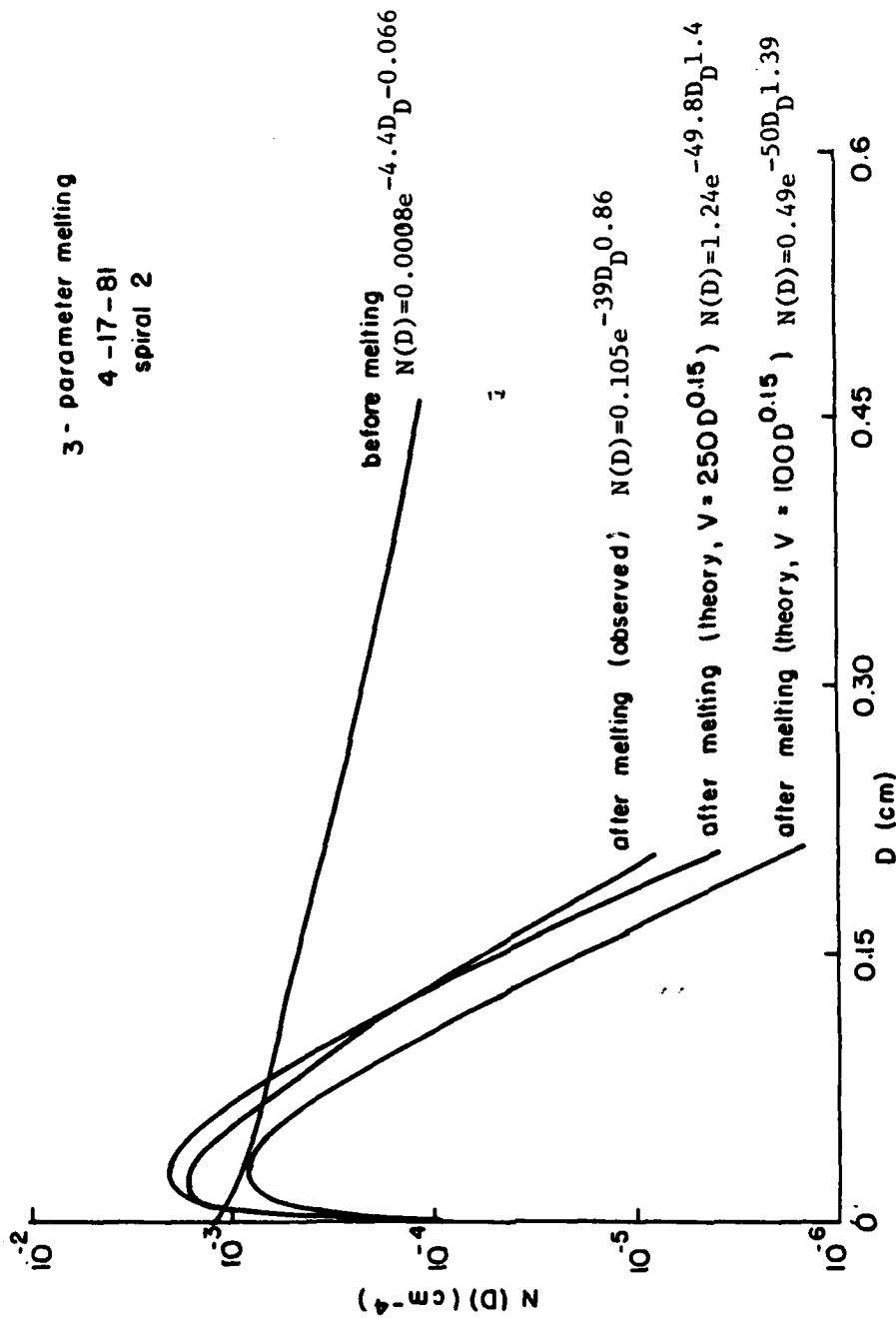


Fig.3.45: Three-parameter fit to melting

## CHAPTER 4

## CONCLUSIONS

Both the observational data and the theoretical models indicate clearly that snow growth goes through three distinct processes, vapor deposition stage, aggregation stage and a secondary production stage. Initially when most of the snow particles are small, they tend to grow by water vapor depositing directly onto them. By the time some of the particles grow to large enough sizes, thus increasing the collisional probability, aggregation sets in. Aggregation causes the depletion of small particles and the increase in large particles. The average size of snow particles therefore increases rapidly.

The third stage of snow growth is the secondary production stage. There has been much discussion on what causes the secondary production. There are two hypotheses, namely rime-splintering and collisional breakup. An important ingredient of rime-splintering is supercooled liquid water. The observational data indicate that supercooled liquid water is present in two of the three

flights considered and is absent in the other flight. But, the secondary production stage is still observed in all three flights. Moreover, in the flights when supercooled liquid water is observed, the occurrence of supercooled liquid water is rare and apparently not correlated with any particular stage of snow growth. Since the secondary production stage can occur even in the absence of supercooled liquid water, rime-splintering is unlikely to be a significant candidate for causing secondary production. On the other hand, the fact that the onset of the secondary production stage causes the snow-size spectra to have an equilibrium slope is indicative of collisional breakup. Physically, aggregation of snow particles increases the sizes of the particles. But, when the particles become too big, they become more fragile. Thus they tend to break up upon collisions.

Theoretical investigations produce similar conclusions. Theoretical models with the processes of vapor deposition, aggregation and collisional breakup give results comparable to the observational data, while theoretical models with the processes of vapor deposition, aggregation and rime-splintering fail to give results similar to the data. Therefore, both theory and observation point out the importance of collisional breakup in snow growth. From the formulations of the collisional breakup term in the theory and the results of the laboratory experiment, it can be

concluded that when two snow particles collide, they are more likely to aggregate than to break up. However, when they do break up, they generate fragments distributed in a somewhat negative exponential manner; the larger the parent particles, the more numerous the fragments. Another important finding in the theoretical studies is that crystal types need not be taken into account in order to produce the different stages of snow growth, although from the 2-D data it is evident that different crystal types dominate at different stages.

Data from two of the spirals indicate that when the atmosphere is subsaturated, evaporation of the particles will prohibit the occurrence of an equilibrium distribution slope. A possible explanation is that the number of large particles is being maintained by aggregation, while collisional breakup generates minute particles that are not detectable by the 1-D precipitation probe. Under conditions of deposition, these small particles will grow into detectable sizes, but, under conditions of subsaturation, these small particles not only cannot grow into detectable sizes, but rather they are evaporated. This causes the spectrum to become 'flatter' and so the slope will decrease below the  $10 \text{ cm}^{-1}$  limit observed in the other spirals. Since only the data from two spirals, both taken on the same day, are available, this finding can be considered to be preliminary. More investigations of snow

growth in subsaturated conditions are needed.

The theoretical models show that increasing the initial concentration without increasing the initial mass (physically equivalent to seeding) causes the onset of the aggregation stage of snow growth to start slightly earlier but delays the onset of the third stage by a more significant amount. Physically the increase in concentration without increasing the mass means that the number of collisions increases. Therefore, the aggregation stage starts earlier. On the other hand, increasing the concentration without increasing the mass means that the average size of particles is smaller. So, it would take longer for them to grow to such a size that collisional breakup becomes efficient. Since neither aggregation nor collisional breakup affects the total mass, so the final slope does not change.

The three-parameter negative exponential, power law size distribution provides a more sophisticated but yet analytically feasible method of describing snow size spectra. This new formulation enables the investigator to have one more degree of freedom in the analysis. The difficulty in using this formulation lies in the instrumentation because there is a great discrepancy between the particle concentration measured by the 1-D cloud probe and the 1-D precipitation probe. A three-parameter analysis of data is

very sensitive to the small end of particle distribution. When the discrepancy between the cloud probe and the precipitation probe is resolved, the three-parameter formulation will become very useful.

When shown in the  $N_0 - \lambda$  space, it is seen that at the third stage of snow growth, the different cases all have the same slope but different intercepts. The differences in intercept are obviously tied to the precipitation rate and are possibly due to the different dynamical conditions.

The studies here make no attempt to explain the initial nucleation of snow particles. For instance, the theoretical model assumes a certain snow-size distribution as initial condition. A full model of snow growth should really start out with primary nucleation. Unfortunately, the current state of ice nucleation is still not adequate to provide enough insight to incorporate this into these models.

It would be good if different investigators could obtain similar data from various types of winter-storms so as to provide a climatology of snow-growth processes. This could facilitate the study of the microphysical processes associated with different storm dynamics. Future studies of snow growth processes can be pursued by using the 2-D data quantitatively. Right now, investigators who use the 2-D

data tend to reduce the 2-D data to 1-D. Perhaps, another approach is to express snow-size distribution as a function of area,  $f(A)dA$ , instead of the conventional function of diameter,  $f(D)dD$ .

## The Growth of Snow in Winter Storms: An Airborne Observational Study

K. KENNETH LO AND RICHARD E. PASSARELLI, JR.

*Massachusetts Institute of Technology, Department of Meteorology and Physical Oceanography, Cambridge 02139*

(Manuscript received 4 May 1981, in final form 28 October 1981)

### ABSTRACT

In studies of precipitation growth, comparisons between theory and observation are difficult because of the problem in obtaining a complete 4-dimensional (space and time) description of the kinematic, thermodynamic and microphysical properties of the atmosphere. A new flight plan has been devised which permits one to observe the height evolution of snow-size spectra in a reference frame where the effects of horizontal gradients and temporal changes are minimized. The flight plan, termed the advecting spiral descent (ASD), requires an aircraft to start aloft in a mesoscale precipitation area and then spiral downward in a constant bank angle, descending at approximately the mean fallspeed of snow. Qualitative comparisons between ASD observations and particle growth theory suggest that snow evolves through at least three stages characterized by deposition, aggregation and breakup. The breakup process serves to limit the number of large snow particles and interacts with aggregation to produce a limiting value of the slope of the snow-size spectrum.

### 1. Introduction

The ultimate test of a theoretical model of a physical process is how well the model can describe the natural occurrence of the process. In studies of precipitation growth, such comparisons are difficult because of the problem in obtaining a complete 4-dimensional (space and time) description of the kinematic, thermodynamic and microphysical properties of the atmosphere. The rather detailed descriptions of the atmosphere obtained from microphysical/dynamical models are typically beyond our observational capability for verification.

The theoretical modeling of snow growth by one of the authors (Passarelli, 1978a,b) raised the question of how to verify the model results using measurements of snow-size spectra obtained by a single aircraft equipped with laser imaging probes. In this paper we present a flight plan which permits one to observe the height evolution of snow-size spectra in a reference frame where the effects of horizontal gradients and temporal changes are minimized. The aircraft is constrained to drift with a region of falling snow in a Lagrangian frame of reference tied to the average particle motion. The height evolution of the size distribution of snow then reduces to a simple 1-dimensional steady-state problem so that a single aircraft can provide sufficient data for comparison with results from 1-dimensional microphysical models.

First, we present a simple sedimentation model of falling snow to provide the physical rationale behind the flight plan, followed by a description of the aircraft flight track. Several examples of data are given

along with a physical interpretation of the results. A detailed quantitative comparison between theory and observation will be presented in a later paper.

The results show that snow growth is a well-behaved phenomenon whose evolutionary processes can, to a large extent, be observed with current instrumentation. Snow growth is apparently dominated initially by deposition, followed by aggregation and then breakup. The results suggest that an aggregation-breakup equilibrium is acting to produce a limiting value of the slope of the size distribution of snow.

### 2. The physical rationale behind the sampling procedure

The change in the size distribution of snow at any point in time and space is governed by advection (air motion and particle fallspeed), primary particle growth (deposition or evaporation and riming of supercooled drops), the redistribution of mass within the size distribution (aggregation and breakup) and the production of new ice particles (nucleation). The question addressed here is whether a single aircraft can sample the atmosphere in such a way so as to separate the effects of advection from these microphysical processes.

Perhaps the most desirable situation for a single aircraft study of snow growth is that of widespread, steady-state snow. In the absence of horizontal gradients, horizontal advective processes make no contribution to changes in the size distribution. An aircraft can merely sample the atmosphere at various heights, at leisure, provided that conditions are

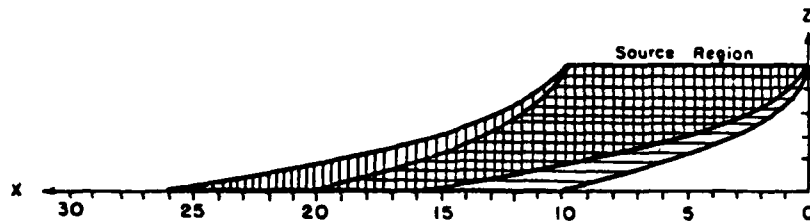


FIG. 1. Particle trajectories from steady-state line source, scales in km.

steady. The particle growth can then be inferred from the height change in the size distribution. Unfortunately, even in widespread storms there are usually mesoscale areas of precipitation which move and change with time. Horizontal gradients in the properties of the atmosphere coupled with the effects of advection, fallspeed dispersion and wind shear create a difficult sampling problem even if conditions are steady.

To illustrate this, consider a simple two-dimensional sedimentation model of a finite, horizontally homogeneous, steady, line source of snow aloft which is 10 km wide and located 5 km above the earth's surface in an atmosphere having constant shear (e.g., Marshall, 1953). We assume that no particle growth occurs and that updrafts are weak compared to fallspeeds. A particle starting from the source at height ( $Z_0$ ) will fall and be deflected from its initial horizontal position ( $X_0$ ) with respect to the source, i.e., the particle trajectory is

$$X = X_0 + \frac{S(Z_0 - Z)^2}{2V_f}, \quad (1)$$

where  $X$  is the horizontal position of the particle with respect to the source,  $S$  the shear,  $Z$  the height below the source and  $V_f$  the fallspeed. Neglecting horizontal gradients in the wind, all particles having the same fallspeed will have parallel trajectories. Fig. 1 is a scale drawing of the precipitation "trails" for two particle fallspeeds ( $80 \text{ cm s}^{-1}$  and  $130 \text{ cm s}^{-1}$ ) assuming a constant wind shear of  $10^{-3} \text{ s}^{-1}$ . Note that the reference frame is fixed to the source. The width of the region occupied by particles of a given fallspeed is always equal to the width at the source. However, because particles of different fallspeeds define different trajectories, size sorting occurs and horizontal gradients develop. The region occupied by

the large ( $130 \text{ cm s}^{-1}$ ) particles is indicated by horizontal hatching and the region occupied by the small ( $80 \text{ cm s}^{-1}$ ) particles is indicated by vertical hatching. The right-hand side of this precipitation trail contains no small particles while the left-hand side contains no large particles. However, the region of overlap for these two fallspeeds has uniform properties which are identical to the source region. If the particle fallspeeds are bounded by these hypothetical limits then the complete size distribution (all fallspeeds) will be constant in the region of overlap. The properties of the snow in the central region in Fig. 1 are identical to those corresponding to an infinite line source aloft.

This example illustrates that for a steady, finite, upper-level source region in which the dynamical and microphysical properties are relatively constant in horizontal space, there will be a limited region below that behaves as if there were an infinite, horizontally-homogeneous source aloft. In this region the effects of horizontal advection can be ignored and snow growth can be treated as a 1-dimensional (height), steady-state problem. Of course the smaller the horizontal gradients, the greater the depth over which this assumption will remain valid.

The problem of temporal variability of the source region can be examined in a similar manner. Let us again consider only two fallspeeds,  $80$  and  $130 \text{ cm s}^{-1}$ , and use the identical geometry and shear as in the previous case. However, let the steady source act for only  $3125 \text{ s}$ . During this time, the small flakes fall  $2.5 \text{ km}$  and the large flakes fall  $4.0 \text{ km}$ . Fig. 2 shows the regions occupied by the two populations after the source terminates at  $3125 \text{ s}$ , and at  $6250 \text{ s}$  when the first small flake hits the ground. After  $3125 \text{ s}$  there is a large region in which the snow has the steady-state properties of the initial source. At  $6250 \text{ s}$ ,  $3125 \text{ s}$  after the source is stopped, there is

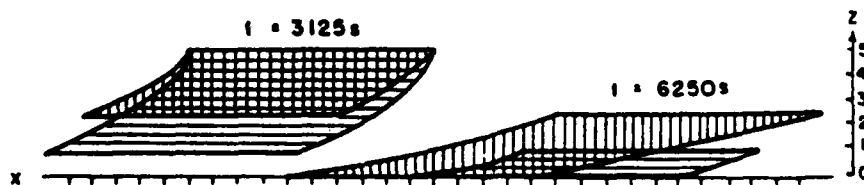


FIG. 2. Particle trajectories from time-dependent line source, scales in km.

still a region close to the surface which has the steady-state properties of the source. Recall that this region also has the properties of a horizontally infinite source.

This example illustrates that for a source which varies slowly in time, there can be a region below that behaves as if the source were infinite and steady. The center of this region falls at a rate equal to the average particle fallspeed. Ideally if one could use an aircraft to follow this region, then the snow growth problem reduces to a 1-dimensional (height) steady-state problem. We will refer to this region as the 1-dimensional region.

The primary assumption in both of these analyses is that the fall-speeds lie between finite limits. Also the lower limit cannot be zero. These are fairly good assumptions for snow since observations show that the fallspeed of snow is only a weak function of particle size. This is particularly true of unrimed crystals and aggregates (e.g., Locatelli and Hobbs, 1974).

To illustrate the narrow dispersion of snowflake fallspeeds we can consider a specific example of an exponential distribution of equivalent melted diameters and a power law fallspeed-melted diameter relationship, i.e.,

$$N(D_m) = N_0 e^{-\lambda D_m}, \quad (2)$$

$$V_f = a D_m^b, \quad (3)$$

where  $N(D_m)\Delta D_m$  is the concentration of particles in the melted diameter interval  $[D_m, D_m + \Delta D_m]$ ,  $N_0$  and  $\lambda$  are the distribution parameters,  $V_f$  is the fallspeed and  $a$  and  $b$  depend on the snowfall type. One can show that the relative dispersion (standard deviation/mean) of the mass flux as a function of fallspeed depends on  $b$  only, i.e.,

$$\frac{\sigma}{\bar{V}} = \left[ \frac{\Gamma(4 + 3b)\Gamma(4 + b)}{\Gamma^2(4 + 2b)} - 1 \right]^{1/2}, \quad (4)$$

where  $\sigma$  is the standard deviation of the mass flux versus fallspeed distribution,  $\bar{V}$  is the mean flux fallspeed and  $\Gamma$  represents the gamma function. For aggregate snow  $b \approx 0.3$  (Langleben, 1954), so that the relative dispersion is only 15%. In the sedimentation examples, we used 80 and 130  $\text{cm s}^{-1}$  as the fallspeed limits. The  $\pm 2\sigma$  fallspeeds are 74 and 137  $\text{cm s}^{-1}$  assuming a mean mass flux fallspeed of 105  $\text{cm s}^{-1}$  and  $b = 0.3$ . Thus for snow, the vast majority of the mass flux is contained within a narrow range of fallspeeds.

Summarizing the discussion of the simple sedimentation models we can say that there is a region below a time-dependent, horizontally finite source which behaves as if the source were steady and infinite. The sampling scheme suggested by these analyses is to start at the center of such a source region and then follow the motion of an "average" particle as it falls and is advected by the horizontal wind.

Observations of the particle-size distribution in this reference frame can then be interpreted by means of a 1-dimensional (height), steady-state model of particle growth.

The technique is likely to succeed in regions of large-scale winter storms in which vertical air velocities, horizontal gradients and temporal variations are small. If these conditions prevail then there is usually very little, if any supercooled water so that riming growth is not significant (e.g., Passarelli, 1978b; Herzegh and Hobbs, 1980). The precipitation is in the form of snow and ice crystals, and nucleation, deposition, aggregation and possibly breakup are the microphysical processes which can act to change the size distribution.

### 3. The aircraft flight track

#### a. Flight procedure

Having defined an optimal region for studying snow growth in the natural atmosphere, we propose the following flight profile for sampling with a single aircraft. Starting aloft in a mesoscale precipitation area, the aircraft is placed in a constant bank angle ( $\sim 15^\circ$ ) and a constant descent rate ( $\sim 1 \text{ m s}^{-1}$ ). The aircraft spirals downward at approximately the mean fallspeed of snow and the loops of the spiral drift with the wind. Ideally, if conditions are quasi-steady and the properties of the atmosphere are fairly uniform over a length scale somewhat larger than the diameter of the loops, then the aircraft will remain in a 1-dimensional region. We call this flight track the advecting spiral descent (ASD).

An important advantage of the ASD in sampling a 1-dimensional region is that one does not require an *a priori* knowledge of the vertical wind profile. The aircraft adjusts automatically to the wind shear since the loops of the spiral are flown relative to the air (bank angle constant) rather than relative to the ground. In principle, knowing the wind as a function of height and an average fallspeed one could construct a series of horizontal passes which would accomplish the same task, but the procedure is relatively complex in four-dimensions as compared to the ASD approach.

The analysis of particle size spectra sampled via the ASD technique can be performed by averaging spectra over a complete loop of the spiral. A loop is defined as when the aircraft completes a  $360^\circ$  turn. This serves to average any horizontal inhomogeneities. Ideally, one would like horizontal inhomogeneities to be minimal over the radius of the loops.

Another approach is to compare particle size spectra at various heights which occurred in the same sector of different loops (e.g., using magnetic heading). Ideally, if all the loops are the same size and the aircraft performs a  $1 \text{ m s}^{-1}$  ASD, then each point

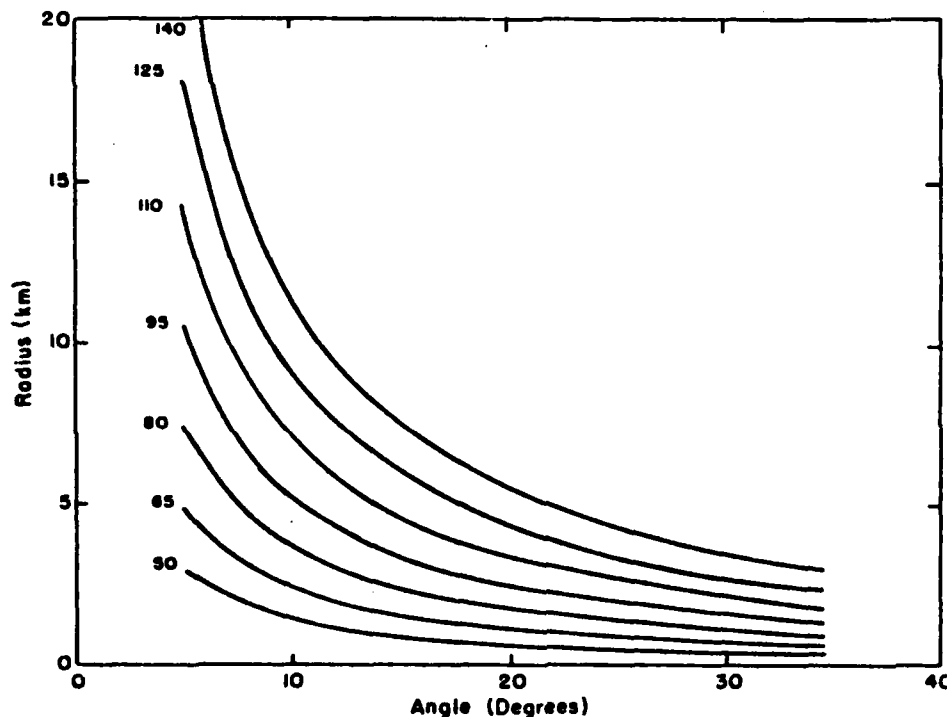


FIG. 3. Turn radius as a function of bank angle for various true air speeds. Air speeds in  $\text{m s}^{-1}$ .

of the aircraft trajectory corresponds to the trajectory of a  $1 \text{ m s}^{-1}$  particle. After turning  $360^\circ$  (completing the next loop) the aircraft should encounter the same  $1 \text{ m s}^{-1}$  particle at a lower altitude. This is stretching the technique to the ultimate limit. In practice, as discussed in the next section, the loops get smaller as the aircraft descends so that the aircraft does not actually re-encounter the same  $1 \text{ m s}^{-1}$  particle. Nevertheless, the observed point-to-point correlations can be quite high as we shall show.

#### b. The ASD flight characteristics

During a coordinated turn at a constant bank angle, the aerodynamic lift, gravitational and centrifugal forces are balanced. One can show that the radius of a turn,  $r$  is

$$r = \frac{(\text{TAS})^2}{g} \cot\theta, \quad (5)$$

where TAS is the aircraft true air speed,  $\theta$  is the bank angle and  $g$  is the gravitational acceleration. The turn radius as a function of bank angle for various true air speeds is plotted in Fig. 3. During a descent, a pilot will usually maintain a constant indicated air speed (IAS) which is related to the true air speed by

$$\rho_0(\text{IAS})^2 = \rho(\text{TAS})^2, \quad (6)$$

where  $\rho_0$  is the density of air at a standard temper-

ature and pressure ( $0^\circ\text{C}$  and  $1013 \text{ mb}$ ) and  $\rho$  is the actual air density. In a descent where the bank angle and indicated air speed remain constant, the true air speed is less at lower levels and the radius of the loops decreases in accordance with

$$r = \frac{\rho_0}{\rho} \frac{(\text{IAS})^2}{g} \cot\theta. \quad (7)$$

Hence, if  $\rho$  doubles over the depth of the spiral, the turn radius will decrease by one-half.

Ideally, one would like to have the turn radius as small as possible to minimize the effects of horizontal inhomogeneities. Practically, the turn radius is dictated by the pilot's ability to safely maintain a given bank angle for long periods of time in instrument flight conditions. A bank angle of  $30^\circ$  is probably a maximum upper limit. In the examples which follow, we used bank angles of  $15^\circ$  to  $20^\circ$ .

## 4. Examples of ASD data

### a. Data and Instrumentation

To illustrate the technique we present data from the Air Force Geophysics Laboratory instrumented C-130 cloud physics aircraft which is equipped with a variety of sensors. Only the data from the Particle Measuring Systems (PMS) 200-Y probe will be discussed here. This is a 1-dimensional laser imaging probe which counts and sizes particles into 15 size

TABLE 1. Summary of spirals.

Storm	Spiral top		Spiral base	
	Height	Temperature (°C)	Height	Temperature (°C)
1	6740 m	-29	3060 m	-6
2	6940 m	-26	2320 m	0
3	5860 m	-21	3630 m	-5

categories ranging from 300 to 4500  $\mu\text{m}$ , each 300  $\mu\text{m}$  wide. Three flights are presented. Two were made off the coast of Washington (25 and 26 February 1980) and one off the coast of New Hampshire (8 March 1980). One ASD was performed on each day and these will be referred to as spirals 1, 2 and 3 respectively.

All three spirals took place in winter cyclonic storms. Spiral 1 was flown just ahead of an occluded front and spiral 2 was flown  $\sim 100$  km east of a low-pressure center. Spiral 3 was flown in the warm sector of a cyclonic storm. The soundings obtained from the aircraft data indicated that the atmosphere was slightly more stable than moist adiabatic and was saturated in all cases. The height and temperature ranges for the three spirals are given in Table 1. No significant supercooled water was detected in any of the storms.

### b. Loop-averaged spectra

Snow-size spectra averaged over a complete loop are shown in Fig. 4 for the first spiral. The spectra are labeled consecutively from the top to the bottom loops of the spiral. The spectra are approximately exponential in form such that

$$N(D) = N_0 e^{-\lambda D}, \quad (8)$$

where  $N(D)\Delta D$  is the concentration in the diameter interval  $[D, D + \Delta D]$ ,  $N_0$  is the intercept and  $\lambda$  the distribution slope. Here  $D$  is the actual particle size measured by the laser imaging probe.

The spectra from the first spiral show an initial monotonic increase in the intercept while the slope remains relatively constant through loop 12, after which there is a rapid decrease in both the slope and intercept during loops 13 and 14. The remainder of the loops show essentially no change. The vertical separation between successive loops is 200 m.

Because of the quasi-exponential behavior it is convenient to characterize the spectra by  $N_0$  and  $\lambda$  which can be done via a least-squares fit. Fig. 5 shows data from the three spirals in  $\log_{10} N_0 - \log_{10} \lambda$  (hereafter  $N_0 - \lambda$  space). The loop numbers are indicated next to the data points which are connected sequentially by a line. Environmental temperatures are indicated for places where significant changes occur.

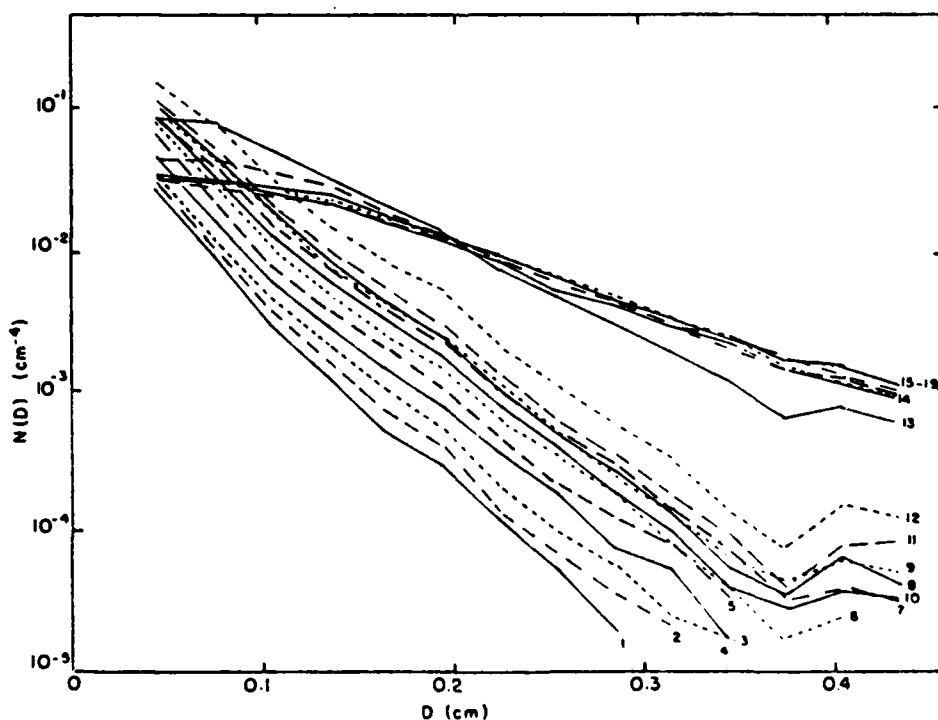


FIG. 4. Snow size spectra for spiral 1 (25 February, 1980) averaged over the various loops. Numbers on the right indicate loop numbers.

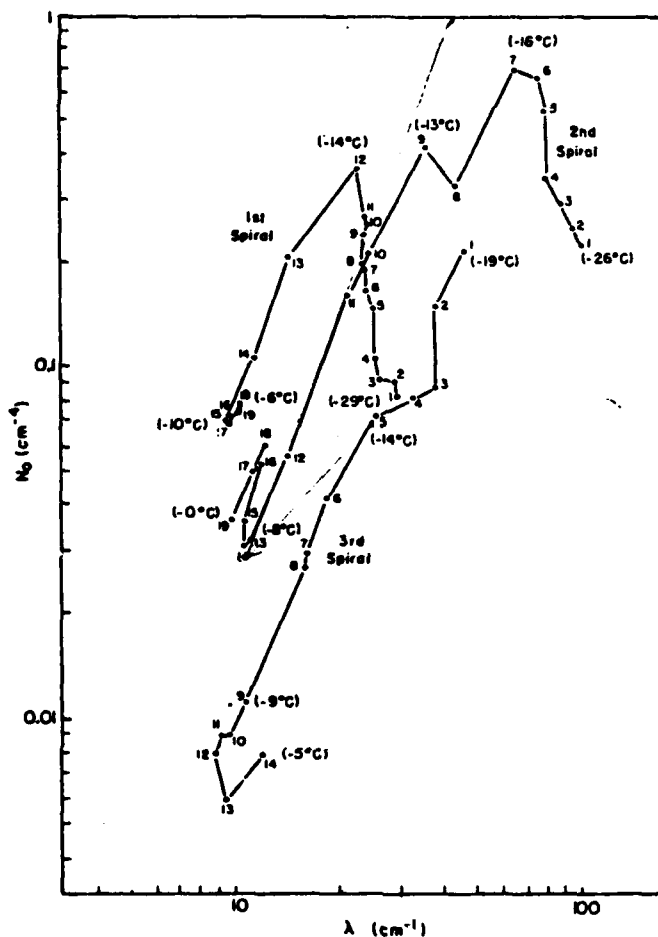


FIG. 5.  $N_0$ - $\lambda$  trajectories for the three spirals. See text for details.

This type of spectral display is convenient because a straight line in  $N_0$ - $\lambda$  space corresponds to a constant moment of an exponential distribution, since the  $j$ th moment of a spectrum is

$$M_j = \int_0^\infty D^j N_0 e^{-D} dD = \frac{N_0 \Gamma(j+1)}{\lambda^{j+1}}. \quad (9)$$

Hence in logarithmic  $N_0$ - $\lambda$  space, the moment  $M_j$  is constant along any straight line having slope  $(j+1)$ .

The behavior of the spectra in Fig. 4 can be discussed in terms of the trajectory of the spectral evolution in  $N_0$ - $\lambda$  space in Fig. 5. The first spiral is characterized by a gradual increase in  $N_0$  and a slight decrease in  $\lambda$  such that the slope of the  $N_0$ - $\lambda$  trajectory is negative, implying that all spectral moments are increasing. At loop 12 the spectral evolution changes dramatically and both  $N_0$  and  $\lambda$  decrease. Eventually  $N_0$  and  $\lambda$  assume approximately constant values. The second spiral shows a similar pattern of three stages of evolution. Stage 1 is char-

acterized by an increase in  $N_0$  accompanied by relatively little change in  $\lambda$ . Stage 2 is characterized by a rapid decrease in both  $N_0$  and  $\lambda$ . Stage 3 is marked by an apparent cessation of spectral evolution. The third spiral only reveals stages 2 and 3.

The  $N_0$ - $\lambda$  trajectories for the second stage of growth are roughly parallel for all three spirals, having slopes ranging from 1.80 to 1.95. This suggests that during this phase of spectral evolution, the sum of the diameters of snow particles is a conservative property of the distribution. These three cases also suggest that the distribution slope,  $\lambda$ , has a minimum value of  $\sim 10 \text{ cm}^{-1}$  which characterizes the third stage of evolution.

### c. Horizontal gradients in the microphysical structure

In order to examine the horizontal gradients in the size distribution, the mean diameter of all particles measured by the 200-Y spectra as a function of aircraft magnetic heading is plotted in Fig. 6 for the

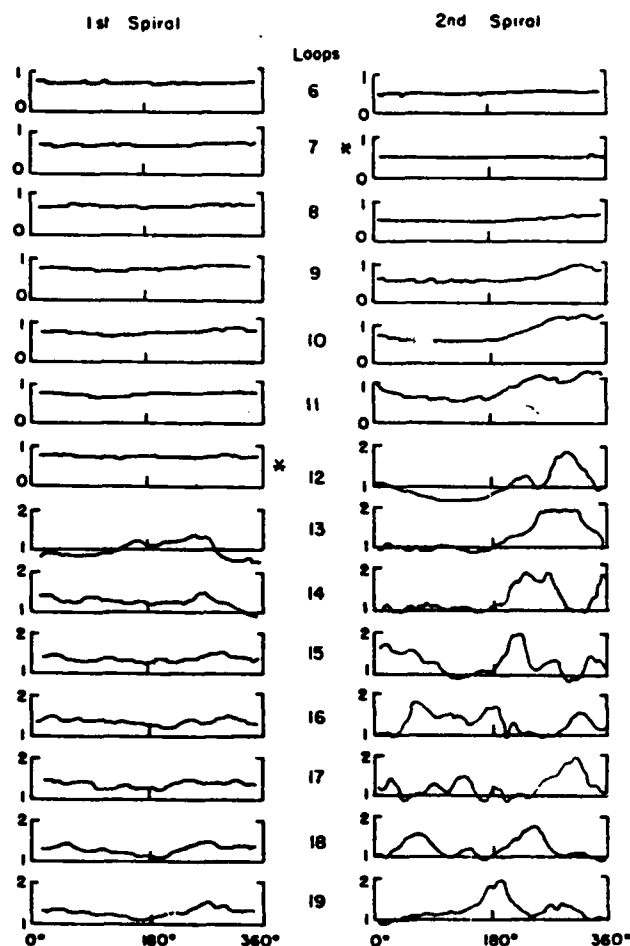


FIG. 6. Average particle diameter as a function of magnetic heading for spirals 1 and 2. Diameters in mm.

1st and 2nd spirals. Each loop is represented by a separate graph and the loops are stacked vertically in accordance with their height. The approximate diameter of each loop is 6 km. The loop in which the spectra transformed from first to second stage growth (the peak in the  $N_0$ - $\lambda$  trajectory) is indicated by a star in each case. Before the transition, the mean diameter is essentially uniform within each loop and gradually increases with depth. (Not all upper-level loops are shown). However, after the transition, horizontal inhomogeneities develop very rapidly. Note that the features are correlated from one loop to the next.

In order to examine the point-to-point behavior of the spectra, we arbitrarily divide each loop into four quadrants bounded by the cardinal directions. Ideally the spectral evolution can be studied by examining the height evolution of spectra averaged over a particular quadrant rather than over an entire loop. Fig. 7 shows an example of the  $N_0$ - $\lambda$  evolution for the second spiral for the four quadrants. The  $N_0$  scale

is different for each quadrant in order to separate the four quadrants. Note that the four  $N_0$ - $\lambda$  trajectories all show the same general features. However, the west-north quadrant starts rapid stage 2 growth earlier than the other quadrants (e.g., examine loops 9 and 10 in Fig. 6).

Fig. 7 illustrates that even if we examine portions of a loop the spectral evolution is coherent. This is consistent with the previous discussions. Also, the rapid development of horizontal gradients of mean diameter are apparently related to the fact that spectra in different regions undergo the transition from stage 1 to stage 2 at different heights.

##### 5. Physical interpretation of ASD profiles

The regular behavior of the size spectra suggests that the ASD technique is sampling a well-behaved physical process in a coherent manner. In this section we will discuss the physical implications of the observations.

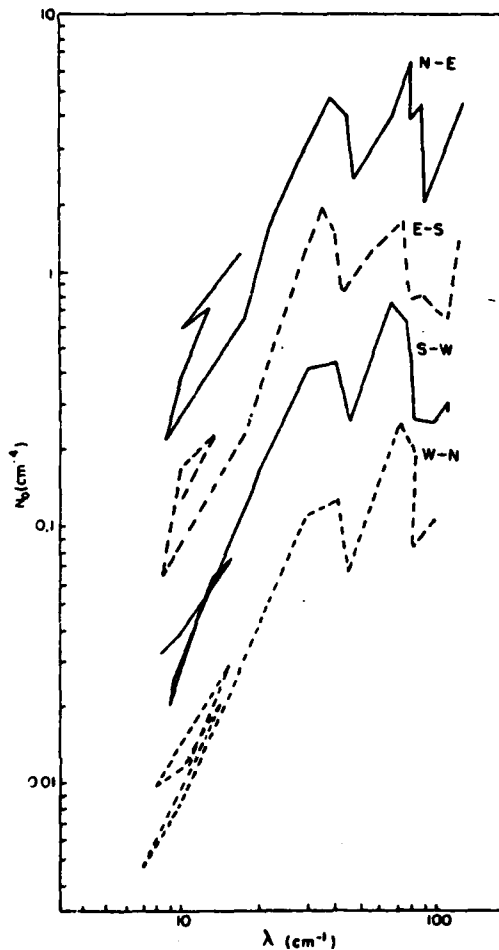


FIG. 7.  $N_0$ - $\lambda$  trajectories for the four cardinal quadrants for spiral 2. The  $N_0$  scale refers to the north-east quadrant. The other quadrants are shifted downward by one-half decade each to differentiate the data.

The effect of deposition growth on the size distribution is characterized by how the rate of change of the particle diameter depends on the particle diameter, i.e.,

$$\frac{dD}{dt} \propto D^\delta. \quad (10)$$

For  $\delta > 0$ , larger particles grow more quickly in diameter space and one would expect the distribution slope to decrease. For  $\delta < 0$ , deposition growth will cause the distribution to steepen. For snow, the particle mass varies approximately with the square of the particle diameter and the rate of change of mass is directly proportional to the particle diameter so that  $\delta \approx 0$ . To a first approximation, all sizes will grow at the same rate in diameter space and the distribution slope will remain constant. The intercept will increase since the smaller, more numerous particles will grow into larger sizes. In the absence of

a source of small particles, a lower limit to the size distribution will develop.

The first stage of particle growth (observed for spirals 1 and 2) is consistent with deposition growth. This is not to say that aggregation is not occurring, but that deposition is dominating. Note that during the first stage, the increase in  $N_0$  and the relatively slow decrease in  $\lambda$  suggests that the concentration increases. This is probably due to the growth of small particles into detectable sizes. The source of these small particles is either nucleation and/or secondary production.

The second stage of growth (in which both  $N_0$  and  $\lambda$  decrease) was observed for all three spirals. This is characteristic of aggregation which depletes small particles and creates large ones. The ASD data for spirals 1 and 2 show a very sudden transition from the dominance of deposition to aggregation. During the deposition growth phase the particles are small and collisions are rare. Eventually deposition produces a sufficient number of large particles for aggregation to commence. Once started, the large particles produced by aggregation accelerate the aggregation process and rapidly deplete the smaller particles. This accounts for the sudden transition and the very rapid evolution of the size distribution after the transition. For spirals 1 and 2 the transition occurs at  $-15^\circ\text{C}$  which is in the dendritic growth temperature range. This implies that the tendency for dendrites to form aggregates (e.g., Jiusto and Weickmann, 1973) may play a role in the transition to aggregation growth. However, the model calculations described by Passarelli (1978a,b,c) do not require a change in the particle geometry or collision efficiency to simulate the first two stages of growth.

The most puzzling behavior is the apparent sudden end to the decrease of  $N_0$  and  $\lambda$ . The spectra cease evolution when the slope reaches  $\sim 10 \text{ cm}^{-1}$ . This suggests that the depletion of small particles is balanced by a production mechanism, and that large particles produced by aggregation are somehow depleted. This is consistent with particle breakup. Another possibility is that the cessation of evolution is merely an instrumental artifact, but we are at a loss to explain how this could account for the observation that all three spirals evolve to the same limiting slope.

The fact that all the spirals evolve to the same slope suggests a collisional breakup mechanism. This hypothesis is drawn from previous work on drop coalescence and breakup which demonstrates that coalescence and collisional breakup lead to equilibrium size distributions that have the same slope, regardless of the precipitation rate (Gillespie and List, 1976; Srivastava, 1978).

Recent studies of ice particle breakup (Hobbs and Farber, 1972; Vardiman, 1978) emphasize that the coexistence of dense, rapidly falling graupel along with fragile aggregates and crystals may be neces-

sary for collisional breakup. However, our observations suggest that the presence of graupel is not required for breakup.

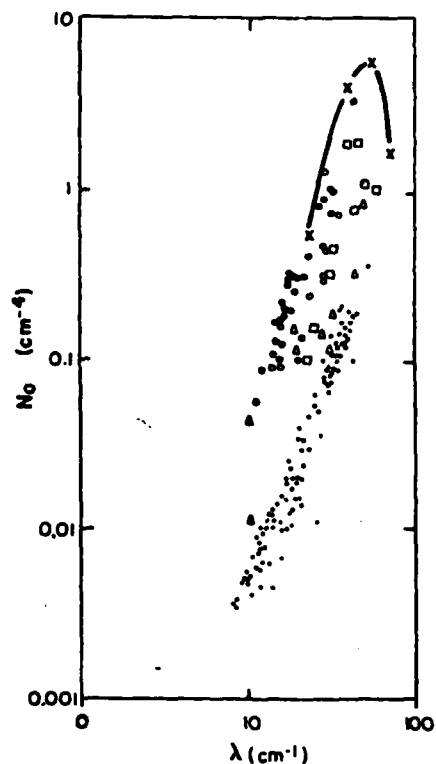
Another feature of the data which could be explained by breakup is the tendency for the small particle concentration to increase downwards. This was detected by a 1-dimensional imaging probe for the small sizes (20–300  $\mu\text{m}$ ). The downward increase in the particle concentration occurred for spirals 1 and 2 and is surprising since aggregation and deposition both deplete small particles. In the absence of supercooled liquid water and at higher temperatures at the low levels it is not likely that nucleation could have been producing the small particles in concentrations of order  $10\text{ L}^{-1}$ . Herzegh and Hobbs (1980) reached the same conclusion based on similar observations in similar storms, i.e., breakup must be the source of these numerous small ice particles.

A detailed quantitative comparison between the observed spectral evolution and model results will be presented in a later paper. It is worthwhile to mention that the first two stages of growth are depicted in Passarelli's (1978a,b,c) analytical model of deposition and aggregation. Incorporating breakup into this model is not difficult, but neither the probability of breakup nor the size distribution of fragments are known for snow. Our modeling results thus far show that one can select a breakup probability function that increases with particle size, and be assured of reaching an aggregation-breakup equilibrium. However, it seems unlikely that one can use the observed spectral evolution to determine the probability of breakup and the size distribution of fragments.

## 6. Related observational studies

Some recent observational studies of snow-size spectra have shown a spectral behavior similar to the ASD results, although the scatter is typically much greater. Passarelli (1978a,c) employed similar instrumentation but a different vertical sampling scheme. The aircraft was placed in either a constant ascent or descent while flying a constant heading. Particle size distributions were averaged over 15 s intervals. The spectra from flights on 6 and 10 March 1975 are shown in  $N_0$ - $\lambda$  space in Fig. 8. While spectra obtained via the ASD technique show a very systematic behavior with height, the spectra obtained on these two days do not. The spectra apparently lie on a line corresponding to the second stage, but the position is random. The spectra for each day are very well differentiated in  $N_0$ - $\lambda$  space which probably reflects the very different environmental conditions on the two days.

Passarelli (1978c) also averaged particle size spectra over 10 km horizontal passes at various altitudes. The data for a flight on 26 November 1975 are also shown in Fig. 8. The passes were spaced at 600 m



- 6 Mar 1975 (Passarelli 1978a)
- 10 Mar 1975 ( " " )
- × 26 Nov 1975 ( " 1978d)
- △ 22 Jan 1976 (Houze et al, 1980)
- 8 Dec 1976 ( " et al 1980)

FIG. 8. Related observational studies. See text for details.

and timed at 10 min apart—approximately the time required for snow to fall from one level to the next. The results show a first and second stage. Vertical incidence radar measurements on this day indicated fairly steady precipitation while the aircraft was sampling.

Houze *et al.* (1979, 1980) employed a similar technique by flying level passes although no attempt was made to follow snow from level-to-level. The spectra for flights on 22 January 1976 and 8 December 1976 are also shown in Fig. 8. The data are more scattered, perhaps because transient environmental conditions are manifested over the long sampling paths that were used. However, the observed spectra are still within the values from the other cases. Although the height for each spectrum is not indicated, House *et al.* (1979) show that  $N_0$  and  $\lambda$  decrease with increasing temperature. Based on the general trend that temperature increases with decreasing altitude, it can be inferred that  $N_0$  and  $\lambda$  decrease with decreasing altitude, which is in agreement with the second stage concept.

It is revealing that all observed values indicate that the slope  $\lambda$  is always  $>10 \text{ cm}^{-1}$ . This is in accord with the ASD results which suggest collisional breakup. No matter what the height and environmental conditions are, the observed  $N_0$  values are within three orders of magnitude and the  $\lambda$  values are within one order of magnitude.

### 7. Summary and concluding remarks

The coherent behavior of the observed size spectra suggests that the ASD technique can successfully trace a 1-dimensional region in which the effects of spatial and temporal gradients are minimized. This technique opens the door for more detailed quantitative comparisons between microphysical theory and observation. The physical interpretation presented here shows that snow growth evolves through at least three distinct stages which we have chosen to name the deposition, aggregation and breakup stages. Initially deposition dominates. When a sufficient number of large particles has been generated aggregation becomes dominant and produces rapid changes in the size distribution. Breakup eventually limits the production of large aggregates.

The observed spectral evolution has some interesting radar implications. The transition from deposition to aggregation might be detectable by vertical incidence radar. The transition should be marked by an increase in the height derivatives of the radar reflectivity and mean fallspeed. Deposition will generate a fairly gradual increase in these quantities, while during the aggregational stage there should be a rapid increase. Also the deposition-aggregation transition should magnify horizontal gradients of radar reflectivity and these may be detectable.

Another interesting aspect of the observations is the rapid aggregational growth which should produce changes in the mean particle fallspeed. If it were possible to perturb the deposition-aggregation transition by injecting artificially nucleated ice crystals, then it might be possible to exploit this for the redistribution of snowfall. The ASD technique could be used to check this hypothesis.

There is a definite need for a larger data base and laboratory studies of ice particle breakup processes. Since there are a number of aircraft equipped to

undertake these measurements, it is hoped that a climatology of spectral behavior can be obtained through the efforts of independent investigators.

*Acknowledgments.* The authors thank the men of the Air Force Geophysics Laboratory Cloud Physics Group and the 4950th Test Wing for their fine efforts in the field, and the University of Washington's Cloud Physics Group for their cooperation during the flights. Thanks are also due to Liz Manzi for typing and Isabelle Kole for drafting. This research was supported by the Air Force Geophysics Laboratory, Air Force Systems Command under contract No. F19628-80-C-0021.

### REFERENCES

- Gillespie, J. R., and R. List, 1976: Evolution of raindrop size distributions in steady-state rainshafts. *Preprints Int. Conf. Cloud Physics*, Boulder, Amer. Meteor. Soc., 472-477.
- Herzegg, P. H., and P. V. Hobbs, 1980: The mesoscale and microscale structure and organization of clouds and precipitation in midlatitude cyclones. II: Warm frontal clouds. *J. Atmos. Sci.*, **37**, 597-611.
- Hobbs, P. V., and R. J. Farber, 1972: Fragmentation of ice particles in clouds. *J. Rech. Atmos.*, **6**, 245-258.
- Houze, R. A., Jr., P. V. Hobbs, P. H. Herzegg and D. B. Parsons, 1979: Size distributions of precipitation particles in frontal clouds. *J. Atmos. Sci.*, **36**, 156-162.
- , D. B. Parsons and P. H. Herzegg, 1980: Reply. *J. Atmos. Sci.*, **37**, 699-700.
- Jiusto, J., and H. K. Weickmann, 1973: Types of snowfall. *Bull. Amer. Meteor. Soc.*, **54**, 1148-1162.
- Langleben, M. P., 1954: The terminal velocity of snowflakes. *Quart. J. Roy. Meteor. Soc.*, **80**, 174-181.
- Locatelli, J. D., and P. V. Hobbs, 1974: Fall speeds and masses of solid precipitation particles. *J. Geophys. Res.*, **79**, 2185-2197.
- Marshall, J. S., 1953: Precipitation trajectories and patterns. *J. Meteor.*, **10**, 25-29.
- Passarelli, R. E., Jr., 1978a: The evolution of snow-size spectra in winter storms. Ph.D. thesis, The University of Chicago, 100 pp.
- , 1978b: An approximate analytical model of the vapor deposition and aggregation growth of snowflakes. *J. Atmos. Sci.*, **35**, 118-124.
- , 1978c: An analytical model of snowflake growth. *Preprints Conf. Cloud Physics and Atmospheric Electricity*, Issaquah, Amer. Meteor. Soc., 142-147.
- Srivastava, R. C., 1978: Parameterization of raindrop size distributions. *J. Atmos. Sci.*, **35**, 108-117.
- Vardiman, L., 1978: The generation of secondary ice particles in clouds by crystal-crystal collision. *J. Atmos. Sci.*, **35**, 2168-2180.

## APPENDIX 2

## LABORATORY INVESTIGATION OF COLLISIONAL BREAKUP

In order to investigate how the collisional fragment sizes distribute, a laboratory experiment is performed. Fig. A.2.1 shows the experimental set-up. The main apparatus is a household freezer. A beaker of water with a submerged heating coil serves as the moisture supply. Two pieces of wire are mounted on clamps and are placed above the moisture supply. One of the clamps is of a movable type. Because the wires are cold, frost crystals will grow on the wire. When the crystals are large enough (at least 3 mm) the moisture supply is removed. A Kodak 7302 blue-sensitive fine grain film is then placed underneath the wires. The movable clamp is then gently moved so that the crystals on it will collide with the crystals on the fixed clamp, and the fragments will fall onto the film. The impact speed between crystals is no more than 2 cm/s. The clamps are then removed from the freezer and a blue strobe light is flashed directly above the film (Edgerton, 1981). The crystal fragments on the film cast shadow on the film which can be measured after development and enlargement. Since fine grain film is used,

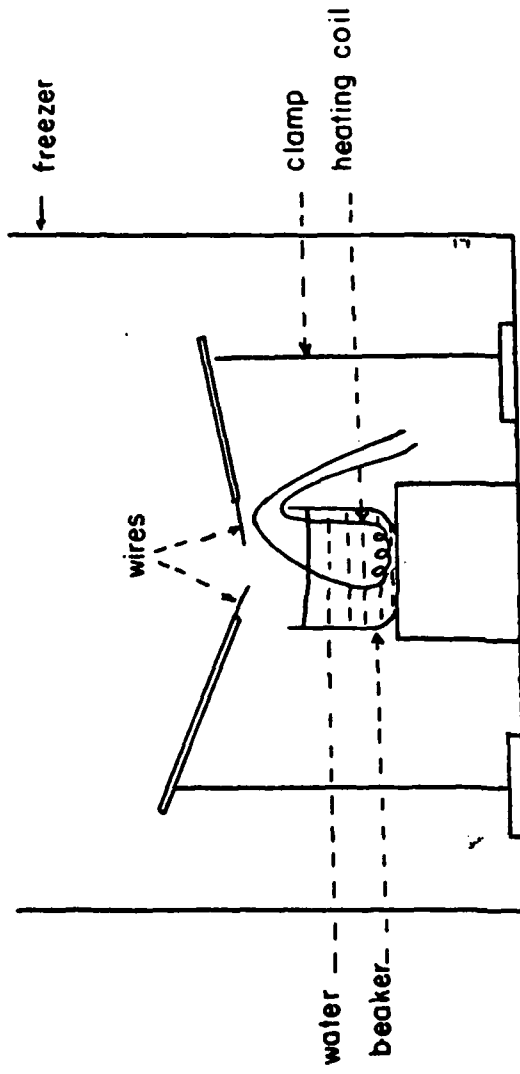


Fig.A.2.1: Laboratory set-up investigating collisional breakup

enlargements up to ten times can be made. Examples of these are shown in Figs. A.2.2 and A.2.3.

This experimental procedure has been repeated many times. The results from typical breakup events are shown in Tables A.2.1. It shows that the number of fragments is high and the fragment distribution is somewhat negative exponential. Therefore, the breakup formulation,  $S(x_1, x_2) dx = (x_1 + x_2) \Lambda^2 e^{-\Lambda x} dx$ , is reasonable.

This experiment has the drawback that crystals are forced to break up and no aggregation is allowed. In this respect, this makes the experiment not too realistic. However, this simple set-up does provide valuable information on the relative breakup size distributions and so it has served its purpose. The many small fragments resulting from collisional breakup are especially significant in cloud physics. These fragments can serve as centers for crystal growth and can also act as agents in the generation and distribution of electric charges (e.g. Latham, 1963; Latham and Stow, 1967).

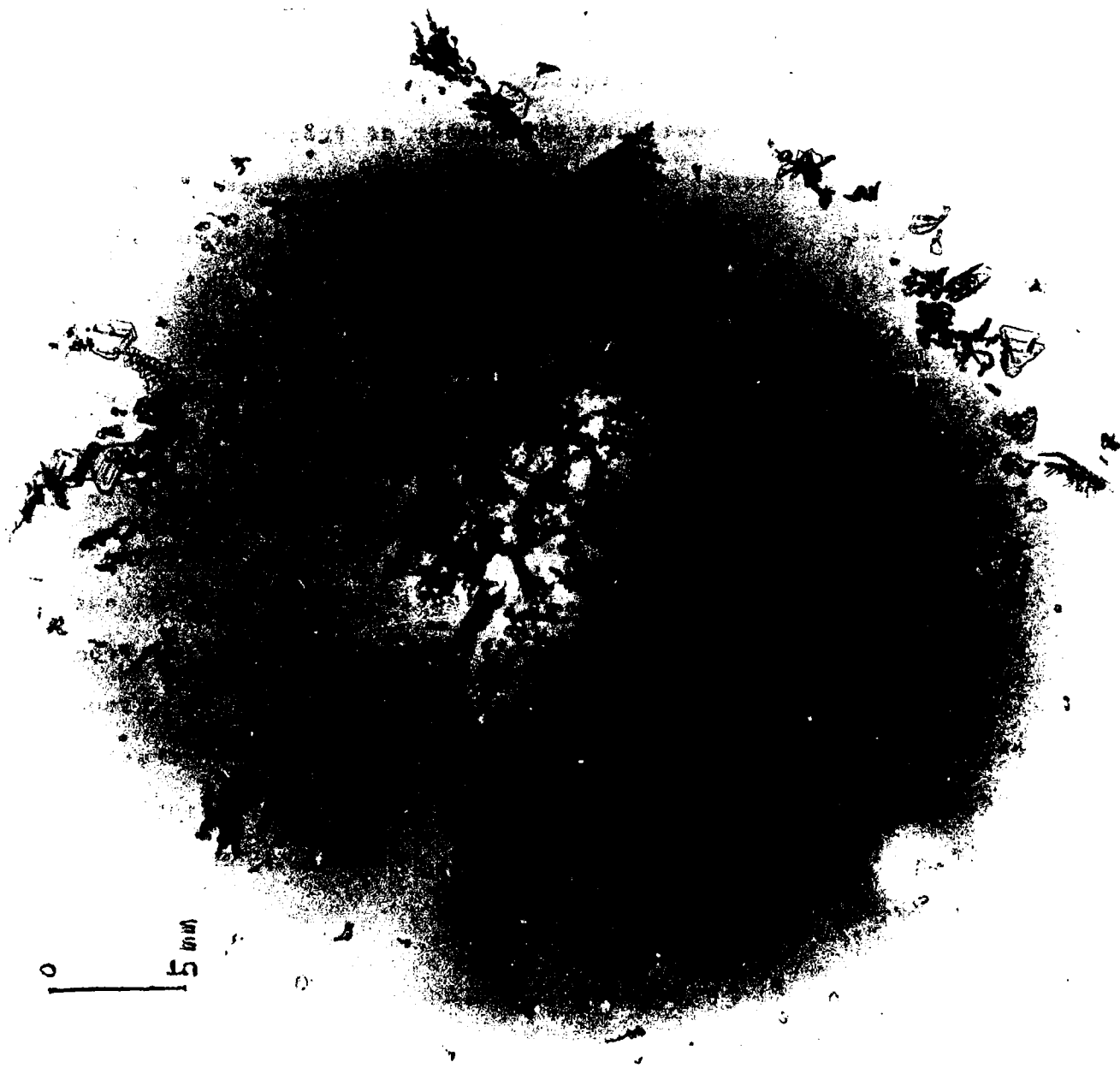


Fig. A.2.2: Sample 1 of crystal fragments

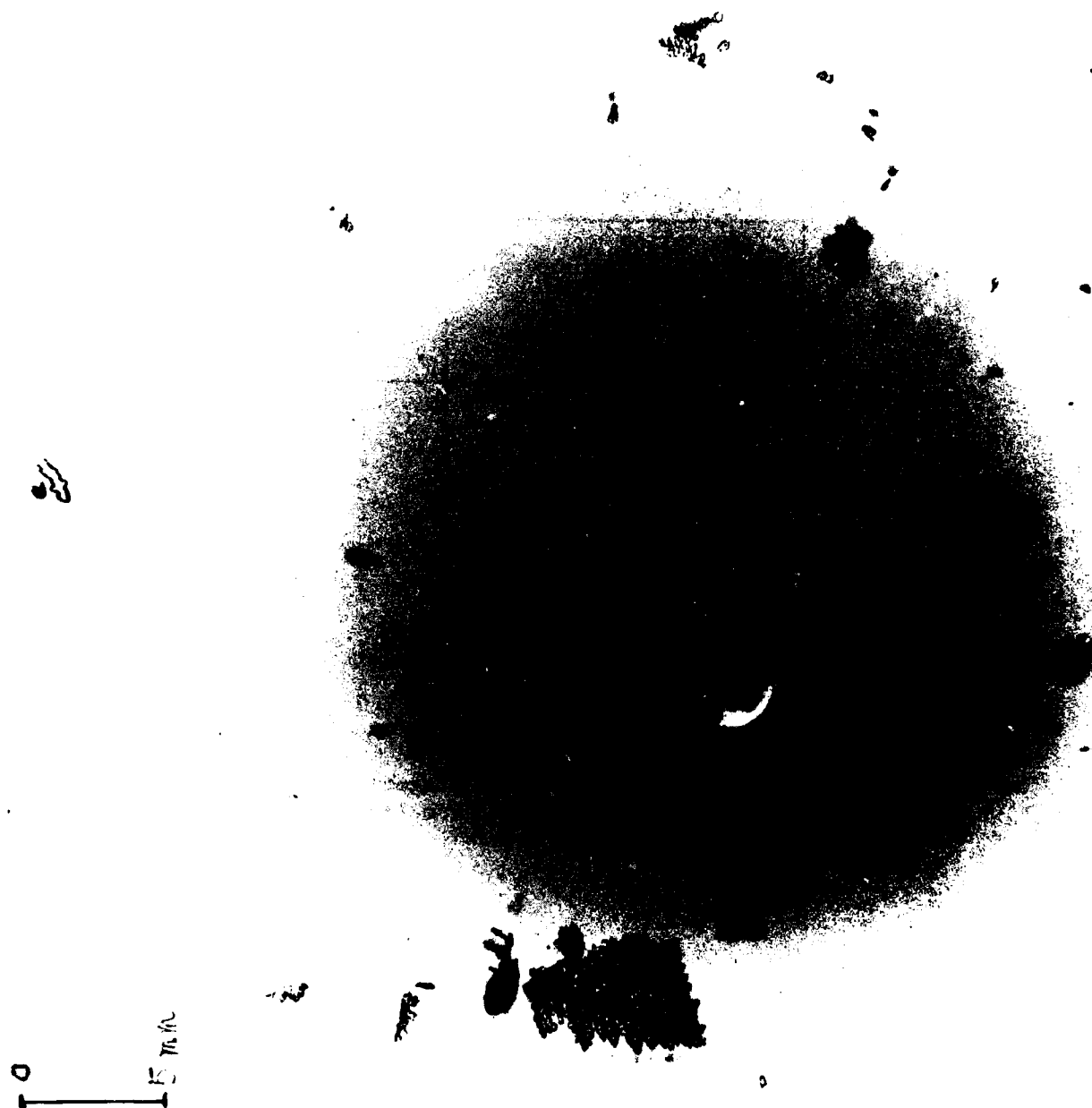


Fig. A.2.3: Sample 2 of crystal fragments

Maximum one-dimensional fragment size (micron)	Number of fragments	
	Case 1	Case 2
0 - 200	28	12
200 - 400	14	7
400 - 600	9	7
600 - 800	3	4
800 - 1000	3	4
1000 - 1200	2	2
1200 - 1400	0	1
1400 - 1600	1	2
1600 - 1800	2	3
1800 - 2000	1	2
2000 - 2200	0	1
2200 - 2400	1	0
2400 - 2600	1	0
2600 - 2800	0	0
2800 - 3000	1	1
3000 - 3200	0	1
3200 - 3400	2	1
3400 - 3600	1	0
3600 - 3800	1	0
3800 - 4000	1	1
4000 <	3	1

Table A.2.1: Samples of fragment size distribution resulting from laboratory breakup experiments

## References

- Barnes, A. A., Jr., I. D. Cohen and D. W. McLeod, 1982: Investigations of large scale storm systems. Final report, AFGL-TR-82-0169. Meteorology Division, Air Force Geophysics Laboratory, Hanscom Air Force Base, Mass. 01731. Air Force Systems Command, USAF ADA119862.
- Beard K. V. and H. R. Pruppacher, 1971: A wind tunnel investigation of the rate of evaporation of small water drops falling at terminal velocity in air. J. Atmos. Sci., 28, 1455-1464.
- Belkys, L. E., S. B. Kaplan, J. P. Lally, D. K. Roberts and T. O'toole, 1981: Development and applications of technique to process hydrometeor distribution data. AFGL-TR-81-0261. Meteorology Division, Air Force Geophysics Laboratory, Hanscom Air Force Base, Mass. 01731. Air Force Systems Command, USAF
- Blanchard, D. C. and A. T. Spencer, 1970: Experiments on the generation of raindrop-size distributions by drop breakup. J. Atmos. Sci., 27, 101-108.
- Drake, R. L., 1972: The scalar transport equation of coalescence theory: Moments and kernels. J. Atmos. Sci., 29, 537-547.
- Dyer, R. M. and M. Glass, 1982: Observed changes in ice crystal type in thick stratiform clouds. Preprints: Conf. on Cloud Physics, Nov. 15-18, Chicago. Amer. Meteor. Soc., 201-202.
- Edgerton, H. E., 1981: Use of blue-sensitive film. Photomethods, 24, 38-40.
- Fletcher, N. H., 1962: The physics of rainclouds. Cambridge University Press, 386 pp.
- Gillespie, J. R. and R. List, 1976: Evolution of raindrop size distributions in steady-state rainshafts. Preprints Int. Conf. Cloud Physics, Boulder, Amer. Meteor. Soc., 472-477.
- Gordon, G. L., J. D. Marwitz and M. Bradford, 1982: Hydrometeor distributions in California rainbands. Preprints: Conf. on Cloud Physics, Nov. 15-18, Chicago. Amer. Meteor. Soc., 207-210.
- Gunn, K. L. S. and J. S. Marshall, 1958: The distribution with size of aggregate snowflakes. J. Meteor., 15, 452-461.
- Hallet J. and S. C. Mossop, 1974: Production of secondary ice

- particles during the riming process, Nature, 249, 26-28.
- Hobbs, P. V., 1974: Ice Physics, Clarendon Press, Oxford, 837 pp.
- \_\_\_\_\_ and R. J. Farber, 1972: Fragmentation of ice particles in clouds. J. Rech. Atmos., 6, 245-258.
- Houze, R. A., Jr., P. V. Hobbs, P. H. Herzegh and D. B. Parsons, 1979: Size distributions of precipitation particles in frontal clouds. J. Atmos. Sci., 36, 156-162.
- \_\_\_\_\_, D. B. Parsons and P. H. Herzegh, 1980: Reply. J. Atmos. Sci., 37, 699-700.
- Jiusto, J. and H. K. Weickmann, 1973: Types of snowfall. Bull. Amer. Meteor. Soc., 54, 1148-1162.
- Kessler, E., 1969: On the distribution and continuity of water substance in atmospheric circulations. Meteorological Monographs Vol. 10. Amer. Meteor. Soc., Boston, Mass.
- Knollenberg, R. G., 1970: The optical array: An alternative to scattering or extinction for airborne particle size determination. J. Appl. Meteor., 9, 86-103.
- Latham, J., 1963: The electrification of frost deposits. Quart. J. R. Met. Soc., 89, 265-270.
- \_\_\_\_\_ and C. D. Stow, 1967: A laboratory investigation of the electrification of snowstorms. Quart. J. R. Met. Soc., 93, 55-68.
- Lee, I. Y. and H. R. Pruppacher, 1977: A comparative study on the growth of cloud drops by condensation using an air parcel model with and without entrainment. Pure and Appl. Geophys., 115, 523-545.
- Leighton, H. G., 1980: A comparison of a numerical model and an approximate analytical model of the growth of snowflakes. J. Atmos. Sci., 37, 1409-1411.
- Lo, K. K. and R. E. Passarelli, Jr., 1981: Height evolution of snow-size distributions. Preprint Volume: 20th Conf. on Radar Meteor., Boston. Amer. Meteor. Soc., 397-401.
- \_\_\_\_\_ and \_\_\_\_\_, 1982a: The growth of snow in winter storms: An airborne observational study. J. Atmos. Sci., 39, 697-706.
- \_\_\_\_\_ and \_\_\_\_\_, 1982b: A three-parameter snow growth model.

- Preprints, Conf. on Cloud Phys., Nov. 15-18, Chicago. Amer. Meteor. Soc., 197-200.
- Locatelli, J. D., and P. V. Hobbs, 1974: Fall speeds and masses of solid precipitation particles. J. Geophys. Res., 79, 2185-2197.
- Marshall, J. S., 1953: Precipitation trajectories and patterns. J. Meteor., 10, 25-29.
- Martner, B. E., 1982: Radar and aircraft observations of generating cells. Preprints, Conf. on cloud Phys., Nov. 15-18, Chicago. Amer. Meteor. Soc., 473-476.
- Mason, B. J., 1971: The Physics of Clouds. Clarendon Press, Oxford. 671 pp.
- \_\_\_\_\_, and C. W. Chien, 1962: Cloud-droplet growth by condensation in cumulus. Quart. J. R. Met. Soc., 88, 136-142.
- Mossop, S. C., 1976: Production of secondary ice particles during the growth of graupel by riming. Quart. J. R. Met. Soc., 102, 45-57.
- Mossop, S. C. and J. Hallet, 1974: Ice crystal concentration in cumulus clouds: influence of the drop spectrum. Science, 186, 632-634.
- Nakaya, U., 1954: Snow Crystals. Harvard University Press, 310 pp.
- Passarelli, R. E., Jr., 1978a: The evolution of snow-size spectra in winter storms. Ph.D. thesis, The University of Chicago, 100 pp.
- \_\_\_\_\_, 1978b: An approximate analytical model of the vapor deposition and aggregation growth of snowflakes. J. Atmos. Sci., 35, 118-124.
- \_\_\_\_\_, 1978c: An analytical model of snowflake growth. Preprints Conf. Cloud Physics and Atmospheric Electricity, Issaquah, WA, Amer. Meteor. Soc., 142-147.
- Pruppacher, H. R. and J. D. Klett, 1978: Microphysics of Clouds and Precipitation. D. Reidel Publishing Co., Boston. 714 pp.
- Rogers, R. R., 1979: A short course in cloud physics, second edition. Pergamon Press, Oxford, England. 232 pp.
- Scott, W. T., 1968: Analytic studies of cloud droplet

coalescence I. J. Atmos. Sci., 25, 54-65.

Srivastava, R.C., 1971: Size distribution of raindrops generated by their breakup and coalescence. J. Atmos. Sci., 28, 410-415.

\_\_\_\_\_, 1978: Parameterization of raindrop size distributions. J. Atmos. Sci., 35, 108-117.

Takeuchi, D.M., 1978: Characterization of raindrop size distributions. Preprints: Conf. on Cloud Physics and Atmos. Electricity, Issaquah, Amer. Meteor. Soc., 154-161.

Twomey, S., 1959: The nuclei of natural cloud formation. Pt. II: The supersaturation in natural clouds and the variation of cloud droplet concentration. Geofisica Pura e Applicata, 43, 243-249.

Uplinger, W.G., 1981: A new formula for raindrop terminal velocity. Preprint Vol: 20th Conf. on Radar Meteor., Boston. Amer. Meteor. Soc., 389-391.

Vardiman, L., 1978: The generation of secondary ice particles in clouds by crystal-crystal collision. J. Atmos. Sci., 35, 2168-2180.

Young, K.C., 1975: The evolution of drop spectra due to condensation, coalescence and breakup. J. Atmos. Sci., 32, 965-973.

END